Advanced Powder Materials 5 (2026) 100373

Contents lists available at ScienceDirect

Advanced Powder Materials

journal homepage: www.keaipublishing.com/en/journals/advanced-powder-materials

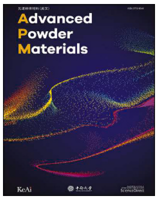

Harvesting energy from friction: the revolutionary decade of triboelectric nanogenerators

Uday Kumar Khanapurarm[a,1], Gokana Mohana Rani[b,1], Swati Panda[c,1], Thitirat Charoonsuk[e,f,1], Krystian Mistewicz[g,1], Sugato Hajra[c,*], Kushal Ruthvik Kaja[d], Reddicherla Umapathi[b], Saichon Sriphan[e,h], Jakub Jała[g,j], Haranath Divi[a], Albert Smalcerz[j], Mohamed Belal[d], Pannur Jaahnavi[b], Moein Safarkhani[b], Hanseung Kim[b], Yogendra Kumar Mishra[k,**], Hoe Joon Kim[d], Yun Suk Huh[b,***], Naratip Vittayakorn[e,l,****], Bartłomiej Nowacki[i,j,*****], Sai Kishore Ravi[m], Stephen James Eichhorn[n], Monica F. Craciun[o], Ana Borras[p], Hamideh Khanbareh[q], Jiaqian Qin[r,******], Rakesh Kumar Rajaboina[a,*******]

[a] Department of Physics, Energy Materials and Devices lab, National Institute of Technology, Warangal, India
[b] NanoBio High-Tech Materials Research Center, Department of Biological Sciences and Bioengineering, Inha University, Incheon, 22212, Republic of Korea
[c] Department of Electrical Engineering and Computer Science, Daegu Gyeongbuk Institute of Science and Technology, Daegu, 42988, Republic of Korea
[d] Department of Robotics and Mechatronics Engineering, Daegu Gyeongbuk Institute of Science and Technology, Daegu, 42988, Republic of Korea
[e] Advanced Materials Research Unit, School of Science, King Mongkut's Institute of Technology Ladkrabang, Bangkok, 10520, Thailand
[f] Department of Materials Science, Faculty of Science, Srinakharinwirot University, Sukhumvit 23, Watthana, Bangkok, 10110, Thailand
[g] Institute of Physics – Center for Science and Education, Silesian University of Technology, Krasińskiego 8, 40-019, Katowice, Poland
[h] Faculty of Science, Energy and Environment, King Mongkut's University of Technology North Bangkok, Bangkok, 10800, Thailand
[i] Joint Doctoral School, Silesian University of Technology, Akademicka 2A, 44-100, Gliwice, Poland
[j] Department of Industrial Informatics, Faculty of Materials Science, Silesian University of Technology, Krasinskiego 8, 40-019, Katowice, Poland
[k] Smart Materials, Nano SYD, Mads Clausen Institute, University of Southern Denmark, Alsion 2, 6400, Sønderborg, Denmark
[l] Department of Chemistry, School of Science, King Mongkut's Institute of Technology Ladkrabang, Bangkok, 10520, Thailand
[m] School of Energy and Environment, City University of Hong Kong, Tat Chee Avenue, Kowloon, Hong Kong Special Administrative Region
[n] Bristol Composites Institute, School of Civil, Aerospace and Design Engineering, University Walk, University of Bristol, BS8 1TR, United Kingdom
[o] Centre for Graphene Science, Faculty of Environment, Science and Economy, University of Exeter, United Kingdom
[p] Nanotechnology on Surfaces and Plasma Laboratory, Materials Science Institute of Seville (CSIC-US), Américo Vespucio 49, 41092, Seville, Spain
[q] Department of Mechanical Engineering, University of Bath, Bath, BA2 7AY, United Kingdom
[r] Center of Excellence on Advanced Materials for Energy Storage, Department of Materials Science, Faculty of Science, Chulalongkorn University, Bangkok, 10330, Thailand

ARTICLE INFO

Keywords:
Nanogenerators
Energy harvesting
Contact electrification
Triboelectricity
Self-powered system

ABSTRACT

Triboelectric nanogenerators (TENGs) have rapidly developed into a transformative energy harvesting technology, enabling self-powered, sustainable electronic systems. This review offers the first comprehensive, multidisciplinary perspective that connects the physics of triboelectric charge transfer with material innovation, device engineering, and real-world applications. We systematically categorize and measure the triboelectric series across a wide range of materials, including polymers, 2D materials, MOFs, perovskites, cellulose, and biodegradable frameworks, using experimentally validated methods. In addition to traditional approaches, this

---

* Corresponding author.
** Corresponding author.
*** Corresponding author.
**** Corresponding author. Advanced Materials Research Unit, School of Science, King Mongkut's Institute of Technology Ladkrabang, Bangkok, 10520, Thailand.
***** Corresponding author. Joint Doctoral School, Silesian University of Technology, Akademicka 2A, 44-100, Gliwice, Poland.
****** Corresponding author.
******* Corresponding author.

E-mail addresses: sugatohajra@dgist.ac.kr (S. Hajra), mishra@mci.sdu.dk (Y.K. Mishra), yunsuk.huh@inha.ac.kr (Y.S. Huh), naratip.vi@kmitl.ac.th (N. Vittayakorn), Bartlomiej.Nowacki@polsl.pl (B. Nowacki), jiaqian.q@chula.ac.th (J. Qin), rakeshr@nitw.ac.in (R.K. Rajaboina).

[1] These authors contributed equally to this work.

https://doi.org/10.1016/j.apmate.2025.100373
Received 27 August 2025; Received in revised form 30 October 2025; Accepted 3 November 2025

work highlights emerging strategies such as machine learning-guided material discovery, 3D printing, and advanced structural engineering to improve charge retention, durability, and power output. Unlike existing reviews, it uniquely combines theory and application insights, presents diverse uses from biomedical sensing and environmental monitoring to underwater communication and mechanoluminescence, and outlines a forward-looking plan for sustainable energy harvesting. This comprehensive synthesis serves as an essential resource for researchers and technologists designing next-generation TENGs and multifunctional self-powered devices.

1. Introduction

The ‘Amber effect’, a millennium-long phenomenon, was detected initially when wool and amber were rubbed together, resulting in an electrostatic charge [1]. This effect garnered substantial scientific interest in the twentieth century because of its potential applications in energy harvesting, and it laid the groundwork for triboelectric power. Triboelectricity, or contact electrification, occurs in various materials, including metals, insulators, and semiconductors [1,2], when two dissimilar substances come into contact and separate. This process results in one material gaining a positive charge and the other a negative charge, generating static electricity [3]. The fundamental processes governing charge transfer are poorly understood and very unpredictable despite their crucial role in electrostatic events. Initial scientific endeavors sought to elucidate triboelectricity via electron transfer and the work functions of materials [4,5]. Subsequent studies have indicated that ion transport, material exchange, and mechanochemical interactions may all be significant factors. Environmental considerations, surface morphologies, and air breakdown effects all influence triboelectric charge, making it one of the most difficult unresolved subjects in physics and materials research [6]. Triboelectricity, which was previously thought to have a negative impact on the electric and electronic industries, had beneficial consequences as well, and it transformed daily living in the late twentieth century [7]. The tribocharging effect is the core principle behind advancements in laser printing and photocopying technology [8,9]. Wang et al. (2012) created the first triboelectric generator, an energy harvesting technology that leverages triboelectric charging and electrostatic induction to convert mechanical energy into electrical energy [10]. This breakthrough is widely regarded as a milestone in the field, paving the way for the efficient conversion of abundant and ubiquitous, low-frequency environmental vibrations into valuable electrical energy [11]. Because triboelectric charging is important in both beneficial technologies (e.g., self-powered electronics, sensors, and nanogenerators) and negative effects (e.g., sparking from charge build up leading to industrial explosions, electronic failures), a better understanding of charge retention and suppression mechanisms is required for advancing practical applications and mitigating potential risks.

Over the last few decades, microelectronic systems have become important in shaping the electronics industry. This industry is paving the way for daily small-scale systems in human life and has become an integral part of automation, digitalization, and intelligence [12,13]. As a result, the power consumption for the distributed systems has dramatically changed from a few mW to μW to power these systems. The mW and μW power supplies have become essential in order to reduce the size of small-scale devices [14]. The reliance on battery networks for power results in size limitations and sustainability challenges. Although microsystems and Internet of Things (IoT) devices have advanced in portability, intelligence, and miniaturization, they encounter a major obstacle in sourcing sustainable power. While flexible batteries are common, concerns about sustainability, pollution, and lifespan restrict their practicality. Therefore, autonomous microsystems require efficient, renewable, and adaptable energy solutions [15].

The IoT exemplifies the energy challenge by utilizing extensive sensing networks to detect environmental changes and convert these changes into electronic signals. Signals traverse an interconnection network for processing prior to arriving at the terminal network, which initiates device responses. The operation of trillions of autonomous sensors highlights the need for efficient energy utilization, driving the development of innovative and sustainable energy solutions [15]. Utilizing ambient energy at micro- and milli-scale levels enables the creation of fully integrated, self-powered devices. Methods such as piezoelectric, triboelectric, thermoelectric, and photovoltaic effects convert environmental energy into electricity, eliminating the reliance on batteries [16]. These techniques effectively harness energy from light, temperature gradients, and electromagnetic fields, providing a sustainable and cost-effective power source for low-energy microsystems [17].

In the past decade, extensive research has explored various materials for triboelectric energy harvesting, including polymers, layered materials, metal-organic frameworks, dielectrics, metal oxides, conductive materials, ceramics, biodegradable and waste-based materials, and textiles [3,18–27]. Apart from the materials aspect, various potential applications have been explored based on TENGs and reported in the literature, for example, wearable devices, IoT-based applications, self-powered devices, self-powered sensing devices, multisource energy harvesters, bio-medical applications, self-healing, actuators, drug delivery, photodetectors, electro-luminescent, self-powered catalysis, self-powered energy storage, etc. [16,28–33]. The growing interest in this field is reflected in the vast number of review articles, approximately 500, covering topics from material selection to application

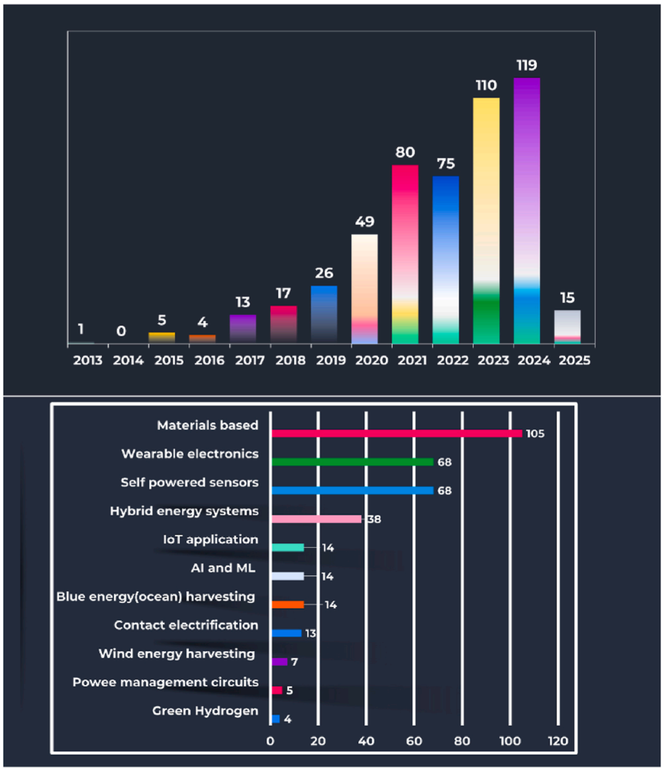

Fig. 1. Number of review papers published on TENGs, and classification of TENG-based review papers over the period 2013–2025. (The data were obtained from Web of Science and Scopus using keywords “triboelectric nanogenerator”, “TENG review”, and “energy harvesting review” for 2013–2025.)

strategies, as depicted in Fig. 1a. However, most of these review articles are limited to mentioning the specific areas presented in Fig. 1b. There are few reviews that provide a comprehensive overview of the full details of TENG operation and functioning. This review article provides a comprehensive overview of TENG technology, encompassing all essential aspects, from materials to device structures, and performance optimization to applications. Importantly, we highlight the characterization tools (Fig. 2) essential for evaluating TENG performance, thereby offering researchers practical guidance that is often overlooked in earlier reviews. The novelty of the present manuscript lies in a comprehensive approach that links the fundamentals of TENGs to advanced applications. Integrating insights on material selection, triboelectric series classification of each type of material, device characterization, and performance enhancement strategies serves as a valuable resource for researchers working in this field. Moreover, advanced techniques such as artificial intelligence (AI)-driven material selection, machine learning advancements, and multifaceted energy harvesting methods provide a complete reference for researchers in this field on energy harvesting and self-powered systems.

2. Tribocharge and the triboelectric series

The triboelectric series is an important and commonly used method for evaluating the triboelectric properties of materials, classifying them based on their ability to lose or gain electrons [34]. However, this classification, based on electron affinities, remains qualitative, as it primarily accounts for charge polarity rather than charge quantity, which is crucial for the design of high-performance TENGs. Recent advances in experimental and theoretical models have yielded new insights into charge transfer dynamics while simultaneously revealing unforeseen behaviors that challenge traditional models. For instance, identical materials might acquire opposite charges upon contact, defying predictions based solely on material composition [35,36]. Despite extensive investigations, triboelectric charging persists in an unresolved scientific challenge, with experimental discrepancies underscoring the complexity of its underlying mechanisms. Historically, electron transfer was deemed the primary cause of charge generation. However, current research studies indicate that ion transfer, material exchange, and mechanochemical interactions also play significant roles. Moreover, triboelectric charging is affected by surface characteristics, ambient conditions, and material deformation, rendering charge transfer exceedingly unpredictable. Additionally, non-uniform charge distributions on triboelectrically charged surfaces demonstrate that localized effects, surface imperfections, and nanoscale interactions profoundly impact charge behavior [37].

Air breakdown is a significant limitation, which causes premature charge dissipation and restricts the maximum charge density that can be achievable in TENGs. Early investigations posited that the charges induced in the external circuit were matched to those generated by triboelectrification. However, subsequent findings revealed that air breakdown transpires in all working modes of TENGs, resulting in charge loss prior to complete induction in the external circuit. As a result, the measured charge density is often lower than the true triboelectric charge density, which has a direct impact on energy conversion efficiency [38]. Air breakdown happens when a strong electric field ionizes surrounding air molecules, leading to charge leakage through spark discharge or gradual atmospheric ionization. Although spark discharge is readily identifiable, the slow dissipation of charge presents a more nuanced and intricate challenge for quantification [38].

Recent studies emphasize that suppressing air breakdown is crucial for optimizing charge retention and TENGs efficiency. Researchers have explored various charge storage enhancement techniques, including operating in vacuum environments, using thin dielectric layers, and implementing external charge excitation strategies to mitigate charge loss [39]. Several investigations have demonstrated the impact of air breakdown suppression, as illustrated in Fig. 3a–f [38]. Fig. 3a outlines the process of charge accumulation and decay, showing how triboelectric charges dissipate over time due to uncontrolled air breakdown. Fig. 3b compares charge density with and without air breakdown, illustrating that suppressing air ionization significantly improves charge retention. Fig. 3c establishes a direct correlation between charge density and energy density, reinforcing that better charge retention enhances overall TENG performance. Further studies have examined structural optimizations, as depicted in Fig. 3d, where material modifications enhance charge storage efficiency, and Fig. 3e, which demonstrates how thin dielectric layers reduce air breakdown effects. Additionally, Fig. 3f presents charge excitation techniques, which increase charge density beyond the theoretical limits of Paschen's Law, improving overall energy harvesting efficiency. These findings underscore the importance of effective charge retention strategies in advancing high-performance TENGs, emphasizing the need for continued research into material engineering, environmental control, and innovative charge transfer mechanisms to optimize energy conversion and ensure the practical implementation of triboelectric systems.

Zhao et al. reported a significant advancement in charge retention by demonstrating the extraction of direct current (DC) output from TENGs, offering advantages over traditional alternating current (AC) TENGs, which rely on electrostatic induction for charge transfer [34]. DC-TENGs leverage contact electrification and electrostatic breakdown to enable continuous charge transfer, eliminating the need for rectifiers and minimizing electromagnetic interference, thereby enhancing energy conversion efficiency. The effective charge density in DC-TENGs is influenced by surface charge density (σ_s), friction coefficient, polarization intensity, and air breakdown effects, where controlled air breakdown plays a crucial role in charge extraction and retention. To optimize performance, Zhao et al. proposed selection rules for triboelectric materials, considering friction coefficient, dielectric properties, and polarization intensity, which directly impact charge transfer efficiency [40,

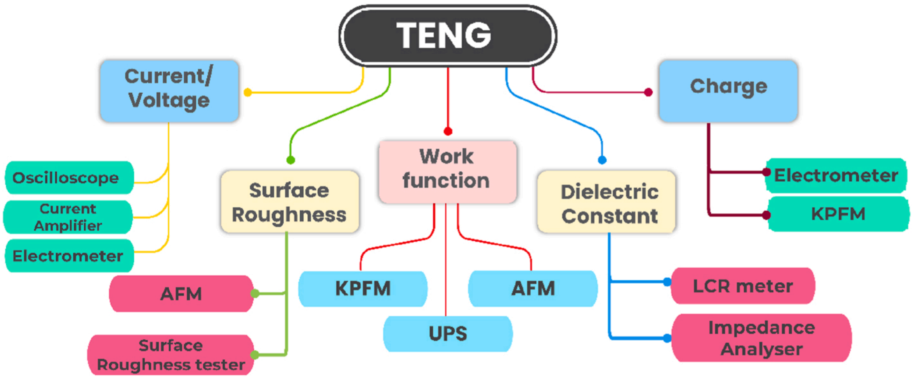

Fig. 2. TENG characterization tools.

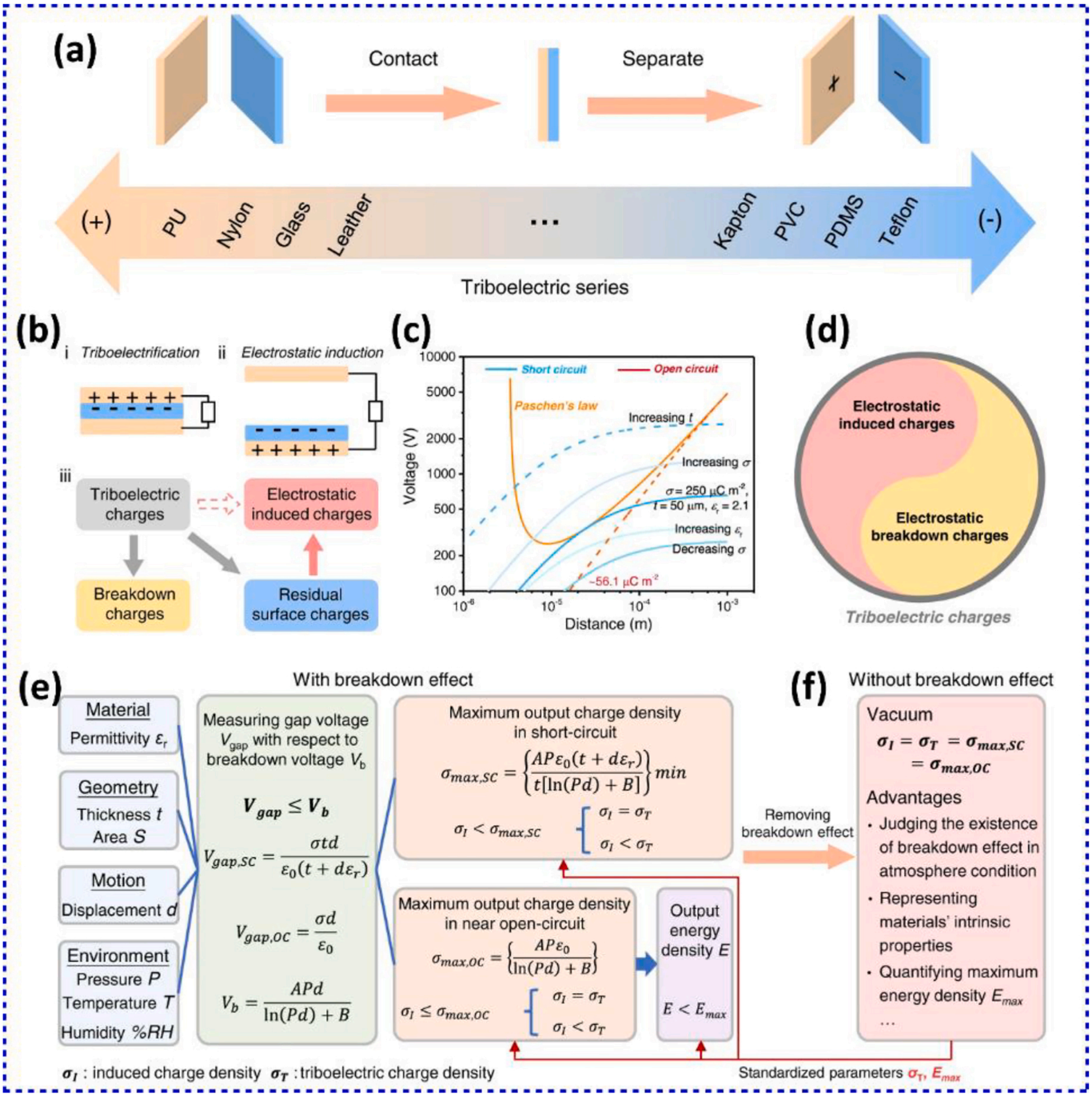

Fig. 3. (a) A schematic qualitative triboelectric series of PU, polyurethane; PVC, polyvinyl chloride; PDMS, polydimethylsiloxane. (b) Illustration of the working mechanism and TENG charge transferring process. (c) Relationship of the breakdown and gap voltages across the triboelectric layers at various distances in TENGs. (d) A schematic showing the relationship between triboelectric charges and induced charges with the existence of a breakdown effect. (e) The comprehensive strategy for assessing TECD with the existence of a breakdown effect. Especially in open circuits, it is difficult to restrict the breakdown effect. (f) Take the vacuum as an example showing the strategy for assessing TECD after removing the breakdown effect, and the potential advantages of TECD in vacuum [38]. Creative Commons Attribution 4.0 International License. Reprinted with permission from Ref. [38]. Copyright © 2022, Springer Nature.

41]. Among the evaluated materials, polyvinyl chloride (PVC) was identified as a high-performance triboelectric material, achieving a record-breaking surface charge density (~8.80 mC/m^2). The ability of PVC-based DC-TENGs to efficiently retain charge and utilize air breakdown underscores the importance of material selection and structural engineering in enhancing TENG performance. Further, unlike AC-TENGs, which depend on cyclical electrostatic induction, DC-TENGs incorporate a direct charge collection mechanism that relies on air ionization in a strong electric field to facilitate continuous charge migration across an air gap. This controlled air breakdown process not only improves charge retention and transfer efficiency but also ensures stable and reliable energy output, making DC-TENGs highly promising for self-powered electronics, IoT devices, and distributed energy systems. It is also worth mentioning that breakdown discharges generated by triboelectrification can be utilized for wireless signal transmission, leveraging the SWISE (self-powered wireless sensing e-sticker) configurations reported for the first time by Zi et al. [42]. Therefore, selection rules and the triboelectric series will play a major role in the performance of TENGs.

2.1. *Triboelectric series/charge measurement methods*

Zhou et al. introduced a standardized and quantitative method for measuring the triboelectric charge density (TECD) of various materials, establishing a more precise triboelectric series [40]. Traditionally, triboelectric ranking has been qualitative, leading to inconsistencies in material classification due to environmental factors and variations in experimental techniques. This research overcomes these challenges by using a controlled experimental setup and a liquid mercury reference electrode to ensure uniform contact with test materials.

The core of the method lies in using liquid mercury as a contact material due to its unique properties. Mercury forms a highly uniform and consistent contact with solid surfaces, eliminating the uncertainties caused by surface roughness in solid-solid contact experiments (**shown in** Fig. 4a). Unlike solid materials, which have varying levels of elasticity and stiffness that affect contact pressure, mercury's liquid state ensures that the same pressure is applied uniformly across all materials tested. Additionally, the high conductivity of mercury facilitates precise charge transfer measurements.

To further improve measurement accuracy, the entire experimental setup is housed within a glove box filled with ultra-pure nitrogen gas. This controlled environment maintains a constant temperature (20 ±1 °C), pressure (∼1 atm), and humidity (≤0.43%), preventing charge dissipation due to air ionization or moisture absorption. The system is designed to eliminate external noise sources through the use of a Faraday cage, shielded electric wires, and a well-grounded setup, ensuring that the measurements remain reliable and reproducible (Shown in Fig. 4a).

The measurement technique involves periodic contact and separation between the test material and the liquid mercury surface. The linear motor moves the sample in a controlled vertical motion, making contact with the mercury and then separating from it. During contact, electrons transfer between the two materials based on their triboelectric properties. As the material is lifted, a potential difference is created, leading to charge induction. The electrometer (in this particular assembly, a high precision electrometer, Keithley 6514) records the transferred charge under both open-circuit voltage and short-circuit current conditions, allowing the TECD to be accurately determined.

The TECD is calculated using the equation:

$$\mathrm{TECD} = \frac{Q}{A}\ldots\ldots\ldots\ldots\ldots\ldots\ldots\ldots \quad (1)$$

where Q represents the total charge transferred, and A is the contact area. To provide a reference scale, the TECD values are normalized against PTFE, a widely used triboelectric material. The normalized triboelectric charge density (α) is defined as:

$$\alpha = \frac{\text{TECD of the material}}{\text{TECD of PTFE}}\ldots\ldots\ldots\ldots \quad (2)$$

A comprehensive study was conducted on over 50 different polymer materials, ranking them based on their ability to gain or lose electrons upon contact with mercury. The results revealed a detailed triboelectric series, with materials such as PTFE, PVC, and polystyrene exhibiting strong negative TECD values, while Buna-N rubber and other elastomers displayed positive TECD values. The ranking of materials in the series indicates their tendency to either donate or accept electrons, allowing for better predictability of triboelectric interactions.

This study marks a significant advancement in triboelectric research by providing a quantitative, reproducible method for evaluating material properties. The use of a liquid-metal reference, controlled environment, and precise instrumentation ensures reliable measurements, reducing the uncertainties that have historically plagued triboelectric studies. By establishing a universal standard for triboelectric charge density, this work sets the foundation for more accurate material selection and further exploration of triboelectric phenomena in fundamental materials science.

In another study, Cruise et al. introduce a comprehensive method for quantifying triboelectric charge accumulation and saturation, emphasizing the impact of dielectric breakdown on charge limitation [43]. The study employs an automated charge measurement system, utilizing a modified Faraday cup integrated with an electrometer for precise real-time charge tracking (shown in Fig. 4b**)**. Unlike previous triboelectric studies, the researchers analyzed charge dynamics under both atmospheric and vacuum conditions, demonstrating that charge saturation in air is primarily governed by electrical breakdown of air molecules, whereas in vacuum, electrostatic adhesion becomes the limiting factor.

A key innovation of the study is its automated particle rotation system, ensuring consistent triboelectric contacts while mitigating external

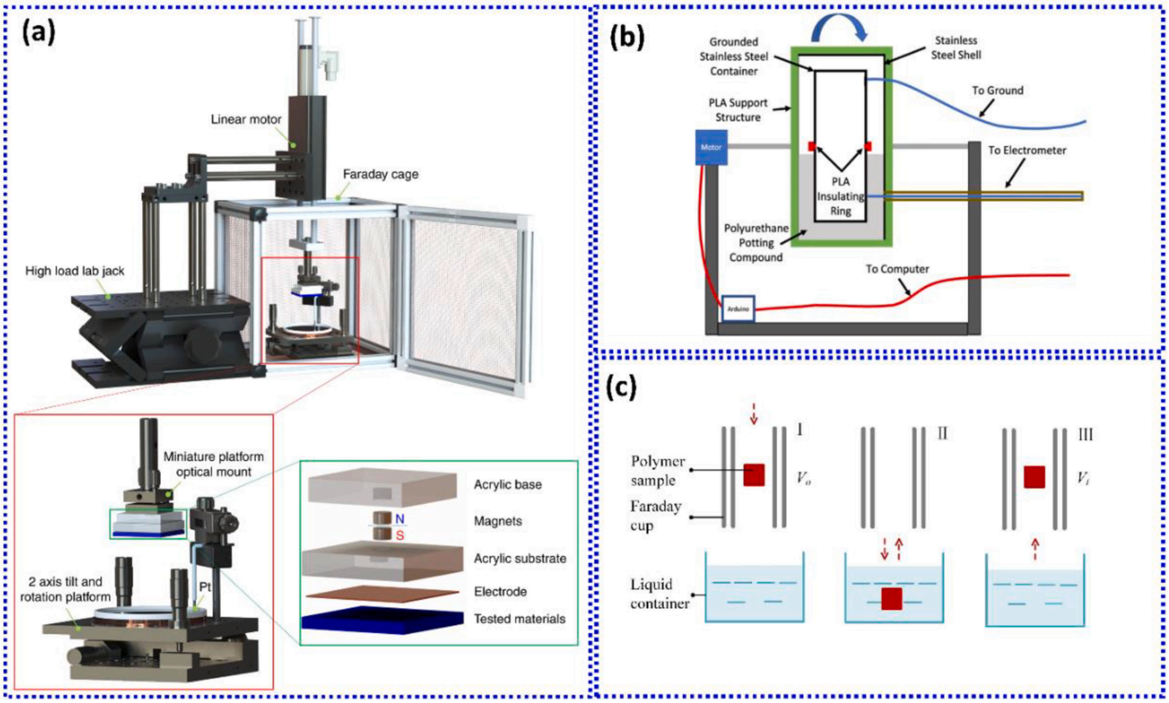

Fig. 4. (a) Experimental set-up for the triboelectric series measurement. The whole measurement was set in a glove box filled with ultra-high purity of nitrogen gas at fixed temperature, pressure, and humidity. Reprinted with permission [40] Creative Commons Attribution 4.0 International License. Copyright © 2019 Springer Nature. (b) Schematic representation of the automated simultaneous triboelectric charging and charge measurement system, Creative Commons Attribution 4.0 International License. Reprinted with permission [43]. Copyright © 2023 Springer Nature. (c) Schematic of the triboelectrification and charge measurement process using NaCl solution, Reprinted with permission [44]. Copyright © 2024 Elsevier.

interference through electromagnetic shielding. Additionally, Cruise et al. provide a mathematical model validating charge accumulation trends, revealing that particle size and environmental conditions significantly influence triboelectric charge density. Their findings contribute to a deeper understanding of charge saturation mechanisms in insulating materials, offering practical insights for electrostatic control in industrial processes. This work advances triboelectric research by bridging theoretical modeling and experimental validation, making it a pivotal reference for future studies on charge accumulation in various environments.

In 2024, Chen et al. reported a solid–liquid triboelectric charge measurement method to quantify charge transfer between 14 common polymers and a NaCl aqueous solution [44]. The experiment was performed in insulated beakers under controlled environmental conditions (temperature: 25 ± 3 °C, humidity: 20 ± 5 % RH) to ensure repeatability (shown in Fig. 4c). Each sample was ultrasonically cleaned with DI water and ethanol, followed by a 24-h resting period to minimize initial surface charges. The polymer samples were then immersed into 3.5 wt% NaCl solution at a fixed speed of 12 mm/s, held in the solution for 5 s, and then withdrawn. After each triboelectrification event, the polymer samples were immediately placed into a Faraday cup to measure their surface charge. The charge transfer density (σ_t) was determined using the formula:

$$\sigma_t = \frac{C_m \times (V_t - V_0)}{(1 - r_l) \times S} \ldots\ldots\ldots\ldots\ldots\ldots \quad (3)$$

where C_m is the capacitance of the Faraday cup, V_t and V_0 are the measured potential differences before and after the experiment, r_l is the leakage ratio, and S is the contact area. This precise and controlled approach enabled the quantification of triboelectric charge transfer between polymers and aqueous solutions, helping to establish a triboelectric series for polymer-liquid interactions [45].

“In summary, the three triboelectric charge measurement techniques each offer unique capabilities suited to specific experimental needs. The liquid mercury contact method provides highly uniform and reproducible contact, unaffected by surface roughness, making it ideal for accurate triboelectric series positioning. However, it requires strict environmental control and careful handling due to mercury's toxicity. The Faraday cup system, a form of direct charge measurement, enables real-time monitoring of net charge buildup and saturation, making it suitable for studies of bulk materials and charge dynamics. However, it is less compatible with flexible or thin-film samples. Meanwhile, the NaCl solution-based liquid contact method enables direct measurement of surface potential at solid–liquid interfaces, particularly in aqueous or biologically relevant conditions; however, its sensitivity to wettability and ionic adsorption can impact accuracy. Together, these complementary methods form a comprehensive toolkit for studying triboelectric behavior across various material systems and application environments from dry solid–solid interfaces to liquid interfaces and dynamic mechanical systems”.

2.2. *Triboelectric series of different materials*

2.2.1. *2D layered materials*

The triboelectric properties of 2D layered materials have recently garnered significant attention due to their potential applications in flexible, lightweight, and high-performance TENGs [5,46]. Seol et al. systematically investigated the triboelectric behavior of MoS_2, $MoSe_2$, WS_2, WSe_2, graphene (GR), and graphene oxide (GO), positioning these materials within the triboelectric series based on their charge transfer tendencies [7]. Their study revealed that MoS_2 and $MoSe_2$ exhibit the most negative triboelectric charging characteristics, placing them between PTFE and PDMS, while WS_2, WSe_2, GR, and GO are relatively more positive, aligning between PDMS and PC as shown in Fig. 5a. By correlating these results with Kelvin-probe force microscopy (KPFM) measurements and first-principles simulations, the authors demonstrated that the effective work function plays a key role in dictating triboelectric polarity, with higher work function materials acquiring more negative charge upon contact. MoS_2, with its work function of 4.85 eV, exhibited the most negative charging tendency, whereas WSe_2, with a work function of 4.45 eV, was the most positive among the tested 2D materials. Further experimental analysis demonstrated that the triboelectric properties of 2D materials remain unaffected by synthesis methods (chemical exfoliation, chemical vapor deposition (CVD), vacuum filtration) and thickness variations, indicating that surface interactions, rather than bulk properties, dictate triboelectric behavior [7]. Additionally, the study explored chemical doping as a method to tune triboelectric charging characteristics, revealing that gold chloride ($AuCl_3$) p-type doping increases the work function, making MoS_2 more triboelectrically positive, while benzyl viologen (BV) n-type doping lowers the work function, enhancing its triboelectrically negative character. These findings establish a clear correlation between electronic properties and triboelectric behavior, providing a tunable approach to optimizing TENG performance.

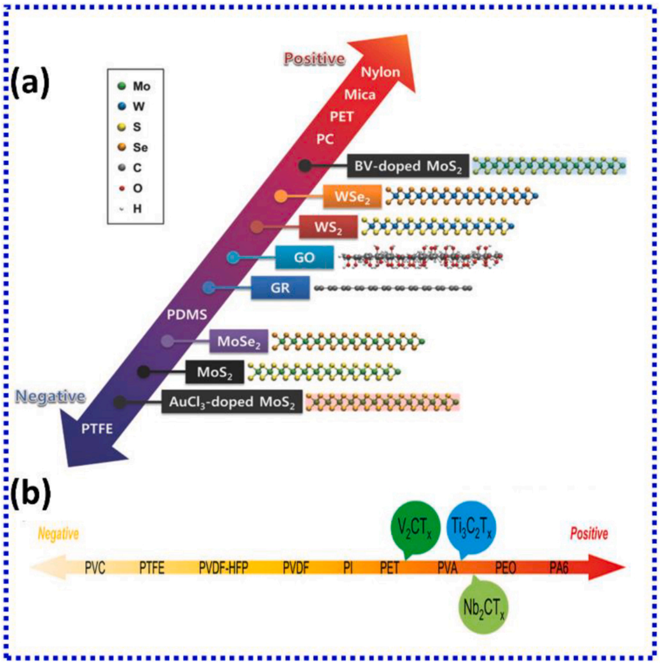

Fig. 5. (a) Modified 2D materials triboelectric series including graphene (GR), reduced graphene oxide (GO), and various transition metal dichalcogenides (TMDs). Reprinted with permission [7]. Copyright © 2018 WILEY-VCH. (b) Modified triboelectric series including V_2CT_x, $Ti_3C_2T_x$, and Nb_2CT_x MXenes. Reprinted with permission [47]. Copyright © 2024 WILEY-VCH.

The study on the triboelectric series of two-dimensional metal carbide MXenes conducted by Shi et al. establishes a refined positioning of MXenes within the triboelectric series [47]. Through a systematic evaluation of MXene-based TENGs, the study assessed the triboelectric performance of V_2CT_x, $Ti_3C_2T_x$, and Nb_2CT_x, positioning them relative to commonly used polymers like polyvinyl chloride (PVC) and polyamide-6 (PA6) (Shown in Fig. 5b). The results reveal that Nb_2CT_x is the most triboelectrically positive, while V_2CT_x is the most negative, establishing a triboelectric ordering of $(-)\ V_2CT_x < Ti_3C_2T_x < Nb_2CT_x\ (+)$. Interestingly, despite this ranking, all three MXenes exhibited relatively positive triboelectric properties, positioning them towards the positive end of the triboelectric series. To validate these findings, the study employed KPFM and photoelectron spectroscopy in air (PESA) to analyze the surface potential and work function differences among MXenes. The results confirmed that differences in work function strongly correlate with triboelectric polarity, with Nb_2CT_x having the lowest work function, leading to its higher positive triboelectric character. In contrast, V_2CT_x had the highest work function, making it the most negative. The triboelectric series was further refined based on short-circuit charge transfer experiments, demonstrating that Nb_2CT_x-PVC TENGs exhibited the highest transferred charge, reinforcing its placement as the most positive MXene.

The triboelectric series of 2D layered materials and MXenes remains incomplete, with challenges in systematically ranking diverse compositions, heterostructures, and phase-engineered variants. The future direction lies in expanding the triboelectric classification to a broader range of 2D materials, incorporating experimental and theoretical insights to refine their positioning. Developing a standardized triboelectric hierarchy across synthesis methods, doping strategies, and environmental conditions will be essential for achieving a more comprehensive and predictive triboelectric series for energy harvesting applications. Finding alternative green chemical solutions to the hydrofluoric acidic exfoliation of the MAX phase is also a current challenge to the sustainable implementation of MXenes in nanogenerators.

2.2.2. MOFs

A study by Slater and Tan provides a comprehensive analysis of the triboelectric behavior of zeolitic-imidazolate frameworks (ZIFs) and their influence on charge transfer mechanisms [48]. This work focuses on the triboelectric properties of MOFs in their pure powdered form, attempting to position MOFs directly within the triboelectric series, as shown in Fig. 6a. The authors evaluated five structurally related ZIF-type MOFs, namely ZIF-8, ZIF-L, ZIF-318, SOD-$Zn(CF_3Im)_2$, and qtz-$Zn(CF_3Im)_2$, using contact electrification tests against multiple counter materials, including Kapton, aluminum, PET, glass, and paper. The results revealed that fluorination and framework topology play a significant role in determining the triboelectric properties of MOFs. Among the tested MOFs, qtz-$Zn(CF_3Im)_2$ exhibited the most triboelectric negative behavior, while ZIF-8 and its structurally similar counterparts (ZIF-L and ZIF-318) were relatively triboelectric positive. The triboelectric series established in the study follows the order: (−) qtz-$Zn(CF_3Im)_2$<SOD-$Zn(CF_3Im)_2$<ZIF-318≈ZIF-L≈ZIF-8(+). The series transitions from the most triboelectric positive (electron-donating) in pink to the most triboelectric negative (electron-accepting) in blue (as shown in Fig. 6a, indicating a clear differentiation in charge transfer behavior among the tested MOFs. However, an important observation in the study is that ZIF-8, ZIF-L, and ZIF-318 could not be distinctly positioned relative to each other within the triboelectric series, as they exhibited similar triboelectric properties and charge transfer tendencies.

The inability to precisely rank ZIF-8, ZIF-L, and ZIF-318 arises from their structural and electronic similarities, which result in near-identical triboelectric outputs. All three MOFs share a $Zn(Im)_2$-based topology, with methyl-functionalized imidazolate linkers (–CH_3), similar electronic structures, and surface potentials. As a result, when tested in triboelectric contact with various counter materials, these MOFs exhibited comparable charge transfer efficiency, making it difficult to differentiate them quantitatively within the triboelectric series. The lack of distinct charge accumulation differences among them suggests that their surface functionalization, rather than their structural variations, dominates their triboelectric properties. In contrast, MOFs with trifluoromethyl (–CF_3) functionalization, such as qtz-$Zn(CF_3Im)_2$ and SOD-$Zn(CF_3Im)_2$, displayed significantly different triboelectric behaviors, positioning them distinctly in the series. The presence of electron-withdrawing (–CF_3) groups enhances electronegativity and charge acceptance, making these MOFs more triboelectric negative. This variation underscores the critical role of chemical functionalization in dictating triboelectric ranking, even when MOFs share similar metal centers and framework structures.

The study by Nitha P.K. and Arunkumar Chandrasekhar provides an in-depth analysis of the triboelectric properties of MOFs, positioning them within the triboelectric series [49]. The work evaluates HKUST-1, MIL-100, UiO-66, ZIF-8, and ZIF-67, revealing that imidazolate-based frameworks (ZIF-8, ZIF-67) tend to be triboelectric negative, whereas carboxylate-based MOFs (MIL-100, HKUST-1) display triboelectric positive behavior as shown in Fig. 6b. The triboelectric series was determined as (−) ZIF-8<ZIF-67<PAN < HKUST-1<MIL-100(+).

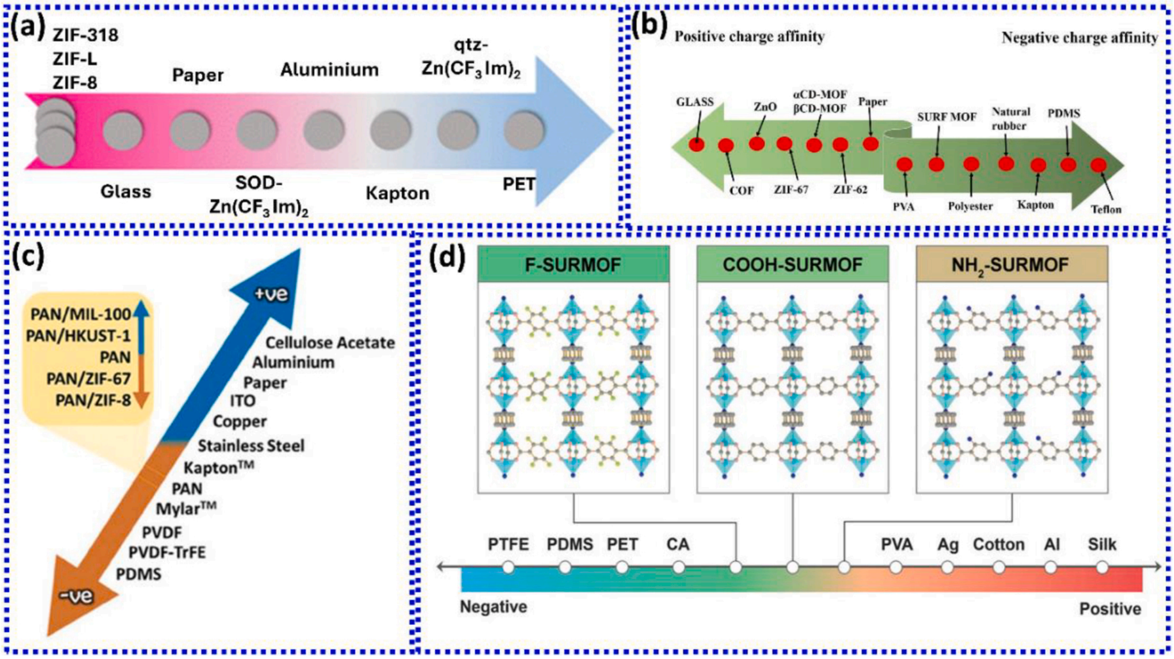

Fig. 6. (a) The triboelectric series of ZIF-8, ZIF-L, and ZIF-318. Reprinted with permission [48], Creative Commons Attribution 3.0 Copyright©2024 Royal Society of Chemistry. (b) Triboelectric series with MOF/COF members. Reprinted with permission [49]. Copyright © 2024 Elsevier. (c) Qualitative triboelectric series of MOF incorporated PAN along with other conventional materials. Reprinted with permission [50]. Copyright©2024 Wiley-VCH. (d) Triboelectric series including three kinds of SURMOFs. The molecular structures of surface-attached metal-organic frameworks (SURMOFs) are shown in the corresponding positions. Reprinted with permission [51]. Copyright©2021 Wiley-VCH.

Further, KPFM confirmed that MOFs with higher work function values tend to be triboelectric positive, while those with lower work functions are more triboelectric negative. Additionally, surface modifications, such as fluorination (–F) and amine functionalization (-NH_2), were shown to fine-tune triboelectric behavior, with electron-withdrawing groups shifting MOFs toward a more negative polarity.

Further, the work expanded into Covalent Organic Frameworks (COFs), which share porous architectures similar to MOFs but are composed entirely of organic linkages, often featuring extended π-conjugated networks. COFs exhibit distinct triboelectric behavior, influenced by functional group modifications and surface charge distribution. While ZIF-based MOFs lie closer to ZnO and paper, recent studies have positioned COFs between glass and zinc oxide in the triboelectric series, confirming their role as moderately triboelectric positive materials [51]. Notably, fluorinated COFs have been reported to be highly triboelectric positive, as electron-withdrawing fluorine groups enhance surface charge density, whereas triazine-based COFs tend to be more triboelectric negative, suggesting a tunable approach to triboelectric performance via synthetic functionalization.

Kallupadi et al. investigated the triboelectric series of MOF-integrated PAN composites [50]. The triboelectric behavior of four different MOFs—ZIF-8, ZIF-67, MIL-100 (Fe), and HKUST-1 was studied but positioned them relative to polyacrylonitrile (PAN) fibers rather than ranking them in isolation (Fig. 6c). The results indicate that the triboelectric polarity of MOF/PAN composites is influenced by factors such as band gap modulation, metal-ligand coordination, and charge transfer efficiency. The study established a qualitative triboelectric series for MOF/PAN composites, ranking ZIF-8 as the most triboelectric negative and MIL-100 as the most triboelectric positive, with the sequence (−) ZIF-8<ZIF-67<PAN<HKUST-1<MIL-100(+). This ranking was derived based on charge transfer efficiency and optical band gap variations of MOF/PAN composites rather than MOFs in their pure form. The MOFs were integrated into PAN fibers through electrospinning, which significantly affected their triboelectric output by altering surface properties, electron transfer behavior, and work function characteristics. Since the MOFs were studied in a polymeric matrix, the study does not explicitly provide a standalone triboelectric ranking of MOFs themselves. Instead, it highlights how MOFs can modulate the triboelectric properties of polymers like PAN by altering charge retention, band structure, and electron affinity.

Li et al. presented an important extension to the triboelectric series of MOFs, particularly by integrating surface-attached metal-organic frameworks (SURMOFs) into TENGs [51]. Unlike conventional MOFs, which are typically studied as powders or composite films, SURMOFs are directly grown onto various substrates, enabling stable, adhesive-free integration for triboelectric applications. This approach provides a systematic method to modify and tune the triboelectric polarity of MOFs by changing ligand functionalities, ultimately refining their positioning within the triboelectric series. Li et al. demonstrated that the triboelectric polarity of MOFs can be systematically adjusted by selecting different ligand end groups, such as fluorinated (–F), carboxyl (–COOH), and amine (–NH_2) functional groups. Their study positioned three types of SURMOFs in the triboelectric series as follows: (−)NH_2-SURMOF<COOH-SURMOF<F-SURMOF(+) (shown in Fig. 6d). This ranking was validated through contact electrification experiments, confirming that fluorinated SURMOFs exhibit the strongest electron affinity, making them highly triboelectric positive, while amine-functionalized SURMOFs are the most triboelectric negative.

The triboelectric series of MOFs and COFs highlights that framework topology, metal-ligand coordination, and structural diversity significantly influence charge transfer behavior. Given the vast number of MOF and COF families, a major opportunity lies in systematically classifying different frameworks across the triboelectric spectrum, which remains largely unexplored. Future research should focus on establishing a comprehensive triboelectric ranking for a wider range of MOFs and COFs, identifying key structure-property relationships, and integrating novel frameworks into TENGs for optimized energy harvesting.

2.2.3. Perovskite materials

Recent research has systematically classified inorganic and hybrid perovskites within the triboelectric series by analyzing their charge transfer tendencies, work functions, and triboelectric outputs in contact-separation mode TENGs. Multiple studies have established the triboelectric ranking of perovskites, demonstrating that their triboelectric polarity is highly tunable through different cationic and anionic substitutions. Wang et al. explored the effect of alkaline earth doping (Mg^{2+}, Ca^{2+}, Sr^{2+}, Ba^{2+}) in $CsPbBr_3$ perovskites, refining their triboelectric ranking to (−) $CsPb_{1-x}Mg_xBr_3$<$CsPb_{1-x}Ca_xBr_3$<$CsPb_{1-x}Sr_xBr_3$<$CsPb_{1-x}Ba_xBr_3$ (+) as shown in Fig. 7a [52]. Ba^{2+}-doped perovskites exhibited the highest triboelectric positive behavior due to their low ionization energy and strong charge donation capacity, whereas Mg^{2+}-doped perovskites were more triboelectric negative due to their higher binding energy and stronger lattice interactions. KPFM studies confirmed that Ba^{2+}-doped $CsPbBr_3$ had the lowest work function, reinforcing its triboelectric positive behavior, while Mg^{2+}-doped perovskites displayed the highest work function, making them triboelectric negative. Triboelectric output measurements further validated that Ba^{2+}-doped perovskites generated the highest charge density, leading to enhanced TENG performance. Yu et al. investigated the triboelectric behavior of halide perovskites ($CsPbCl_3$, $CsPbBr_3$, and $CsPbI_3$) by pairing them with conventional polymers, revealing the triboelectric ranking: (−) $CsPbI_3$<$CsPbBr_3$<$CsPbCl_3$ (+) shown in Fig. 7b [53]. The increasing electronegativity of halides (Cl > Br > I) significantly influenced charge transfer properties, with $CsPbCl_3$ exhibiting the strongest electron affinity, making it highly triboelectric positive. Kelvin-probe force microscopy (KPFM) confirmed that $CsPbCl_3$ displayed the highest work function, reinforcing its triboelectric positive nature, whereas $CsPbI_3$ had the lowest work function, making it triboelectric negative. Contact-separation TENG experiments demonstrated that $CsPbCl_3$, when paired with a triboelectric negative material like PTFE, generated the highest triboelectric output, affirming its strong triboelectric positive behavior.

In another study, Yang et al. examined the effect of alkali metal ion substitution (Li^+, Na^+, K^+, Rb^+) in $CsPbBr_3$, showing that smaller alkali cations (Li^+) enhanced triboelectric negative characteristics, whereas larger cations (Rb^+) increased triboelectric positivity [54]. The triboelectric ranking was established as (−) $Cs_{1-x}Li_xPbBr_3$<$Cs_{1-x}Na_xPbBr_3$<$Cs_{1-x}K_xPbBr_3$< $Cs_{1-x}Rb_xPbBr_3$ (+) as shown in Fig. 7c. Work function analysis using ultraviolet photoelectron spectroscopy (UPS) confirmed that Rb^+-doped perovskites had the lowest work function, enhancing their electron-donating ability. X-ray photoelectron spectroscopy (XPS) studies demonstrated that alkali metal ion incorporation led to electron density redistribution, shifting the perovskites' charge transfer behavior. The variation in triboelectric behavior was attributed to changes in lattice strain, dielectric properties, and work function modifications induced by different cation sizes.

Similarly, comparative studies of perovskites with commonly used polymers (PTFE, PVDF, PDMS, PE, PC, PET, PI, Nylon) revealed that perovskites are positioned between PE and PC in the triboelectric series. They exhibited positive charge accumulation when paired with PTFE, PDMS, and PVDF, while becoming negatively charged when in contact with PET, PC, and PI, confirming their intermediate triboelectric nature. The classification of perovskites within the triboelectric series broadens the material selection for high-performance TENGs; however, challenges remain in terms of stability, environmental tolerance, and charge retention.

2.2.4. Metal-oxides

Kim et al. reported triboelectric properties of metal oxides, focusing on their positioning within the triboelectric series and their role in enhancing TENGs [55]. Metal oxides such as SiO_2, Al_2O_3, HfO_2, Ta_2O_5, and TiO_2 were evaluated based on their charge transfer tendencies,

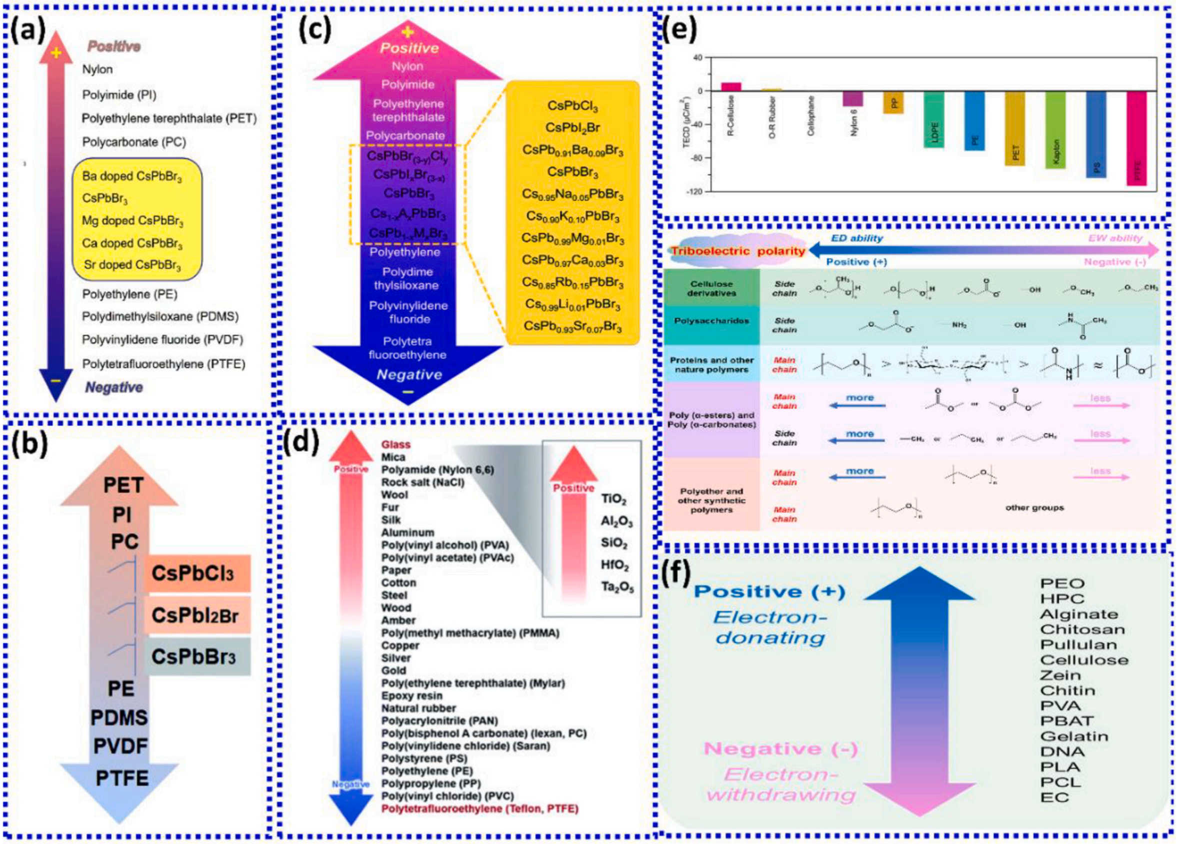

Fig. 7. (a) Extended qualitative triboelectric series of the pristine $CsPbBr_3$ and $CsPb_{1\text{-}x}M_xBr_3$ perovskites, Reprinted with permission [52]. Copyright©2020 Elsevier. (b) Supplemented qualitative triboelectric series with pristine $CsPbBr_3$, alkali metal ion doped $Cs_{1-x}A_xPbBr_3$, alkaline earth ion doped $CsPb_{1-x}M_xBr_3$ and $CsPbI_xCl_{3-x}$ perovskites, Reprinted with permission [53]. Copyright©2020Royal Society of Chemistry. (c) Triboelectric series containing $CsPbBr_3$, $CsPbI_2Br$ and $CsPbCl_3$ perovskites, Reprinted with permission [54], Copyright©2020 Royal Society of Chemistry. (d) Triboelectric series and an experimentally determined triboelectric series of oxide dielectric materials, Reprinted with permission [55], Creative Commons Attribution 3.0. Copyright©2017 Royal Society of Chemistry. (e) Quantified triboelectric series, showing R-cellulose, cellophane, oil-resistant Buna-N rubber, nylon 6, PP, LDPE, PE, PET, Kapton, PS, and PTFE, Reprinted with permission [56]. Copyright©2020 Wiley-VCH. (f) Influences of main- or side-chain chemical groups on triboelectric polarities of different BPs and the triboelectric performances and triboelectric series of BP films, Reprinted with permission [57]. Copyright© 2023 Elsevier.

permittivity, and triboelectric output, revealing a distinct ranking: (−) $Ta_2O_5 < HfO_2 < SiO_2 < Al_2O_3 < TiO_2$ (+). Among them, Ta_2O_5 exhibited the most triboelectrically negative behavior, whereas TiO_2 emerged as the most triboelectric positive, with a strong correlation between dielectric permittivity and triboelectric performance as shown in Fig. 7d. Higher permittivity oxides, such as TiO_2 ($\varepsilon_r \sim 80$), yielded superior triboelectric output, with measured V_{oc}=124.1 V, an I_{sc}=14.88 mA, and power output 392.08 mW, indicating that permittivity plays a dominant role in oxide-based triboelectrification. The study further explored PMMA-oxide composite TENGs, demonstrating that oxide nanoparticles retain their triboelectric polarity even when embedded in polymer matrices, though surface roughness and filler-matrix interactions influence charge transfer efficiency. Unlike conventional triboelectric materials, metal oxides exhibit relatively weak polarity differences, making their triboelectric ranking more dependent on permittivity rather than inherent charge affinity [55].

2.2.5. *Cellulose and derivatives*

The triboelectric series of cellulose and its derivatives has been explored as a key factor in the development of biodegradable and sustainable TENGs. Zhang et al. (2020) systematically investigated the triboelectric behavior of regenerated cellulose and cellophane, positioning them within the triboelectric hierarchy based on their charge transfer tendencies [56]. Their study demonstrated that regenerated cellulose exhibits a highly triboelectric positive character with a TECD of +10.05 $\mu C/m^2$, which is almost 60 times higher than that of cellophane (0.17 $\mu C/m^2$) (shown in Fig. 7e). This ranking was validated through contact electrification experiments and X-ray photoelectron spectroscopy (XPS) analysis, confirming the significant charge transfer capabilities of regenerated cellulose. The positioning of cellulose and its derivatives in the triboelectric series suggests a tunable charge polarity based on structural modifications and processing methods. The study revealed that microfibrillated cellulose (MFC) and cellulose nanofibrils (CNF) generally exhibit lower triboelectric effects due to their porous nature, which facilitates moisture adsorption and hinders effective charge transfer. In contrast, dense cellulose-based films, such as R-cellulose and cellulose acetate, demonstrated enhanced triboelectric performance due to their reduced water absorption and higher surface charge density. This was further confirmed using an electron-potential-well model, illustrating how water adsorption acts as a barrier in fibrillar cellulose films, reducing charge accumulation. The exceptionally positive charge density of regenerated cellulose makes it a viable candidate for high-performance sustainable TENGs, with Zhang et al. reporting an output power density of 307 W/m^2, which is comparable to fluoropolymer-based TENGs. By modifying the structure and surface chemistry of cellulose, its triboelectric properties can be tuned to meet specific application needs. For instance, functionalized cellulose films can be engineered to act as either strong electron donors or acceptors, making them suitable for use in green FG-TENGs.

2.2.6. *Bio-degradable polymers and derivatives*

Fluoropolymers such as PTFE and PVDF are commonly used in

TENGs due to their high electronegativity and ability to generate charge. However, they are also classified as Per- and polyfluorinated alkyl substances (PFAS) “forever chemicals," known for their persistence and toxicity, and are facing increasing regulatory scrutiny, such as the EU's proposed ban on PFAS by 2027 [58]. The challenges of recycling these materials, along with their energy-intensive processing, have prompted a shift towards sustainable alternatives. Non-fluorinated polymers such as PDMS, PLA, EVA, and polystyrene can be engineered into porous or layered structures, emulating piezoelectric properties by generating internal charges, potentially matching or even surpassing the performance of fluoropolymer TENGs in both acoustic and compressive modes [59]. While there are still hurdles regarding charge retention, durability, and vibration performance, bio-based and biodegradable materials present a promising path towards creating high-performance, environmentally friendly TENGs suitable for wearables, sensors, and autonomous energy systems.

In a recent study, Meng et al. reported a comprehensive investigation of 40 biodegradable polymers and classified them into five distinct groups: (1) cellulose and its derivatives, (2) polysaccharides, (3) proteins and natural biodegradable polymers, (4) poly(α-esters) and poly (α-carbonates), and (5) polyether and other synthetic biodegradable polymers (SBPs) [57]. The results highlight that both main-chain and side-chain chemical groups play crucial roles in determining a polymer's triboelectric polarity. Among these groups, polyether-based polymers exhibit the highest triboelectric positivity, while poly(α-esters) and proteins tend to be closer to neutral or slightly negative.

Focusing on cellulose and its derivatives, the study established the following triboelectric ranking (from most positive to most negative): (+) Hydroxypropyl Cellulose (HPC)>Hydroxyethyl Cellulose (HEC)> Carboxymethyl Cellulose (CMC)>Bacterial Cellulose (BC)>Microcrystalline Cellulose (MCC)>Methyl Cellulose (MC)>Ethyl Cellulose (EC) (−) Fig. 7f. This sequence is dictated by the electron-donating (ED) and electron-withdrawing (EW) properties of their functional groups. HPC and HEC, which contain abundant polyether (–OCH_2CH_2O–) side groups, exhibit strong tribo-positive polarity, making them effective electron donors. In contrast, CMC, with its carboxylate (–COO–) functionality, maintains moderate triboelectric positivity, while BC and MCC, containing only hydroxyl (–OH) groups, demonstrate weaker triboelectric performance. The trend continues with MC and EC, where the presence of methyl (–OCH_3) and ethyl (–OCH_2CH_3) groups reduces their electron-donating ability, pushing them further toward tribonegativity.

From a broader perspective, the study by Meng et al. provided a generalized triboelectric ranking for biodegradable polymers, categorizing them based on their charge transfer characteristics: Highly tribopositive polymers, including polyether-based polymers such as polyethylene oxide and polyurethane, demonstrated strong electron-donating properties. Moderate tribo-positive polymers, including cellulose derivatives like hydroxypropyl cellulose and hydroxyethyl cellulose, also exhibited positive triboelectric effects. Near-neutral polymers, such as polysaccharides like alginate and chitosan, as well as proteins like gelatin and collagen, showed intermediate behavior. Weakly tribonegative polymers, including poly(α-esters) and poly(α-carbonates) like polylactic acid and polycaprolactone, had lower electron-donating properties. Highly tribo-negative polymers, such as synthetic polymers with electron-withdrawing groups like polyphosphazene, polyvinyl alcohol, and polyvinyl pyrrolidone, were the strongest electron acceptors.

Among the tested materials, polyethylene oxide exhibited the highest tribo-positive polarity, attributed to its high density of ether (-CH_2-CH_2-O-) bonds, which favor electron donation. Conversely, polyvinyl pyrrolidone was identified as highly tribo-negative, likely due to the presence of electron-withdrawing functional groups. Positioning of these polymers within the triboelectric series has significant implications for material selection in TENGs, where maximizing charge transfer efficiency is essential for enhanced power generation. Meng et al. emphasized that pairing materials with contrasting triboelectric properties, such as hydroxypropyl cellulose and polyvinyl pyrrolidone, can significantly enhance triboelectric effects and improve energy output in TENGs. Furthermore, cellulose-based materials provide a biodegradable, sustainable alternative to synthetic polymers, making them ideal candidates for eco-friendly energy-harvesting applications.

2.2.7. Polymer materials

The triboelectric series of polymers plays a critical role in various applications, including TENGs, electrostatic sensors, and energy harvesting devices. Contact electrification has been under investigation for more than 250 years, yet the exact mechanism of this charge transfer is still not fully understood. Researchers have debated whether the charge carriers are electrons, ions, or small material fragments. The empirical nature of the triboelectric series has led to inconsistencies in reported rankings, with variations attributed to factors such as surface roughness, humidity, and material purity. Numerous physical properties, including work function, molecular orbitals, ionization potential, dipole moment, and dielectric constant, have been investigated to explain triboelectric rankings, yet no single property has provided a universally accurate prediction.

A key breakthrough in understanding the positioning of polymers in the triboelectric series comes from the study by Zhang et al. which proposes that the Lewis acidity/basicity of polymer repeat units governs their ranking [60]. By measuring Lewis basicity using a reference molecule, 4-fluorophenol, the researchers established a strong correlation between Lewis basicity and triboelectric polarity. Their experiments demonstrated that polymers with higher Lewis basicity, which are stronger electron donors, tend to charge positively, while those with lower Lewis basicity, acting as electron acceptors, charge negatively. Through a 10 × 10 polymer contact matrix, the study confirmed that triboelectric ranking follows a linear pattern rather than a cyclic one, reinforcing the idea that ion transfer, rather than electron transfer, is the dominant mechanism in polymer contact electrification (shown in Fig. 8a).

The positioning of polymers in the triboelectric series follows a predictable hierarchy based on their molecular structure and functional groups. Polymers with electron-donating groups, such as hydroxyl and amine groups, tend to rank higher in the series and charge positively. Examples include poly(vinyl alcohol) (PVA), poly(methyl methacrylate) (PMMA), and polyacrylonitrile (PAN). Conversely, polymers with electron-withdrawing groups, such as fluorinated or nitro-containing polymers, tend to charge negatively and are positioned lower in the series. Polytetrafluoroethylene (PTFE) and other fluorinated polymers are commonly found at the bottom of the series. Neutral or slightly negative polymers, such as polystyrene (PS) and polyvinyl chloride (PVC), occupy an intermediate position. Environmental factors, including humidity, temperature, and pressure, also influence triboelectric behavior, potentially shifting a polymer's ranking.

Furthermore, the study provides predictive insights into how modifications to polymer structures affect their triboelectric positioning. Increasing the electronegativity of polymer substituents, such as by adding fluorine or nitro groups, tends to shift the material downward in the series, making it more negatively charged. Conversely, incorporating functional groups that enhance Lewis basicity, such as amines or hydroxyl groups, moves the polymer upward, making it more positively charged (shown in Fig. 8b). This rationalized framework offers a systematic approach to selecting materials for triboelectric applications without the need for extensive experimental trials. In conclusion, the triboelectric series of polymers, while historically empirical, can be understood and predicted through the principles of Lewis acid-base interactions. By establishing a direct correlation between Lewis basicity and triboelectric ranking, researchers have provided a fundamental explanation for a phenomenon that was previously based on experimental observations.

The triboelectric series of polymers, traditionally understood

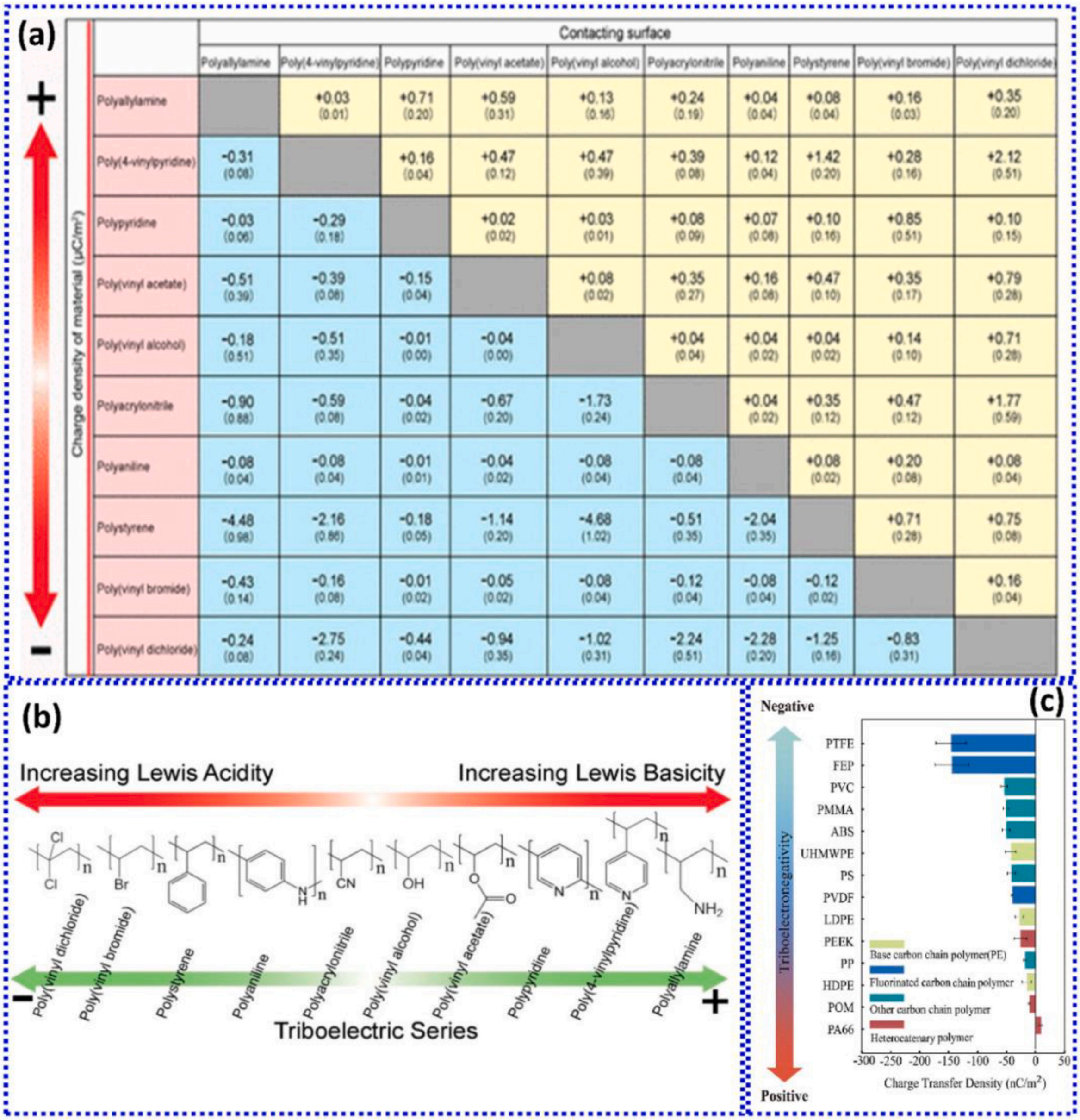

	Contacting surface									
	Polyallylamine	Poly(4-vinylpyridine)	Polypyridine	Poly(vinyl acetate)	Poly(vinyl alcohol)	Polyacrylonitrile	Polyaniline	Polystyrene	Poly(vinyl bromide)	Poly(vinyl dichloride)
Polyallylamine		+0.03 (0.01)	+0.71 (0.20)	+0.59 (0.31)	+0.13 (0.16)	+0.24 (0.19)	+0.04 (0.04)	+0.08 (0.04)	+0.16 (0.03)	+0.35 (0.20)
Poly(4-vinylpyridine)	-0.31 (0.08)		+0.16 (0.04)	+0.47 (0.12)	+0.47 (0.39)	+0.39 (0.08)	+0.12 (0.04)	+1.42 (0.20)	+0.28 (0.16)	+2.12 (0.51)
Polypyridine	-0.03 (0.06)	-0.29 (0.18)		+0.02 (0.02)	+0.03 (0.01)	+0.08 (0.09)	+0.07 (0.08)	+0.10 (0.16)	+0.85 (0.51)	+0.10 (0.15)
Poly(vinyl acetate)	-0.51 (0.39)	-0.39 (0.08)	-0.15 (0.04)		+0.08 (0.02)	+0.35 (0.27)	+0.16 (0.08)	+0.47 (0.10)	+0.35 (0.17)	+0.79 (0.28)
Poly(vinyl alcohol)	-0.18 (0.51)	-0.51 (0.35)	-0.01 (0.00)	-0.04 (0.00)		+0.04 (0.04)	+0.04 (0.02)	+0.04 (0.02)	+0.14 (0.10)	+0.71 (0.28)
Polyacrylonitrile	-0.90 (0.88)	-0.59 (0.08)	-0.04 (0.02)	-0.67 (0.20)	-1.73 (0.24)		+0.04 (0.02)	+0.35 (0.12)	+0.47 (0.12)	+1.77 (0.59)
Polyaniline	-0.08 (0.04)	-0.08 (0.04)	-0.01 (0.01)	-0.04 (0.02)	-0.08 (0.04)	-0.08 (0.04)		+0.08 (0.02)	+0.20 (0.08)	+0.08 (0.04)
Polystyrene	-4.48 (0.98)	-2.16 (0.86)	-0.18 (0.05)	-1.14 (0.20)	-4.68 (1.02)	-0.51 (0.35)	-2.04 (0.35)		+0.71 (0.28)	+0.75 (0.08)
Poly(vinyl bromide)	-0.43 (0.14)	-0.16 (0.08)	-0.01 (0.02)	-0.05 (0.02)	-0.08 (0.04)	-0.12 (0.04)	-0.08 (0.04)	-0.12 (0.02)		+0.16 (0.04)
Poly(vinyl dichloride)	-0.24 (0.08)	-2.75 (0.24)	-0.44 (0.04)	-0.94 (0.35)	-1.02 (0.31)	-2.24 (0.51)	-2.28 (0.20)	-1.25 (0.16)	-0.83 (0.31)	

Fig. 8. (a) Charge density (i.e., the charge per unit contact area) of the polymers (indicated in the first column) after contacting with another different polymer (indicated in the top row). Reprinted with permission [60]. Copyright © 2019, American Chemical Society. (b) Correlation between the ordering of materials in the triboelectric series established experimentally and Lewis basicity/acidity. Reprinted with permission [60]. Copyright © 2019, American Chemical Society. (c) Triboelectric series of different polymers rubbing with 3.5 wt% NaCl solution. Reprinted with permission [44]. Copyright © 2024 Elsevier.

through solid–solid contact electrification, has been explored using different approaches to understand the underlying charge transfer mechanisms. One approach, as mentioned above is based on Lewis acid-base interactions, suggests that the Lewis basicity of polymer functional groups dictates their position in the triboelectric series, with electron-donating groups favoring positive charging and electron-withdrawing groups promoting negative charging. Another perspective, as investigated by Chen et al., focuses on solid–liquid triboelectrification, particularly the interaction between polymers and aqueous NaCl solutions, revealing that electron transfer is the primary mechanism of charge accumulation, with additional influences from ion transfer and wettability [44].

Expanding the triboelectric series beyond solid–solid interactions, this study systematically measured the charge transfer properties of 14 common polymers when in contact with NaCl solution (shown in Fig. 8c). Unlike dry contact electrification, where charge transfer mechanisms remain debated, these findings strongly indicate that electron transfer is the dominant process in polymer-aqueous solution triboelectrification. The study introduces the concept of "triboelectronegativity", a parameter quantifying the ability of a polymer to attract negative charges during contact electrification. It establishes a ranking where highly electronegative polymers such as PTFE and FEP accumulate the most negative charge, while materials like PA66 and POM exhibit minimal or even positive charging due to cation attraction.

The positioning of polymers in the triboelectric series is influenced by multiple factors, including functional group electronegativity, polymer structure, the electric double layer (EDL), and wettability. Fluorinated polymers (PTFE, FEP, PVDF) rank highest in triboelectronegativity due to their strong electron-withdrawing functional groups (-F, $-CF_3$). Intermediate polymers such as PS, PVC, and PMMA contain moderately electronegative groups, leading to moderate charge accumulation. Weakly negative or neutral polymers, including

PP and various forms of polyethylene (LDPE, HDPE, UHMWPE), have mostly non-polar functional groups (-H, -CH_3), resulting in lower charge transfer. Finally, heterocatenary polymers such as PA66, POM, and PEEK exhibit the least negative or even positive charge transfer. This is mainly due to their amide or oxygen-containing groups, which attract cations from the NaCl solution, neutralizing the negative charge. This study also compares triboelectrification in NaCl solution versus deionized water (DI water), revealing that while charge transfer between DI water and polymers remains consistently negative, some polymers exhibit positive charging in NaCl solution. The electric double layer formed at the polymer–solution interface plays a key role in determining charge retention. Additionally, wettability influences charge transfer by controlling how much liquid remains on the polymer surface after contact, with hydrophilic materials attracting more cations, thereby reducing negative charge density. Ultimately, this work provides a quantitative framework for understanding solid–liquid triboelectrification, introducing triboelectronegativity as a key metric for ranking polymers in the triboelectric series. It highlights that while electron transfer is the dominant mechanism, ion transfer and liquid retention effects also play significant roles.

2.2.8. *Inorganic non-metallic materials*

The triboelectric series of inorganic non-metallic materials is a ranked list that quantifies materials based on their ability to gain or lose electrons when in contact with a reference material, in this case, liquid mercury (Hg, work function=4.475 eV). The TECD for nearly 30 inorganic materials was systematically measured by Zou et al. using a contact-separation method with a liquid metal interface, ensuring precise and reproducible data collection (shown in Fig. 9a) [61]. Materials with lower work functions tend to lose electrons and acquire a positive charge, positioning them at the top of the series. Examples include mica (+61.8 μC/m^2), float glass (+40.2 μC/m^2), and borosilicate glass (+38.6 μC/m^2). Conversely, materials with higher work functions tend to gain electrons and become negatively charged, such as aluminum nitride (−13.2 μC/m^2), boron nitride (−16.9 μC/m^2), and ultra-high-temperature quartz glass (−62.7 μC/m^2) (shown in Fig. 9b). The study confirmed a linear correlation between work function differences and TECD, reinforcing that electron transfer, rather than mechanical friction or dielectric properties, governs triboelectric charging. The dielectric constant, while crucial for charge retention, was found to have minimal influence on triboelectric charge transfer.

Additionally, the dielectric constant plays a role in determining the material's ability to store and retain charge. However, the study found that the TECD values were not significantly affected by the dielectric constant, as the charge transfer was primarily governed by electron transitions between surface states rather than capacitive effects. This reinforces the quantum mechanical transition model, where electron migration is dictated by energy level alignments rather than macroscopic material properties. The findings provide a quantitative triboelectric series for inorganic non-metallic materials.

2.2.9. *Textile based materials*

The triboelectric series of textile-based materials ranks different textile fibers based on their ability to gain or lose electrons when brought into contact with other materials. Textile materials, particularly those used in TENGs, exhibit unique triboelectric properties due to differences in their fiber composition, surface chemistry, and work function (shown in Fig. 9c). Natural fibers such as cotton, wool, and silk are generally tribo-positive, in contrast, synthetic fibers like nylon, PET, PTFE, and PVDF tend to be tribo-negative, meaning they readily gain electrons and become negatively charged. The ranking of textile materials in the triboelectric series is determined by factors such as electron

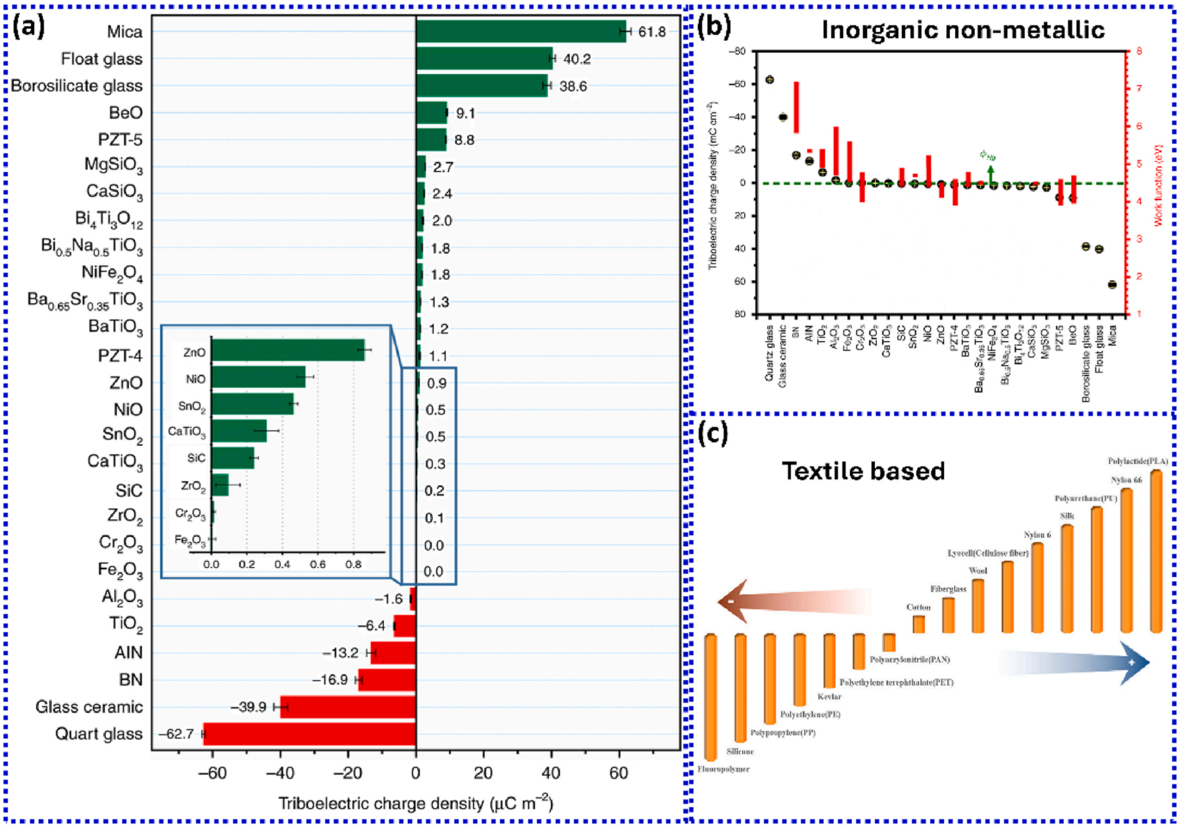

Fig. 9. (a) Quantified triboelectric series of some common inorganic non-metallic materials. Reprinted with permission [61]. Copyright © 2022, Springer Nature. (b) The influence of work function and dielectric constant on contact-electrification. Reprinted with permission [61]. Copyright © 2022, Springer Nature. (c) Triboelectric series of textile-based materials. Reprinted with permission [24]. Creative Commons CC BY license. Copyright©2022Wiley-CH.

affinity, electronegativity, and surface functional groups. The work function difference between two materials governs the electron transfer process, with materials having a lower work function losing electrons more easily, thereby acquiring a positive charge. Additionally, the dielectric constant of textile materials plays a role in charge retention, where materials with higher dielectric constants tend to hold charge for longer periods.

3. Various energy harvesting methods

The triboelectric effect was first employed in 2012 to develop the TENG by Professor Wang and his colleagues, which converts waste mechanical energy to electrical energy [62,63]. The main working mechanism of the TENG includes the triboelectricity and electrostatic induction effect [3,41]. Four basic modes of operation have been proposed for TENGs: vertical contact mode, lateral displacement mode, single electrode mode, and free-standing triboelectric layer mode [13,27] (shown in Fig. 10(a–d)). These modes can be applied depending on the direction of the polarization shift, the arrangement of the electrodes, and the applications.

The vertical contact separation mode, which uses relative motion parallel to the interface, is the most basic and commonly used mode of the TENG. At the initial state, the two layers of the TENG remains separated, so no electrons flow occurs [64]. Differences in the potential charge of the two electrodes appear during the contact separation process. The charge imbalance results from the movement of electrons from one electrode to the other during contact. An electric potential difference is also created in the TENG when the two materials are separated. This electrical potential difference causes electrons to flow through the external circuit, producing an electrical output. The contact-separation mode is a direct and efficient method for harvesting energy from mechanical motion, with potential applications in wearable technology, self-powered sensors, and other portable devices.

One of the unique operating modes of TENGs, the lateral sliding mode, uses the relative sliding motion of two materials with different triboelectric characteristics to generate power. When the TENG materials come into contact with each other during sliding, surface charges are produced due to the differences in their triboelectric characteristics [65]. One substance becomes negatively charged as a result of this transfer, while another substance becomes positively charged. Electrons are driven around the outer circuit by the electric potential difference created by this charge separation, which powers the TENG and produces an electrical output suitable for electronic devices. Additionally, this mode of operation provides a stable and reliable electrical output for various applications [66].

The TENG based on the single-electrode mode is characterized by a simple structure that contains only one triboelectric layer and one electrode [67]. In single-electrode mode, any mechanical vibration can cause the TENG material to come into contact with another free-standing material such as air, human skin, droplets, etc [68]. As these materials separate, they undergo triboelectric effect, which results in the transfer of electrons between them. The TENG material gains or loses electrons based on its triboelectric charges and the type of material it encounters. This mode provides a lightweight, compact device capable of generating power through intermittent contact and separation, making it excellent for small electronic power and sensing applications.

In the free-standing TENG mode, a single material with intrinsic triboelectric characteristics serves as both the contact and separation material, thereby avoiding the requirement for a separate counter material [69]. A free-standing TENG is often made of a flexible thin sheet of material that can move and deform in response to mechanical stimulation. When the TENG is subjected to mechanical deformation or movement, the triboelectric effect causes charge separation in the material, resulting in an electrical potential difference across the TENG. This potential difference can be used to generate electricity for a variety of purposes, including electronics and small-scale sensing. The free-standing mode has various advantages, including ease of fabrication, high flexibility, and potential for incorporation into wearable or flexible devices. This mode-based TENG can be incorporated into soft or flexible application areas because it can harvest energy from many types of mechanical deformations, including twisting, stretching, and bending.

4. Materials based TENGs so far

4.1. Conducting materials

TENGs typically use metals as conducting materials due to their

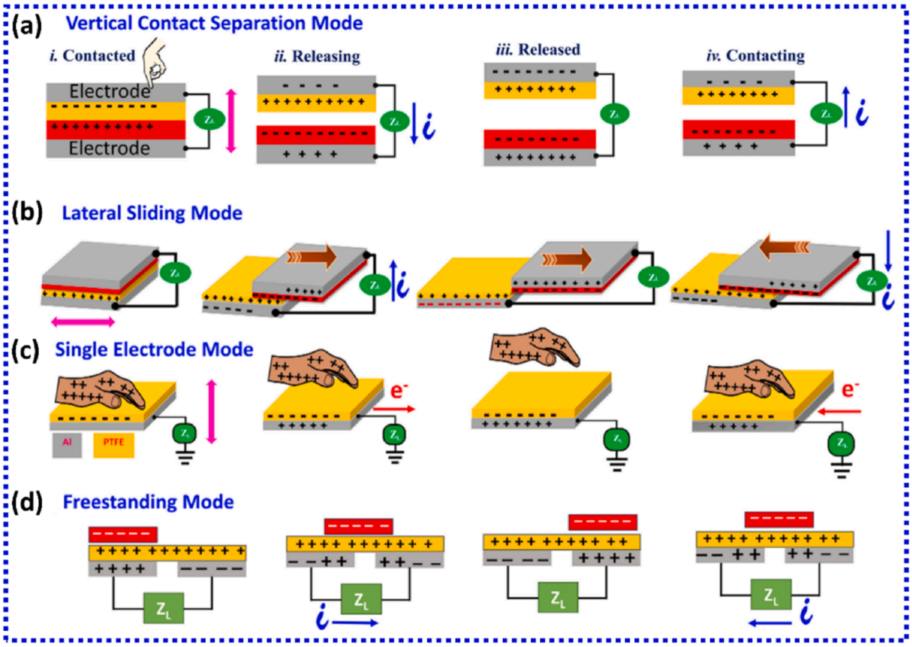

Fig. 10. Working mechanism of the four different modes of the TENG device. Reprinted from Ref. [13]. Copyright © Springer, 2024.

exceptional electrical conductivity, durability, and ease of incorporation into various device designs. Typical metals utilized such as aluminum (Al), Silver (Ag), copper (Cu), and gold (Au) are chosen according to their distinct electrical characteristics, cost, and application needs [70–74]. The strength and resilience of these metals guarantee the long-lasting performance of the TENGs, even in demanding circumstances. However, their inherent inflexibility and heaviness make them difficult in applications that demand flexibility and lightweight properties [71]. Therefore, Carbon-based materials, such as graphite, graphene, and carbon nanotubes (CNTs), are becoming more popular as good conductive materials in TENGs [75,76]. This is because they have great electrical properties and high flexibility. This is why employing graphite sheets as electrodes, leveraging their layered structure to enhance electron transfer efficiency during the triboelectric process. The integration of various conductive materials into hybrid systems or composites has greatly enhanced the performance of TENG [77,78].

A study by Sun et al. [76] went through the improvement of triboelectric materials on multiple scales using silver nanoparticles decorated by carbon shell (Ag@C) as a dielectric doping along with a two-step O_2+CF_4 plasma treatment. This modification aims to overcome challenging conditions such as high salt content, humidity, and biological fouling, which currently hinder efficient ocean energy harvesting,

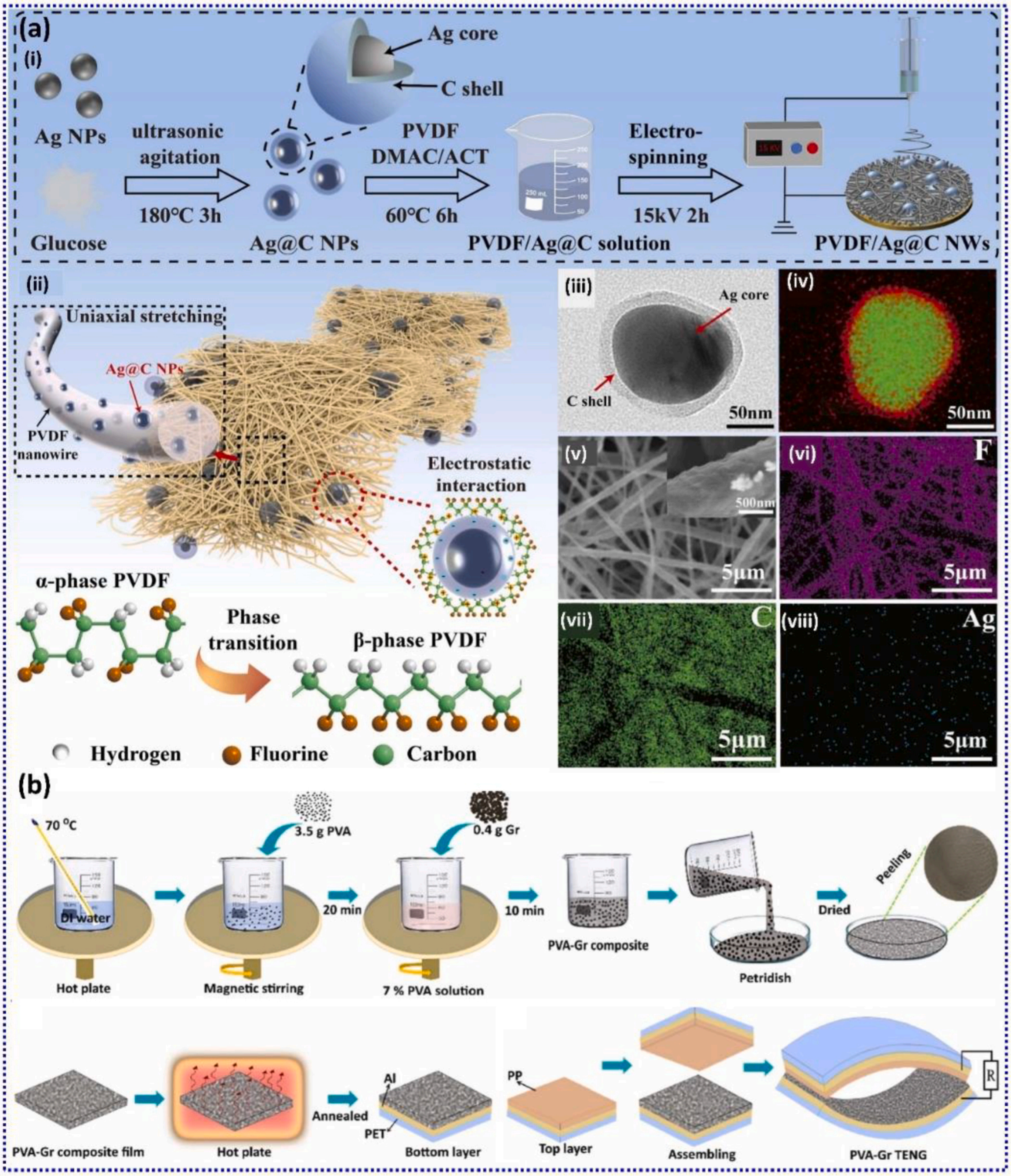

Fig. 11. (a) Synthesis procedure and morphology characterization of PVDF/Ag@C composite films. (i) Schematic diagram of the preparation process of PVDF/Ag@C composite film. (ii) Ag@C fillers and the electrospinning process cause the regulation of the crystalline phase of PVDF. (iii) TEM and (iv) EDS images of Ag@C core-shell NPs. (v) Top-plane FE-SEM images and (vi-vii) EDS maps of PVDF/Ag@C nanowires. Reprinted with permission [76]. Copyright 2024, Elsevier. (b) Schematic illustration of PVA-Gr TENG fabrication. Reprinted with permission. [75]. Copyright 2024, Elsevier.

Fig. 11a. In their work, they fabricated PVDF/Ag@C nanowires by incorporating Ag@C into the PVDF layer, which led to an enhanced dielectric permittivity and the moisture-resistance, salt-resistance, and anti-bioadhesive properties. For the effect of annealing on the performance, durability, and lifetime of TENGs, Amini et al. [75] investigated this factor to improve the performance, as seen in Fig. 11b. By accurately regulating the annealing conditions to adjust the material properties, it is possible to optimize the overall efficiency of TENG devices for a wide range of practical applications. Their work involved preparing composite films made of PVA embedded with graphite (Gr) using a solution casting approach, followed by annealing at various temperatures below the glass transition temperature (Tg) of PVA. To assess the impact of annealing on the device's performance, they constructed TENGs using the previously annealed composite films as the tribo-positive material and polypropylene as the tribo-negative material. Moreover, exploiting modified silver nanowires brings up the added value of transparency in flexible metal electrodes [70,79]. The detailed summary of conducting materials based TENG performance is presented in Table 1.

4.2. Polymers

Some of the most extensively researched polymers include PDMS, biodegradable polymers, and PVDF [20,88,89,91,96] (see Table 2). These materials are recognized for their simplicity in creating, ability to bend without breaking, and capacity to adjust their electrical characteristics by adding chemicals or making structural changes [21,89]. Researchers have investigated the incorporation of conducting polymers into TENGs to improve their overall functionality. Due to their exceptional electrical conductivity and flexibility, they are highly suitable for wearable and stretchable TENG applications. Several parameters, such as the conductivity, surface roughness, and chemical composition of the polymer, influence the performance of conducting polymer-based TENGs [96,92].

Li et al. [90] fabricated biodegradable and biocompatible polymer (BPs) TENGs, as shown in Fig. 12a. However, biodegradable triboelectric nanogenerators (BD-TENGs) usually have a low performance due to triboelectric polarity. Therefore, molecular doping is a direct and efficient technique for altering the triboelectric polarity of BPs, thereby improving the performance of BD-TENG. There is currently a lack of knowledge on the mechanisms and laws that determine the variances in triboelectric polarities among different doped molecules, especially those that are both biodegradable and biocompatible. This study involved selecting and applying several doping compounds to both tribopositive and tribonegative materials with an extensive examination of the triboelectric polarities and associated behaviors of BPs. Doping BD-TENGs with modest quantities of poly (propylene glycol) (PPG) and ethyl cellulose significantly enhanced their output generation performance.

As shown in Fig. 12b, Mudgal et al. [91] looked into the use of TENGs made of a composite of polystyrene (PS) and silver nanowires (Ag-nWs). They introduced a new design to harness wind energy, featuring a top electrode with a fluttering hook form. The PS:Ag-nWs solution was dropped over the lightweight rectangular aluminum foil with polyimide tape protection of the edges of the film from wind flow. The hook-shaped electrode (HSE-TENG) was made for harvesting energy using a strip of Al foil with a thickness of 18 μm in a rectangular shape. The HSE-TENG demonstrated consistent and reliable operation even in extreme outside conditions with elevated temperatures and humidity levels. Furthermore, they installed the HSE-TENG on the upper surface of a moving vehicle, which effectively captured energy from the wind force during movement. This study emphasizes the potential of integrating material techniques with inventive device designs to provide exceptional performance and durability for targeted applications.

Zheng et al. [89] investigated the energy density and recyclability of TENGs by incorporating imine connections into fluorine-containing polymers, as shown in Fig. 12c. The TENG was fabricated using a coating of a copolymer PHFAx-co-PVMAy which is composed of 2,2,3,4,4,4-Hexafluorobutyl acrylate (HFA) and Vanillin methacrylate (VMA) on polyimide substrate. The coating was prepared using a film applicator, followed by drying in a vacuum oven. To ensure the recyclability of TENG, a closed-loop procedure was used to recycle the copolymer in a mixed solution of tetrahydrofuran (THF) and hydrochloric acid (HCl), as shown in Fig. 12d. Integrating imine connections improves TENG electrical output and ensures their long-term sustainability as an energy solution.

Hajra et al. [92] prepared TENGs applying a 3D printing technique, followed by attaching a double-sided conductive copper electrode to the printed substrate using silver paste to investigate the process of harvesting biomechanical energy, as shown in Fig. 12e. The spring-assisted vertical contact separation mode TENG was created using a coating of immobilized living microalgae (Chlorella sp.) as a positive electrode on an aluminum sheet and polyimide tape as a negative electrode. Microalgae, which are photosynthetic microorganisms capable of capturing carbon and generating bioelectricity through photosynthesis and cellular respiration, have gained significant attention in the field of bio-photovoltaics (BPV). These results show that microalgae can be a great triboelectric layer in TENGs for biomechanical energy harvesting.

4.3. 2D materials

As we have already discussed in the previous section, two-dimensional (2D) materials have captured significant interest from the scientific community since their initial discovery. Researchers are actively investigating different methods for synthesizing these materials over large surfaces. Some of the prominent techniques include mechanical exfoliation, CVD, and the hydrothermal method. The range of 2D materials continues to grow, including types such as graphene and its derivatives, MXenes, 2D chalcogenides, transition metal dichalcogenides (TMDs), metal phosphorus trichalcogenides, metal monochalcogenides, and transition metal trichalcogenides. These materials are especially useful in the development ofTENGs, as they offer unique properties that enhance their efficiency in energy harvesting applications [97,98].

4.3.1. Graphene and derivatives of graphene

Graphene is a 2D monolayer of carbon organized in a hexagonal

Table 1
Summary of conducting materials based TENG performance.

Ref	Material	Triboelectric material pair	Size of the device	Voc	Isc	Power
[75]	PVA-Graphite	polypropylene	5 × 4.8 cm^2	200.24 V	12.68 μA	4.5 mW
[80]	Aluminum	PDMS	3 × 3 cm^2	288 V	17 μA cm^{-2}	13.6 W/m^2
[81]	Aluminum	PTFE	5 × 5 cm^2	80 V	6.6 μA	0.14 W/m^2.
[82]	Copper	PTFE	–	15 V	6 nA	–
[83]	Copper	FEP	5 × 5 cm^2	490 V	10 μA	160 μW
[84]	PVA-MWCNT	FEP	4 × 4 cm^2	354.53 V	17.63 μA	12 mW
[85]	PDMS-MWCNT	P(VDF-TrFE)	8 mm × 8 mm	25 V	6.5 μA	1.98 mW/cm^3
[86]	Gold	PDMS	___	83V	4.5 μA	11 mW/cm^2
[87]	CNT-Silk	PET	2 × 4 cm^2	262 V	8.73 μA	285.91 μW/cm^2

Table 2
Summary of polymer materials based TENG performance.

Ref	Material	Triboelectric material pair	Size of the device	Voc	Current/Current Density	Power Max/Power Density
[88]	RHSC-TENG (rotary) FEP/PU FOAM	acrylic substrate/Cu electrode/PET	55 by 65 by 1 mm^3	8000 V	36 μA	14.1 W/m^2
[89]	recycled vitrimer	Nylon 11/PI film/Cu electrode	4cm × 4 cm	964 V	29.5 μA	33 mW
[90]	PEO/PPG	PTMC/Mg/PCL/EC	1.5 cm × 1.5 cm	6.2 V	75 nA	2.3 $\mu W/m^2$
[91]	PS:Ag-nW composite film	Aluminum foil/Acrylic	2 cm × 3 cm	200 V	15 μA	395 mW/m^2
[92]	Algae	PI/Cu electrode	2 cm × 2 cm	20 V	140 nA	–
[93]	monolithic conjugated microporous polymer aerogel (CMPA)	FEP/Cu electrode	thinner cylinder (thickness: ≈2 mm; diameter: ≈25 mm)	72 V	3.2 μA	0.25 W/m^2
[71]	natural rubber (NR) electrode	PTFE/Cu electrode	–	4.5 V	0.19 μA	0.14 mW/m^2
[72]	SPTA	Al foil	1 cm × 3 cm	40 V	15 μA	98 μW
[94]	Silicon/g-C_3N_4	PI/Al	6 cm × 6 cm	550 V	110 μA	4.19 W/m^2
[25]	Graphene	PET/Graphene	2 mm × 2 cm	9 V	1.2 μA cm^{-2}	2.5 $\mu W/cm^2$
[95]	graphene oxide/carboxymethyl cellulose/Al film	FEP/Au/PET	3 cm × 3 cm	97 V	1.2 μA	41.4 μW

pattern with certain atomic structure called sp^2. The material demonstrates exceptional physical characteristics, such as an extremely high electron mobility of up to 26,000 $cm^2/V{\cdot}s$, outstanding optical transparency of around 97 %, and notable mechanical flexibility. Graphene possesses a significant elastic modulus of around 1 TPa, along with good thermal stability, chemical inertness, and the ability to facilitate ballistic charge-carrier movement. The distinctive characteristics of graphene indicate its considerable potential for many technological applications [94]. These versatile properties make graphene an ideal choice for applications in flexible electronics, transparent protective coatings, and barrier films. Its characteristics are particularly well-suited for use in transparent and flexible electrodes in devices like solar cells, photodetectors, nanogenerators, and light-emitting diodes (LEDs). For the first time in 2014, Kim et al. [25] developed a transparent flexible graphene-based triboelectric nanogenerator (GTNG). In this work, they developed GTNGs using large-scale graphene produced by CVD on copper and nickel foils. They created flexible, transparent GTNGs by transferring monolayer (1L), bilayer (2L), trilayer (3L), and quad-layer (4L) graphene onto polyethylene terephthalate (PET) substrates using a layer-by-layer transfer technique as shown in Fig. 13a. They found that monolayer graphene (1L-GTNG) provided the highest output, generating 5V and 0.5 $\mu A/cm^2$ under a compressive force. The performance decreased with additional layers due to weak interlayer interactions. However, regularly stacked multilayer graphene showed improved output. This work showed the potential of graphene in cost-effective energy-harvesting applications, emphasizing the role of the triboelectric effect enhanced by air gaps between graphene and the substrate. This result shows graphene's suitability for flexible electronics and self-powered systems [25]. Recently Mohan et al. [95] and his team developed a TENG using a composite film of graphene oxide (GO) and carboxymethyl cellulose (CMC) as the tribo-positive layer, paired with fluorinated ethylene propylene (FEP) as the tribo-negative layer Fig. 13b. Incorporating GO into the CMC matrix significantly enhanced the energy harvesting performance of the device. The enhancement is ascribed to the elevated surface charge of CMC resulting from the presence of GO sheets, which was confirmed through KPFM analysis as shown in Fig. 13c. The GO/CMC TENG works by the principle of contact-electrification and electrostatic induction. When both layers come into contact, electrons are transferred from the GO/CMC layer to the FEP layer due to their different electron affinities. Upon separation, the charge imbalance creates a potential difference, driving electrons to flow between the electrodes to maintain electrostatic equilibrium. This process generates an alternating current in the external circuit. In addition, the GO/CMC TENG demonstrated superior performance compared to the bare CMC-based TENG, with an output voltage of 97V and a short-circuit current of 1.2 μA, resulting in a peak power of 41.4 μW. This output is notably higher than many existing TENG devices, highlighting the effectiveness of GO incorporation. The enhanced performance is primarily due to the increased surface charge density provided by the GO sheets, which have a high surface area and abundant oxygenated functional groups. These characteristics allow for better charge transfer and retention during the triboelectric process. The researchers also demonstrated the practical applicability of the GO/CMC TENG for monitoring human body motions and powering portable electronic devices, showcasing its potential for self-powered systems [95].

Sun et al. [99] designed a machine learning-coupled vertical graphene triboelectric pressure sensor array (ML-vGTEPS) to act as an artificial tactile receptor for recognizing finger actions (see Fig. 13d). They employed vertical graphene (vG) due to its unique nanostructure and excellent electrical properties, which enhanced the sensitivity and sensing range of the triboelectric sensors. These sensors were integrated into a wearable device to transmit multi-channel tactile signals with minimal interference. The study demonstrated the effectiveness in a table tennis scenario, where it successfully recognized 16 different finger actions with a high accuracy of 98.1% using a neural network model. Potential applications of the ML-vGTEPS array covers human-machine interfaces, intelligent sports training, telemedicine, and virtual/augmented reality [99]. In another study, Sadeque et al. [100] incorporated graphene nanoplatelets (GNP) into polyvinylidene difluoride (PVDF) nanocomposite fibers using a thermal drawing process, which is both scalable and efficient (see Fig. 13e). Also in this example, the use of graphene resulted in significant enhancements in the performance of the TENG. Initially, it enabled the conversion of non-piezoelectric PVDF' α phase into the electroactive β phase, augmenting the β phase content by as much as 13% relative to untreated PVDF films. This phase transformation is crucial for enhancing triboelectric charge generation The addition of 5% graphene to the PVDF fibers led to a 1.41-fold enhancement in open-circuit voltage and a 1.48-fold enhancement in short-circuit current relative to unmodified PVDF fibers. The TENG fabric exhibited a peak power output of 32.14 μW at a matched load of 7 MΩ, with a notable power density of 53.57 mWm^{-2}. Beyond electrical performance improvements, the graphene-integrated fibers exhibited remarkable stability under challenging circumstances, including alkaline media, extreme temperatures, multiple washing cycles, and prolonged usage. Outstandingly, their approach of using thermal drawing to create continuous, kilometer-long fibers with integrated electrodes and triboelectric materials in a single process overcomes limitations of previous fabrication methods, such as solution processing or electrospinning, which often require separate electrode deposition steps [100].

4.3.2. *Hexagonal boron nitride*

Hexagonal boron nitride (h-BN), commonly referred to as "white

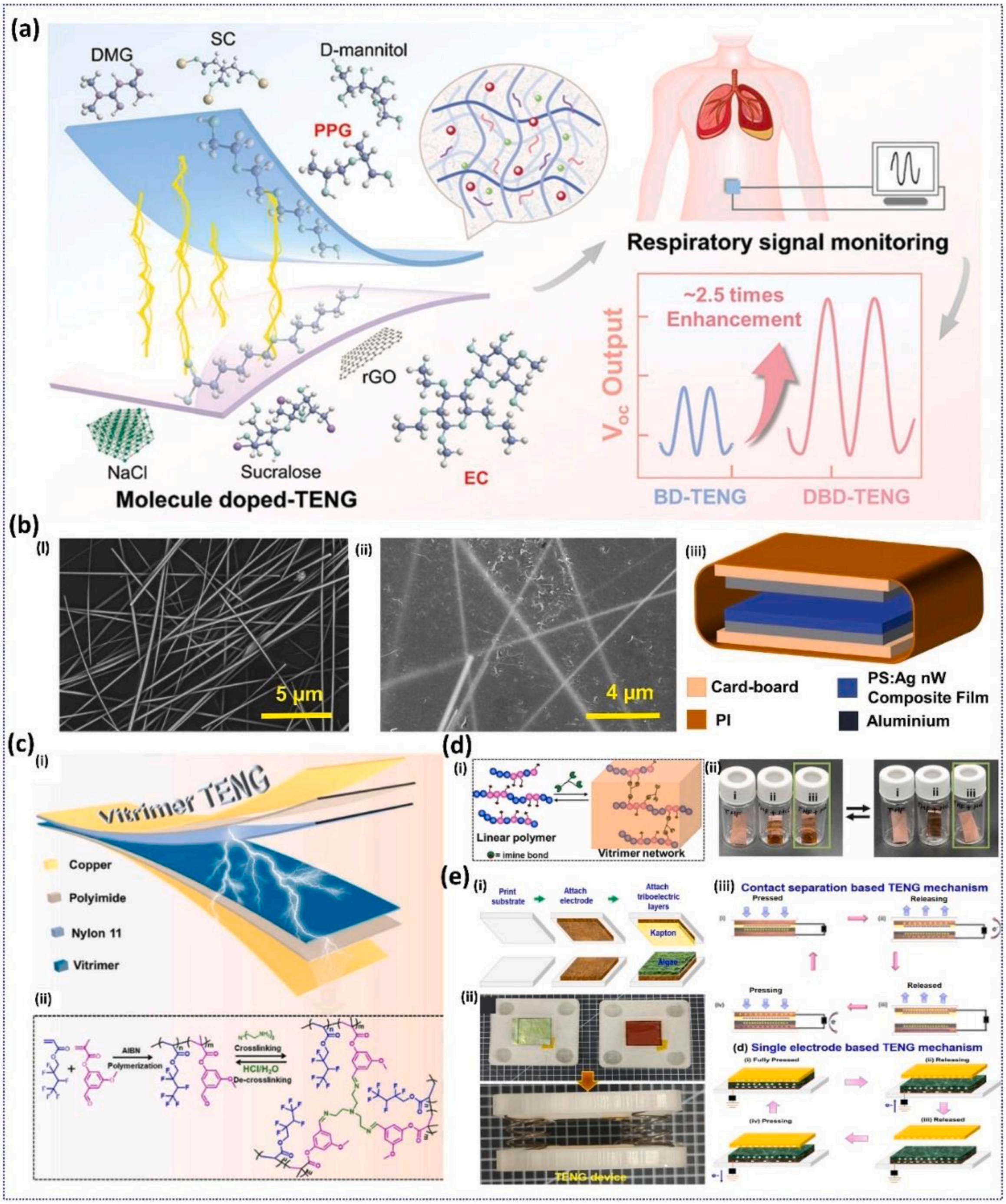

Fig. 12. (a) Schematic illustration of DBD-TENG and its application in respiratory signal monitoring. Reprinted with permission [90]. Copyright 2024, Elsevier. (b) SEM images of (i) Ag nanowires and (ii) PS: Ag nanowires composite film, (iii) TENG structure utilized to examine triboelectric properties of various PS: Ag-nWs composite films. Open-circuit voltages and short-circuit currents for various PS: Ag-nW composite films. Reprinted with permission [91]. Copyright 2024, Elsevier. (c) (i) Schematic diagram of the structure of the vitrimer-based TENG, (ii) molecular structure of vitrimers. (d) Illustration of the dynamic structure of the vitrimer network showing recyclability. Photo illustration of (i) VF5N5/PI film before and after immersion in pure THF, (ii) PI film before and after immersion in THF/HCl solution, and (iii) VF5N5/PI film before and after immersion in THF/HCl solution. Reprinted with permission [89]. Copyright 2024, Elsevier. (e) Fabrication steps for (i) vertical contact separation (CS) TENG, (ii) digital picture of TENG (3D printed substrate, electrode, and different triboelectric layers), (iii) working mechanism of CS TENG and d Working mechanism of the SE mode TENG. Reprinted with permission [92]. Copyright 2023, Elsevier.

graphene," is a two-dimensional nanomaterial with a structure like graphene, but it consists of alternating boron and nitrogen atoms. It has exceptional properties such as high thermal stability, chemical inertness, and a wide bandgap of about 6 eV, which makes it an electrical insulator. These characteristics make h-BN a promising material for enhancing TENGs, which can improve performance by providing a robust and stable surface that enhances charge transfer efficiency. Its high surface area and mechanical strength contribute to increased energy conversion efficiency and device longevity. The resistance to oxidation and chemical degradation ensures that TENGs remain effective over extended periods, even in harsh conditions [101,102]. Zhao et al. [103] developed an innovative rotational TENG using h-BN

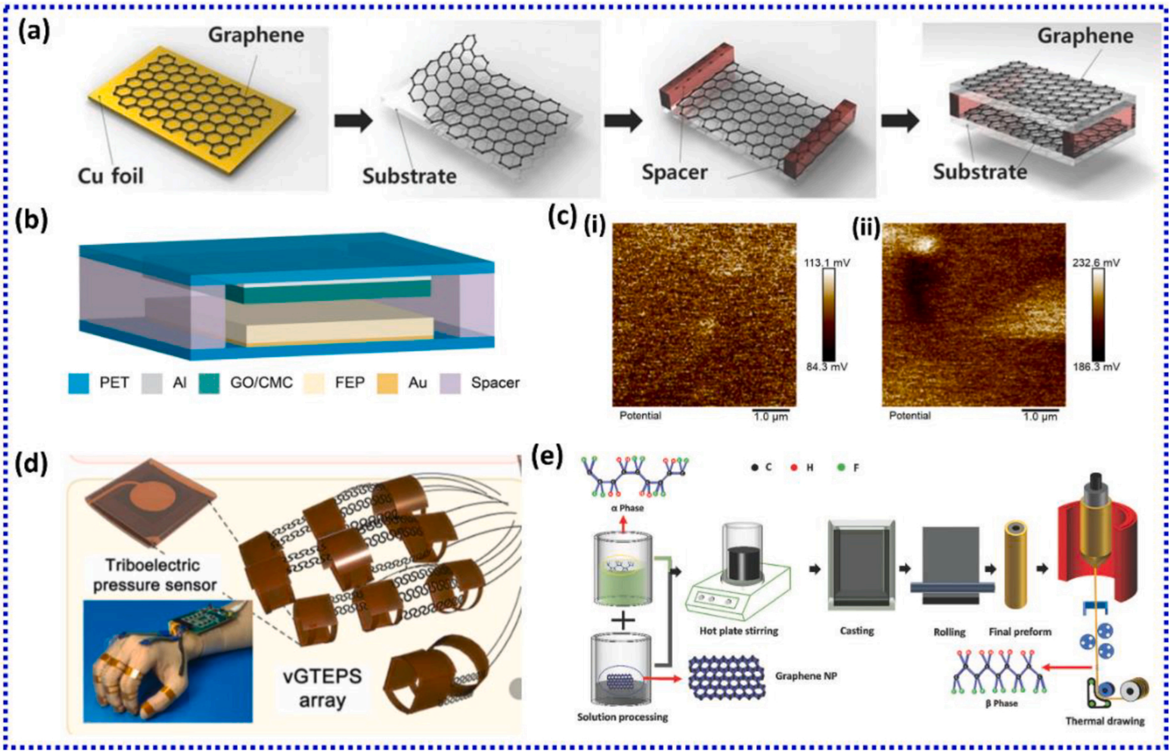

Fig. 13. (a) Schematic diagrams of device fabrication and compatibility of graphene with an arbitrary substrate. Reprinted with permission [25]. Copyright 2014, Wiley. (b) Schematic representation of GO/CMC fabricated TENG device. (c) Kelvin probe force microscopic analysis: surface potential mapping of (i) CMC film and (ii) GO/CMC film. Reprinted with permission [95]. Copyright 2024, Elsevier. (d) Schematic of the ML-vGTEPS array as the artificial finger receptor for finger action recognition (Reprinted with permission [99]. Copyright 2024, Elsevier). (e) Solution processing of GNP and PVDF to produce a dry nanocomposite film. Reprinted with permission [100]. Copyright 2024, Wiley.

nanosheets incorporated into polyvinyl chloride (PVC) composite films as the triboelectric material. This method resulted in considerable enhancements in output efficiency, thermal management, and device longevity. The procedure started with the synthesis of monolayer-multilayer hybrid h-BN nanosheets via a hydrothermal technique, then incorporating them into PVC to fabricate composite films. These composite films were then employed as the negative triboelectric material in the TENG, paired with copper sheets as the positive triboelectric material as shown in Fig. 14a. The impact of hBN nanosheets was multifaceted and substantial. The optimized TENG, using a 2 wt% h-BN nanosheets/PVC composite, demonstrated remarkable performance improvements compared to pure PVC counterparts. It achieved a maximum output voltage of 142V and a current of 272 μA at a rotating speed of 400 r/min, yielding a peak power output of 30.7 mW. The hBN nanosheets contributed to an 87.3% increase in surface charge density, reaching 620 $\mu C/m^2$, a 36.8% improvement in thermal conductivity, up to 0.26 W/mK, and a 32.5% reduction in friction coefficient to 0.27, compared to pure PVC films. These improvements resulted in more efficient heat dissipation, with the device's surface temperature being 2.4 °C lower compared to pure PVC-based TENGs after 10 min of continuous operation at 250 r/min (see Fig. 14b). The improved thermal management and reduced wear contributed to an extended device lifetime, surpassing that of pure PVC-based TENGs by a factor of 1.05. The fabricated TENG successfully powering small electronics is shown in Fig. 14c. Moreover, the TENG demonstrated potential as a self-powered sensor for detecting rotational speed and pressure [103]. Recently Das et al. [104] prepared three types of TENGs using different waste plastic vs different layered materials: plastic-VS_2, plastic-SnS_2, and plastic-hBN (see Fig. 14d). The plastic-hBN TENG demonstrated superior performance, generating the highest output power density of 460 mW/m^2. This exceptional performance was attributed to h-BN high resistivity and dielectric constant. It exhibited long-term stability, maintaining its performance over 10,000 cycles. The researchers discovered a correlation between the output power density and the product of resistivity and dielectric constant of the layered materials, with hBN having the highest value at 197×10^5 Ωm. The plastic-hBN TENG was able to switch on the 76 LEDs when driven by footsteps. Additionally, the TENG is integrated into a shoe and connected to an Arduino system, enabling the monitoring of distance traveled and walking/running speed is as presented in Fig. 14e. This innovative approach not only addresses the issue of plastic waste but also provides a promising solution for mechanical energy harvesting and wearable electronics [104].

In another study, Hyun et al. [105] incorporated h-BN alongside multi-walled carbon nanotubes (MWCNT) into thermoplastic polyurethane (TPU) to create an enhanced electrification layer for TENG (see Fig. 14f). Although h-BN is an electrical insulator, it played a key role in enhancing the overall electrical and dielectric properties of the composite. The addition of h-BN facilitated the formation of a more efficient conductive network of MWCNT through a volume exclusion effect, where the MWCNTs aligned around the two-dimensional h-BN particles, forming a denser conductive structure. This synergistic interaction resulted in a significant improvement in electrical conductivity, especially at lower MWCNT concentrations. The amalgamation of h-BN with MWCNT greatly increased the dielectric constant of the composite, with the optimal blend of 6 vol% h-BN and 1.05 vol% MWCNT achieving a balanced performance of real permittivity (232) and loss tangent (2.4), as shown in Fig. 14g. This optimal composition generated a voltage of 47 V and a current of 244 nA. Furthermore, the TPU/h-BN/MWCNT composite presented stable TENG performance under 60% strain, with only a slight increase in electrical resistance. The composite retained high elasticity and a low Young's modulus (2–3 MPa), comparable to soft tissues, making it ideal for wearable and skin-mountable applications. The TENG device made with this composite effectively sensed various

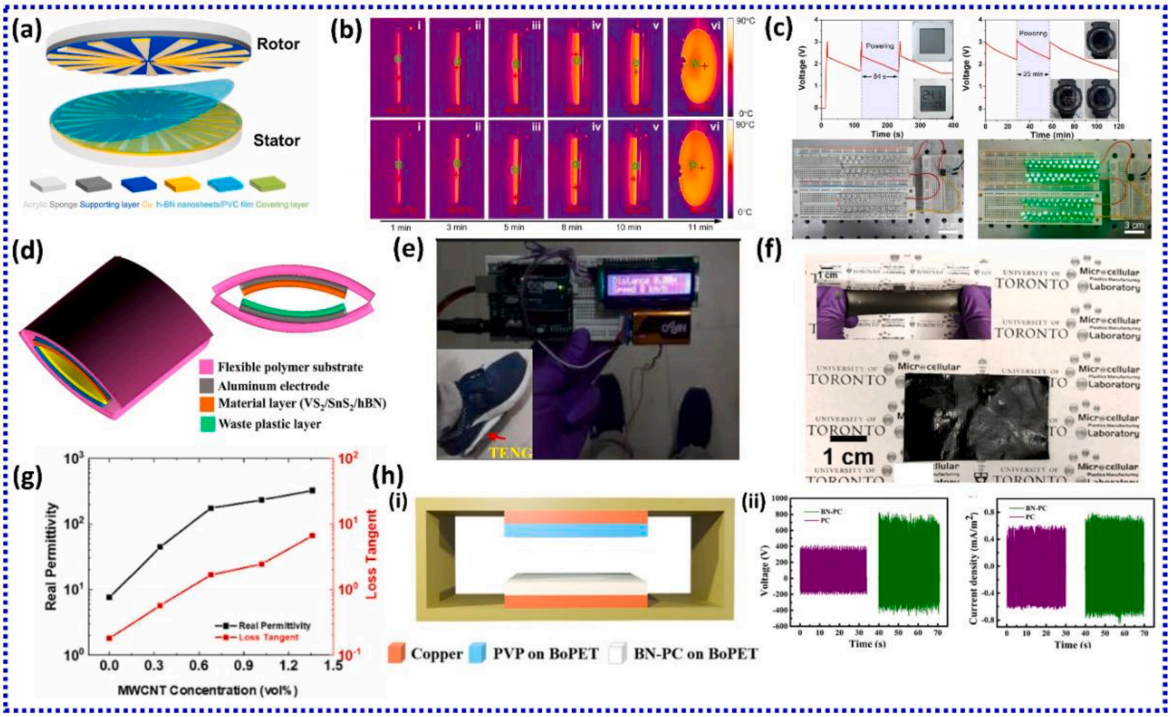

Fig. 14. (a) A schematic diagram of the TENG. (b) Temperature variation of the PVC film-based TENG and the h-BN nanosheets/PVC composite film-based TENG at each stage (i) to (vi) during continuous operation. (c) Powering the electronics. Reprinted with permission [103]. Copyright 2024, Elsevier. (d) Schematic of the fabricated TENG with aluminum foil as an electrode and plastic and layered materials (VS_2, SnS_2, and h-BN) as a triboelectric layer. (e) Photograph of the distance-meter cum speedometer during walking. Reprinted with permission [104]. Copyright 2024, American Chemical Society. (f) Photo of TPU/h-BN/MWCNT hybrid film. Inset is a stretched state of the hybrid film. (g) Dielectric properties of the TPU/h-BN 6/MWCNT composites as a function of MWCNT concentration. Reprinted with permission [105]. Copyright 2024, Elsevier. (h) (i) Schematic model of the FS-TENG, (ii) output voltage and short-circuit current density generated from the PC/PVP and BN-PC/PVP FS-TENG, respectively, under a mere tapping force of ~10 N at 5 Hz. Reprinted with permission [106]. Copyright 2024, American Chemical Society.

complex hand gestures by producing distinct output voltages, demonstrating its potential as a self-powered motion sensor. The addition of h-BN to the TPU/MWCNT composite enhanced its electrical and dielectric properties and improved its mechanical performance, making it a versatile material for TENG applications [105]. In 2023, Bhavya et al. [106] developed a high-performance flexible triboelectric nanogenerator (FS-TENG) using hexagonal boron nitride nanosheets (BNNSs) as a crucial component. They created novel ink by blending BNNSs with polycarbonate (PC) and organic additives, resulting in a screen-printable BN-PC ink. This ink was then printed onto Mylar substrates to serve as the triboelectric negative layer, while polyvinylpyrrolidone (PVP) was printed as the positive layer. The FS-TENG exhibited excellent performance, generating a high voltage of around 800V and a short-circuit current density of approximately 0.78 mA/m^2 under a 10N actuating force at a frequency of 5 Hz, as schematized in Fig. 14h. Notably, the device achieved a power density of around 1.36W/m^2 at a 200 MΩ resistive load, which was seven times higher than a TENG without BNNSs. The practical applications of FS-TENG successfully power electronic devices using only a finger-tapping force of about 5 N [106].

4.3.3. MXenes

MXenes are a group of 2D materials made up of transition metal carbides, nitrides, and carbonitrides that were first identified in 2011. Their chemical formula is typically represented as $M_{n+1}X_nT_x$, where M is a transition metal (such as Ti, V, Nb, or Mo), X is carbon or nitrogen, and Tx indicates surface terminations such as hydroxyl, fluorine, or oxygen groups. As 2D transition metal compounds, MXenes offer several significant benefits when incorporated into TENG devices, which exhibit exceptional triboelectric properties comparable to well-established materials like PTFE while also offering superior electrical conductivity. This dual functionality allows them to serve as electrodes, electron trappers, and friction layers in TENGs [107,108]. Their 2D structure provides a large surface area, facilitating rapid charge carrier flow and enhancing device efficiency. The abundance of surface termination groups on MXenes contributes to their high electronegativity and enables fine-tuning of surface chemistry, resulting in strong interactions with composite polymers and improved adhesion. It also boosts the dielectric permittivity of composite materials, a critical factor influencing surface charge density and power output. Their mechanical flexibility and robustness enable the design of durable TENG devices. The compositional diversity of MXene allows for customization and optimization of TENG performance for specific applications. These characteristics collectively lead to TENG devices with improved flexibility, transparency, cycle stability, and power yields, making MXenes highly promising materials for advancing TENG technology in applications such as portable electronics, IoT devices, and sustainable energy solutions [23]. Fan et al. [109] fabricated Ti_3C_2 MXene and integrated it with water-soluble polyurethane (TPU) to produce a composite film with remarkable extensibility and triboelectric characteristics. The MXene/TPU composite film was used as the core component in two types of TENGs: MT-TENG-E for energy harvesting and MT-TENG-S for flexible sensing. The inclusion of MXene significantly boosted the dielectric constant of the composite film, reaching a value of 73 at approximately 1000 Hz, which is crucial for improving triboelectric performance. The MT-TENG-E was designed with the MXene/TPU film serving as the positive triboelectric layer and a silicone rubber film as the negative layer, with copper foils acting as conductive layers for both electrodes. The design demonstrated outstanding energy harvesting capabilities, achieving an open-circuit voltage of 83 V, a short-circuit current of 10.6 μA, and a peak power density of 231 mW/m^2 in vertical contact-separation mode. Notably, the superior triboelectric properties of the MXene/TPU film led to the creation of the MT-TENG-S, a highly stretchable TENG without a metal conductive layer. In this innovative design, a novel method was used to establish an electron exchange system by bonding an MXene/TPU film with a silicone rubber film. A silver wire attached to the film at one end collected electric signals, allowing the device to stretch up to 200 % of its original length. The MT-TENG-S operates using a new deformation mode, where electron exchange between the MXene/TPU film and the silicone rubber film during stretching generates electrical signals (presented in Fig. 15a). This approach addresses the limitations of conventional TENGs that depend on contact-separation or sliding modes. During deformation, the electron adsorption capabilities of the two triboelectric films change significantly, and the contact area of the dielectric elastomer also shifts. This leads to a redistribution and transfer of charges. The MT-TENG-S demonstrated excellent performance as a self-powered sensor, accurately detecting and measuring various human body movements, including finger, wrist, elbow, and muscle movements, without the need for external power [109]. Jayarathna et al. investigated the potential of MXene for smart sensing and energy harvesting applications. They developed a pure MXene-based device using a freeze-drying method and evaluated its performance as both a piezo-resistive stress sensor and a TENG. The chemical representation of the material and device is shown in Fig. 15b. For the TENG application, they constructed a device operating in vertical contact separation mode. The fabricated device's performance was evaluated under various conditions, demonstrating its capability to generate voltage and current outputs. It was observed that the TENG current output increased with higher frequencies due to faster charge flow. They also tested TENG's long-term stability over 1600 s and its ability to charge capacitors of different capacities. The TENG achieved a maximum power output of 16 μW at 100 MΩ load resistance (Fig. 15c). The device showed promise as a self-powered weight-sensing unit, with higher outputs corresponding to increased mechanical stress from heavier weights. This dual functionality of sensing and energy harvesting positions MXene-based devices as potential candidates for sustainable and autonomous operation in weight-sensitive applications [110].

In another study, Tao and his team [111] developed a spring-shaped multilayer TENG (S-TENG) using a Nb_2CT_x MXene-PVDF composite as the triboelectric electrode. They synthesized the MXene through a one-step hydrothermal method, which resulted in an accordion-like structure that increased electron transport pathways and surface area. MXene was then combined with PVDF to create a composite film. The interface between MXene and PVDF formed strong hydrogen bonds, enhancing dielectric properties and surface charge density. This composite showed a remarkable 300% increase in output power compared to pure PVDF, demonstrating the effectiveness of MXene in improving TENG performance. They optimized the device by designing a spring-like multilayer structure, which improved space utilization and contact area, as shown in Fig. 15d. The multilayer spring structure increased the contact area of the triboelectric layers and reduced the overall resistance of the S-TENG [111]. This structural innovation, combined with the MXene-PVDF composite, resulted in an S-TENG with impressive performance metrics: a voltage of 420 V, a current density of 1.47 mA/m^2, and a power density of 619 mW/m^2. The potential of the device was demonstrated through several practical applications, functioning as a fluid energy harvester in an urban river setting and a real-time water level monitor with the capability to trigger automatic alarms (see Fig. 15e). Recently, Mao et al. [112] designed a novel single-electrode TENG skin patch (TESP) for wound healing and tactile

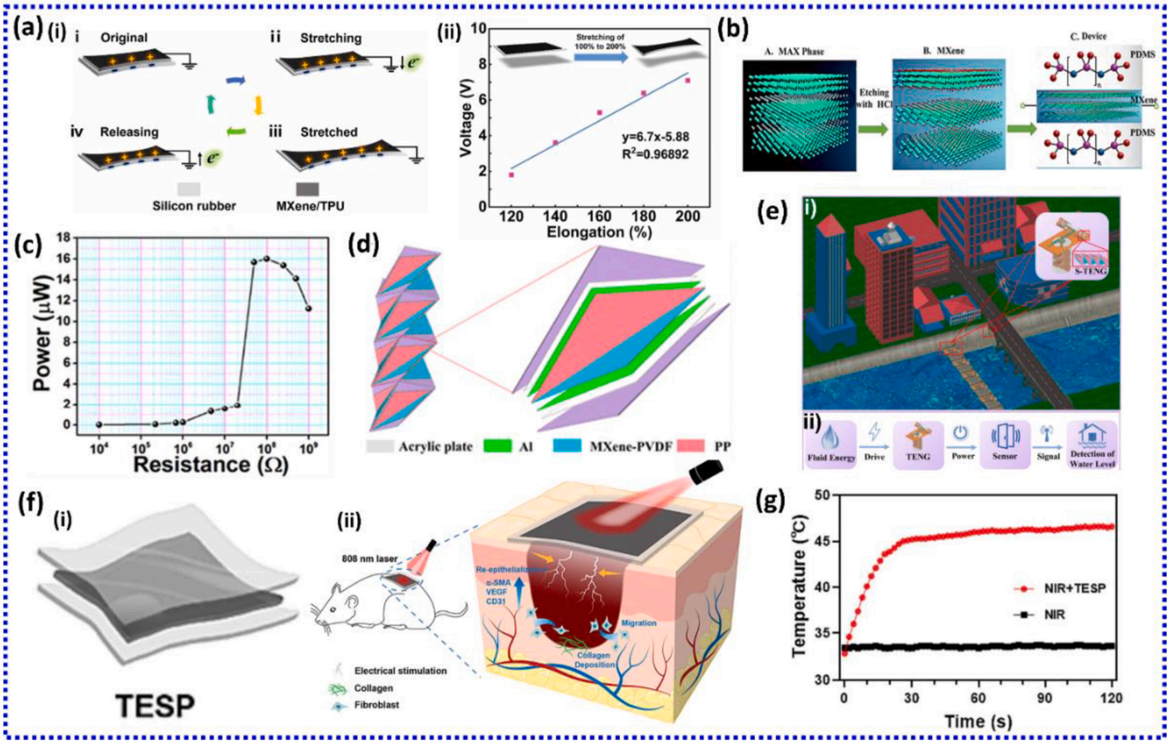

Fig. 15. (a) (i) The working mechanism of MT-TENG-S in the stretching state, (ii) output voltages of the MT-TENG-S under elongation electronics. Reprinted with permission [109]. Copyright 2024, Elsevier. (b) Chemical representation of the material and device. (c) Power of TENG at various load resistances electronics. Reprinted with permission [110]. Copyright 2024, Elsevier. (d) Schematic diagram of the S-TENG with an enlarged sandwiched structure. (e) (i) scene graph of the S-TENG for fluid energy harvesting and water level sensing device configuration of the S-TENG installed on the urban river is shown in the inset, (ii) basic working process of the S-TENG-driven water level sensor electronics. Reprinted with permission [111]. Copyright 2024, American Chemical Society. (f) (i) Schematic illustration of TESP, (ii) Schematic depiction of wound healing using NIR responsive MXene-based TESP. (g) Under irradiation for 120s, the photothermal heating curves of the wound with or without the TESP electronics. Reprinted with permission [112]. Copyright 2024, Elsevier.

sensing by Ti_3C_2 MXene nanosheets. The researchers synthesized Ti_3C_2 nanosheets from Ti_3AlC_2 MAX phase material through a two-step process involving hydrofluoric acid treatment and tetrapropyl ammonium hydroxide dispersion. MXene was then combined with gelatin to create a conductive and photothermal hydrogel, encased in silicone rubber. The incorporation of MXene enhanced the TESP's functionality by enabling it to harvest biophysical energy, generate an electric field around damaged tissues, and provide near-infrared photothermal effects. The device achieved impressive electrical outputs, with peak-to-peak voltage and current reaching 163.7 V and 8.1 μA, respectively. MXene's electrical conductivity and excellent photothermal conversion properties contributed to multiple benefits in wound healing applications. In vitro studies demonstrated accelerated cell migration of mouse fibroblasts, while in vivo experiments on mice revealed enhanced collagen deposition and angiogenesis, leading to faster tissue regeneration and wound healing (Fig. 15f). The MXene-based TESP could rapidly raise wound temperature to 45 °C under near-infrared laser exposure, promoting vascular regeneration, as shown in Fig. 15g. Additionally, the device functioned as a real-time physiological signal monitor and motion sensor, capable of detecting movements such as finger touches and monitoring body motions of mice. The TESP exhibited excellent durability, withstanding 6000 stretches without losing functionality [112].

4.3.4. Transition metal dichalcogenides

Transition metal dichalcogenides (TMDs) are semiconductors described by the chemical formula MX_2, where M represents a transition metal such as tungsten (W) or molybdenum (Mo), and X represents a chalcogen element which is tellurium (Te), selenium (Se), or sulfur (S). The two-dimensional forms of TMDs include compounds like MoS_2, $MoSe_2$, WS_2, and WSe_2. These materials have garnered considerable attention for their potential use in energy harvesting, spintronics, and optoelectronics. This is because they possess direct band gaps, atomic-scale thickness, and quantum confinement features. Within the TMD family, MoS_2 has been widely studied and may be found in several structural phases, such as 1H and 2H (both hexagonal), 1T (trigonal), and 3R (rhombohedral). MoS_2 has been employed as a charge-trapping material, effectively reducing charge recombination and thereby enhancing the performance of TENGs. The 1T phase of metallic MoS_2 demonstrates high electrical conductivity, making it an ideal choice for electrode materials in TENG applications [113,114]. Recently Liu et al. [115] incorporated MoS_2 into a polyvinyl alcohol (PVA) matrix to improve the performance of a TENG. The addition of MoS_2 is intended to exploit their extensive electrochemically active surface area, strong surface adaptability, and abundant coordination sites. The researchers employed electrospinning to fabricate PVA/MoS_2 nanofiber membranes, resulting in the formation of a consistent filamentous structure and enhancing the surface area of contact between the friction layers. This nanostructured surface improved the device's ability to capture and transfer charges during the contact-separation process. They examined various factors affecting the triboelectric output, including the PVA and MoS_2 doping ratio, electrospinning duration, operational frequency, load resistance. They also explored the effects of different layer configurations, layer spacing, and parallel connections of multiple TENG units to optimize the overall device performance. Through this comprehensive optimization process, they developed a rotational contact TENG (RC-TENG) inspired by waterwheels, as shown in Fig. 16a. The optimized RC-TENG, when combined with a power management circuit (PMM), achieved a peak power density of 157 mW/m^2 at 1 Hz frequency for a single TENG unit. This significant improvement in power output demonstrates the effectiveness of incorporating 2D-TMDs into the friction layer of TENGs. The enhanced device showed practical applications in powering a digital thermo-hygrometer and removing lead ions from water, showcasing its potential for energy harvesting from pipeline water flows and environmental protection [115]. In another

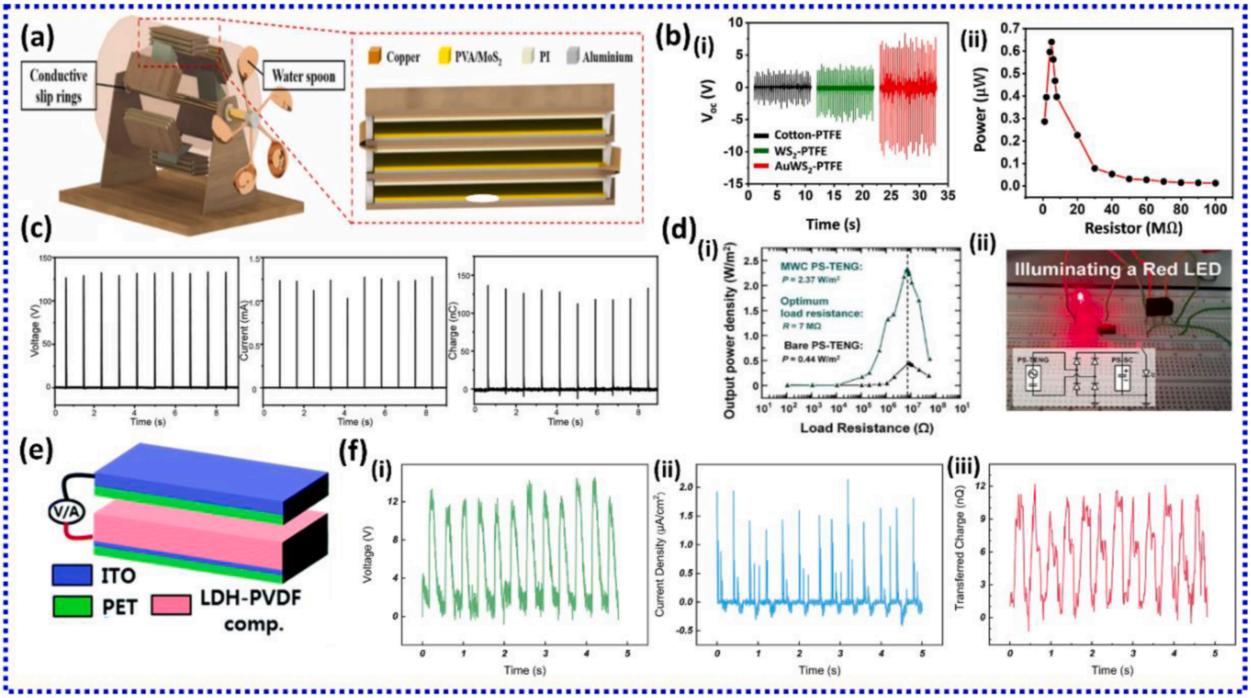

Fig. 16. (a) Drawing of the main structure of RC-TENG electronics. Reprinted with permission [115]. Copyright 2024, Elsevier. (b) (i) comparison of Voc on the bare cotton, WS_2, and AuWS_2-based STENG, (ii) power plot. Reprinted with permission [117]. Copyright 2024, Springer. (c) V_{oc}, I_{sc}, and Q of the TENG with $MoSe_2$. Reprinted with permission [118]. Copyright 2024, Wiley VCH. (d) (i) Output power density for the dependence of the load resistance in an MWC $Co_{0.5}Ni_{0.5}$-PS-TENG system and (ii) demonstration of feasible application by lighting up a commercial LED. Reprinted with permission [119]. Copyright 2023, Polymers. (e) Schematic illustration of ZnAl–LDH–PVDF composite-based TENG. Reprinted with permission [120]. Copyright 2021, Royal Society of Chemistry. (f) Output performance of modified LDHs based WD-TENG: (i) Output voltage, (ii) current density, (iii) transferred charge of the water droplets passing throughout the triboelectric layer (modified LDHs) of the WD-TENG. Reprinted with permission [121]. Copyright 2020, Elsevier.

study, Zhou et al. [116] utilized atomic-crystal TMDs to create high-performance Schottky direct-current triboelectric nanogenerators (DC-TENGs). They synthesized atomic-crystal WSe_2, WS_2, $MoSe_2$, and MoS_2 using chemical vapor deposition methods. The working mechanism relies on sliding a conductive atomic force microscope (AFM) tip across the atomically flat TMD surfaces, creating a Schottky junction that facilitates efficient charge separation and transfer. This approach resulted in an exceptionally high current density of 10^{10}A/m^2, surpassing previous records by two orders of magnitude. The improved performance was ascribed to the atomic flatness of TMDs, which optimizes the effective contact area and reduces the average contact distance, resulting in more efficient interfacial charge transfer. The robust local electric field produced by the nanoscale AFM tip facilitates improved non-equilibrium carrier movement. Density functional theory computations and finite element simulations demonstrate the significance of atomic-level interfacial characteristics in optimizing charge transport. To demonstrate the scalability, they produced a high-crystalline monolayer MoS_2 sheet utilizing a sliding electrode. This work established a novel benchmark for DC-TENG performance and provided significant insights into the optimization of interfacial features at the atomic scale to improve triboelectric energy production efficiency [116].

Chekke et al. [117] developed a self-powered temperature sensor based on a TENG by using tungsten disulfide (WS_2) augmented by gold (Au) nanoparticles as the active triboelectric layer and a cotton platform. WS_2, a 2D TMD material, was essential because of its distinctive characteristics, including layer-dependent band gap, substantial surface area, and high mobility. The preparation of WS_2 nanosheets is processed by lithium-ion intercalation and exfoliation, then augmented with Au nanoparticles to create an AuWS_2 nanocomposite. The nanocomposite was applied onto the cotton substrate using drop-casting, creating the active triboelectric layer of the STENG. The use of Au nanoparticles enhanced the efficacy of WS_2. Various triboelectric counter layers were investigated, with the AuWS_2-PTFE pair-based STENG demonstrating the highest output voltage of approximately 11.6 V and generating a power of 0.64 μW as shown in Fig. 16b. This configuration was able to charge a capacitor up to 60 nC within 10 s. STENG demonstrated temperature-dependent behavior, producing increased output voltage upon contact with PTFE at higher temperatures, thereby facilitating its use as a temperature sensor with a sensitivity of around 0.14V K^{-1}. The researchers demonstrated the device's capability to detect body temperature by observing variations in output voltage in response to elevated human body temperatures. The stability and durability of the fabricated STENG suggested its potential for long-term applications in wearable sensing devices [117]. In 2023, Zheng et al. [118] developed a droplet-based TENG by using $MoSe_2$ nanosheets as an intermediate layer. The TENG was constructed with a Pt wire electrode, a hydrophobic PTFE membrane, a $MoSe_2$: PI mixture intermediate layer, and an ITO-coated glass substrate. The working mechanism of the device relies on the coupling of triboelectrification and electrostatic induction. Initially, the PTFE surface becomes negatively charged due to triboelectrification, while the ITO layer develops induced positive charges, forming an equivalent capacitor. As water droplets interact with the device, they contact the Pt wire electrode, closing the circuit and creating a second capacitor between the water and Pt. The alternating contact and separation of water droplets with the Pt wire cause these two capacitors to charge each other alternately, resulting in a back-and-forth transfer of charges and generating an observable current in the external circuit. By incorporating the $MoSe_2$ intermediate layer, the TENG performance improved significantly. The device achieved a short-circuit current of 1.2 mA, which was double that of a TENG without the intermediate layer, and nearly four times that of a basic TENG. The open-circuit voltage reached 120 V, and the transferred charges were 120 nC (see Fig. 16c). This enhancement was attributed to $MoSe_2$'s ability to trap electrons, reduce charge recombination, and improve charge retention on the TENGs surface. The $MoSe_2$s layered structure and defect energy levels created electron-trapping sites, effectively hindering the recombination of electrons and positive charges on the electrode. To further analyze the energy conversion process, the team developed a more precise model, based on the modified kinetic energy calculation and current integration (KECCI) method, for calculating input energy, considering factors such as air buoyancy and resistance correction. The maximum energy conversion efficiency of this TENG reached 32.82%. The fabricated TENG is integrated with an all-solid supercapacitor for energy storage and demonstrated its application in powering a wireless sensing system for environmental monitoring [118].

4.3.5. Layered Double Hydroxides

Layered Double Hydroxides (LDHs) are a versatile class of 2D materials characterized by positively charged metal hydroxide layers interspersed with anions and water molecules. These materials have garnered significant interest owing to their highly customizable composition, enabling the incorporation of various divalent (Mg, Ni, Zn) and trivalent (Ga, Al, Fe, Mn) metal cations within the hydroxide layers. The general formula for LDH compounds is $[M^{2+}{}_{(1\text{-}x)}\ M^{3+}{}_{x}\ (OH)_2]\ [A^{n-}]_{x/n}.zH_2O$, where A^{n-} (such as cl$^-$, CO_3^{2-}, SO_4^{2-}) represents the interlayer anions, and x, the ratio of $M^{3+}/(M^{3+}+M^{2+})$, it normally lies between 0.2 and 0.3. The structural adaptability of LDHs, combined with their ion-exchange properties, makes them highly attractive for applications in catalysis, environmental cleanup, drug delivery, and energy storage. Additionally, their surface modifiability and the potential to construct hierarchical structures enhance their applicability in areas such as photochemistry, electrochemistry, and biomedicine. Due to their extensive functionality, LDH-based materials are promising candidates for the next generation of advanced materials [122]. Ritu et al. [123] developed a high-performance, temperature-stable TENG by using ZnAl LDH nanosheets reinforced in a PVA matrix. The ZnAl LDH nanosheets were synthesized via the hydrothermal method and incorporated into a PVA matrix at various concentrations (1%, 3%, 5%, and 10% by weight) to form nanocomposite films and subsequently employed as the active layers in a flexible TENG. The impact of LDH on the performance was significant and multifaceted. Firstly, the LDH nanosheets contributed to an exceptional thermal stability, allowing them to maintain ultra-stable output performance at temperatures up to 200 °C. This addresses a common challenge in polymer-based devices, which typically suffer from performance degradation at high temperatures. The fire-retardancy and high-temperature stability (up to ~500 °C) of the LDH nanosheets played a crucial role in this aspect. The polar and electropositive laminar nature of LDH nanosheets enhanced the electropositive triboelectric nature of the active layers, improving the overall performance of the device. The LDH-PVA nanocomposite also demonstrated a remarkably exceptional dielectric constant of 5×10^5 at low frequencies, which is reported for the first time for this material. This high dielectric constant, along with the synergistic effect between the LDH nanosheets and PVA, contributed to an enhanced output voltage. The nanogenerator achieved a voltage of 60V under a low vertical pressure of 1 kgf. Furthermore, LDH nanosheets improved the mechanical strength and surface properties of the polymer composite, which are crucial factors for triboelectric performance. The device having potential for monitoring human body movements showcasing its applicability as a self-powered sensor [123]. Jo et al. [119] employed an innovative approach to create self-charging hybrid supercapacitors by combining Ni-Co LDHs with a polystyrene (PS) substrate. The use of LDHs had a significant impact on both the supercapacitor and TENG components of the system. They employed a two-step synthesis method, utilizing microwave assistance for just 1 min to create a hierarchically designed flake-like morphology of Ni-Co LDHs on transitioned PS. This unique structure enhanced surface-active sites and improved electrochemical properties. The optimized MWC $Co_{0.5}Ni_{0.5}$ electrode demonstrated impressive performance, including an aerial capacity of 100 μAh/cm^2 at 1 mA/cm^2 current density and 91.2%

capacity retention over 5000 cycles. When assembled into a hybrid supercapacitor (HSC) device with activated carbon as the negative electrode, it exhibited a high areal capacitance of 531.25 mF/cm^2 at 5 mA/cm^2 current density. The HSC device achieved a power density of 16 mW/cm^2 at an energy density of 0.058 mWh/cm^2, maintaining 82.8% capacity retention after 10,000 cycles. When the HSC was implemented into the TENG, the device performance was enhanced in comparison to the bare PS-TENG. As the MWC PS-TENG achieved an output of 54V and 3.7 μA respectively, whereas bare PS-TENG achieved 23V and 2.4 μA. The MWC PS-TENG achieved a peak instantaneous output power density of 2.37 W/m^2 with a load resistance of around 7 MΩ. In comparison, the bare PS-TENG generated only 0.44 W/m^2 under similar load resistance conditions. The device successfully turns on the red LED as shown in Fig. 16d [119].

Ippli et al. [120] explored the use of ZnAl-CO_3-LDH (layered double hydroxide) in combination with PVDF (poly vinylidene fluoride) to create a high-performance TENG (see Fig. 16e). They fabricated transparent and flexible ZnAl-LDH-PVDF composite films with varying amounts of LDH (0–30 wt%) using a spin-coating method. The addition of LDH significantly enhanced the formation of the electroactive β-phase in PVDF and improved its dielectric properties, eliminating the need for electrical poling. They investigated the effects of LDH concentration on the composite's properties and TENG performance. They found that the 20 wt% composite-based TENG demonstrated the best output, generating a voltage of 230.6 V, a current density of approximately 5.6 μA cm^{-2}, and a power density of 0.43 mWcm^{-2}. The device also showed promising applicability as a self-powered sensor, exhibiting excellent pressure sensitivity (13.07 V kPa^{-1}) and humidity response (259.4% in voltage detection mode) [120].

In another study, LDHs were utilized as a novel triboelectric layer for water-driven TENGs (WD-TENGs). Cui et al. [121] developed a bottom-up approach to grow LDH nanosheets perpendicularly on an aluminum substrate through a corrosion process. This in-situ growth method ensured strong adhesion between the triboelectric layer and the electrode, thereby enhancing the device's durability. The unique layered structure of LDHs provided the necessary surface roughness for achieving super-hydrophobicity, which is crucial for efficient water energy harvesting in this architecture. The LDH surface was further modified with fluorine-containing functional groups using CVD, resulting in a superhydrophobic triboelectric layer with a water contact angle of approximately 159°. This modification created an almost "friction--free" surface, reducing abrasion and improving the WD-TENG performance and longevity. The operational principle of the WD-TENG encompasses contact electrification and electrostatic induction at the liquid-solid interface. As water droplets descend through the air, they become positively charged due to friction. When these charged droplets approach the modified LDH surface, they induce an electric potential difference, causing electrons to flow from the ground to the aluminum electrode. As the droplets leave the surface, the electrons flow back to the ground, generating an electric current. The modified LDH-based WD-TENG demonstrated excellent stability, maintaining consistent performance over extended periods and even withstanding harsh acidic and basic conditions. The device achieved an output of 13 V and a current density of 1.6 μA/cm^2, with transferred charges of approximately 8.5 nC per stream of water droplets as shown in Fig. 16f. The fabrication process proved to be scalable, allowing production of meter-scale WD-TENGs. This scalability is a significant advancement for practical applications and potential commercialization. The researchers discovered a linear correlation between the frequency of the triboelectric output signals and the water flow rate, allowing the device to operate as a self-sustaining water flow rate meter or rainfall sensor. The multifunctionality enhances the utility of the WD-TENG beyond simple energy harvesting [121]. The detailed summary of 2D materials based TENG performance is presented in Table 3.

4.4. *Organic frameworks*

Metal-organic frameworks (MOFs) and covalent organic frameworks (COFs) represent cutting-edge materials in TENG. These crystalline structures, characterized by their exceptional porosity and adaptability, are revolutionizing energy harvesting techniques [22,129]. MOFs, composed of metal nodes linked by organic ligands, and COFs, formed through covalent bonds between organic molecules, offer unparalleled surface areas and customizable chemical properties [130,131]. When incorporated into TENGs, these frameworks enhance charge separation and storage, improving power output significantly. Their nanoscale pores act as charge-trapping sites, while their tunable surface chemistry allows for optimized triboelectric effects [132,133]. Moreover, the inherent stability of MOFs and COFs contributes to the longevity of TENG devices, making them suitable for harsh environments. Researchers are exploring various MOF and COF compositions to fine-tune electron affinity, work function, and dielectric properties, pushing the boundaries of TENG efficiency [134–136]. This synergy between MOFs, COFs, and TENGs opens new avenues for harvesting waste mechanical energy in applications ranging from wearable electronics to large-scale energy systems, potentially transforming our approach to sustainable power generation [137,138]. Zeolitic imidazolate frameworks (ZIFs), a subset of metal-organic frameworks (MOFs), constitute a unique class of porous hybrid materials that have been thoroughly investigated in the last decade for their prospective applications in drug delivery, gas sorption and separation, catalysis, and sensing. Recently, Dhal et al. [139] synthesized Zeolitic Imidazolate Framework-4 (ZIF-4), a type of MOF, using an innovative and cost-effective solvothermal method. They replaced the traditional expensive Teflon autoclave with a common kitchen pressure cooker, addressing limitations in existing synthesis techniques. The synthesis involved combining zinc nitrate hexahydrate

Table 3
Summary of 2D materials based TENG performance.

Ref	Material	Triboelectric material pair	Size of the device	Voc	Isc	Power Max
[25]	Graphene	PET	–	9 V	1.2 μA cm^{-2}	2.5 μW/cm^2
[95]	Graphene oxide/carboxymethyl cellulose	FEP	2 × 2 cm^2	97 V	1.2 μA	41.4 μW
[99]	Graphene sheets	FEP	4 × 6 mm^2	6.3 V	22 nA	–
[102]	polyimide/boron nitride nanosheet	Al	2 × 2 cm^2	65.9 V	4.5 μA	21.4 μW/cm^2
[106]	boron nitride nanosheet/polycarbonate	PVP	3 × 3 cm^2	800 V	0.78 mA/m^2	1.36 W/m^2
[105]	h-BN-CNT-TPU	polymide	1.5 × 1.5 cm^2	47 V	244 nA	50.8 mW/m^2
[104]	hBN	Plastic	3 × 3 cm^2	68 V	6.1 μA	460 mW/m^2
[110]	MXene	Kapton	4 × 2 cm^2	100 V	400 nA	16 μW
[124]	MXene	PET	2.5 × 5 cm^2	650 V	7.5 μA	0.65 mW
[111]	MXene-PVDF	polypropylene	–	420 V	1.47 mA/m^2	619 mW/m^2
[117]	$AuWS_2$	PTFE	2 × 3 cm^2	11.6 V	–	0.64 μW
[125]	WS_2	PTFE	–	11.02V	1.072 μA	1.7 μW
[126]	ligand-conjugated -WS_2	PET	2 × 2 cm^2	12.2 V	0.5 μA	138 mW/m^2
[127]	PVDF-MoS_2	PDMS	–	211 V	1.6 μA	104.5 μW/cm^2
[128]	PDMS-MoS_2	Skin	2 × 1 cm^2	320 V	15.4 μA/cm^2	3.2 mW/cm^2,

and imidazole in dimethylformamide (DMF) solvent, stirring the mixture, and then heating it in sealed glass vials placed in a sand bed within the pressure cooker at 135 °C for 48 h. This method not only reduced costs but also maintained the quality and efficiency of the produced ZIF-4 particles. The characterisation analyses confirmed the crystallinity, purity, and morphology of the ZIF-4 particles, which exhibited irregular sizes ranging from 1 to 2 μm with an orthorhombic crystal structure. The synthesized ZIF-4 was utilized as a positive triboelectric layer in the fabrication of a TENG, as presented in Fig. 17a. The fabricated TENG is operated in VCS mode and the highest power output achieved was 18 μW at a load resistance of 50 MΩ. This innovative approach not only contributes to the development of sustainable energy solutions but also highlights the potential of ZIF-4 in advancing TENG technology for powering various consumer electronics [139]. In another study, Kakim and his team [140] utilized MIL-125 to develop flexible TENG. MIL-125 was synthesized by dissolving terephthalic acid in a mixture of DMF and methanol and then titanium isopropoxide. The solution was autoclaved, centrifuged, washed, dried, and then calcined to obtain the final MIL-125 powder. They incorporated MIL-125 into a silicone rubber (Ecoflex) matrix at various concentrations (0.1, 0.25, 0.5, and 1.0 wt%) to create flexible TENG devices. MIL-125 and Ecoflex mixture was ultrasonicated and then molded it with embedded carbon cloth electrodes. The impact of MIL-125 on the TENG performance was significant, with the optimal concentration of 0.25 wt% MIL-125 producing an output of up to 305 V and 13 μA, more than doubling the power density compared to pristine Ecoflex-based TENGs. This enhanced performance is attributed to MIL-125's high charge-inducing and charge-trapping capabilities, as well as its molecular porosity that increases the internal surface area and facilitates charge transfer. They demonstrated the practical applications of their MIL-125/Ecoflex TENG by powering small electronic devices such as calculators, humidity sensors, and cardiac pacemakers as shown in Fig. 17b. Furthermore, they developed a robotic gripper with embedded self-powered MIL-125/Ecoflex TENG sensors, capable of identifying various objects through machine learning techniques [140]. Liu et al. [141] fabricated a smart bandage system based on a zeolite imidazolate framework-8 (ZIF-8) TENG for in situ real-time monitoring of drug concentration. They first synthesized ZIF-8 nanoparticles and loaded them with gentamicin sulfate (GS) as the antibiotic. These drug-loaded ZIF-8 particles were then incorporated into polycaprolactone (PCL) nanofibers through electrospinning to create a composite PCL/ZIF-8@GS fiber membrane. This membrane served as both the tribo-positive electrode material for the TENG and an antibacterial dressing. The smart bandage was assembled by combining the PCL/ZIF-8@GS fiber membrane with a FEP industrial film (as the negative friction layer), medical bandages, and aluminum electrodes in an arched structure (see Fig. 17c). The electrical output of the TENG changed as drugs were released from the ZIF-8 carriers, allowing for real-time drug concentration monitoring. The researchers connected the smart bandage to energy management and signal comparison modules, and indicator lights to provide visual feedback on drug levels. They found that the electrical output of the TENG gradually decreased with the continuous release of GS during the wound healing process. The system used green, yellow, and red indicator lights to show high, normal, and low drug concentrations, respectively. They showed that this smart bandage could guide medical staff on when to replace bandages, potentially reducing drug waste and minimizing the risk of secondary damage or cross-infection from frequent bandage changes. The composite PCL/ZIF-8@GS fibers exhibited good tensile properties, water contact angle, and air permeability, making them suitable for wound dressing applications [141]. Despite all these examples, the direct utilization of MOFs in TENG devices remains a relatively unexplored area, with most existing research focusing on composite materials that combine MOFs with polymers or binders. Babu et al. [142] addressed a critical gap in the field by developing a method for the direct growth of ZIF-67, a zeolitic imidazole framework MOF, on an aluminum substrate for use in TENGs. The synthesis process involved a simple, cost-effective hydrothermal method. Initially, they grew cobalt carbonate hydroxide (CCH) on the

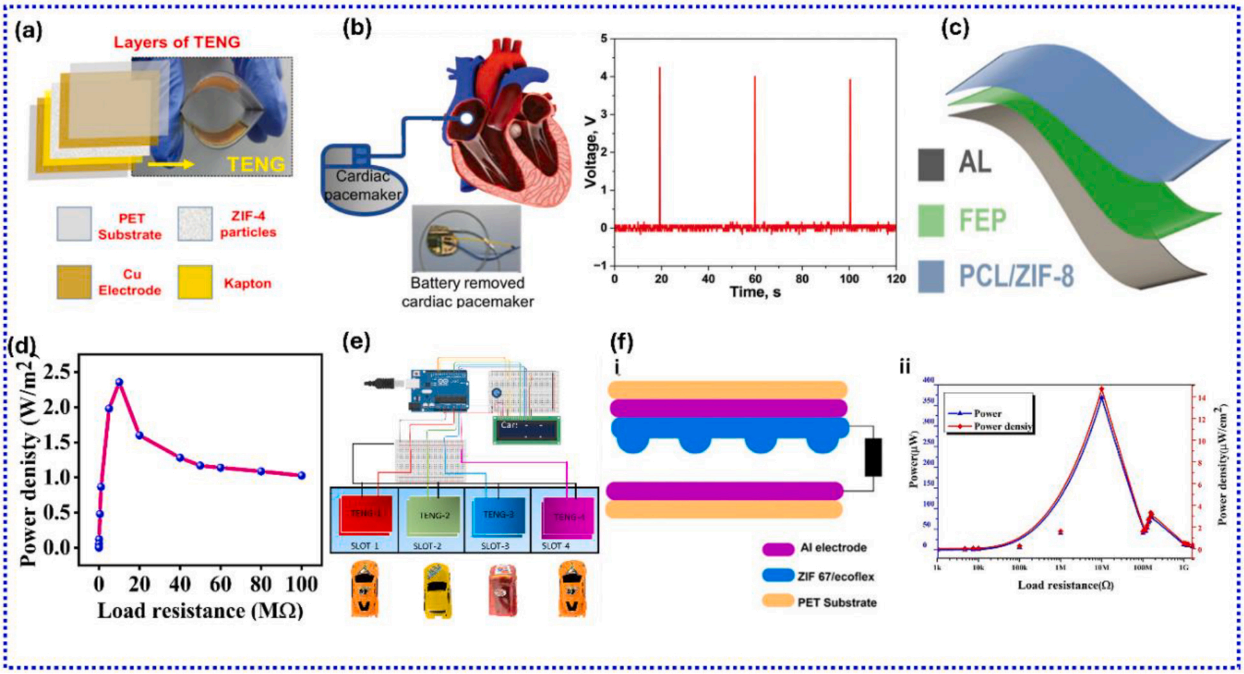

Fig. 17. (a) Digital image of a MOF based TENG. Reprinted with permission [139]. Copyright 2024, Willey. (b) Battery removed cardiac pacemaker enabled by a MIL-125/Ecoflex TENG, and its diagram with generated impulses. Reprinted with permission [140]. Copyright 2024, Willey. (c) 3D Structure diagram of PZ-TENG. Reprinted with permission [141]. Copyright 2024, American Chemical Society. (d) The power density of the fabricated TENG device. (e) Schematic illustration of a smart parking prototype model utilizing an Arduino board and four TENG devices. Reprinted with permission [142]. Copyright 2023, American Chemical Society. (f) (i) Equivalent layers in FZ-TENG e-skin, (ii) detailed analysis of FZ-TENG power and power density. Reprinted with permission [143]. Copyright 2024, American Chemical Society.

aluminum substrate, serving as a precursor for the ZIF-67 growth. This direct growth approach avoiding polymer composites or binders, allowed for a more accurate assessment of the MOF's inherent triboelectric properties. The innovative method resulted in a ZIF-67-based TENG that demonstrated impressive performance, achieving a maximum power density of 2.35 W/m^2 as shown in Fig. 17d. This output significantly surpassed previous MOF-based TENGs, highlighting the potential of directly grown MOFs for energy harvesting applications. The high performance can be attributed to the porous nature of ZIF-67, which increases the effective surface area for triboelectric charge generation. The fabricated TENG was integrated into an intelligent parking system where the TENG was placed beneath a parking slot, generating electrical signals when vehicles entered or left the space (see Fig. 17e). These signals could be used to power LED indicators showing parking spot occupancy, potentially connecting to a central monitoring unit for real-time tracking of available spaces [142]. In another study by Nikita et al. [143], ZIF-67 was incorporated into a composite structure with ecoflex polymer to create an innovative TENG. They utilized 3D-printed molds to form dome and pyramidal structures mimicking fingerprints, which enhanced the device performance through increased surface roughness and charge trapping sites. This ZIF-67/ecoflex composite film served as the negative material, paired with aluminum as the positive material in a contact-separation mode TENG. The novel design achieved an impressive open circuit voltage of 401 V, short circuit current of 12.8 μA, an instantaneous power of 366 μW, and a power density of 14.64 $\mu W/cm^2$ (Fig. 17f). This high-performance TENG was then integrated into a self-powered smart glove for paralyzed patient care, incorporating IoT technology for remote monitoring and emergency alerts [143].

Covalent organic frameworks (COFs) have lately been investigated as viable options for TENG applications owing to their structural variety, tunability, and capacity to enhance charge transfer. However, the inadequate electrical conductivity of COFs has hampered their efficacy [144]. To overcome this constraint, researchers have explored metal-covalent organic frameworks (MCOFs) to improve the electron transport capabilities of COFs while preserving their advantageous structural attributes [145]. Qiao et al. [146], synthesized a trifluoromethyl-substituted covalent organic framework (CF_3-COF) using 2,4,6-trihydroxybenzene-1,3,5-tricarbaldehyde and 2'-(trifluoromethyl)-[1,1':4′,1"-terphenyl]-4,4"-diamine via a solvothermal method. This CF_3-COF was then post-modified by introducing copper ions through coordination bonds, resulting in Cu-COF as shown in Fig. 18a. They found that the Cu-COF maintained the crystalline structure of the original CF_3-COF while incorporating copper ions, which was confirmed by inductively coupled plasma mass spectrometry. When used as a triboelectric material in a TENG device, Cu-COF exhibited superior output compared to CF_3-COF. Specifically, the Cu-COF-based TENG showed a peak short-circuit current of 104 μA and an output voltage of 1107 V, which were 1.47 and 1.39 times higher than those of the CF_3-COF-based TENG, respectively. This enhanced performance was attributed to the improved charge density, conductivity, and narrower band gap of Cu-COF [146]. Sathiyanathan et al. [147] fabricated a novel disposable TENG (Di-TENG) using a nitrogen and sulfur-rich covalent organic framework (NSCoF) composited with chitosan (CS). They synthesized the NSCoF material and prepared free-standing, flexible CS-NSCoF composite films by incorporating different weight percentages of NSCoF into the chitosan matrix. Then, TENG devices were fabricated using these composite films against FEP, and their performance was compared to that of pristine chitosan. Including NSCoF in the chitosan matrix significantly improved the output performance of the

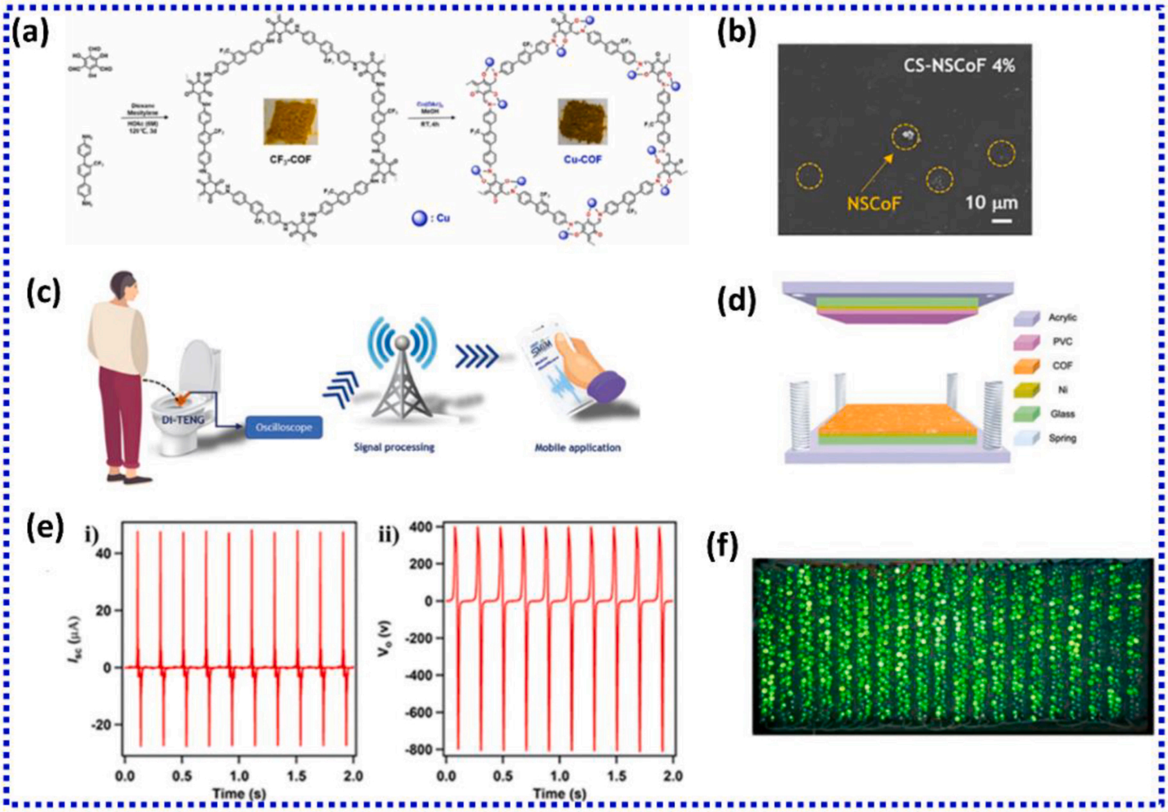

Fig. 18. (a) Schematic synthesis route of CF_3-COF and Cu-COF. Reprinted with permission [146]. Copyright 2024, Elsevier. (b) Surface morphology of CS-NSCoF 4% composite. (c) Hypothesis of the proposed urination evaluation application. Reprinted with permission [147]. Copyright 2023, Wiley. (d) 3D schematic illustration of the fabricated TENG device for highly fluorinated Tp-TFAB COF and a non-fluorinated Tp-TAPB COF. Reprinted with permission [148]. Copyright 2023, Wiley. (e) (i) Short-circuit current, (ii) open-circuit voltage of TFP-DB-COF at 5 Hz. (f) Lighting of 1338 LEDs using TFP-DB-COF-based TENG. Reprinted with permission [149]. Copyright 2020, American Chemical Society.

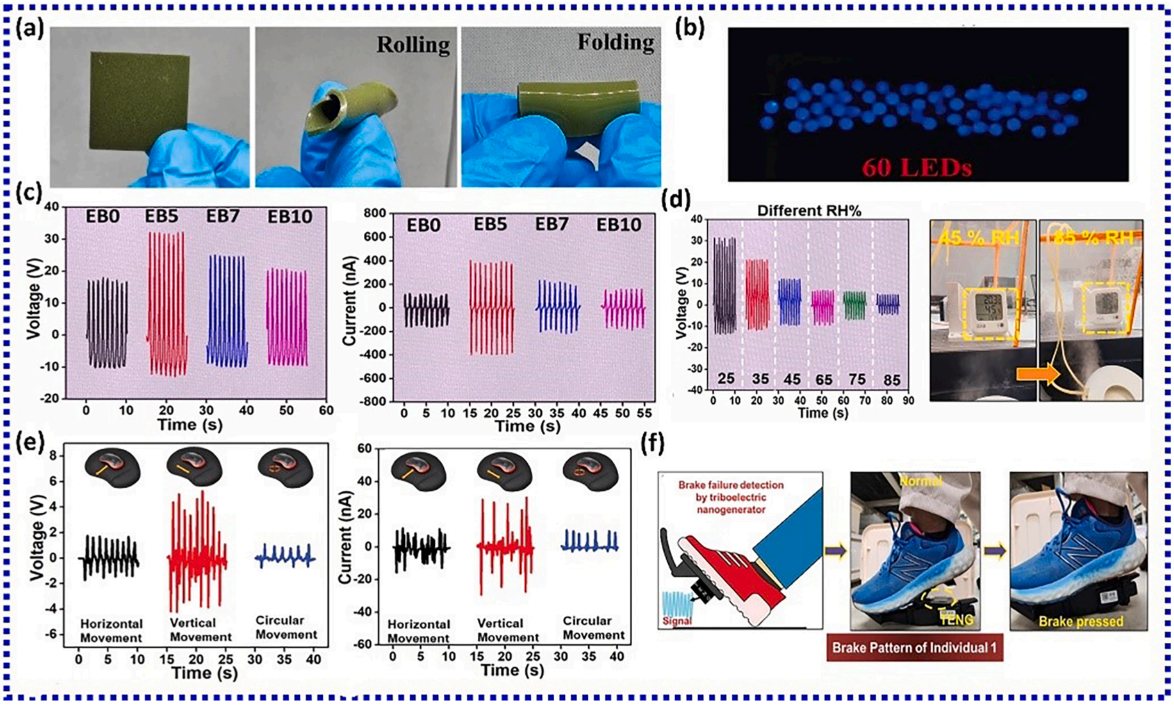

Fig. 19. (a) Digital camera images of the PDMS/$LaCrO_3$ films at 10 wt% by showing its flexibility after folding and rolling. (b) Brightening 60 LEDs. Reprinted with permission [150]. Copyright 2025, Elsevier. (c) Voltage and current of TENG based on fixed FEP layer and changing opposite layer as pure EVA, EVA-BFO5 wt.%, EVA-BFO7 wt.% and EVA-BFO10 wt%. (d) Humidity sensing data using TENG based on FEP-EVA-BFO5 wt.% at different relative humidity%, and digital image of the TENG based humidity sensor at different level of relative humidity (45 % and 85 % RH). Reprinted with permission [151]. Copyright 2024, Elsevier. (e) Voltage and current output by varying movement angle (horizontal, vertical, and circular) of the computer mouse by using aluminum as opposite friction layer in SBTO-PDMS TENGs. (f) Illustration of the SBTO-PDMS TENG being attached to brakes and digital image, detection of the normal braking. Reprinted with permission [152]. Copyright 2024, Wiley.

TENG. The optimized CS-NSCoF (4%) composite yielded a peak-to-peak voltage of 132 V, which was nearly double the output of pristine chitosan (69 V) under identical testing conditions. The short-circuit current reached approximately 2.38 μA, and the average power density was measured at 10.89 mW/m^2 when connected to a load resistance of 200 MΩ. This enhancement in triboelectric energy generation was attributed to increased surface roughness due to the presence of NSCoF particles (see Fig. 18b), improved dielectric constant from interfacial polarization, and enhanced electron-donating ability from the functional groups in NSCoF. The authors found that the CS-NSCoF 4% composite exhibited the most effective electrostatic interaction and optimal performance. The study also explored the application of this Di-TENG system for evaluating human urination conditions, integrating it with artificial intelligence algorithms for data analysis as presented in Fig. 18c [147]. Shi et al. [148] developed triboelectric TENGs using COF materials, specifically a highly fluorinated Tp-TFAB COF and a non-fluorinated Tp-TAPB COF. These COFs were synthesized through solvothermal reactions using triformylphloroglucinol (Tp) with 1,3,5-tris(2,3,5,6-tetrafluoroaniline) benzene (TFAB) or 1,3,5-tris(4-aminophenyl) benzene (TAPB). They then fabricated TENGs using these COFs as positive triboelectric materials, with polyvinyl chloride (PVC) films as the negative triboelectric layer (see Fig. 18d). The fluorinated Tp-TFAB COF-based TENG (PVC-FTC TENG) demonstrated superior performance compared to the non-fluorinated Tp-TAPB COF-based TENG (PVC-TC TENG), with a peak short-circuit current density of 16.25 mA m^{-2}, a transferred charge density of 94.6 μC/m^2, and an output voltage of 137.8 V. To further enhance this performance, the researchers developed hybrid films by incorporating the COFs into polyvinyl alcohol (PVA). The resulting PVC-PVA/FTC TENG showed even more impressive output, with a short-circuit current density of 26.34 mA m^{-2}, a transferred charge density of 148.5 μC/m^2, and a maximum peak power density of 8.24 W/m^2, which was nearly six times higher than that of the PVC-PVA TENG without COF [148].

In another study Zhai et al. [149] prepared a cationic TFP-DB-COF and a neutral TFP-DP-COF. The cationic COF was prepared using 1,3,5-triformylphloroglucinol (TFP) as a neutral knot and dimidium bromide (DB) as a cationic linker, while the neutral COF used TFP and 3,8-diamino-6-phenylphenanthridine (DP) as linkers. Both COFs were synthesized through imine condensation in a mixture of mesitylene and 1,4-dioxane, with acetic acid as a catalyst, under solvothermal conditions at 120 °C for 3 days. Then, these COFs were used to fabricate TENGs, and their performance was compared. The cationic TFP-DB-COF-based TENG demonstrated significantly improved output performance compared to its neutral counterpart. At a frequency of 5 Hz, the TFP-DB-COF-based TENG produced a short-circuit current of 47.9 μA and an open-circuit voltage of 815 V as shown in Fig. 18e, which were approximately 2 and 2.2 times higher than those of the TFP-DP-COF-based TENG, respectively. The charge density of the cationic COF was also twice that of the neutral COF. The enhanced performance was attributed to the cationic groups in TFP-DB-COF, which improved charge transport and conductivity within the material. The cationic COF-based TENG was successfully used to charge commercial capacitors, light up LEDs (see Fig. 20f), and power a stopwatch, showcasing its potential as an efficient energy harvesting device [149]. The detailed summary of MOF based TENG performance is presented in Table 4.

4.5. Perovskite-based TENG

Perovskite materials are compounds characterized by ABX_3, where A and B are cations and X is an anion. These materials have gained a lot of interest in the last few years due to their unique properties, such as ferroelectricity, superconductivity, and impressive optoelectronic characteristics. The capacity to adjust their composition and characteristics

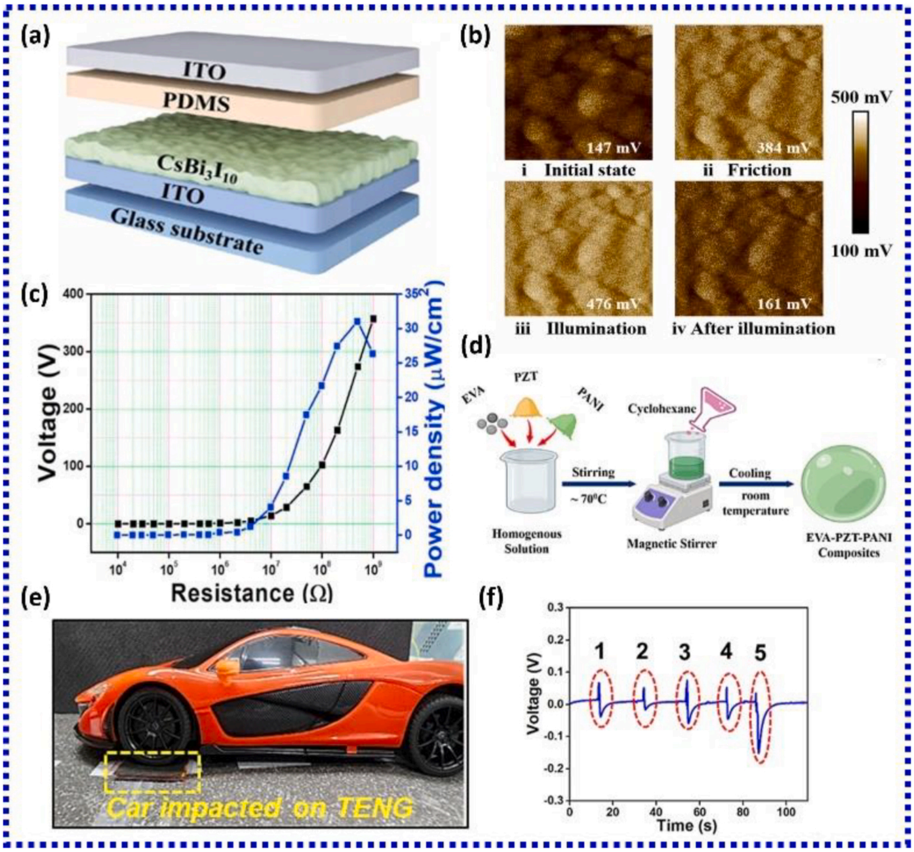

Fig. 20. (a) Schematic structure of the CBI/PDMS TENG. (b) Surface potential mappings of the four states. Reprinted with permission [153]. Copyright 2023, Elsevier. (c) Maximum power density of rough surface-based TP-TENG. Reprinted with permission [154]. Copyright 2021, Elsevier. (d) Synthesis procedure of EVA-PZT-PANI composites. (e) Digital image of the TENG sensor installed on road as well as side view image of the car step upon the TENG unit. (f) Estimation of the number of vehicles passed by the road using the peak produced by TENG output. Reprinted with permission [155]. Copyright 2024, Elsevier.

Table 4
Summary of metal-organic materials based TENG performance.

Ref	Material	Triboelectric material pair	Size of the device	Voc	Isc	Power Max
[156]	ZIF-8	Kapton	2.5 × 2.5 cm^2	164 V	7 μA	392 mW/m^2
[129]	PDMS-HKUST-1	Cu	2 × 2 cm^2	205 V	37 μA,	7.92 W/m^2
[157]	ZIF-7, ZIF-9, ZIF-11, ZIF-12	Kapton/ethyl cellulose	2.5 × 2.5 cm^2	60 V	1.1 μA	2.45 μW
[158]	ZIF-62	Teflon	2.5 × 2.5 cm^2	70 V	1.9 μA	9.68 mW/m^2
[159]	MIL-88A	EC (ethyl cellulose)	2.5 × 2.5 cm^2	90 V	2.5 μA	16.2 mW/m^2
[138]	ZIF-4	Kapton	_____	100 V	0.7 μA	18 μW
[142]	ZIF-67	FEP	4.5 × 4.5 cm^2	280 V	70 μA	2.35 W/m^2
[160]	ZUT-8	PVDF	5 × 5 cm^2	562.78 V	76.18 μA	2217.18 mW/m^2
[161]	UiO-66-NH_2	Al	3 × 3 cm^2	375 V	8 μA	1.69 W/m^2
[162]	ZIF-8HG	Kapton	____	150 V	4.95 μA	62.42 μW
[163]	MOF-5	PTFE	2.5 × 2.5 cm^2	484 V,	40 μA	3174 μW
[164]	Co/Zn bimetal organic framework	PTFE	1.5 × 1.5 cm^2	47 V	7 μA	1.1 μW/cm^2
[165]	ZIF-8/MO PPy@CelF	PTFE	4 × 4 cm^2	129 V	6.8 μA	33.3 mW/m^2
[166]	ZUT-75	PVDF	5 × 5 cm^2	565.67 V	90.72 μA	3100 mW/m^2
[140]	MIL-125	Cu	5 × 2 cm^2	305 V	13 μA	150 μW/cm^2
[167]	MIL-101	FEP	4 × 4 cm^2	194 V	14 μA	20.3 μW/cm^2
[168]	PAN@ZIF-8	PTFE	2 × 2 cm^2	260 V	24.5 μA	1.91 W/m^2
[149]	TFP-DB-COF	PVDF	5 × 5 cm^2	815 V	47.9 μA	_____
[148]	Tp-TFAB COF	PVC	2 × 2 cm^2	156.3 V	20.44 mA m^{-2}	8.24 W/m^2
[147]	CS-NSCoF	FEP	6 × 6 cm^2	132 V	2.38 μA	10.89 mW/m^2

has rendered perovskites appealing for various applications, including solar cells and light-emitting diodes. Their distinctive electronic structure, characterized by direct tunable bandgaps and balanced electron-hole effective masses, has placed perovskites at the leading edge of materials exploration. The integration of these materials into TENG offers high power density, enhanced polarizability, and improvement of surface charge density. Certain TENGs that utilize perovskite materials have shown markedly superior open-circuit voltages and power densities when compared to traditional designs. Furthermore, specific perovskite materials demonstrate photoinduced charge enhancement, which significantly increases the output current of the TENG when subjected to light exposure.

Recently, Saichompoo et al. developed a TENG using the rare earth oxide $LaCrO_3$. They prepared a PDMS/$LaCrO_3$ composite film by simple casting Fig. 19a, achieving a voltage and current of 89 V and 488 μA, respectively. The performance of the device is improved up to 161 V and 963 μA when subjected to gamma radiation at 150 kGy. Under these conditions, the device turns on 60 LEDs and charges 0.22 μF and 0.33 μF capacitors as shown in Fig. 19b [150]. In another study, Behera et al. developed a TENG using a bismuth ferrite (BFO) as a perovskite-type multiferroic material. They synthesized BFO particles using a sol-gel method, employing bismuth nitrate pentahydrate and iron nitrate nonahydrate as precursors in a solvent mixture of ethylene glycol and citric acid. The BFO particles were then incorporated into an Ethylene-vinyl acetate (EVA) polymer matrix to create EVA-BFO composites with varying weight percentages (5%, 7%, and 10%) of BFO. They then constructed a single-electrode mode TENG with the EVA-BFO composite as a triboelectric layer. The inclusion of BFO in the EVA matrix enhanced the device's triboelectric performance by improving charge generation and transfer efficiency. The optimized TENG, based on 5 wt% BFO-EVA composites, generated a voltage of 45V and a current of 800 nA. Additionally, they explored its potential as a self-powered humidity sensor, achieving a sensitivity of 0.53 V/RH% over a relative humidity range of 25%–85% is presented in Fig. 19c-d [151]. Kim et al. utilized $SrBi_2Ta_2O_9$ (SBTO), a lead-free perovskite material, to enhance the performance of TENG. They prepared SBTO nanoparticles using a solid-state reaction technique and then incorporated them into a PDMS matrix to create a composite film. The SBTO-PDMS composite (15 wt% SBTO) was fabricated using a solution casting method and applied as a free-standing layer in a TENG device with an interdigitated aluminum electrode. The addition of SBTO to the PDMS matrix improved the dielectric constant and charge storage capacity of the composite, leading to enhanced surface charge density and output efficiency of the TENG. The optimized TENG device, utilizing 15 wt% SBTO in the PDMS composite, delivered an impressive output of 13.5V, 45 nA, and a power of 0.98 μW. The device is then used for harvesting energy from computer mouse movements by fixing it under the mouse and a self-powered sensor for brake pattern recognition in automobiles (see Fig. 19e-f). By integrating digital signal processing techniques, the TENG-based sensor could distinguish between normal and abnormal braking patterns, potentially improving vehicle safety and enabling real-time monitoring and predictive maintenance in the automotive industry [152].

Wei and his team first reported on low-toxic lead-free bismuth halide, $CsBi_3I_{10}$ (CBI) perovskite. They prepared CBI for TENG to capture mechanical and optical energy by the triboelectric-photoelectric coupling effect. The device achieved an output of 158 V and 45.5 mA m^{-2}, respectively. There is an improvement of about 21.7% and 15.8% when it is subjected to 1.5 G illumination. The improvement in performance results from the photogenerated carriers migrating to the surface of the material, thereby increasing the surface charge density. Additionally, the mechanism of photo-induced enhancement can be validated through KPFM measurements, where an increase in surface potential from 384 mV to 476 mV was observed for the CBI film after illumination is shown in Fig. 20a-b [153]. In another study, Sahu et al. utilized a triple perovskite, $Sr_3Co_2WO_9$ (SCWO), which was synthesized using a modified aqueous sol-gel method, offering advantages such as low cost, uniform particle size, and high yield. The SCWO particles were incorporated into a polydimethylsiloxane (PDMS) matrix to create a composite film that served as the negative triboelectric layer in a triboelectric nanogenerator (TP-TENG). The TP-TENG operated in a vertical contact-separation mode with aluminum as the positive layer. The PDMS-SCWO composite film was fabricated with micro-roughness using soft lithography to enhance triboelectric performance. The device demonstrated exceptional output performance, generating 300 V, 2.2 mA, and a power density of 30.5 mW/cm^2 (see Fig. 20c). The TP-TENG was applied for real-time gait monitoring (walking, running, jumping) by embedding it in shoe soles and for self-powered information signaling via Morse code. Its flexibility and durability make it suitable for healthcare sensors and charging commercial capacitors, showcasing its potential in energy harvesting and wearable electronics [154]. In another study Behera and his team utilized composites of poly (ethylene-co-vinyl acetate) (EVA), lead zirconate titanate (PZT), and polyaniline (PANI). PZT was synthesized via calcination, PANI through oxidative polymerization, and EVA-PZT-PANI films were prepared by solvent evaporation. The TENG benefited from the synergistic combination of EVA flexibility, PZT piezoelectricity, and PANI conductivity. The optimized device (EVP3) generated 17.8V and 190 nA under 2 Hz and 5 N force. The device is used for real-time traffic monitoring by embedding TENG in roads to measure vehicle speed, and advanced self-powered systems for smart transportation infrastructure as shown in Fig. 20d-f [155]. In a recent study, Jayarathna et al. explored the use of lead-free potassium sodium niobate (KNN) ceramics in TENG. KNN was synthesized via a solid-state reaction using potassium carbonate, sodium carbonate, and niobium pentoxide. The TENG was fabricated with KNN as a positive triboelectric layer, Kapton as a negative layer, and PET as a substrate. It achieved an output of 70 V and 1100 nA, powering LEDs, charging capacitors, and harvesting energy from body motions. This environmentally friendly TENG demonstrates potential applications in wearable electronics and self-powered sensors, offering a sustainable solution for energy needs [169].

Metal halide, hybrid, and perovskite materials (MHPs) deserve special emphasis as they are at the forefront of optoelectronic materials, given their applications and record efficiency values in photovoltaic solar cells, photodetectors, and light emission devices [170]. These materials are a subgroup of the perovskite family, where the A-site is occupied by organic or inorganic cations (such as methylammonium, formamidinium, or cesium), the B-site by metals (like lead or tin), and the X-site by halides (such as iodide, bromide, or chloride). Their ionic nature makes these materials unstable under environmental conditions [171]. However, early results can already be mentioned for their implementation as triboelectric surfaces or fillers, opening the path to new tribovoltaic devices. Wang et al. explored the triboelectric charging behavior and photoinduced enhancement of $CsPbBr_3$ perovskites doped with alkaline earth ions (Mg^{2+}, Ca^{2+}, Sr^{2+}, Ba^{2+}) in a vertical contact-separation TENG configuration [52]. Their research demonstrated that Ba^{2+} doping significantly improved the triboelectric output, achieving a V_{oc} of 220 V, an I_{sc} of 28.2 μA, and a power density of 3.07 W/m^2. The study also revealed that photoexcitation played a crucial role in further enhancing triboelectric charge density, making perovskite-based TENGs a potential candidate for hybrid photovoltaic-triboelectric applications. Another study by Yu et al. investigated halogen regulation in perovskite TENGs by systematically analyzing the triboelectric performance of $CsPbX_3$ (X=Cl, Br, I) perovskites [53]. The findings indicated that $CsPbCl_3$ exhibited the highest triboelectric output, with a V_{oc} of 257 V, an I_{sc} of 27.87 μA, and a power density of 3.04 W/m^2. This enhancement was attributed to the improved dielectric properties and surface charge retention caused by chloride substitution. Additionally, the study established a modified triboelectric series ranking perovskite materials based on their charge affinity. Importantly, $CsPbCl_3$-based TENGs demonstrated excellent durability in ambient conditions, highlighting their suitability for long-term energy harvesting applications. Yang et al. focused on alkali metal ion doping in perovskite TENGs, examining the effect of substituting Cs^+ in $CsPbBr_3$ with Li^+, Na^+, K^+, and Rb^+ [54]. The research found that triboelectric properties could be systematically tuned through compositional engineering. The highest output was achieved using pristine $CsPbBr_3$, with a V_{oc} of 182 V, an I_{sc} of 23 μA, and a transferred charge (Q_{sc}) of 73 nC. However, Na^+, K^+, and Rb^+ doping further optimized the triboelectric charge transfer efficiency. The study also utilized finite-element simulations to analyze charge transfer mechanisms, confirming that alkali metal doping could effectively modify charge polarity and surface potential distribution, improving TENG performance. Comparing the results from these studies, it is evident that doping strategies significantly impact the triboelectric output of perovskite-based TENGs. Alkaline earth ion doping, particularly with Ba^{2+}, led to higher power densities, while halogen substitution optimized charge retention and durability. Alkali metal ion doping provided a means to tune triboelectric polarity and charge transfer efficiency. These findings collectively offer a framework for designing high-performance perovskite-based TENGs for mechanical energy harvesting. Overall summary of perovskite materials-based TENG performance is presented in Table 5.

4.6. Dielectric materials for TENG

As is well known, there are two categories of TENG devices based on the types of contacted materials (triboelectric materials): 1) conductor-to-dielectric and 2) dielectric-to-dielectric TENG (Fig. 21a) [62]. Chitosan (CS) is a polysaccharide derivative that has emerged as a candidate for tribo-positive friction material. It can be synthesized from chitin sources through a deacetylation process, which converts N-acetyl groups into amine functional groups. Depending on the degree of deacetylation, both hydroxyl (-OH) and amino (-NH_2) groups can be present. However, both –OH and –NH_2 groups tend to lose their electrons due to the inductive effect. Thus, implementation of CS in TENGs needs further efforts in charge tuneability, contact efficiency, and surface charge density to improve charge tuneability, contact efficiency, and surface charge density have been decided as crucial roles needing improvement for potential use. It is known that the CS needs to be dissolved in an acidic solution for preparation through the protonation reaction. After attracting proton (H^+) from acids, the –NH_2 group turns to be –NH_3^+. Lastly in 2024 (Fig. 23b-c), T. Charoonsuk and co-workers [172] published the controlling fraction of –NH_3^+ for designing triboelectric properties of CS by studying the dissolving in various acids, including acetic (CH_3COOH; ACA) acid, succinic ($C_4H_6O_4$; SA) acid, and citric ($C_6H_8O_7$; CA) acid. They showed that the choice and concentration of acids have a crucial role in influencing CS performance. Under optimized conditions (2.5% CA), the TENG exhibited maximum output of V_{OC} and I_{SC} of 157 V and 53 μA, which is three times higher than that of pristine CS. Ionic salt, $CaCl_2$, was added as a solid electrolyte to enhance the charge density of CS simultaneously by improving the contact area by casting CS solution on the sandpaper. The appropriate concentration of $CaCl_2$ significantly affects achieving the highest V_{OC} and I_{SC}. The optimized condition at 3% $CaCl_2$ can yield maximum V_{OC} of approximately 149 V and I_{SC} at ~15 μA, which is four- and three-fold more than the pristine CS [173]. Adding $CaCl_2$ ionic salts can form homogeneously with the CS chain without losing its transparency and flexibility. Ionic salt embedding can create higher ionic charges and electrons unoccupied states, resulting in higher charge density and mobility during the contact-separation process. Composite CS has also been attractive to study. Several researchers have tried to improve the triboelectric output performance by incorporating metal, dielectric, piezoelectric, and semiconductor materials.

The dielectric composites mixing solid dielectric fillers with the main triboelectric polymers have mainly been focused on so far. In polymer matrices, enhancing the dielectric constant is basically limited by atomic and electronic polarizations because of the molecular bonding; other types of polarizations play a crucial role in improving the polymer composite's dielectric constant. Upon incorporating dielectric/conductive nanoparticle (NPs) as filler phase or dispersed phase, the electric field (E) induction from TENG gives rise to the polarization of free electrons, resulting in the interfacial polarization effect in overall dielectric composites (Fig. 21) [174]. Under the action of induced E, the charge will be accumulated at the interface between NP and the main triboelectric layer. The interface polarization enhances the dielectric constant, surpassing surface charge density of the composite film as compared to the pristine one.

In this review, the dielectric composites are divided into two main categories: metallic materials and inorganic non-metal materials depending on the type of fillers. High difference dielectric constant between the polymer matrix and inorganic particles/nanoparticle results in nonuniform E distribution in final composite [175].

$$E_P = E_0\left[f_P\left(1-\frac{\varepsilon_{r,P}}{\varepsilon_{r,F}}\right)+\frac{\varepsilon_{r,P}}{\varepsilon_{r,F}}\right]^{-1} \tag{4}$$

$$E_F = E_0\left[f_P\left(\frac{\varepsilon_{r,F}}{\varepsilon_{r,P}}-1\right)+1\right]^{-1} \tag{5}$$

According to equations (4) and (5), where E_P and E_F are the E in polymer matrix and fillers, f_P denotes the volume fraction of the matrix. The $\varepsilon_{r,P}$ and $\varepsilon_{r,F}$ are ε_r of the polymer matrix and fillers. From these equations, the the E_P is basically higher and E_F is lower than the applied external E, thus in accordance with $E_P > E_0 > E_F$ [175–177]. As illustrated in Fig. 23c, upon incorporating metallic NPs fillers, the polarized electrons will occur leading to E=0, or it can be said that metallic NPs contain $\varepsilon_{r,F}$ at around infinity.

The external electric field induction results in the amount of interfacial polarization owing to the free electrons, as can be seen in Fig. 23c. For non-metallic or ceramic NPs fillers, the E_F is found to be > 0, depending on the f of fillers/matrix and their ε_r contrast ($\frac{\varepsilon_{r,F}}{\varepsilon_{r,P}}$). Once the E is generated by TENG, two polarized NPs align along E direction, the local field in the composite will further increase $> E_P$, resulting in electron conduction. So far, various forms of solid particles, nanoparticles, nanowires, nanotubes, nanoplates, nanoflakes, *etc.*, have attracted much attention from several researchers [26,178].

4.6.1. Polymer/dielectric filler composites for TENG

Inorganic non-metallic materials have been adopted in several publications as an effective way to enhance dielectric constant for improving charge density of polymer. Metal oxides are normally utilized as dielectric fillers in polymer layers of TENG because of their excellent dielectric properties. Not only dielectric properties, many of dielectric fillers also provide permanent polarization by exhibiting piezoelectric and ferroelectric as well. In recent years, various amazing properties of metal oxide filler materials, such as $CaTiO_3$ [179], $NaNbO_3$ [180], $BaTiO_3$ [181,182], $CaCu_3Ti_4O_{12}$ (CCTO) [77]etc., have been gradually discovered. In 2024, the vanadium-doped sodium niobate (V-$NaNbO_3$ or VNNb) micron-size powders were synthesized and incorporated in PDMS for composite TENG (Fig. 22a). The dielectric constant PDMS/V-$NaNbO_3$ was enhanced 1.3 times, allowing improving of electrical output for more than 2 times from pristine PDMS [183]. For biomechanical energy harvesting, the orthorhombic $CaTiO_3$ particles synthesized by a solid-state reaction were embedded into PVDF polymer. The β-phase PVDF could be improved, benefiting from polarization of $CaTiO_3$, thereby increasing the overall polarization, dielectric

Table 5
Summary of perovskite materials based TENG performance.

Ref	Material	Triboelectric material pair	Size of the device	Voc	Isc	Power Max
[52]	$CsPbBr_3$ doped with Ba^{2+}	PVDF	–	222V	28.2 μA	–
[53]	$CsPbCl_3$	PVDF	–	257V	27.87 μA	3.04 W/m^2
[54]	$CsPbBr_3$	PVDF	–	182V	23 μA	–
[150]	PDMS/$LaCrO_3$	Al	–	161V	963 μA	3.3 μW
[151]	EVA: BFO	FEP	2cm × 2 cm	45V	800 nA	3.6 μW
[152]	$SrBi_2Ta_2O_9$/PDMS	–	–	13.5V	45 nA	0.98 μW
[153]	$CsBi_3I_{10}$	PDMS	–	158V	45.5 mA m^{-2}	3.86 W/m^2
[154]	$Sr_3Co_2WO_9$/PDMS	Al	2.5cm × 2.5 cm	300V	2.2 μA	30.5 mW/cm^2
[155]	EVA-PZT-PANI	Kapton	–	17.8V	190 nA	–
[169]	(K, Na)0.5NbO_3	Kapton	2.5 cm × 2.5 cm	70V	1100 nA	–

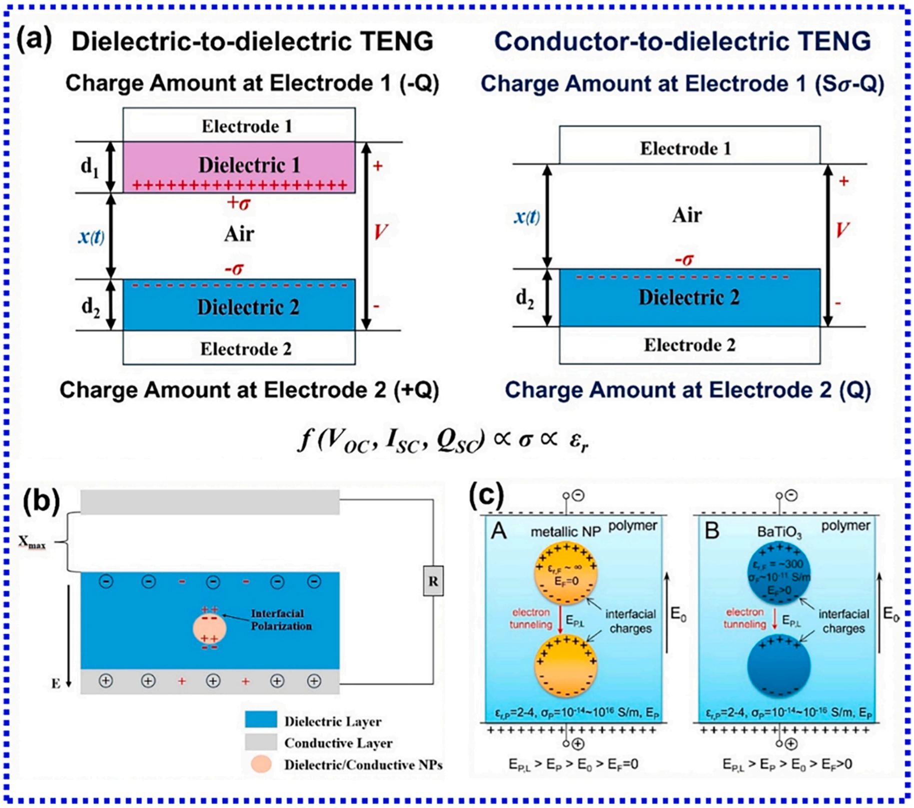

Fig. 21. (a) Parallel-plate contact-modes and equivalent circuit diagram for dielectric-to-dielectric and conductor-to-dielectric, theoretical models for TENG. Reproduced from Ref. [62]. Copyright 2015, Elsevier. (b) Schematic diagram of interfacial polarization occurring in polymer matrix. Reproduced from Ref. [174]. Copyright © 2025, American Chemical Society. (c) Schematics of interfacial polarization in (A) metallic and (B) ceramic (e.g., $BaTiO_3$) nanoparticles in a dielectric polymer matrix due to large contrasts in dielectric constants ($\varepsilon_{r,\,F} \gg \varepsilon_{r,\,P}$) and bulk conductivity ($\sigma_F \gg \sigma_P$). Reproduced from Ref. [175]. Copyright 2014, American Chemical Society.

constant and charge density. The appropriate 8% $CaTiO_3$ addition delivers the highest output of ~20 V, ~250 nA, and ~0.19 μW/cm^2. Some parts of the results can be found in Fig. 22b [179]. Fig. 22(c)shows the construction of nanostructure for adding in polymer TENG. Nanopillar $SrTiO_3$ prepared from the anodic aluminum oxide (AAO) template method, was used as dielectric fillers for PDMS TENG. The V_{OC} and I_{SC} about 130 V and 1.4 μA is reached using 9 wt% of $SrTiO_3$ nanopillar (aspect ratio=3) owing to the obtaining of maximum dielectric constant value at 4.85 [184]. Advanced composite was done by compositing between PVDF and nafion-assisted $BaTiO_3$. As illustrated in Fig. 22d, the $BaTiO_3$ (BT) nanoparticles were dispersed in Nafion solution to achieve functionalized BT before loading into PVDF. Impressive output performance (307 V, 1.8 μA/cm^2, and 1.12 mW/cm^2) was obtained because the presence of the sulfonic groups ($–SO_3H$) and perfluoroalkyl backbones allows both hydrophobic and hydrophilic moieties of $BaTiO_3$ and Nafion and the Nafion and PVDF. These unique properties prevent BT from agglomeration and enhance the interaction between PVDF and BT nanoparticles [185]. In addition to exhibiting dielectric properties, the permanent polarization by means of ferroelectric materials was enhanced by doping Sr^{2+} into $BaTiO_3$ (BST). According to the P–E loops (Fig. 22e) of BST, P_r of 2.12 μC/cm^2 was exhibited, 16 times more than $BaTiO_3$, at 2 wt% of doping concentration. It led to the high output performance of overall composite TENG after loading into PDMS [186]. Fig. 22f illustrated the use of colossal dielectric for the TENG output improvement. Lately in 2024 [77], the calcium copper titanate ($CaCu_3Ti_4O_{12}$ (CCTO)) synthesized by a solid-state reaction were composited with PDMS polymer for TENG, including an analysis of the effect of the thickness and concentration for performance optimization. Adding an appropriate amount of CCTO plays an important role in achieving the highest electrical output owing to the percolation threshold of composites. The summary of polymer/dielectric oxide composite TENG device performance is presented in Table 6.

The highest V_{OC} of ~250 V, I_{SC} of ~6.5 μA, charge density ~70 μC/m^2, and power density of ~3.15 W/m^2 could be reached. Table 1 provides an overview of dielectric composites exploited for TENGs, including available information for a quantitative comparison of the performances.

In addition to being used as electrodes, metallic materials can also be utilized to enhance the dielectric constant and output efficiency of the TENG contact layer. When metallic micro- or nanoparticles are incorporated into a polymer matrix, they are uniformly dispersed and act as micro-capacitors within the matrix. This enhances the charge-capturing ability to collect induced charges and prevent charge loss, enabling a high surface charge density in the TENG device while maintaining flexibility.

4.7. Degradable materials for TENG

In recent years, the development of advanced attachable, wearable, and implantable electronic devices has progressed rapidly, offering functionalities in monitoring, diagnosis, and therapy. However, the next generation of such devices must be designed with a focus on eco-friendly and sustainable materials to minimize risks to both human health and the environment, avoiding toxicity and pollution. Among the various components of these electronic devices, energy supply plays a crucial role in supporting their operation. As a result, research on TENGs fabricated from biodegradable materials has gained significant attention. Herein, we summarize the current progress in developing biodegradable materials for TENG applications (detailed performance of the degradable materials based TENG device is presented in Table 7). These materials can be broadly classified into three categories: 1) animal-based, 2) plant-based, and 3) synthetic biodegradable materials. In this section, we focus on reviewing the animal-based and plant-based biodegradable materials developed for TENGs.

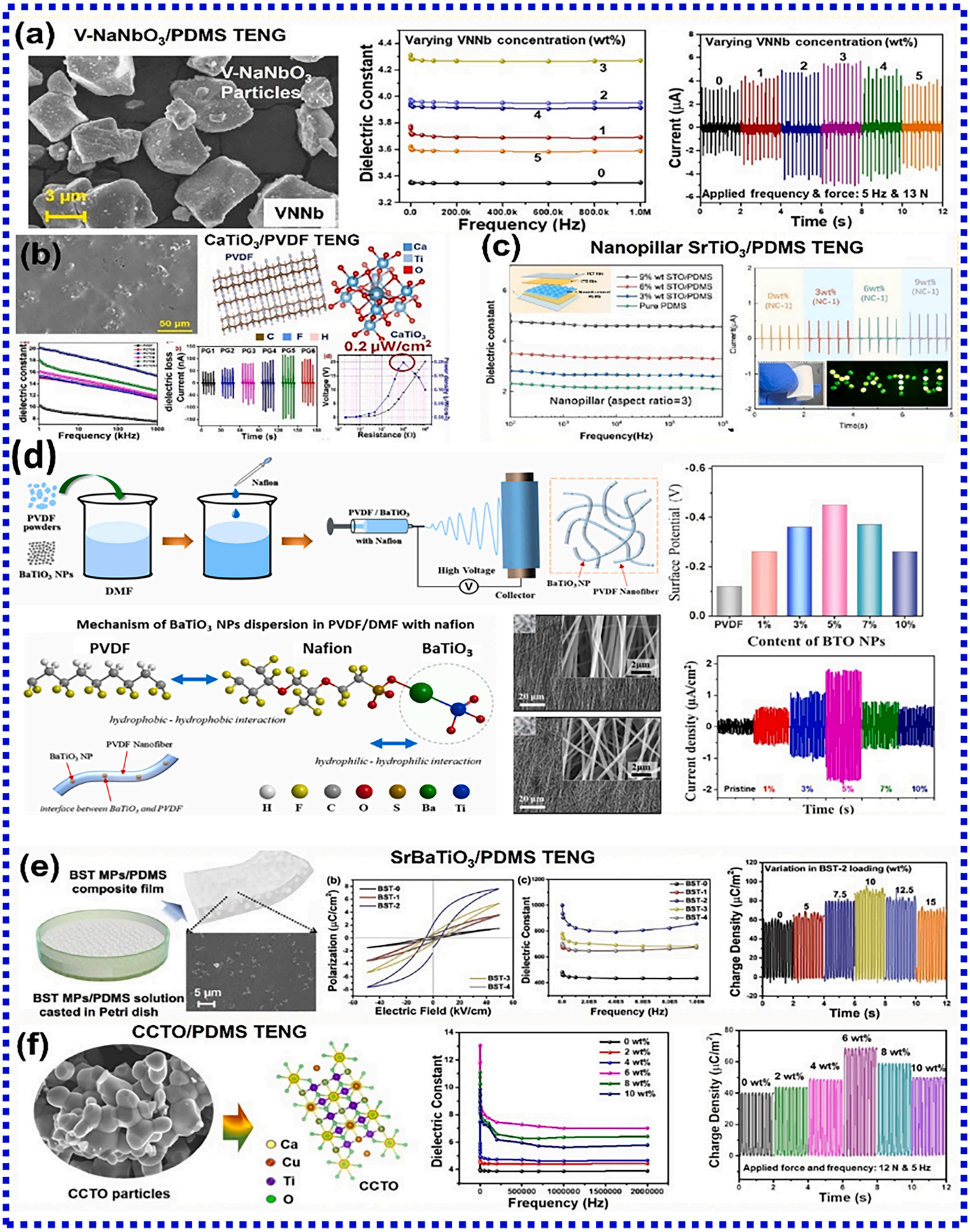

Fig. 22. Summary of polymer/dielectric composite TENG including: (a) vanadium doped sodium niobate (V-NaNbO$_3$)/PDMS. Reproduced from Ref. [183]. Copyright 2024 Elsevier, (b) orthorhombic CaTiO$_3$/PVDF. Reproduced from Ref. [179]. Copyright 2022 Elsevier, (c) nanopillar SrTiO$_3$/PDMS. Reproduced from Ref. [184]. Copyright 2024 American Chemical Society, (d) Nafion modified BaTiO$_3$/PVDF composites. Reproduced from Ref. [185]. Copyright 2023 Elsevier. (e) Sr doped BaTiO$_3$/PDMS. Reproduced from Ref. [186]. Copyright 2023 Wiley, and (f) CCTO/PDMS colossal dielectric composites. Reproduced from Ref. [77]. Copyright 2024 Elsevier.

4.7.1. *Animal-based source materials for TENG*

In this context, animal-based source materials refer to degradable materials derived from animal sources, including chitin/chitosan, silk and silk fibroin, gelatin, and others. To date, animal-based degradable materials have been successfully applied as triboelectric layers in TENGs, demonstrating excellent triboelectric performance. These materials have been utilized in a wide range of applications, including self-powered signal sensing and energy harvesting systems. Chitin, commonly found in the exoskeletons of crustaceans such as crabs, is considered a promising tribo-positive material in TENG applications due

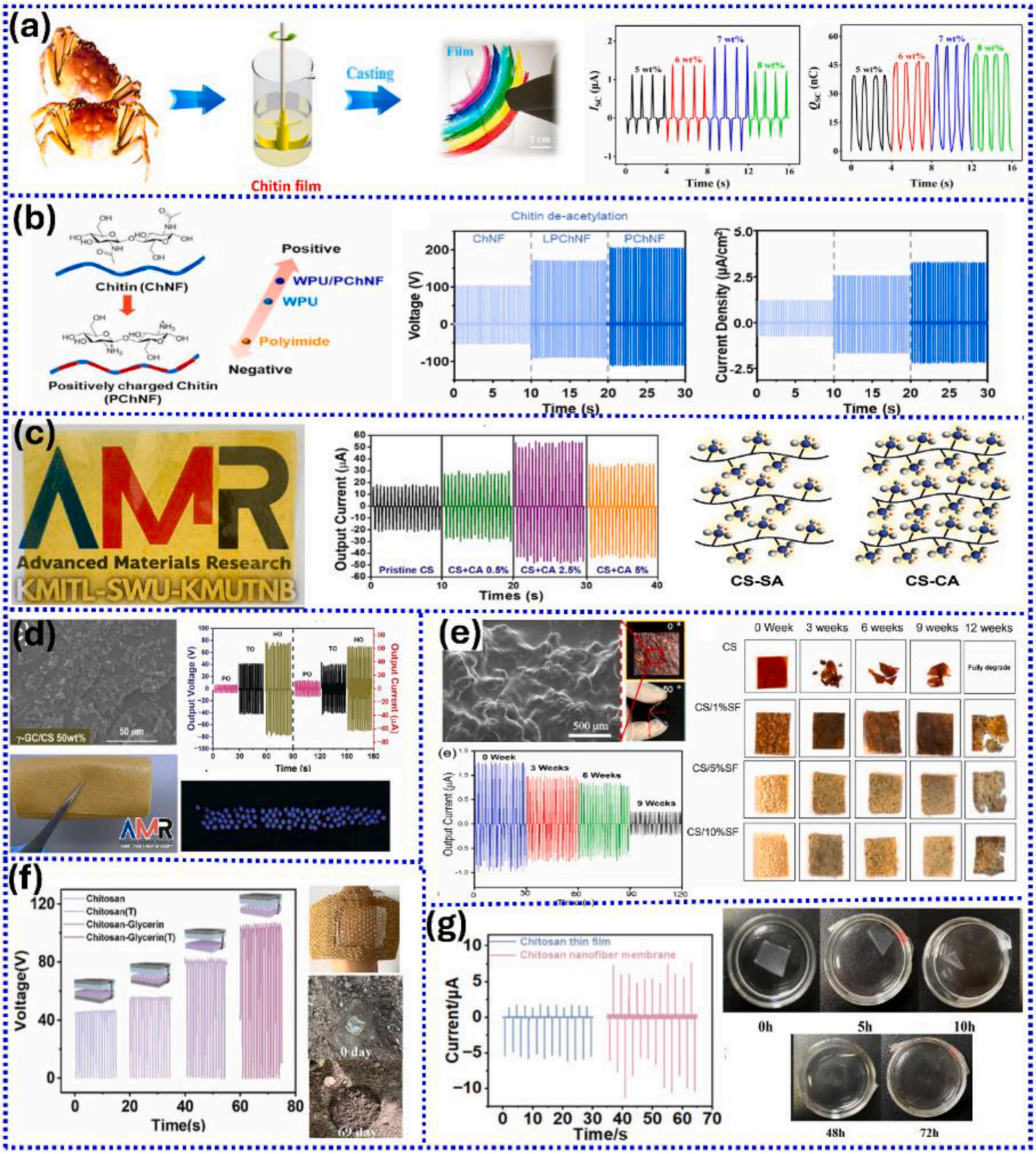

Fig. 23. Summary of animal resource-based materials for degradable TENG including (a) chitin film preparation for TENG and its output performance V_{OC} and I_{SC}. Reproduced from Ref. [187]. Copyright 2022 Elsevier. (b) Chitin nanofiber modified high degrees of electron donating by degree of de-acetylation process. Reproduced from Ref. [188]. Copyright 2023 Elsevier. (c) Chitosan-based TENG modified by dissolving in various acidic solutions. Reproduced from Ref. [172]. Copyright 2024 Springer. (d) Chitosan/amino acid TENG. Reproduced from Ref. [189]. Copyright 2024 Elsevier, and (e) chitosan/protein biodegradable TENG. Reproduced from Ref. [190]. Copyright 2021 Elsevier. (f) Chitosan/glycerin gel. Reproduced from Ref. [191]. Copyright 2023 Elsevier, and (g) chitosan/PVA films fully degradable TENG. Reproduced from Ref. [192]. Copyright 2023 American Chemical Society.

to its strong tendency to donate electrons, which is attributed to the abundance of amino (-NH2) groups.

According to Fig. 23a–J. Zhang et al. [187], reported the extraction of chitin from natural sources using a non-freezing dissolution process in a KOH/urea solvent, followed by casting to produce transparent and flexible chitin films for use as a tribo-positive material. The mechanical properties of the resulting chitin films were significantly superior to most existing biodegradable films, achieving tensile strength of 84.7 MPa and an elongation at break of 14.5%. As the chitin concentration increased, the output of V_{OC}, I_{SC} and surface charge (Q_{SC}) of the chitin TENG gradually increased until reaching a maximum value at 7.0 wt%. The V_{OC} of ~182.4 V, I_{SC} of ~1.9 μA and Q_{SC} of ~57.2 nC were reached. The power density of 1.25 W/m^2 was generated, providing efficiency to further use for self-power sensing devices. Increasing the amount of chitin (up to 8.0 wt%) prevented further improvement in the performance due to the aggregation of chitin chains. In 2023 (Fig. 23b), chitin was blended with waterborne-based polyurethane (WPU) by dispersion of chitin nanofiber in WPU solution before casting to a proposed new class of tribo-positive materials [188]. Owing to the amine branches of chitin that are embedded in the WPU chain, the electron donor ability of WPU-chitin could be enhanced. The deacetylated degrees of chitin show a potential role in turning more tribe-positive

Table 6
Summary of polymer/dielectric oxide composite TENG.

Ref.	Materials	Triboelectric material pair	Size (cm^2)	V_{OC} (V)	I_{SC} (μA)	P_{max} (μW/cm^2)	Applications
[193]	PVDF–MXene composite and PDMS–$NaNbO_3$	Cu	1.5 × 1.5	150	4.3 μA	134 μW/cm^2	wireless communication
[183]	vanadium-doped sodium niobate/ PDMS	Al	2 × 2	~200	~5.7 μA	4.8 W/m^2	biomechanical energy harvester.
[194]	PDMS/$ZnSnO_3$-surface-modified carbon nanotubes	Al	2 × 2	665.6	137.08 mA m^{-2}	10.57 W/m^2	energy harvesting and self-powered systems
[195]	Ordered mesoporous SiO_2-PDMS	Cu	5 × 5	156	10.5 μA	5.26 W/m^2	charge storage
[196]	surface engineered PDMS-TiO_2	Al	2 × 2	~50	~8 μA	~90 mW/m^2	self-powered motion-driven humidity sensor
[197]	PVDF-TrFE/reduced graphene oxide (rGO)/PMN-PT	PET	4 × 3	200	0.33 μA	–	energy harvesting
[184]	Nanocone-Structured $SrTiO_3$/PDMS	ITO film	–	130	1.4 μA	90 μw	elf-powered sensing systems and flexible devices
[198]	MoS_2-PVDF	PDMS	–	35.3	20.8 μA	~220 μW/cm^2	smart wearable electronic devices
[77]	CCTO/PDMS	Cellulose paper	2 × 2	~250	~6.5 μA	~3.15 W/m^2	self-powered sensor
[185]	Nafion-functionalized barium titanate nanoparticles/PVDF	Cu	2 × 2	307	1.8 μA/cm^2	1.12 mW/cm^2	self-powered human-machine interactive interface
[199]	$FeNbO_4$-PDMS	Al	–	200	0.84 μA	0.4 μW/cm^2	self-powered sensor
[180]	$NaNbO_3$/PDMS	Al	3 × 3	40	0.95 μA	200 μW/cm^2	–
[200]	Asymmetric TiO_2/PDMS	Al	5 × 5	~5	–	0.28 W/m^2	–
[201]	BFO@PDMS	Al	5 × 5	180	30 μA	1.05 mW	microelectronic devices
[186]	$SrBaTiO_3$/PDMS	Al	2 × 2	280	8.5 μA	4.41 W/m^2	Floor Energy Harvesting
[202]	BZT–BCT/PDMS	PVA	2.5 × 2.5	127	67 mA m^{-2}	7.5 W/m^2	scavenging mechanical energy
[203]	SiC@SiO_2/PDMS	Al plate	4 × 4	200	30 μA	2.24 mW	–
[204]	BTO@ZnO core-shell nanorods/PDMS	ITO	4 × 4	512	1.73 mA/m^2	82.99 mW/m^2	–
[205]	SnO_2 nanoparticles/PVDF	Al	2 × 2	81.1	6 μA	1.25 × 10^{-4} W cm^{-2}	–
[206]	SnO_2/PVDF	Paper	2 × 2	62	1.55 μA	0.81 W/m^2	–

Table 7
Summary of degradable materials based TENG performance.

Ref	Material	Triboelectric material pair	Size of the device	Voc	Current/Current Density	Power Max/Power Density
[187]	Chitin film	VHB film	2.5 cm × 2.5 cm	182.4 V	4.8 μA	1.25 W/m^2
[188]	Waterborne polyurethane (WPU)–chitin nanofiber (ChNF)	Polyimide film	1.5 cm × 1.5 cm	210 V	3.2 μA/cm^2	3 W/m^2
[174]	Chitosan- acid films	PTFE/Al	3 cm × 3 cm	157 V	53 μA	169 μW
[173]	Chitosan	Teflon	3 cm × 3 cm	38 V	5.1 μA	101 μW
[207]	Chitosan-polyethylenimine-grafted graphene oxide (PEI-GO) nanocomposite	PTFE	6 cm × 6 cm	222 V	6.6 μA	407 mW/m^2
[190]	Chitosan-protein composite	PTFE	3 cm × 3 cm	77 V	13 μA	22.4 μW/cm^2
[191]	Chitosan-glycerol composite film	FEP	2 cm × 2 cm	110 V	0.9 μA	270 mW m^{-2}
[192]	Chitosan–poly (vinyl alcohol) (CS–PVA) nanofiber	FEP	3 cm × 4 cm	115 V	20 μA	37.5 mW m^{-2}
[208]	Silk fibroin film	PET	2 cm × 2 cm	268 V	5.78 μA	193.6 μW/cm^2
[209]	Silk fibroin film	PET	4 cm × 6 cm	213.9 V	–	68.0 mW/m^2
[210]	Silk fibroin film	PET	2 cm × 2 cm	260 V	6.2 μA	161.5 μW/cm^2
[211]	Silk fibroin film	PDMS	5 cm × 5 cm	166.4 V	2.7 μA	79.677 μW
[212]	Sil fibroin/sericin/polyvinyl alcohol (FSP) film	Fluoro-nylon	2 cm × 2 cm	745 V	22.5 μA	760 μW/cm^2
[213]	Electrospun poly-lactic acid (PLA) film	Modeled gelatin film	4 cm × 4 cm	500 V	10.6 mA/m^2	5 W/m^2
[214]	Fish bladder film	FEP	–	106 V	4.56 mA/m^2	200 mW/m^2
[215]	Fish gelatin film	PTFE/PDMS composite film	5 cm × 5 cm	130 V	0.35 μA	45.8 μW cm^{-2}
[216]	Calcium alginate	Aluminum (Al) film	5 cm × 5 cm	33 V	150 nA	9.5 μW
[217]	Pistachio reusing abundant waste fruit shell (WFS)	PTFE	4.5 cm × 4.5 cm	700 V	95 μA	416.14 μWcm^{-2}
[218]	Polyvinyl alcohol- natural fibers (PVA-NF) films	PU film	4 cm × 4 cm	162.10 V	7.20 μA	0.458 mW
[219]	Bamboo leaf	PTFE	5 cm × 5 cm	191 V	5 μA	409.6 μW
[220]	Deciduous leaf	PTFE	3 cm × 3 cm	150 V	4.2 μA	72.2 μW
[221]	Rose petal	Poly (methyl methacrylate) (PMMA)	3 cm × 3 cm	30.6 V	0.78 μA	27.2 mW/m^2
[222]	*Delonix regia* flowers (DRFs) thin films	PTFE	20 cm × 20 cm	655 V	59 μA	220.2 μW/cm^2

charges on the material surfaces. During contact with polyimide, WPU-chitin at 25 wt% of deacetylated chitin generated an electrical output four times higher than that of a pristine WPU is obtained. Maximum V_{OC} of ~210 V and short circuit current density (J_{SC}) of ~3.2 μA/cm^2 could be achieved [188]. This enhancement could be attributed to the dielectric constant improvement owing to the polymer chain densification and the work function reduction of the amine branches in the chitin.

Chitosan (CS) is a polysaccharide derivative that has emerged as a candidate for tribo-positive friction material. It can be synthesized from chitin sources through a deacetylation process, which converts N-acetyl groups into amine functional groups. Depending on the degree of deacetylation, both hydroxyl (-OH) and amino (-NH_2) groups can be present. However, both -OH and -NH_2 groups tend to lose their electrons due to the inductive effect. Thus, the implementation of CS in TENGs requires further efforts to enhance charge tunability, contact efficiency, and surface charge density, thereby improving the triboelectrical output for potential applications. It is known that the CS needs to be dissolved in an acidic solution for preparation through the protonation reaction. After attracting a proton (H^+) from acids, the -NH_2 group turns to be –NH^{3+}. Lastly in 2024 (Fig. 23c), T. Charoonsuk and co-workers [172] published the controlling fraction of –NH_3^+ for designing triboelectric properties of CS by studying the dissolving in various acids, including acetic (CH_3COOH; ACA) acid, succinic ($C_4H_6O_4$; SA) acid, and citric ($C_6H_8O_7$; CA) acid. They showed that the choice and concentration of acids have a crucial role in influencing CS performance. Under optimized conditions (2.5% CA), the TENG exhibited maximum output of V_{OC} and I_{SC} of 157 V and 53 μA, which is three times higher than that of pristine CS. Ionic salt, $CaCl_2$, was added as a solid electrolyte to enhance the charge density of CS simultaneously with improving the contact area by casting CS solution on the sandpaper. The appropriate concentration of $CaCl_2$ significantly affects achieving the highest V_{OC} and I_{SC}. The optimized condition at 3% $CaCl_2$ can give maximum V_{OC} at ~149 V and I_{SC} at ~15 μA, which is four- and three-fold more than the pristine CS [173]. Adding $CaCl_2$ ionic salts can homogeneously form with the CS chain without losing its transparency and flexibility. Ionic salt embedding can create higher ionic charges and electrons unoccupied states, resulting in higher charge density and mobility during the contact-separation process. Composite CS has also been attractive to study. Several researchers have tried to improve the triboelectric output performance by incorporating metal, dielectric, piezoelectric, and semiconductor materials. For fully degradability, organic fillers have been searched. Incorporation of 10 wt% polyethyleneimine-grafted graphene oxide (PEI-GO) into CS was proposed by S. Shyju et al. [207] to improve the V_{OC} and I_{SC} to ~222 V and ~6.6 μA from 10 V 1.1 μA of pristine CS. The P_{max} (~1465.2 μW) was increased almost 5.5-fold to light up 126 blue LEDs. As depicted in Fig. 23d, organic piezoelectric gamma glycine (γ-GC) was involved in re-crystallizing and incorporated into CS. Fully organic CS/γ-GC (50 wt%) composite resulted in 6 times enhancement of V_{OC} and I_{SC}, benefiting from interaction of an aligning interface polarization coherently and robust hydrogen bond network between γ-GC and CS. The V_{OC} ~79 V, I_{SC} ~64 μA and P_{max} ~705.96 μW could be reached [189]. Electrical output stability based on biodegradable test was evidently shown by T. Charoonsuk, and et al., [190] according to Fig. 23e. The different types of protein; albumin, egg-shell membrane (ESM) and silk fiber (SF), with the different loaded content was explored on incorporating in CS. The presence of SF in CS showed the highest performance due to the containing ordered glycine, alanine and serine amino acids creating polar domains. The 10 wt% of SF made CS/SF TENG achieve ~77 V and ~13 μA with a power density of ~22.4 μW/cm^2, 6 times higher than the pristine CS TENG. Possible degradation was tested in soil, showing stability of signal within 3 weeks. After 9 weeks, the existing CS/SF film for 70% could still generate V_{OC} and I_{SC} for ~20 V and ~2.5 μA. Regarding Fig. 26f–C. Gau and colleagues [191] designed the CS with an additional glycerin plasticizer to provide fully degradable friction material for the TENG-based sensor. Not only making full-degradable CS, the high surface of glycerin also helps enhance output performance owing to its high surface area. This CS-glycerin provided the V_{OC} ~127 V, which is 2.32 times higher than that of pristine CS TENG. The I_{SC} of 0.9 μA, and 36 nC of Q_{SC} could be achieved that was applied for being a smart sensing patch. The in vitro biodegradation was studied by burial in soil to evaluate sensor biodegradability. After 15 days, the film hydrated slowly and lost shape, becoming brittle until it completely degraded within 69 days. The CS and poly (vinyl alcohol) (PVA) nanofiber with Mg electrode was prepared for a degradable TENG by electrostatic spinning.

The rough surface and many nanopore networks of nanofiber form caused the TENG to achieve 37.5 mW/m^2 of power density. The I_{SC} was 2 times higher than that of pristine CS TENG. Mixing with PVA caused the CS/PVA to degrade within 3 days by soaking it in a degradation solution, as shown in Fig. 23g [192]. It can be noted that chitin and CS polymers can be degraded into smaller molecules corresponding to the weakened C–O–C stretching, proving the breaking of glycosidic bonds. They can be degraded in the environment and the human body, exhibiting good biocompatibility biodegradability, and bioabsorbability of materials. The protein and its derivatives can serve as a triboelectric layer in TENG with a strong ability to transfer electrons due to the strongest functional group that has a robust electron-donating tendency from –NH_2 and C=O group [223]. Silk fiber [224], and silk fibroin [225] have been concentrated as triboelectric friction layer (positive side) on recent years, especially in fibroin form because of its unique transparency.

4.7.2. Plant-based source materials for TENG

Currently, plant-based degradable materials for TENGs can be broadly classified into five categories: leaves, wood, paper and rice paper (starch), alginate, cellulose, and cellulose-based materials.

Alginate and its composites, such as metal or ion-mixed alginate materials, are polysaccharide derivatives recognized for their high biodegradability and excellent biocompatibility [226]. The alginate family is derived from brown sea algae, where it polymerizes through alternating units of α-L-guluronic acid and β-D-mannuronic acid in a linear chain [227]. Beyond its traditional applications in wound dressings, drug delivery, artificial skin, food, and the textile industry, alginate has recently been explored for TENG applications due to the strong electron-donating properties of its -C=O and -OH functional groups. Fig. 24a highlights a report by Y. Pang et al., [216] which proposed the use of alginate extracted from ocean plants as a tribo-positive friction layer in TENGs. The alginate film exhibits a rough, porous surface that enhances the contact area, optimizing TENG performance. In this study, the thickness and concentration of alginate were systematically examined to achieve the best electrical output, including a V_{OC} of 33 V, I_{SC} of 150 nA, and P_{max} of 9.5 mW. The full degradability of the alginate film was confirmed by immersing it in a 3.5% NaCl solution, simulating seawater conditions. The film completely dissolved within 80 h, demonstrating its high degradation rate in oceanic environments. As shown in Fig. 24b–a multifunctional alginate TENG based on alginate-metallic complex materials was reported. The incorporation of various metal ions into the alginate structure allows for tunable properties and electrical output as a tribo-positive material. The electrical output, from highest to lowest, was observed in the following order: Cu-alginate, Fe-alginate, Na-alginate, Mg-alginate, and Al-alginate [228].

Starch is one of the easiest materials to fabricate into flexible films by dissolving the starch in a salt solution and casting it into film form. When combined with the electrolyte $CaCl_2$, starch can significantly increase the triboelectric potential from 0.5 V to 1.5 V, a threefold enhancement using just a 0.5% $CaCl_2$ solution. The thickness of the film and its moisture content were found to be crucial parameters influencing TENG performance [232]. As shown in Fig. 24c, N. Zheng et al., [229] proposed the casting of biodegradable films made from a starch and carboxymethyl cellulose (CMC) composite for TENG applications. This configuration achieved the highest output of V_{OC} and I_{SC} at 151.4 V and 47.1 μA, respectively, with a power density of 113.2 μW/cm^2 (for a 25 cm^2 device operating at 4 Hz). The starch-based TENG demonstrated the ability to power 100 LEDs and can be used as a self-powered sensing device.

Lignocellulose refers to plant dry matter, also known as lignocellulosic biomass, which is primarily composed of cellulose and hemicellulose, along with lignin, an aromatic-rich macromolecule. Lignin is the second most abundant biopolymer and is commonly produced in the paper industry, often recycled from black liquor. Due to its oxygen-based functional groups, such as -OH and -COOH, lignin has emerged as a promising material for next-generation biodegradable TENGs.

In relation to lignin sourced from bio-waste, Q. M. Saqib et al. [217] investigated the preparation of lignocellulosic-based films using waste fruit shells (WFS) from almonds (A), walnuts (W), and pistachios (Pi) as tribo-positive layers for TENGs. Due to its high lignin (43.7%) and cellulose (43.1%) content, the Pi-WFS TENG demonstrated the highest I_{SC}

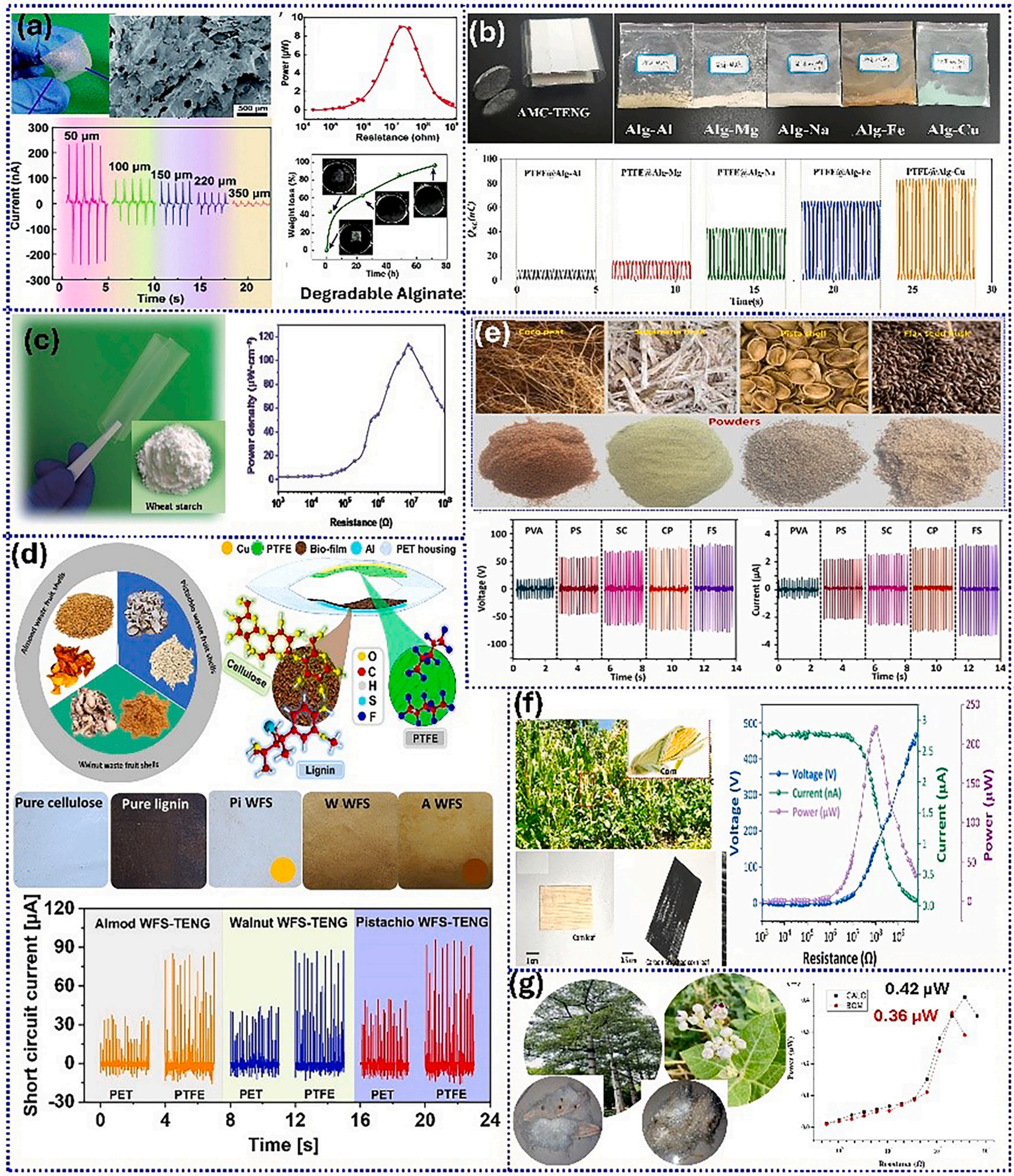

Fig. 24. Summary of plant-based degradable resource materials for TENGs. (a) Degradable alginate films. Reproduced from Ref. [216]. Copyright 2018 Royal Society of Chemistry, (b) metal alginate films. Reproduced from Ref. [228]. Copyright 2020 Elsevier, (c) starch films. Reproduced from Ref. [229]. Copyright 2022 Springer, (d) lignocellulosic-based films. Reproduced from Ref. [217]. Copyright 2022 Elsevier, (e) biowaste resources-based films. Reproduced from Ref. [218]. Copyright 2024 Elsevier, (f) leaf waste-based films. Reproduced from Ref. [230]. Copyright 2024 Cell Press, and (g) fiber leaves for TENG. Reproduced from Ref. [231]. Copyright 2023 Sage Journal.

and power density, reaching 416.14 mW/cm^2, attributed to its superior electron-donating capability. This can be observed in Fig. 24d.

Natural materials have been widely reported in several publications to offer sustainable solutions for applications such as self-powered sensors, body information monitoring, and healthcare electronics. Many natural materials also originate from the agro-industry and agricultural waste, including crop residues such as wheat straw, corn stalks, sugarcane, coconut, and flax. These materials have been explored for use in TENGs. Fig. 24e illustrates the development of bio-waste-based TENGs using recycled natural resources from agriculture, including coco peat, sugarcane husk, pistachio shell, and flax shive. By mixing these agricultural composites with PVA and casting them into films, the resulting TENGs achieved V_{OC} values ranging from 50 to 90 V and ISC values between 2 and 4 μA [218]. As illustrated in Fig. 24f, using plant leaves as a friction layer for TENG is a cost-effective approach. Huifang Hu [230] proposed a dual-function device (for both sensing and energy harvesting) fabricated from corn leaves combined with conductive carbon. The corn leaf TENG achieved a maximum power output (P_{max}) of approximately 222 μW, making it suitable for integration into self-powered strain sensors for monitoring activities such as running.

Additionally, naturally available fibers from the *Bombax ceiba* (BOM) tree and the Calotropis (CALO) plant were proposed by J. Kaur and coworkers [231] as tribo-positive friction materials for TENG devices. BOM- and CALO-based TENGs generated open-circuit voltages (V_{OC}) of 10.7 V and 11.1 V, respectively, with maximum power outputs (P_{max}) of 0.36 μW and 0.42 μW when rubbed against PTFE, as shown in Fig. 24g.

4.7.3. Leaf and flowers for TENG

A promising approach for green TENGs is the exploitation of live plants in energy harvesting and self-powered sensor technologies [226]. All plant leaves have an outer surface covered by a polymer layer of epicuticular waxes, known as the cuticle. This cuticle plays a vital role as a dielectric phase, contributing to polarization, which can be advantageous for TENG applications. Additionally, the cellular tissue beneath the cuticle acts as an ionic conductor due to its water and ion content. In TENGs, a potential difference can be generated between the static charges on the leaf's surface (cuticle) and the cellular tissue (ion-conductive electrode), resulting in energy generation [233]. Regarding this plant feature, charges are generated when the plant comes into contact with another material. As illustrated in Fig. 25a-b, Xu et al. [219] proposed a bamboo leaf TENG, which demonstrated promising triboelectric properties, with a V_{OC} of 191 V and I_{SC} of 5 μA. The device achieved a maximum power output (Pmax) of 409.6 μW (at a matching resistance of 40 MΩ), sufficient to power 18 commercial LEDs. More recently, a dry deciduous leaf was tested against PTFE, generating an I_{SC} of 4.2 μA, a V_{OC} of 150 V, and a power output of 72.2 μW [220], as shown in Fig. 25c.

In addition to leaf-based materials, flowers have also been explored for TENG applications. As illustrated in Fig. 25d, the use of fresh rose petals for TENG was studied by pairing them with poly(methyl methacrylate) (PMMA). Under a constant applied force of 100 N at a frequency of 2 Hz, a maximum V_{OC} of approximately 30.6 V, I_{SC} of ~0.8 μA, and P_{max} of ~27.2 mW/m^2 were achieved. Additionally, the rose petal TENG generated an ISC of 7.84 nA from water droplets falling on its surface [221]. In 2022, *Delonix regia* flowers (DRFs) were utilized in a TENG device [222]. The presence of functional groups such as C=O, –OH, and –NH$_2$ contributed to the flower's strong electron-donating ability. The DRF TENG, with a size of 20 cm^2, exhibited impressive electrical performance, generating a V_{OC} of 655 V, I_{SC} of 59 μA, and P_{max} of 220.2 μW/cm^2, which was sufficient to power 210 LEDs. The results of the DRF TENG study are presented in Fig. 25e. As shown in Fig. 25f, the *Clitoria ternatea* (CT) flower, which contains a high concentration of

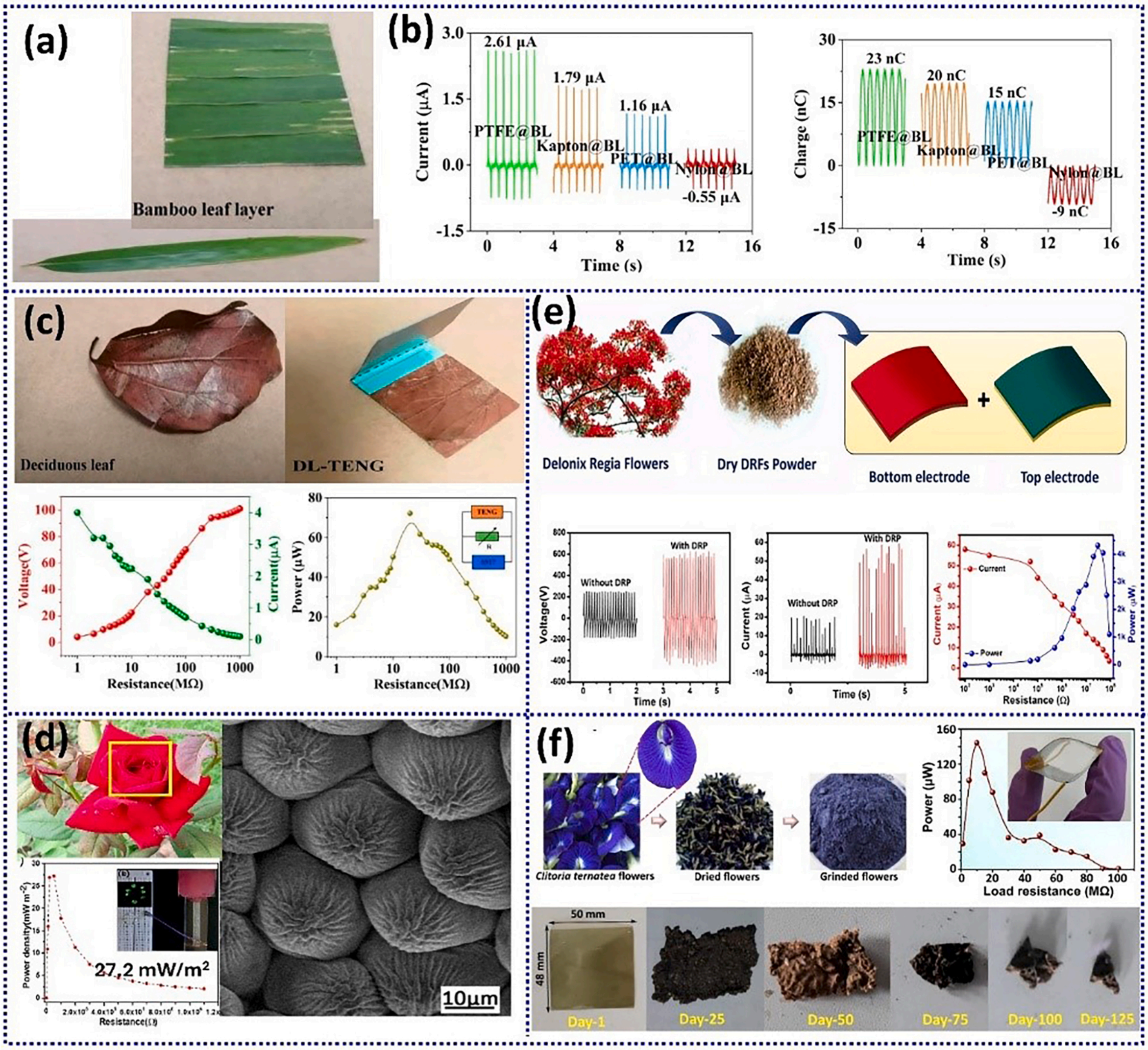

Fig. 25. Summary of leaves and flowers-based TENG including. (a,b) Bamboo leaf. Reproduced from Ref. [219]. Copyright 2024 Multidisciplinary Digital Publishing Institute, (c) deciduous leaf. Reproduced from Ref. [220]. Copyright 2021 Multidisciplinary Digital Publishing Institute, (d) rose petal. Reproduced from Ref. [221]. Copyright 2018 Elsevier, (e) delonix regia flower. Reproduced from Ref. [222]. Copyright 2022 Wiley, and (f) clitoria ternatae flower-based TENG. Reproduced from Ref. [234]. Copyright 2023 Elsevier.

anthocyanins, triterpenoids, steroids, flavonol glycosides, and trace metal ions, was proposed as a tribo-positive layer for TENG. When combined with polyvinyl alcohol (PVA), the PVA/CT composite film exhibited enhanced triboelectric performance, attributed to the intermolecular hydrogen bonding between PVA and taraxerol. The composite film generated V_{OC} and I_{SC} values 14.8 and 32.7 times higher, respectively, than those of pristine PVA and several other polymers [234].

4.8. Cellulose-based materials for TENG

Cellulose is the most abundant polysaccharide polymer globally, widely recognized for its diverse applications. Its macromolecular structure consists of repeating D-glucose units $(C_6H_{10}O_5)n$ joined by β-1,4 glycosidic bonds. As displayed in Fig. 26a, these glucose units are repeatedly linked in a linear chain by β-1,4 glycosidic bonds [235]. The molecular chains of cellulose are further connected through van der Waals interactions and hydrogen bonds, forming cellulose fibers. For over a century, cellulose has been used in a wide range of applications, including clothing, food packaging, biomedical devices, green

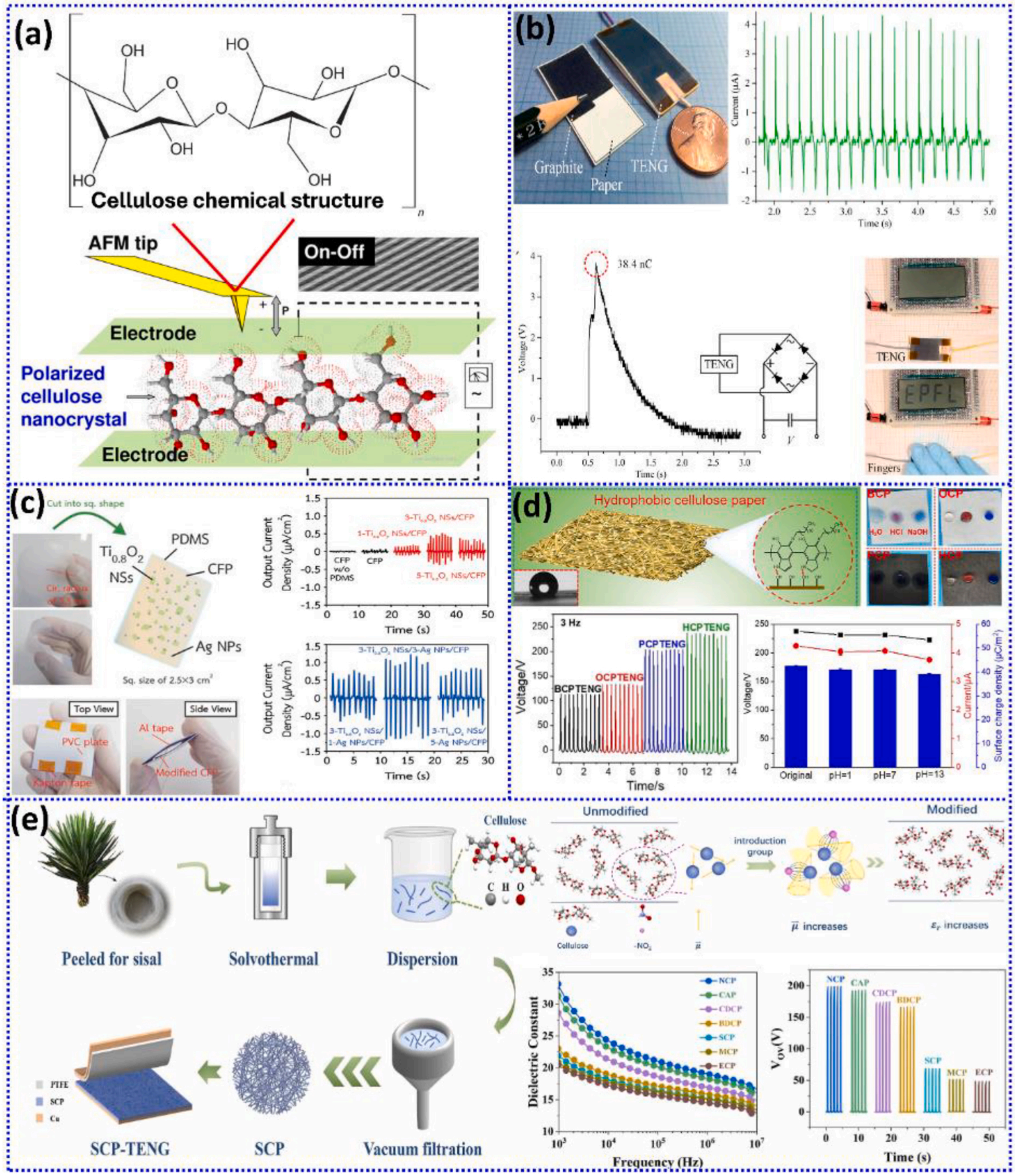

Fig. 26. Summary of cellulose paper TENG, including (a) chemical structure of cellulose and its chain polarization. Reproduced from Ref. [235] Creative Commons CC BY license. Copyright 2024 Taylor & Francis Group, LLC, and reproduced from Ref. [244]. Copyright 2012 American Chemical Society, (b) cellulose paper TENG. Reproduced from Ref. [245]. Copyright 2017 Elsevier, (c) cellulose filter paper. Reproduced from Ref. [246]. Copyright 2020 Wiley, (d) hydrophobic cellulose paper. Reproduced from Ref. [247]. Copyright 2022 American Chemical Society, and (e) Sisal cellulose natural paper. Reproduced from Ref. [248]. Copyright 2022 Elsevier.

electronics, and energy materials [19,236]. This section focuses specifically on the application of cellulose in TENGs, where its use as a friction layer, electrode, and spacer plays a critical role in energy generation within the contact-separation (CS) mode [237,238]. Due to its abundant hydroxyl groups, cellulose is classified as a tribo-positive material, with a strong tendency to donate electrons, making it highly suitable as a tribo-positive friction layer in TENGs [239–241]. Additionally, cellulose has been reported to exhibit dielectric and piezoelectric properties. As shown in Fig. 26a, the ordered, non-centrosymmetric arrangement of polar hydroxyl groups gives rise to the piezoelectric properties of cellulose, with a shear piezoelectric constant of $d_{25}=-d_{14}$, on the order of 10^{-9}, approximately 0.05 times that of the d_{11} of quartz [242]. The d_{33} value of cellulose has been reported to be around 0.4 $pC\cdot N^{-1}$ [243]. While this piezoelectric constant is significantly lower than that of synthetic piezoelectric polymers, such as PVDF (d_{33}=21 pC N^{-1}), cellulose remains an attractive option for TENGs due to its natural abundance, biodegradability, and biocompatibility, making it ideal for applications in the medical and healthcare fields. Therefore, in addition to its role as a friction material, cellulose has also been utilized as a dielectric and piezoelectric filler to enhance the efficiency of TENG devices. The performance metrics of the cellulose-based TENG devices are presented in Table 8.

4.8.1. *Cellulose paper TENG*

Cellulose paper (CP) has garnered significant attention for TENG applications due to its versatility, including being shapable, flexible, foldable, and cost-effective. Commercial paper cards (TC-62, Pyramid Co., Ltd., 220 ± 10 μm thick) were used, with graphite applied as the electrode via pencil, and Teflon as the friction material, as illustrated in Fig. 26b. The paper card TENG demonstrated an impressive V_{OC} of ~85 V and I_{SC} of ~3.8 μA, achieving a power density of ~39.8 $\mu W/cm^2$ with stable performance over 30,000 cycles. With a matched load of 20 MΩ, it was able to drive low-power electronic devices [245]. An X-shaped TENG structure was proposed using CP and Teflon. When six units were integrated into one device, the X-shaped TENG generated sufficient electrical output to light up 101 blue LEDs [251]. Additionally, a CP was rubbed against a poly(caprolactone) (PCL)/graphene oxide (GO) composite, producing an output of 120 V, 2.5 mA/m^2, and 72.5 mW/m^2 [260]. Although the triboelectric charge density (TECD) of cellulose is relatively low [56], it still shows potential as a primary friction layer for TENGs through various modification methods. As illustrated in Fig. 26c–a high-performance cellulose filter paper (CFP)-based TENG was developed by dip-coating the paper with dielectric $Ti_{0.8}O_2$ nanosheets and Ag nanoparticles. The output performance was significantly enhanced by modifying the CFP with a three-layer coating of both $Ti_{0.8}O_2$ and Ag. The ε_r was increased to ~12, approximately eight times higher than that of pristine CFP. Under optimal conditions, the TENG generated ~42 V and ~1 $\mu A/cm^2$ during friction with an Al plate. The maximum surface charge density of ~75 $\mu C/m^2$ was 39 times greater than that of pristine CFP [246]. Compared to previous studies, significant advancements have been made in enhancing the dielectric fillers and electrode materials in the cellulose paper (CP) tribo-positive layer and the overall TENG structure. As depicted in Fig. 26d, the hydrophobicity of CP was addressed to overcome limitations in real-world applications of CP TENGs. Octadecylamine (ODA) was coated onto CP after surface modification with polydopamine (PDA). The ODA and PDA co-modification formed hydrogen bonds with cellulose, imparting hydrophobicity and remarkable acid/base resistance. This modification resulted in a hydrophobic CP TENG that exhibited a maximum V_{OC} of 237.8 V and I_{SC} of 4.2 μA, which are significantly higher than those of pristine CP TENGs [247]. As shown in Fig. 26e, sisal cellulose paper (SCP) was chemically modified with different polar groups, including $-NO_2$, $-COCH_3$, –Cl, –Br, $-CH_3$, $-C_2H_5$ to enhance its dielectric properties and improve TENG efficiency. Nitrated SCP proved to be the most effective, delivering the highest electrical output of 198 V, 20.78 μA, and 827.03 mW/m^2 for V_{OC}, I_{SC}, and P_{max}, respectively. In comparison, pristine SCP produced 118 V, 6.13 μA, and 256.97 mW/m^2 [248]. Additionally, a multilayer CFP-based TENG was fabricated by M. Yang and co-workers [250] using the sliding electrification (SE) mode. The CFP was synthesized from cotton fiber. Tannic acid (TA) was coated onto the CFP by immersing it, forming intermolecular hydrogen bonds before immobilizing $PdCl_4^{2-}$ and dispersing copper to serve as the electrode layer. The top layer was coated with polyvinylidene fluoride (PVDF), which acted as the friction layer. The optimum condition was achieved by varying the amount of PVDF, with a coating of 10 mL resulting in a maximum V_{OC} of ~192 V, I_{SC} of ~9.3 μA, and a power density of 736.7 mW/m^2. This configuration demonstrated the capability of generating trigger signals for controlling computer programs and playing games.

In another approach, polyethylene oxide/cellulose composite paper (PEO/CCP) was successfully prepared by mixing PEO with cationic CP. The incorporation of PEO and $-NH_2$ groups significantly enhanced the output, achieving a V_{OC} of ~222 V, I_{SC} of ~4.3 μA, and a power density of ~217.3 mW/m^2. This device was effectively used as a human-health detection device, capable of monitoring physiological signals such as heartbeat, wrist pulse, respiration, and eye muscle movement [249]. In conclusion, CP-based materials have shown great potential for expanding the application range of paper-based materials in advanced TENGs, paving the way for future innovations.

4.8.2. *Bacterial cellulose TENG*

In addition to being extracted from various plants, cellulose can also be synthesized through the glucose consumption of specific bacteria, such as *Agrobacterium*, *Acetobacter*, *Rhizobium*, and *Sarcina* [261]. This type of cellulose is known as bacterial cellulose (BC). Among the various types of cellulose, BC has become the most popular for use as a

Table 8
Summary of cellulose-based materials for TENG device performance.

Ref	Material	Triboelectric material pair	Size of the device	Voc	Isc	Power Max
[249]	PEO/cellulose composite paper	PDMS	4 × 4 cm^2	222.1 V	4.3 μA	217.3 mW/m^2
[250]	PVDF-coated Cellulose filter paper	Skin	–	192 V	9.3	736.7 mW/m^2
[245]	Paper	Teflon	2 cm × 4 cm	85 V	3.75	39.8 $\mu W/cm^2$
[251]	Paper	Teflon tape	3 × 3 cm^2	326 V	45	542.22 $\mu W/cm^2$
[248]	Sisal cellulose paper	PTFE	3 × 3 cm^2	198 V	20.78	827.03 mW/m^2
[252]	Nanocoated bacterial cellulose	PVDF	4 × 4 cm^2	1010 V		8.7 W/m^2
[253]	Sodium alginate/Bacterial cellulose	FEP	6 cm	302.9 V	27 μA	1.81 mW
[254]	Bacterial cellulose (BC) and BaTiO3	PTFE	5 × 5 cm^2	414 V	48.3	6.94 mW
[255]	SSCNT/BC/WPU	Ecoflex	3 × 3 cm^2	130 V	2.4	129.4 mW/m^2
[246]	Modified cellulose filter paper	PDMS	3.5 cm	42 V	1 $\mu A/cm^2$	25 $\mu W/cm^2$
[256]	PDMS/CNCFs	Al	1.5 × 1.5 cm^2	320 V	5 $\mu A/cm^2$	1.65 mW
[257]	Cellulose/polydimethylsiloxane	Al	3 × 3 cm^2	28 V	2.8	576 μW
[247]	Hydrophobic cellulose paper	PDMS	4 × 4 cm^2	237.8 V	4.2 μA	208.1 mW/m^2
[258]	BC/HEC	PVDF	5 × 5 cm^2	76.61 V	8.68	290.7 μW
[259]	CNF-SO_3Na	PTFE	4 × 4 cm^2	125 V	8.2 μA	2.5 W/m^2

triboelectric friction layer. As mentioned earlier, the primary functional groups in BC are hydroxyl (–OH) groups, which can easily donate electrons, making it suitable as a tribo-positive material. BC has been employed as a friction layer in TENGs since 2017. Kim et al. [262] applied BC in a TENG, achieving a V_{OC} of 13 V in a 25 × 25 cm^2 sample. Since then, BC-based TENGs have become a prominent area of research, with many developments focused on enhancing BC and its modified forms for high-performance friction layers in TENGs.

Fig. 27 shows the modified surface potential of BC when treated with hydroxyethyl cellulose (HEC). After a single dip-coating of BC with HEC, a noticeable difference in surface potential was observed. Compared to pristine BC, the BC-HEC film exhibited a lower surface potential, indicating an improved ability to donate electrons. This effect is attributed to the presence of ethyl groups, which reduce the electron attraction between the -OH group and carbon in the side chain. When in contact with polyvinylidene fluoride (PVDF), a tribo-negative material, the electrons transfer more easily, thereby enhancing the electrical output of the BC TENG. The V_{OC}, I_{SC}, and charge density reached ~76.6 V, ~8.7 μA, and ~26.9 nC, respectively—significantly higher than those of pristine BC TENGs. This improvement was demonstrated by powering 30 blue LEDs when the device was placed under a sock and walked on [258]. Nanocoating is another potential approach for tuning the surface potential of BC in TENG applications. As shown in Fig. 27b, BC was modified with coatings of polypyrrole (PP), polydopamine (PD), and silicon dioxide (SiO_2) to achieve superior performance. The BC became more positively charged due to the incorporation of amino groups from PP and PD via in-situ polymerization. Additionally, coating BC with SiO_2 nanoparticles using the Stöber method transformed the BC into a highly negative triboelectric material. When in friction with PVDF (a tribo-negative material), the BC-PD TENG exhibited a maximum V_{OC} of ~1010 V and a power density of ~8.7 W/m^2, representing a 7-fold enhancement compared to the pristine BC TENG, which produced a V_{OC} of ~530 V and a power density of ~1.1 W/m^2 [252]. Through 2023 and 2024, increasing the charge density of BC remains a challenge. Various methods, including nanocoating, electrolyte addition, and compositing, have been proposed. S. Sriphan and colleagues [263] introduced multifunctional Ti_2NbO_7 nanosheets (NSs), known for their semiconductor and dielectric properties, as fillers in the BC matrix. Both experimental and simulation results indicated that the electrical output was enhanced by the electron-rich Ti_2NbO_7 NSs. The incorporation of Ti_2NbO_7 NSs altered the work function of BC, leading to a higher concentration of charge transfer, thus increasing the electrical output. A possible electronic band diagram was proposed. Under optimal conditions with 5 vol% Ti_2NbO_7 NSs loading, the TENG achieved a VOC of ~36 V, an ISC of ~8.8 μA, and a Pmax of ~28 μW, as shown in Fig. 27c [263]. Additionally, classic piezoelectric material $BaTiO_3$ (BT) was incorporated into BC for material modification, along with a structural design based on Miura origami (MO) pattern folding, as seen in Fig. 27d [254]. Upon adding 10 wt% BT, the coupling effect of triboelectric and piezoelectric phenomena produced a V_{OC} of ~100 V and an I_{SC} of ~1.5 μA. Further enhancement through MO folding increased the V_{OC} and I_{SC} to ~414 V and ~48.3 μA, respectively, with a P_{max} of ~6.9 mW. This output was significantly higher than the ~50 V and ~0.5 μA generated by pristine BC TENGs, attributed to the increased contact surface area due to the folding structure [254]. As shown in Fig. 27e, the incorporation of sericin-modified carbon nanotubes (SSCNT) into waterborne polyurethane (WPU) networks within BC significantly enhanced the performance of BC-based TENGs. This improvement stems from SSCNT acting as both a charge-trapping layer and a charge transfer pathway [255]. The SSCNT/BC/WPU composite samples were engineered by optimizing the interactions between WPU and SSCNT through controlled dispersion. At the optimal SSCNT content of 6%, the device achieved a V_{OC} of 82 V, I_{SC} of 0.45 μA, and a transferred charge (Q_{SC}) of 32 nC. The underlying mechanism of charge trapping and transfer was proposed: without SSCNT or at low CNT content (i), the low dielectric constant leads to air breakdown, resulting in charge loss. As SSCNT content increases, the number of microcapacitors exponentially rises under electrostatic induction during TENG operation. Charge accumulation reaches a peak at the percolation threshold before further increases in SSCNT reduce the distance between nanotubes, leading to electric leakage [255].The surface charge density of BC can also be modulated by blending it with other polymers. Sodium alginate (SA) was one such polymer used to blend with BC, as shown in Fig. 27f. At an optimal SA content of 16.7 %, the polymer chains, containing Na^+ ions, effectively enhanced the charge density, resulting in a maximum I_{SC} of ~25 μA [253].

More recently, a composite material consisting of BC, a conjugate blend of polydimethylsiloxane (PDMS), and poly(3,4-ethylenedioxythiophene): polystyrene sulfonate (PEDOT) was developed as a multifunctional material for TENGs, particularly for insole monitoring technology, as shown in Fig. 27g. When mixed into a gel, this composite produced a short-circuit current density (J_{SC}) of around 40–50 μA/cm^2 and a power density of 500–600 μW/cm^2, activated by human walking [264].

4.8.3. *Derivative cellulose TENG*

Various forms of cellulose have been commercialized, including microcrystalline cellulose (MCC), cellulose nanocrystals (CNC), cellulose macrofibers (CMF), and cellulose nanofibrils (CNF), all of which offer potential for development in TENG applications as fillers and friction layers [265]. Although the triboelectric polarity of micro/-nanocellulose (based on tribo-positivity) is relatively weak, these materials remain attractive due to their excellent dielectric properties, making them suitable as both fillers and matrix materials. MCC, which is odorless, and highly crystalline compared to other forms of cellulose, was used as a dielectric filler in 2017 [257]. MCC was incorporated into polydimethylsiloxane (PDMS) via gel-casting, as illustrated in Fig. 28a, with various MCC contents studied to determine the conditions that provide maximum electrical output. Based on the CS mode operation between a PDMS/MCC composite film and an aluminum film, 5 wt% MCC generated a maximum V_{OC} of ~28 V, I_{SC} of ~2.8 mA, and P_{max} of ~576 mW for a 3 × 3 cm^2 device. The MCC-based TENG was proposed for applications such as a self-powered charging unit and a self-powered locomotion detector [257]. CNC, with its crystalline structure in plate-, rod-, or fiber-like shapes (diameters or thickness <10 nm and lengths around 100–500 nm), was also explored. As illustrated in Fig. 28b, oriented flakes of CNCs were used as an effective dielectric material in TENGs, capable of lighting up around 100 LEDs in CS mode [256]. The uniformly distributed CNC flakes contributed to a V_{OC} of ~320 V, J_{SC} of ~5 μA/cm^2, and a P_{max} of about 1.65 mW using a matching load resistance of 10 MΩ. Macro-fibers were fabricated and woven into gel fabrics to act as triboelectric friction layers. The developed BC macro-fiber was modified with polypyrrole (PPy) semiconductor and carbon nanotubes (CNT) to form a BC/CNT/PPy fiber composite, enhancing output efficiency. This composite generated an electrical output of ~170 V, ~0.8 μA, and 352 μW for V_{OC}, I_{SC}, and Pmax, respectively, as shown in Fig. 28c [266]. CNFs are another interesting form of nanocellulose. As illustrated in Fig. 28d, Xing and colleagues incorporated CNFs within a spider-web-like structure as a triboelectric layer for TENGs. The CNFs, even without modification, provided a high voltage (>400 V) when in contact with Teflon, thanks to the nano-surface roughness of CNF, which increased the contact area, making it highly electropositive in the triboelectric series [267]. CNF's output performance was further improved by incorporating 2D nanosheet MXene (M-$Ti_3C_2T_x$). At an optimal loading of 60% MXene, the V_{OC} exceeded 700 V, with a high charge density of 100 μC/m^2. Using CNF as the contact layer in TENGs showed higher performance in terms of ISC, as demonstrated in Fig. 28e. CNF-based TENGs generated higher I_{SC} (~2 μA) compared to traditional cellulose films (~1 μA). CNF also exhibited excellent stability, with I_{SC} remaining at 2 μA after more than 50,000 cycles. Moreover, when CNF was incorporated with SO_3Na, the I_{SC} increased to ~7.8 μA, making it suitable for self-powered systems such as flexible switches and wireless

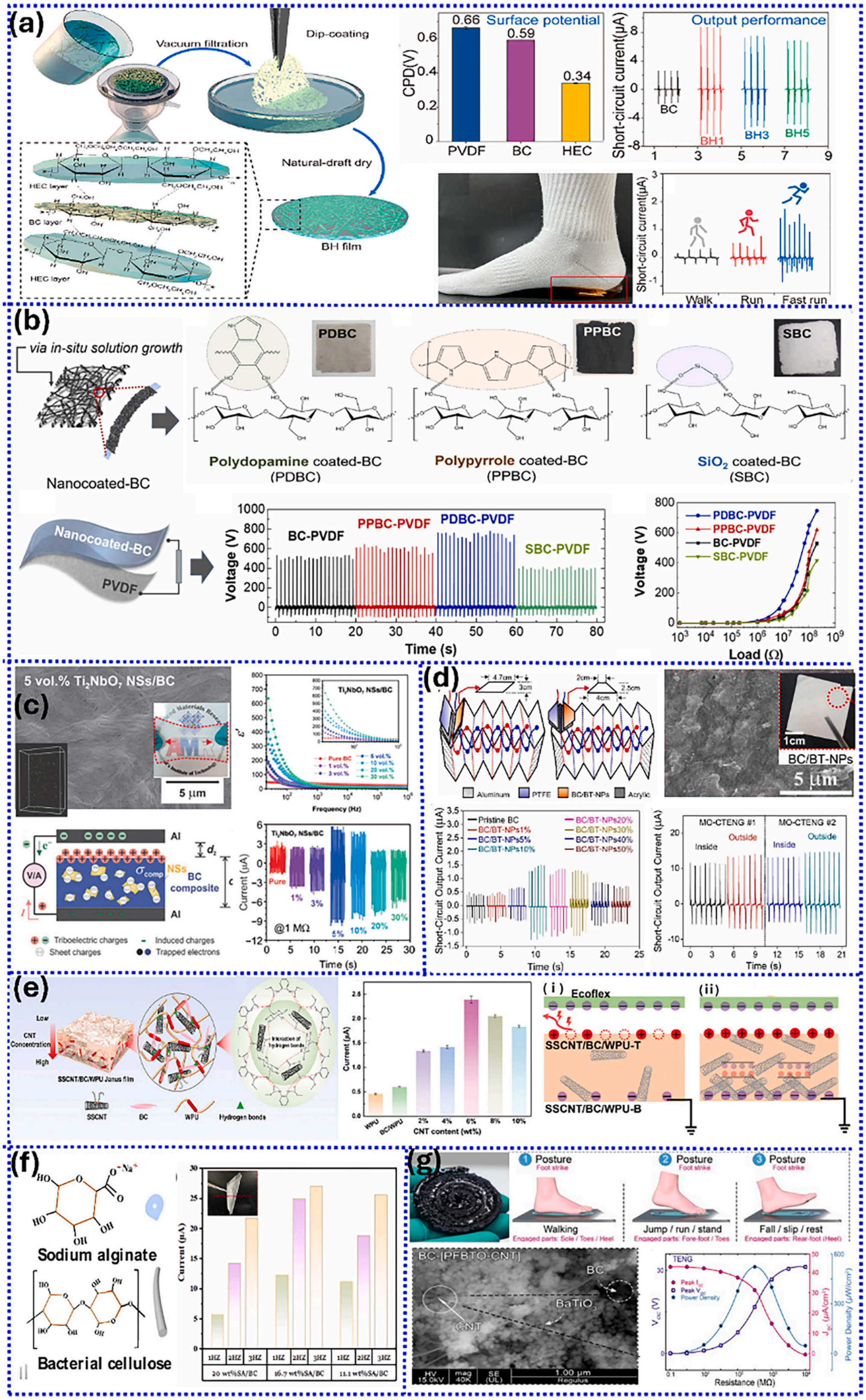

Fig. 27. Summary of bacterial cellulose (BC)-based TENG including (a) hydroxyl ethyl BC-based films. Reproduced from Ref. [258]. Copyright 2022 American Chemical Society, (b) Nanocoated BC films. Reproduced from Ref. [252]. Copyright 2023 Elsevier, (c) BC/Nanosheet composite films. Reproduced from Ref. [263]. Copyright 2023 Springer, (d) structural design BC. Reproduced from Ref. [254]. Copyright 2023 Elsevier, (e) conductive CNT modified BC. Reproduced from Ref. [255]. Copyright 2024 Wiley, (f) BC/sodium alginate blend films. Reproduced from Ref. [253]. Copyright 2024 Elsevier, and (g) BC/PEDOT/CNT three-phase composite films. Reproduced from Ref. [264]. Copyright 2024 Springer.

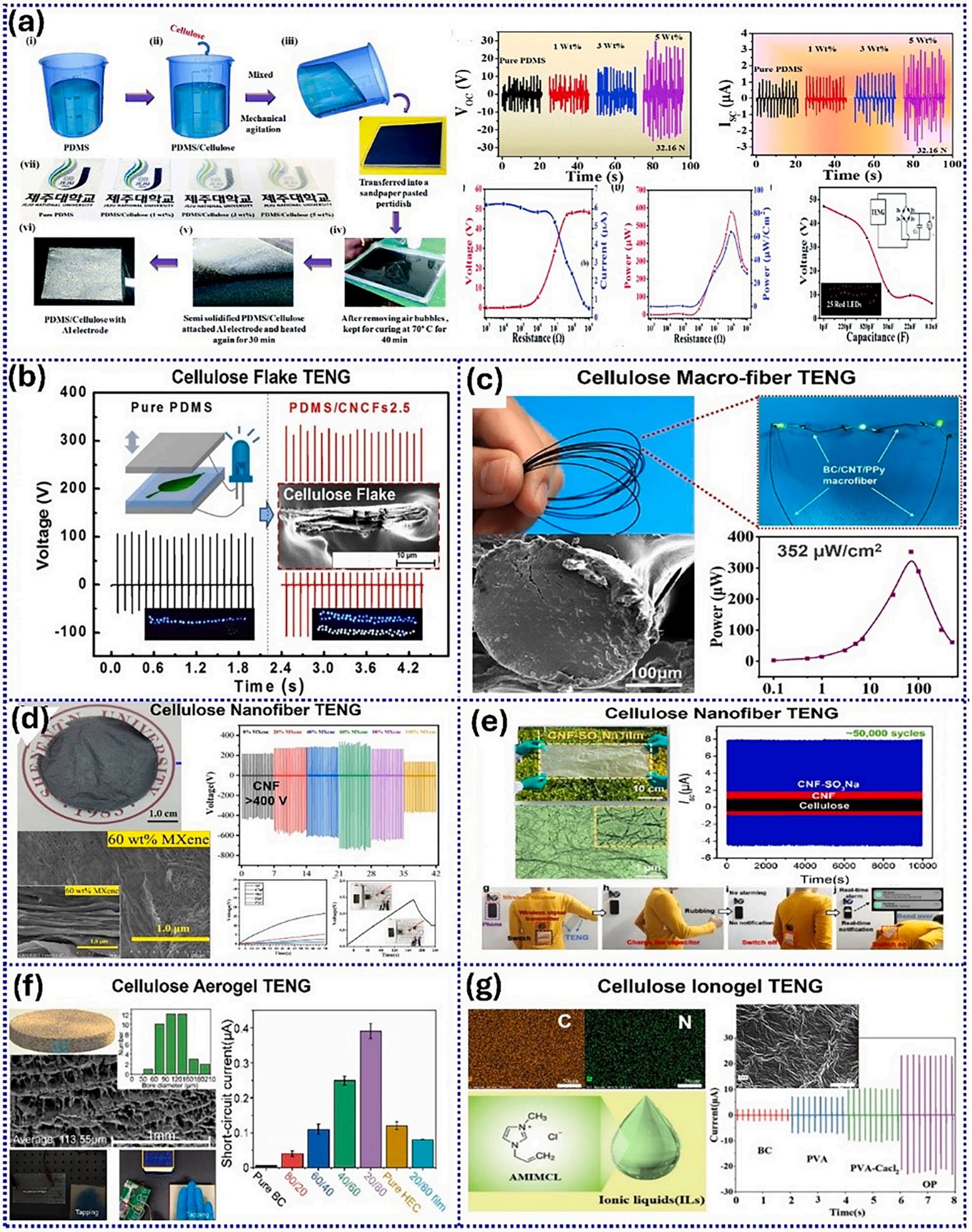

Fig. 28. Summary of cellulose derivative materials for TENG including (a) microcrystalline cellulose. Reproduced from Ref. [257]. Copyright 2017 Royal Chemical Society, (b) cellulose flake. Reproduced from Ref. [256]. Copyright 2017 Royal Chemical Society, (c) cellulose macro-fiber. Reproduced from Ref. [266]. Copyright 2022 Springer, (d) nanofiber cellulose. Reproduced from Ref. [267]. Copyright 2022 American Chemical Society, (e) modified cellulose nanofiber. Reproduced from Ref. [259]. Copyright 2023 American Chemical Society, (f) cellulose aerogel. Reproduced from Ref. [269]. Copyright 2023 American Chemical Society, and (g) cellulose ionogel. Reproduced from Ref. [270]. Copyright 2024 Elsevier.

signal receivers and transmitters attached to the human body [259]. In line with this study, Wicklein et al. demonstrated that blending cellulose pulp, microcrystalline cellulose, and cellulose nanofibers with carbon black, carbon nanotubes, and graphene nanoplatelets further enhances the piezo and triboelectric response at microscopic and macroscopic scales of the nanocomposites for biodegradable nanogenerators [268]. The highest generated output voltage in triboelectric mode was obtained from MCC films with CNTs and carbon black, while the highest piezoelectric voltage was produced in CNF-CNT films. The analysis of the microscopic response demonstrated a higher local piezoelectric d33 coefficient (145 pC/N) for the pulp than for the CNF (14 pC/N), while the macroscopic response was greatly influenced by the excitation mode and the effective orientation of the crystals relative to the mechanical stress.

Expanding the applications of cellulose, aerogels were also utilized as contact layers in TENGs, offering I_{SC} values four times higher than smooth cellulose forms, as shown in Fig. 28f. When hydroxyethyl cellulose (HEC) was introduced at 80%, the performance of the aerogel improved by more than 30 times. BC/HEC aerogels were further combined with wood panels to create a self-powered smart door, capable of lighting a commercial LED through tapping or knocking [269].

In addition to the aerogel form, an ionogel, incorporating a liquid phase as an ionic electrolyte, was developed, as proposed by X. Bu and colleagues in 2024 (Fig. 31g). Cellulose from orange peel was mixed with polyvinyl alcohol (PVA) and $CaCl_2$ to create a solid polymer electrolyte, utilizing weak hydrogen bonds between PVA and the molecular chains of cellulose. The ionic liquid provided an ion-conductive phase, increasing charge density and enabling efficient conductivity to the load. The ionogel form of cellulose TENG achieved a high V_{OC} of ~280 V, I_{SC} of ~24 μA, and P_{max} of ~5.78 W/m^2. This form of TENG was capable of lighting up 306 commercial LEDs and powering other small electronic devices [257,270].

4.9. Hydrogel materials for TENG

Hydrogels are typically water-based materials consisting of a network of polymers that form a gel with water absorption. These materials offer remarkable advantages, including transparency, flexibility, stretchability, and high conductivity, outperforming traditional rigid materials. These characteristics make hydrogels promising candidates for next-generation multifunctional and soft wearable devices in human-machine interfaces. Hydrogel-based materials have also gained popularity in TENG fabrication, as they are well-suited for stretchable energy harvesting devices and self-powered sensors. The introduction of hydrogel and ionic hydrogel materials has enabled electricity generation from mechanical motion through ion migration, offering a new pathway for energy harvesting in flexible and wearable electronics. Summary of cellulose-based materials for TENG device performance is presented in Table 9.

As illustrated in Fig. 29a–H. Park and colleagues proposed PVC and plasticized PVC gels for highly transparent and stretchable TENGs used in tactile sensors [278]. By introducing a plasticizer into the PVC gel, a 20-fold enhancement in Pmax was achieved compared to pristine PVC gel. The device generated an electrical output of 24.7 V and 0.83 μA with stable V_{OC} and I_{SC} under 80% stretching conditions during simple touch operations. As shown in Fig. 29b, an ionic conductive hydrogel based on PVA and CMC was prepared by soaking the hydrogel in an ionic salt solution, studying the effects of CMC concentration, type, and concentration of the ionic solution. The optimized condition for the ionic PVC/CMC hydrogel resulted in a V_{OC} of ~584 V, an I_{SC} of ~25 μA, and a power density of ~120 μC/m^2, making it suitable for smart touch applications [281]. Self-healing is another attractive property of hydrogels in TENGs due to their built-in ability to automatically repair damage through polymer self-healing mechanisms. Fig. 29c illustrates a self-healing TENG designed by C. Li and co-workers, where disulfide bonds and polydimethylsiloxane (PDMS) were incorporated into the polyimide (PI) backbone [272]. The dynamic disulfide bonds provide the PI with self-healing properties, while the addition of PDMS significantly reduces the rigidity of the PI backbone. This increase in free volume allows the PI chains more mobility. The device achieved an electrical output of 124 V, 0.75 μA, and 47 nC, and these values could be fully recovered after the device was damaged.

In 2023, P. Kanokpaka and colleagues proposed a self-healing, glucose-adaptive PVA hydrogel TENG for simultaneous glucose monitoring, as shown in Fig. 29d [273]. Benefiting from a β-cyclodextrin inclusion complex, the PVA hydrogel was functionalized to interact with the glucose oxidase enzyme. When this hydrogel TENG was attached to the human body, electrical output was generated by glucose motion stimuli in sweat. The higher the glucose concentration, the greater the electrical output, due to the increase in ionic strength resulting from enzymatic activity [273]. Phase-locked structures in gels and hydrogels, constructed via phase separation, have recently emerged as promising candidates for TENG applications. These two-phase structures in hydrogels form due to differences in polymer solubility between the hard and soft phases. A triboelectric electronic skin was proposed using an iontronic gel constructed by mixing 2-hydroxyethyl methacrylate (HEMA), poly(ethylene glycol) dimethacrylate (PEGDA), Irgacure 184, α-cellulose, and chitosan, as shown in Fig. 29e [284]. This phase-locked gel TENG can generate electrical output when in contact with tribo-negative materials, making it suitable for smooth bonding with human and robotic interfaces. Additionally, natural resource-based hydrogels for TENG applications have gained interest. A collagen-based conductive hydrogel, made from collagen extracted from cattle Achilles tendons, oxidized hyaluronic acid (OHA), and black wattle bark tannin-reduced AgNPs, was proposed as another triboelectric electronic skin, as illustrated in Fig. 29f. This collagen-based hydrogel exhibited enhanced mechanical properties, including self-healing capabilities, and provided sufficient electrical output for real-time monitoring of human body movements [271].

4.10. Textile-based materials for TENG

Textiles encompass various fiber, yarn, filament, mat, and thread-based materials that can be formed from several types of polymers. Textile TENGs (T-TENGs) have emerged as a promising option for wearable electronics due to their excellent deformability, flexibility, and breathability. To date, several fabrics and yarns have been proposed and proven to deliver high performance in TENGs and triboelectric sensors

Table 9
Summary of hydrogel-based materials-based TENG device performance.

Ref	Material	Triboelectric material pair	Size of the device	Voc	Isc	Power Max
[271]	PCOBE organohydrogel	Skin	4 × 4 cm^2	80 V	5 μA	–
[272]	6FDA-4PDA-PDMS-PI	Copper	3 × 3 cm^2	124 V	0.75	–
[273]	self-healable glucose adaptive hydrogel (GAH-TES)	Nylon	2 × 2 cm^2	65 V	3.5 μA	65 μW
[274]	PVA/TA/PAA/CNT hydrogels	Skin	5 × 5 cm^2	180 V	0.8 μA	37.8 mW/m^2
[275]	TOCNF/PANI hydrogel	ISM	10 × 10 × 3 mm	–	18.5 nA/cm^2	–
[276]	PVA-PA/silicone rubber hydrogel	ITO	4 × 4 cm^2	240 V	4 μA	–
[277]	Ag@rGO/PVA-PAAm organohydrogel (silicon rubber)	Kapton	2 cm × 3 cm	130 V	2	349.3 mW/m^2
[278]	PVC-gel	Nylon	2.5 cm × 3 cm	24.7 V	0.83	8.7 μW cm^{-2}
[279]	MAGP hydrogel/CNTs/PDMS film	Al	42 cm^2	141 V	0.8	–
[280]	Graphene oxide (GO) hydrogel	Pen	–	–	–	–
[281]	CMC/PVA hydrogel/silicon rubber	Skin	2 × 2 cm^2	584 V	25	25 W/m^2
[282]	Ionic hydrogel (PTSM)	PI	5 × 2 × 0.4 cm^3	150 V	2	54.24 mW/m^2
[283]	PAOAM-PDO organohydrogel/VHB	PVC	–	350 V	–	0.81 W/m^2

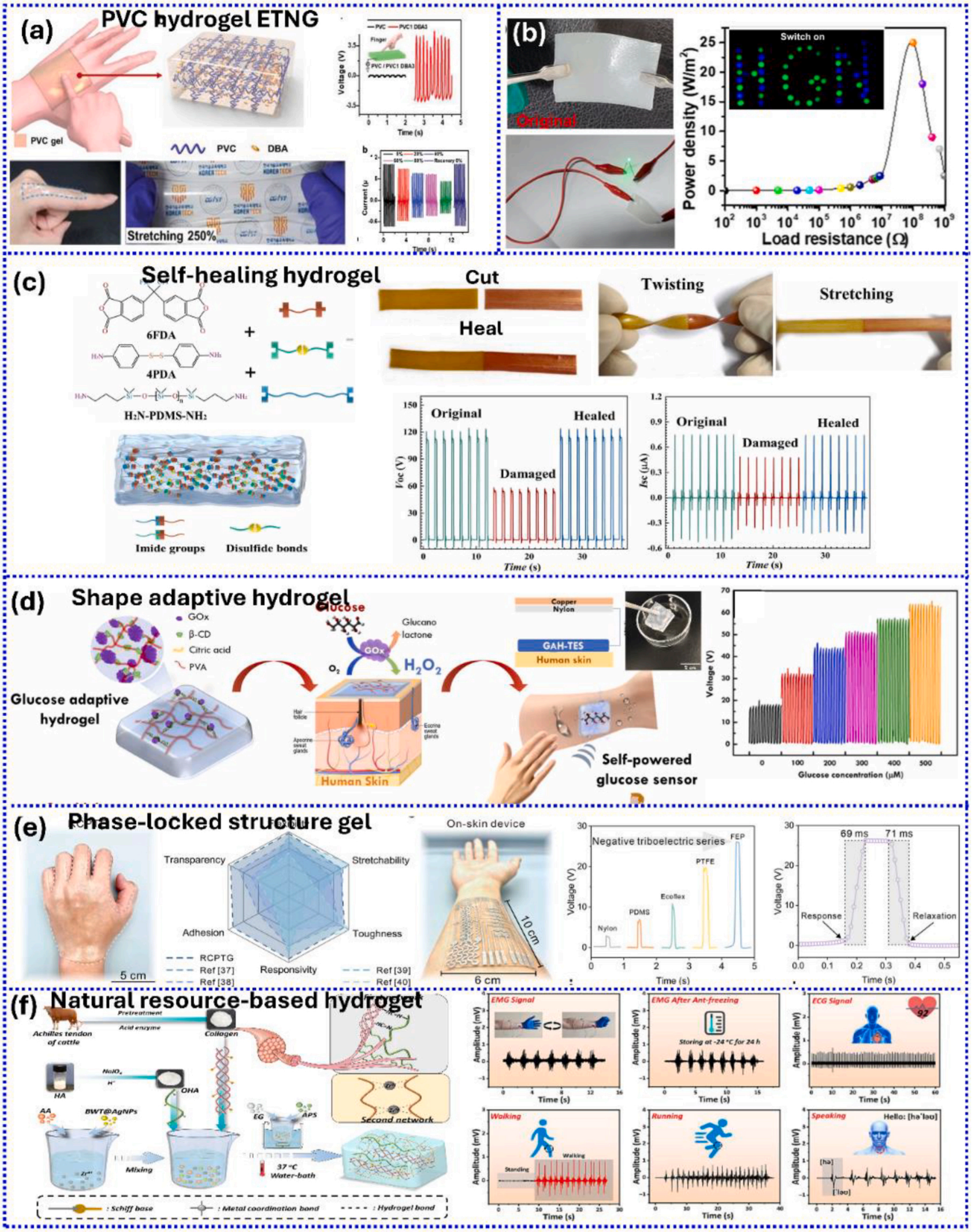

Fig. 29. Summary of hydrogel-based materials for TENG including (a) PVC hydrogel TENG. Reproduced from Ref. [278]. Copyright 2022 Wiley, (b) PVC/CMC blend. Reproduced from Ref. [281]. Copyright 2023 American Chemical Society, (c) self-healing PDMS gel. Reproduced from Ref. [272]. Copyright 2023 Elsevier, (d) shape-adaptive hydrogel. Reproduced from Ref. [273]. Copyright 2023 Elsevier, (e) phase-locked structure gel. Reproduced from Ref. [284]. Copyright 2024 Springer, and (f) natural resource-based hydrogel. Reproduced from Ref. [271]. Copyright 2023 Elsevier.

(TES) for various applications beyond clothing. In this section, we will review the recent developments in TENG textiles, divided into two subsections: fabric and yarn, both of which have been proposed for TENG applications in recent years. The performance metric of textile–based TENG device are presented in Table 10.

4.10.1. Fabric-based materials for TENG

As mentioned earlier, various textile materials have been proposed for TENG applications. In this sub-section, we review some recent publications, starting with materials on the negative side of the triboelectric series. A 3D woven T-TENG with integrated spacer layers, serving as an intermediate layer between two distinct materials, was

Table 10
Summary of textile materials-based TENG device performance.

Ref	Material	Triboelectric material pair	Size of the device	Voc	Isc	Power Max
[285]	LC/PPy/CS/PA film	Skin	4 × 4 cm^2	0.3 V	1.8 μA	7 μW/cm^2
[286]	Polypropylene non-woven fabrics	Polyamide 66 fabrics	1 × 1 cm^2	210 V	28.3 μA	901.7 mW/m^2
[287]	PTFE	PA	7 × 7 cm^2	14.06 V	0.36	0.02 mW/m^2
[288]	T-CSY	–	3 × 10 cm^2	43.2 V	6.12	11.89 μW/cm^2
[289]	PTFE	PA66	2 cm × 10 cm	43.82 V	21.79	4.219 mW/m^2
[290]	MoO_3 nanostructures on carbon cloth	PDMS	5 × 5 cm^2	55 V	0.19	4.17 μW
[291]	Conductive fiber (Ecoflex coating with polyaniline (PANI))	–	20 turn/cm	3 V	2.86 nA	2.23 nW
[292]	PTFE-Ag yarn	PA66-Ag yarn	8 × 8 cm^2	32 V	1.9 μA	7531 μW/m^2
[293]	Kevlar/STF/SSG/graphene	PMMA	5 × 5 cm^2	45 V	5.7	25.8 mW/m^2
[294]	PTFE	BW-coated MLG on polyester	1.5 cm × 2.5 cm	80 V	0.76	147 mW/m^2
[295]	CuNi-BEF	PET	2 × 2 cm^2	199 V	22	2992 mW/m^2
[296]	PDMS-CNT	Nylon	3 × 3 cm^2	51.2 V	3	9.98 μW/cm^2
[297]	PVDF	PBU	5 × 5 cm^2	113 V	8	16 mW
[298]	PVDF-TrFE conductive Yarn and PU coated polyester copper yarn	Nylon	1 cm × 1.5 cm	100 V	–	–
[299]	PTFE	Rayon fabric	–	23 V	13	53 μW

designed [287]. PTFE and nylon (PA) fabrics were chosen as the negative and positive materials, respectively, based on their positions in the triboelectric series, while PET yarn was selected as the fabric spacer. The structural design was achieved through weaving technology, as shown in Fig. 30a. The distance and height of the spacer layers were optimized to provide the highest output performance, generating ~14.1 V and 30.7 nA at a frequency of 1 Hz and an applied force of 50 N. The rectangular hollow structure of this 3D woven T-TENG offers comfort and flexibility, making it suitable for integration as an insole to generate electrical output during walking or running. Another design using nylon and PTFE as a material pair was also proposed for T-TENG, woven in a plain-weave structure [289]. As shown in Fig. 30b, the nylon/PTFE T-TENG was integrated inside a tire for use as a self-powered skid resistance monitoring system, demonstrating a significant difference in signal amplitude between rough and smooth driving conditions, with an accuracy of 96%. In Fig. 30c–a low-cost thermoplastic polymeric fabric-based TENG, composed of non-woven polypropylene (NW-PP), polyamide 66 (PA-66-F), and nickel conductive fabrics (Ni@fabrics), was proposed by F. Peng and colleagues [286]. This device generated a high power density of 901.7 mW/m^2 with a matching external resistance of 70 MΩ, and it successfully illuminated 124 LEDs spelling "ZZU & TENG."

As represented in Fig. 30d, the enhanced Kevlar (EK) TENG was developed by incorporating Kevlar fabric with SiO_2, graphene, and a mixture of shear thickening fluid (STF) and shear stiffening gel (SSG). This configuration achieved a power density of 25.8 mW/m^2 under a loading force of 40 N and a fixed frequency of 10 Hz. The combination of anti-ballistic properties and a self-powered sensor, even after being shot by a bullet, was suggested as a potential application [293]. According to Fig. 30e, modified electrodes for PET-based TENG were recently proposed in 2024 by A. K. Aliyana and co-workers [295]. Three types of electrode fabrics were studied: Copper Monometallic (Cu-MEF), Copper-Tin Bimetallic (CuSn-BEF), and Copper-Nickel Bimetallic (CuNi-BEF). The CuNi-BEF electrode fabric produced the highest electrical output, with values of ~199 V, ~22 μA, and ~2992 mW/m^2, showcasing significant potential for power generation in IoT-enabled touch sensor systems.

Additional functionalities such as biodegradability, self-healing, flame retardancy, and dual-structure fabrication (for charge storage, supercapacitors, etc.) in textile TENGs are increasingly attractive for broadening their applications. T. D. Khanh and et al., [297] utilized polybutadiene-based urethane (PBU) fabricated via a non-woven method as a triboelectric friction layer, adding washability and self-healing capabilities to the T-TENG. The abundant -NH_2 groups played a critical role in facilitating electron transfer, enhancing the electrical output when rubbing against polyvinylidene fluoride (PVDF). A 2500 mm^2 device generated ~113 V and ~8 μA at a constant 5 Hz with 0.98 kPa external force, as shown in Fig. 31a. As displayed in Fig. 31b–a natural and eco-friendly fabric based on beeswax (BW) was developed as a multifunctional triboelectric layer, using graphene as the electrode. By incorporating 10% BW, the TENG achieved a maximum V_{OC} of ~80 V, I_{SC} of ~0.76 μA, and Q_{SC} of ~30 nC, benefiting from its enhanced hydrophobicity [294]. As illustrated in Fig. 31c–a flame-retardant, cellulose-based fabric TENG was developed through the self-assembly of natural chitosan/phytic acid (CS/PA) and the incorporation of polypyrrole (PPy) as a conductive polymer. This fabric TENG provided an electrical output of 0.3 V (at 2 N, 5 Hz) while also demonstrating biodegradable and flame-retardant properties, with a limiting oxygen index of 35.2% [285]. A demonstration of a dual-function T-TENG device, designed for both energy harvesting and storage, was proposed. Molybdenum trioxide (MoO_3), a dual-function material, was grown on carbon cloth (CC) to construct a charge-storing electrode for supercapacitors and a charge-sharing electrode for TENG. This system provided a highly efficient ISC of 30 μA, capacitance of ~97.86 F/g, energy density of ~40.50 Wh/kg, and power density of ~28,125 W/kg, suggesting significant potential for use in both energy storage and energy harvesting technologies. The results of this work are initially shown in Fig. 31d [290].

4.10.2. Yarn-based materials for TENG

Modifying fibers and yarns before fabricating them into TENG fabrics is recommended in several studies. For instance, stretchable fiber coated with Ecoflex and polyaniline (PANI), along with varnished wires, was developed, as shown in Fig. 32a. This design aimed to couple thermoelectric and triboelectric effects for smart clothing applications, including motion sensing and bio-detection. The maximum power output (Pmax) reached 2.23 nW under a matching resistance of 1 GΩ. A remarkable result was observed with the stretch tensor, which increased from 50% to 175%, enhancing the I_{SC} from ~1.8 to ~5.9 nA [291]. W. J. Kim and colleagues [288] proposed a modified one-dimensional coaxial stretchable yarn with high water resistance for TENG applications. The combination of latex, multi-wall carbon nanotubes (CNTs), and PDMS provided stretchability of over 100%, allowing the yarn to twist, turn, and remain effective in strained states. The device demonstrated sustained output performance due to the high charge transfer capability from the added CNTs. A practical application of this yarn powering a commercially available thermometer was demonstrated, as shown in Fig. 32b. As seen in Fig. 32c–a 2D planar structure was designed for a polyvinylidene fluoride-trifluoroethylene (PVDF-TrFE) fabric TENG [298]. The PVDF-TrFE yarn was wrapped with polyurethane (PU)-coated polyester-Cu. Among four different wrapping materials, this configuration showed the best enhancement in output performance due to the significant electronegativity difference between the -F group of PVDF-TrFE and the –CONH group of PU. Additionally, the design offered a high degree of washability. However, these wearable generators, which are constructed in a dual-electrode mode, rely on friction between

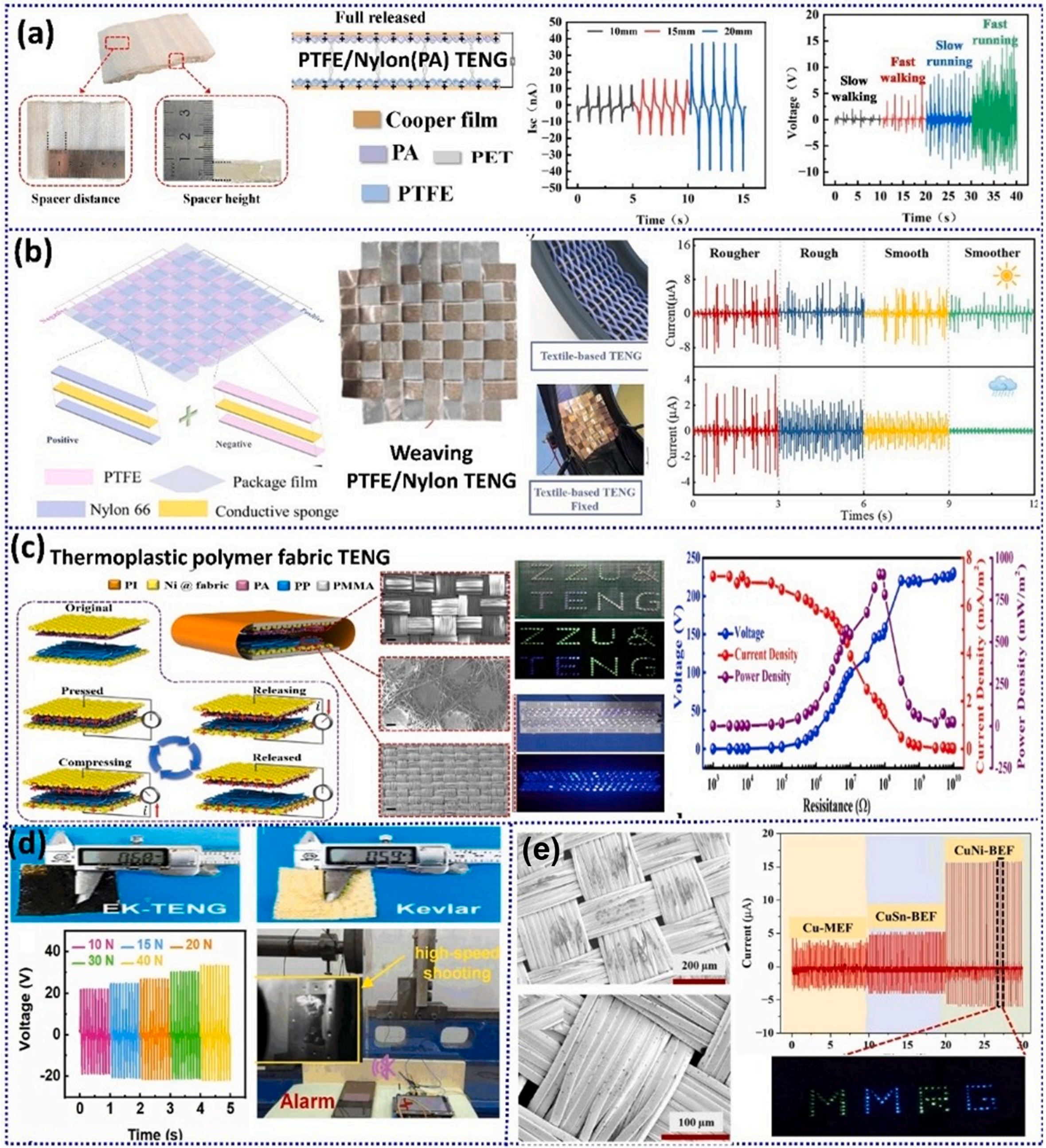

Fig. 30. Summary of fabric-based materials for textile TENG (T-TENG) including (a) PTFE/Nylon TENG. Reproduced from Ref. [287]. Copyright 2023 Elsevier, (b) PTFE/Nylon weaving TENG. Reproduced from Ref. [289]. Copyright 2023 Elsevier, (c) thermoplastic polymeric fabrics. Reproduced from Ref. [286]. Copyright 2019 Elsevier, (d) Kevlar. Reproduced from Ref. [293]. Copyright 2022 Elsevier, and (e) modified electrodeds for PET T-TENG. Reproduced from Ref. [295]. Copyright 2024 Elsevier.

adjacent fibers/yarns or face-to-face fabrics coated with different synthetic polymers or metallic patterns, often leading to poor breathability and reduced comfort. While many publications propose new or modified natural fabrics for TENG, such as cellulose acetate and rayon [299], these challenges remain significant.

The preceding sections have provided a comprehensive overview of the diverse material classes explored for TENGs, ranging from polymers and inorganic frameworks to textiles and biodegradable alternatives. While the choice of materials establishes the fundamental charge transfer characteristics, the overall device efficiency is equally governed by strategies that enhance charge retention, structural design, and environmental adaptability. Therefore, the next section shifts the focus from material selection to performance improvement approaches, highlighting how device architecture, surface modification, and hybridization techniques can significantly optimize TENG output for practical applications.

5. TENG performance improvement methods

The values of the output open-circuit voltage, short-circuit current, electric power, and surface power density, generated by the TENG device, are crucial for its potential future applications [300,301]. The performance of the triboelectric nanogenerators can be enhanced in many different ways [302–305]. These strategies may be distinguished in the four main groups: physical modifications, chemical modifications, charge boosting methods, and power management methods. The

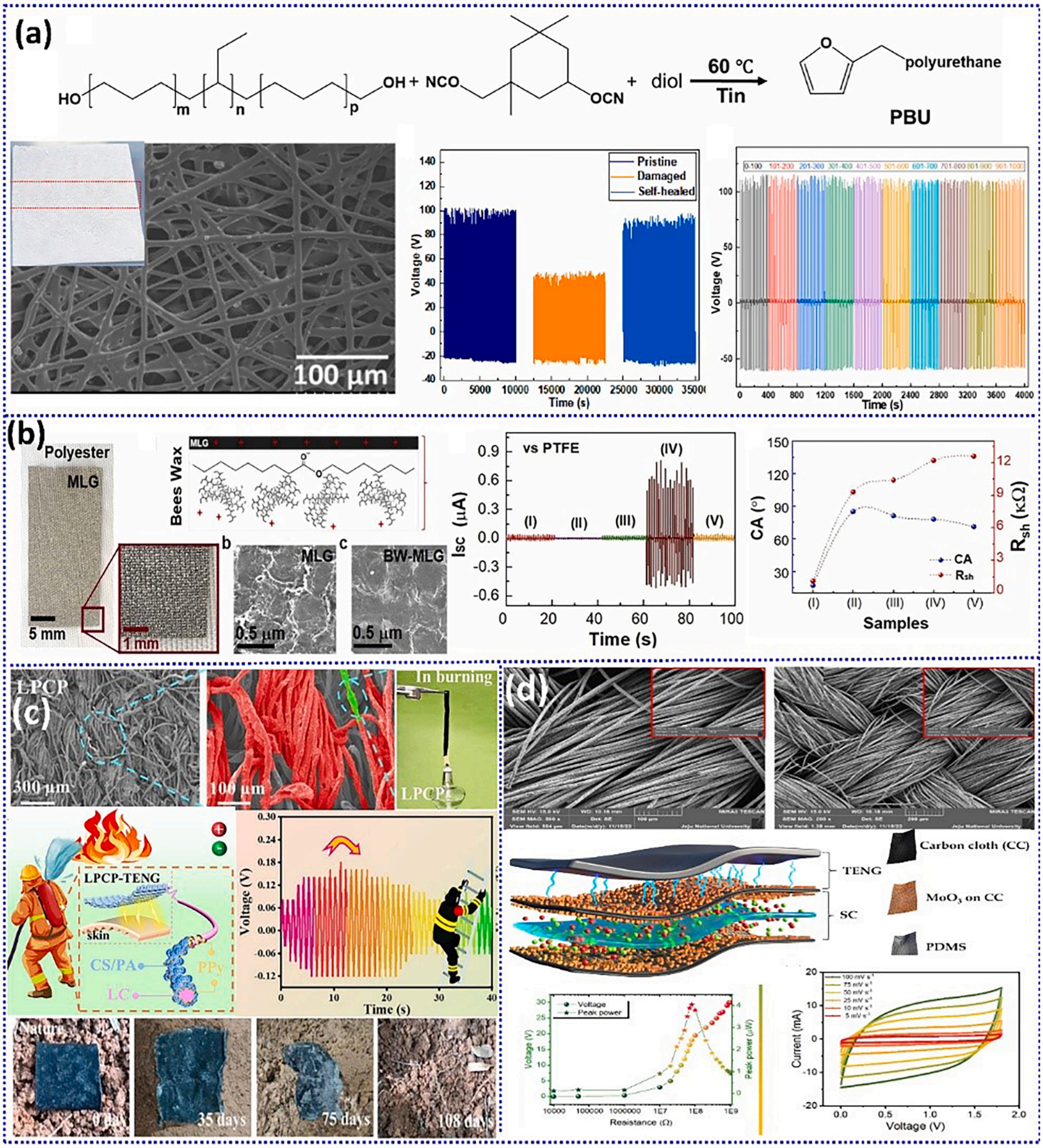

Fig. 31. Summary of advanced fabric-based materials for textile TENG (T-TENG) including (a) self-healing textile. Reproduced from Ref. [297]. Copyright 2023 Elsevier, (b) hydrophobic polyester fabrics. Reproduced from Ref. [294]. Copyright 2024 Elsevier, (c) flame retardant cellulose fabric. Reproduced from Ref. [285]. Copyright 2024 Elsevier, and (d) dual properties fabric. Reproduced from Ref. [290]. Copyright 2024 Elsevier.

detailed insight into the mentioned methods is presented below.

5.1. Physical modifications

5.1.1. Engineering of surface microstructure

The contact charging performance of the TENG device depends strongly on roughness and surface structure of the friction film. The surface charge density increases with increase of the roughness of the interface and contact area during contact electrification [301]. Therefore, the output voltage and power of the TENG can be enhanced by engineering of the triboelectric surface in the nano- and microscale [306–308]. The laser micropatterning [309–312], lithography [313, 314], 3D printing [315–317], polishing [318], molding-based patterning [319–324], blade-coating [325], electrodeposition [321], and fabrication of porous materials [326] are technologies frequently applied to obtain desired roughness and surface microstructure of triboelectric layer.

A fabrication of hierarchical micro/nanostructure patterns on polydimethylsiloxane (PDMS) surface was demonstrated by Kim and coworkers [309]. They studied an influence of parameters of femtosecond laser operation on patterned PDMS surface morphology. It was found that application of laser radiation with moderate laser power resulted in gained effective contact area between PDMS friction layer and metal electrode in comparison to this obtained without laser processing. This method allowed to enhance the TENG open-circuit voltage from 32 V to 42.5 V and short-circuit current from 7 µA to 10.1 µA [309]. Mahmud et al. [314] applied thermal nanoimprint lithography method to modify the surfaces of poly(methyl methacrylate) (PMMA) and PDMS

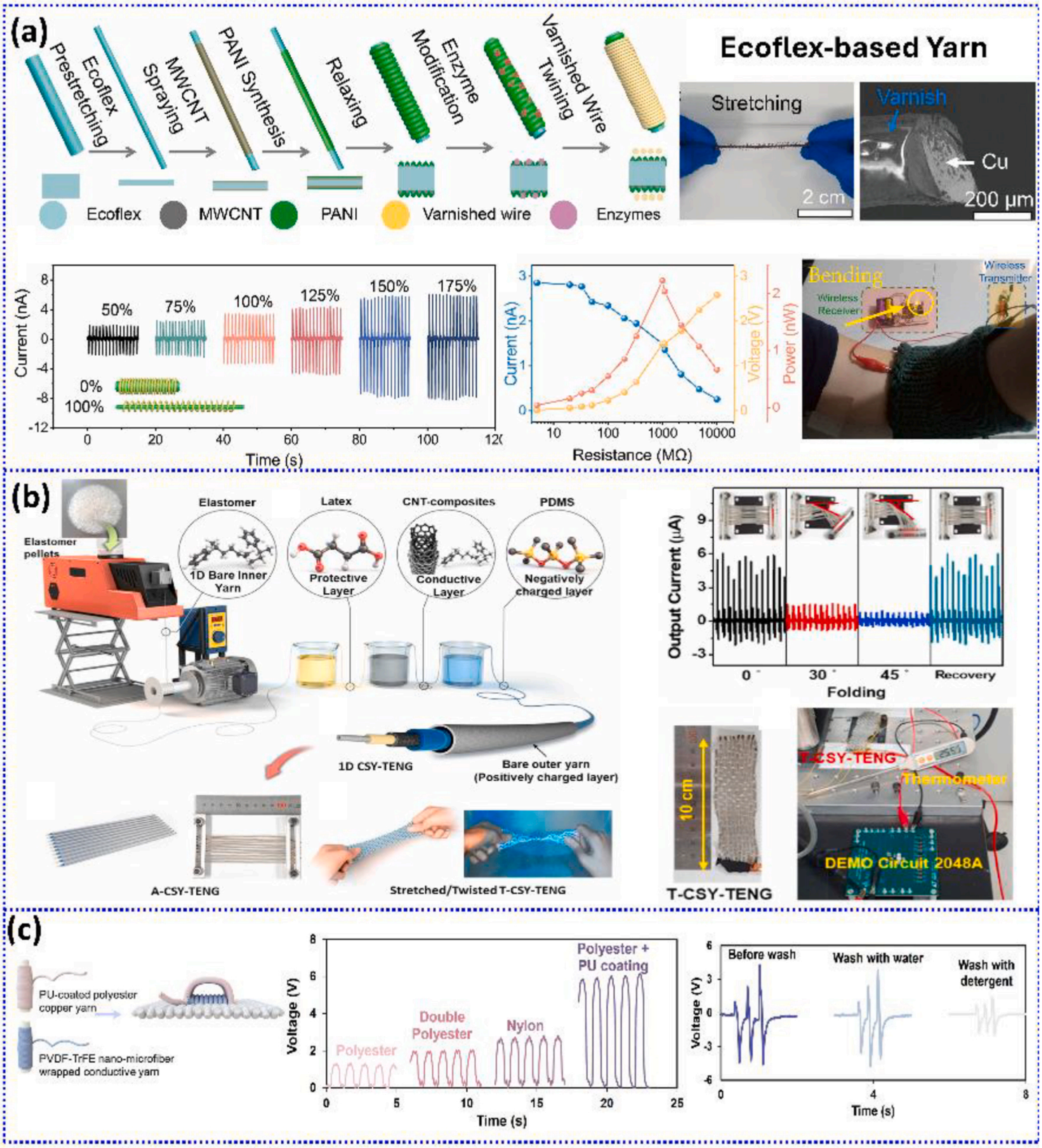

Fig. 32. Summary of yarn-based materials for textile TENG (T-TENG) including (a) Ecoflex-based yarn. Reproduced from Ref. [291] Copyright 2022 Elsevier, (b) modified PDMS yarns. Reproduced from Ref. [288]. Copyright 2022 Elsevier, and (c) coated PVDF-TrFE yarns. Reproduced from Ref. [299]. Copyright 2024 Cell Press.

films by creating line, pillar and hexagonal cone nanopatterns. The highest output power of a TENG was observed for a device with a 300 nm hexagonal cone-shaped patterned on triboelectric layer. A simple and scalable method of triboelectric surface modification was proposed [318]. Aluminum and Kapton layers were polished using sandpapers with different grit size. After surface polishing, the output voltage and power of TENG were gained three and five times, respectively. Similar method of TENG surface processing was described by Mishra et al. [327]. Al substrates were scratched with emery papers with various grits to create desired micro-roughness. After Al surface scratching, the open-circuit voltage and short circuit current were increased by 2.4 and 2.5 times, respectively. According to Ref. [328], an increase of crumple degree for graphene based TENG led to the rise of the device output voltage, output current and power density. Sun et al. [319] demonstrated a cheap and environmental friendly utilization of natural leaf as a mold to create ramified texture and micro-nano pattern on the PDMS surface. The open-circuit voltage and short-circuit current of leaf-molded TENG attained 56 V and 3.1 μA, respectively. Lin and associates [329] developed an advanced design method of TENG based on plant fibers with cocklebur structure. The cellulose fibers were subjected to the mechanical shearing in order to micro fibrillation in the longitudinal direction of cellulose fibers leading to formation of the cocklebur structure of fibers. Furthermore, Ag nanoparticles were grown on cellulose fibers surfaces using chemical reduction method of $AgNO_3$. A remarkable durability of TENG was demonstrated. The open-circuit voltage and short-circuit current of TENG were equal to 142.6 V and 31.2 μA, respectively [329]. A fabrication of PDMS films with open porous structures was proposed in Ref. [326]. Silicon oil, dibutyl phthalate, and NaCl microparticles were used as pore-forming agents. The open porous structure of PDMS allowed to obtain an excellent device performance which was attributed to enhanced contact area and reduced effective thickness. The TENG generated open-circuit voltage of 600 V, short-circuit current of 15 μA, and surface power density of 5.67 W/m^2 [326].

5.1.2. An introduction of intermediate layer into TENG device

An interesting approach to increase the output performance of the TENG is adding a transition layer between electrode (conducting layer) and friction layer or between two triboelectric layers. Such transition layer is responsible for accumulating the electric charges resulting in improvement of TENG output performance. Feng et al. [330] described an application of the polyimide film as a charge storage layer in TENG device composed of nylon (NY) and polyvinylidene fluoride (PVDF). It resulted in enhancement of TENG voltage from 110 V to 1010 V and electric current from 9.2 μA to 65 μA. A change in TENG performance depended on physical properties of polyimide transition layer such as its morphology, polarity, charge decay characteristic, and film thickness. An use of ZnS nanosheets as an additional layer in PDMS based TENG was shown in Ref. [331]. The output performance of this device was increased due to rise of the surface area and roughness after adding the ZnS nanosheets film. The TENG operated in vertical contact-separation mode and generated open-circuit voltage, short-circuit current, and maximum power density of 8 V, 7.12 μA, and 0.18 μW/cm^2, respectively. Kim et al. [332] presented an inserting the PDMS intermediate layer between electrode and triboelectric layer. A long term conservation of electric charges was achieved due to an existence of deep charge traps in the PDMS interlayer. The output power density of TENG was increased by over two orders of magnitude due to inserting the PDMS interlayer into the device structure [332]. A fabrication of TENG device with antiferroelectric ceramic $Pb_{0.94}La_{0.04}Zr_{0.98}Ti_{0.02}O_3$ (PLZT) interlayer was reported in Ref. [333]. The PLZT based TENG generated large voltage of 456 V and current density of 11.6 μA/cm^2. Its power density attained high value of 5.3 W/m^2 for a load resistance of 8.0 MΩ [333]. Cao et al. [334] showed boosting of TENG output power density through introducing the ferroelectric polymer composite interfacial layers. Similarly, it was reported in Ref. [335] that film of piezoelectric ZnO nanosheets can also serve as interfacial layer in TENG. Park et al. [336] applied TiO_x as an electron blocking layer in the TENG composed of aluminum and PDMS films. It led to the 25 fold increase of output peak power of TENG. A preparation of TENG using an Al electrode and commercial PVDF filter membrane was demonstrated in Ref. [337]. The conductive interlayer, composed of Ag nanoparticles (AgNPs) and reduced graphene oxide (rGO), was filtrated onto PVDF membrane. It played a key role in trapping electric charges and preventing them diffusing and drifting.

5.1.3. Construction of multilayered TENG devices

A proper design of multilayered TENGs allows to boost the generated electric output by synergetic behavior of different part of such complex device. Such strategy was successfully applied by Cheng and co-workers [338] to fabricate self-improving TENG. The device consisted of two main parts (Fig. 33 a-b). The polyvinylidene fluoride (PVDF) and polyamide-6 (PA-6) films served as friction layers in first part of TENG. It operated in vertical contact-separation mode (Fig. 33c). The second part of device was composed of PVDF/epoxy resin (EP) layers and Cr/Ag electrodes arranged in plane-parallel capacitor structure (PPCS). These two elements of TENG were connected together with a rectifier bridge. The first part generated a large voltage under periodic pressing and releasing. The electric charge was injected into the plane-parallel capacitor structure. The electric charge was stored in the PPCS since the used rectifier bridge prevented the charge in the PPCS flowing back. Then, under vibration applied to the device, the electric charges, stored in the PPCS, generated AC voltage in the external circuit. The output current (Fig. 33d), charge density (Fig. 33e), and voltage (Fig. 33f) of multilayered self-improving TENG were much higher than those measured for separate part of the device. Moreover, effective charge density reached a huge value of 490 μC/m^2 [338]. As presented in Fig. 33g, self-improving TENG exhibited a outstanding durability and output current stability during 150,000 cycles of operation.

Fabrication and characterization of multilayered fiber-based TENG with an excellent performance was described by Li et al. in Ref. [339]. The device was composed of copper, cellulose acetate, polyethersulfone, polystyrene, and carbon black which played the roles of electrode, positive triboelectric friction component, negative triboelectric friction component, charge-storage layer, and charge-transport layer, respectively. A presence of charge-storage and charge-transport layers resulted in significantly enhanced TENG performance. The open-circuit voltage of multilayered TENG was three times higher than open-circuit voltage of single-layered TENG [339].

5.1.4. Interface liquid lubrication

The inserting an appropriate lubricant into the interface between two friction layers is a promising strategy to overcome major electrical and mechanical drawbacks of the TENG devices. This method provides

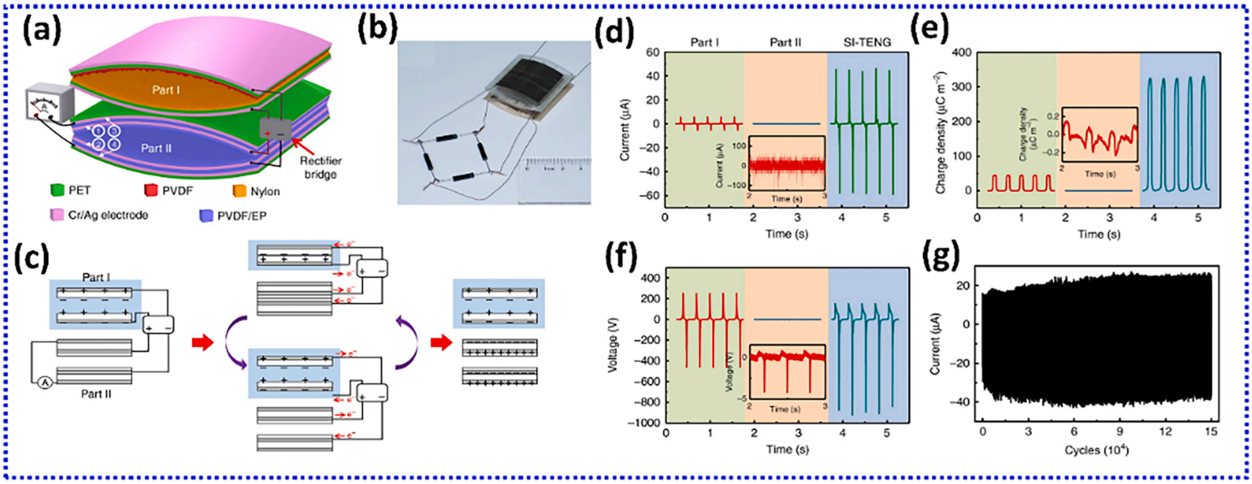

Fig. 33. A scheme (a), photograph (b), working mechanism (c), short-circuit current (d), charge density (e), open-circuit voltage (f), and output current stability (g) of the multilayered self-improving TENG. A detailed description is provided in the text. Adapted from Cheng et al. [338] under the terms of the Creative Commons Attribution 4.0 International License (CC BY 4.0). Copyright (2018) Springer Nature.

numerous significant advantages, including an improvement of the TENG output signal stability [340], increase of device durability by lowering the interface material abrasion [341,342], prevention of an interfacial electrostatic breakdown [341,343], and increase of TENG output voltage [342,344,345] due to reduction of charge loss after the triboelectrification. Zhou et al. [344] studied the influence of different liquid lubricants (squalane, heptane, water, alcohol) on the charge output of sliding-mode TENG. This device consisted of acrylic boards with a thickness of 5 mm, Kapton film with a thickness of 25 μm, and conductive fabrics. Among the examined lubricants the squalane was found to be the most beneficial in promoting charge generation. The electrostatic field strength in the micro-gap between triboelectric electrode and triboelectric layer was diminished. In result, the amount of collected electrostatic charges was gained leading to improvement of TENG output. Wu and co-workers [342] constructed novel TENG from polymethyl methacrylate (PMMA) boards, polytetrafluoroethylene (PTFE) layer, Kapton film, and polyamide 6,6 (Nylon) film. The device structure is depicted in Fig. 34a. The comparative experiments were conducted for dry and lubricated TENG under different applied load forces (Fig. 34b). The open-circuit voltage (Fig. 34c) and short-circuit current (Fig. 34d) of TENG were measured using various lubricants: squalane, paraffin oil, PAO10, olive oil, rapeseed oil, pluriol A 500 PE, [Emim][NTf$_2$], PEG 200, and water. It was observed that the lubrication of TENG with squalane led to enhancement of TENG output by over three times [342]. It was attributed to the increase of contact area between sliding parts by avoiding the air contact with triboelectric layers.

The remarkable improvement of stability of TENG output due to interface liquid lubrication was reported in Ref. [340]. The experiments were conducted for many PAO lubricants with different viscosities. The viscosity of the PAO lubricant was found as a key factor affecting the TENG performance. The presence of the lubricant resulted in rise of the breakdown field strength and reduction of the triboelectric charges loss. Similarly, He et al. [341] confirmed that liquid lubrication is a convenient method of improvement of TENG durability and signal stability. The energy conversion efficiency of TENG attained high value of 48%. The change of output signal did not exceed 10% after 500,000 operation cycles [341].

5.1.5. *Fabrication of advanced nanocomposites*

The output of TENG device strongly depends on the electric properties of applied materials [346], such as electric permittivity, resistance, electric conductivity, capacitance, and dielectric loss. These parameters can be adjusted in the case of advanced polymer composite by applying a special method of its fabrication. Xia et al. [347] developed a technique of alignment of graphene sheets in the PDMS matrix toward boosting the TENG output. It involved ultrasonic homogenization and spin-coating of a mixture of graphene sheets, PDMS, and the curing agent. During the spin-coating process, two-dimensional graphene sheets were arranged parallelly to the nanocomposite surface due to the action of shear forces. It resulted in the formation of micro capacitors composed of aligned graphene sheets. The dielectric loss of TENG was decreased and the device output was enhanced 3 times [347]. Sun et al. [348] developed a method of magnetic polymeric composite preparation for improving the TENG performance. It contained nickel particles which were aligned under a magnetic field. Another method of preparation of advanced nanocomposite with aligned ZnO nanowires in PVDF and nylon-11 nanofibers was described in Ref. [349]. In this approach, the electrospinning technique was applied to arrange ZnO nanowires parallelly to the fiber axis. The TENG open-circuit voltage and short-circuit current were equal to 330 V and 10 μA, respectively. The maximum output power density attained a high value of 3 W/m^2 [349]. Singh an coworkers [350] developed a method of fabrication of nanocomposites of PVDF polymer and ZnO nanorods. An incorporation of ZnO nanorods into the PVDF matrix provided an opportunity to change the surface topography, polarizability, and hydrophobicity of obtained ZnO/PVDF nanocomposite and gain the output of the ZnO/PVDF based TENG. Choi et al. [351] demonstrated that adding the conductive carbon black as filler into the PDMS matrix led to an increase of dielectric constant of contact layer and an improvement of long-term output performance of TENG. Amorntep et al. [352] presented a strategy

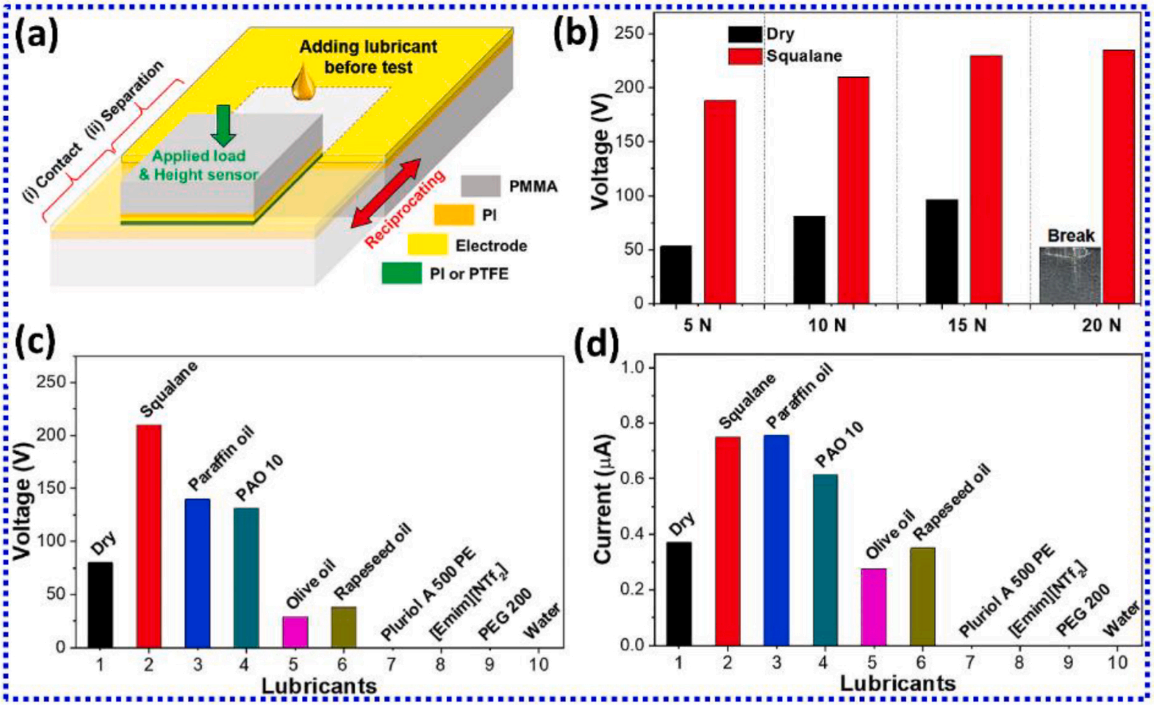

Fig. 34. (a) Schematic diagram of liquid lubricated TEM. (b) The open-circuit voltage of dry and lubricated TENG under different load forces. (c,d) The open-circuit voltage (c) and short-circuit current (d) registered using various lubricants at the constant load force of 10 N. Reprinted from Wu et al. [342] under the terms of the Creative Commons Attribution 4.0 International License (CC BY 4.0). Copyright (2020) Elsevier.

to modulate electrical properties of triboelectric material by changing the Al filler concentration in the nanocomposite of epoxy resin, ferroelectric nanoparticles of $BaTiO_3$, and Al nanoparticles. Garcia-Casas et al. applied plasma nanoengineering to fabricate supported core-shell Ag-ZnO piezoelectric nanowires and embedded them on a PDMS matrix that was functionalized with PFOTES [353]. The complex system was tested as mode I hybrid piezo and triboelectric nanogenerator, i.e., sharing both top and bottom electrodes, demonstrating long durability (ca. 300000 cycles) and converting from 1-2 Hz–800 Hz efficiently.

5.2. *Chemical modifications*

5.2.1. *Doping of nanomaterials*

The doping of the material is a common method used for change of its dielectric constant and improve the charge storage capability of the friction layer [301]. Firdous et al. [354] reported doping of PVDF polymer with Fe_3O_4 and P/Fe_3O_4. In this method, an inward negative center and outward positive hydrogen regions were created as the result of interaction of Fe with fluorides. The permanent alignment of PVDF dipolar regions was achieved. The interfacial charge recombination was reduced, leading to an increase of current output from 0.8 μA to 17.3 μA and surface power density enhancement from 0.26 W/m^2 to 0.6 W/m^2 in the case of TENG composed of four units. Xi et al. [355] presented hydrothermal synthesis of La-doped $BaTiO_3$ ($BaTiO_3$: La) which possessed a higher dielectric constant than the pristine $BaTiO_3$. Furthermore, La-doped $BaTiO_3$ was embedded into poly (vinylidene fluoride-trifluoro-ethylene) (PVDF-TrFE) nanofibers using the electrospinning method. It allowed the construction of a high-performance TENG with a large triboelectric charge density of 87.3 $\mu C/m^2$ and output power density of 2.52 W/m^2 [355]. Lee and co-workers provided a comparative study [356] of influence of ZnO doping with Ga on TENG output. The different devices were constructed from PDMS films and Ga doped or undoped ZnO layers. In the case of 0.93 at% Ga-doped ZnO film the open-circuit voltage and short-circuit current were respectively 16 and 13 times higher than those determined for TENG based on an undoped ZnO film [356]. Similarly, Chen et al. [357] confirmed that Ga doping of ZnO promoted charge transfer in the ZnO/PDMS based TENG, leading to voltage and current enhancement by 13 and 90 times, respectively. Chen et al. [358] reported that doping of n-type ZnO nanorods with Sb allowed to obtaining of p-type semiconductors. Replacing the n-type with p-type ZnO nanorods in ZnO/PDMS based TENG resulted in an increase of output voltage and current by 24 and 5.5 times, respectively.

5.2.2. *Surface functionalization*

A generation of the triboelectric charge during electrification can be significantly enhanced through an introducing the functional groups (e.g. hydroxyl [359,360], carboxyl [360], aminomethoxy [301], trifluoromethyl [361] groups) into the triboelectric surface that are able to gain or lose electrons during contact electrification [301,362]. The functional groups are distinguished in two types: electronegative and positive ones. The electronegative functional groups allow to generate more negative charges, i.e. electrons, whereas positive functional groups are responsible for positive charging through holes generation. A creation of the functional groups can be achieved in many different ways, including UV irradiation [363–365], ion irradiation/injection [366, 367], monolayer self-assembly [368,369], and coating methods [296, 370,371].

An influence of the UV-ozone exposure on performance of PDMS based TENG was investigated in Ref. [363]. It was found that UV-ozone treatment led to creation of oxygen radicals which interacted with methyl groups ($Si–CH_3$). Finally, the silanol groups (Si–OH) were formed at PDMS surface as depicted in Fig. 35a. In result, the changes in surface wettability and output performance of the TENG were observed (Fig. 35b-c). The stability of the short-circuit current response was improved in comparison to this recorded before UV-ozone treatment.

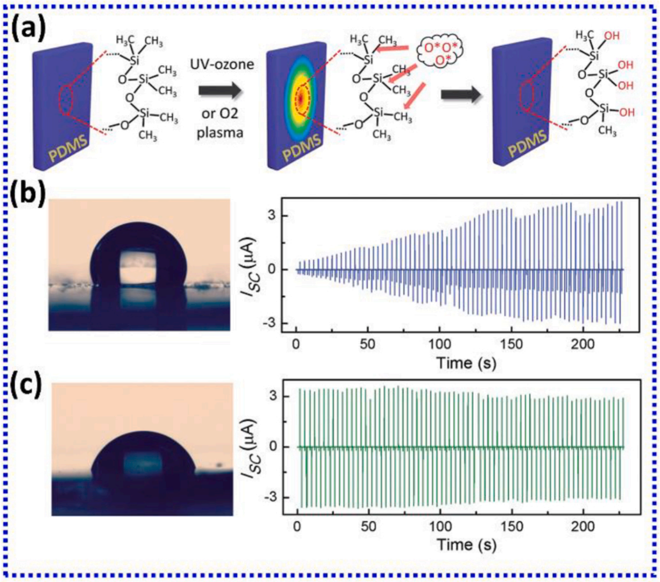

Fig. 35. The UV-ozone processing of PDMS surface toward improvement of the electrical output of the PDMS based TENG. (a) Scheme presenting a modification of the molecular structure of the PDMS surface during UV-ozone treatment leading to formation of Si–OH groups. (b,c) The changes in the wettability of the PDMS film and short-circuit current generated by PDMS based TENG before (b) and after (c) UV-ozone treatment. Reprinted from Fan et al. [363] under the terms of the Creative Commons Attribution 3.0 International License (CC BY 3.0). Copyright (2014) The Royal Society of Chemistry.

Shin and co-workers [364] demonstrated novel method to increase the surface charge density of the photopolymer–ferroelectric nanoparticle composite. It was based on UV treatment and application of electric field. The surface functionalization was achieved by using photopolymer which was able to reconFig. its original chemical structure upon exposure to UV radiation. In result, the output power of TENG device was enhanced approximately four times. The ultraviolet-ozone treatment of the polydimethylsiloxane (PDMS) was reported in Ref. [365]. It was done to boost 15 times the voltage and electric current generated by the PDMS-based TENG. The improvement of the TENG performance was attributed to the modification of non-polar $Si–CH_3$ bonds in PDMS into polar Si–O bonds after exposure of PDMS to UV-ozone.

The low-energy ion irradiation is another method to introduce the functional groups into polymer materials. Li and co-workers irradiated different triboelectric polymer films (Kapton, polyethylene terephthalate (PET), polytetrafluoroethylene (PTFE), fluorinated ethylene propylene (FEP)) using Helium ions with low energy of 50 keV [366]. In the case of He ion irradiated Kapton layer, a high surface charge density of 332 $\mu C/m^2$ was obtained with negligible change of the surface roughness and mechanical performance. The new technique of injecting single-polarity ions into surfaces for an efficient generation of surface charges in contact-mode TENG was proposed in Ref. [367]. In this method, air-ionization gun was used to introduce various negative ions (CO_3^-, NO_3^-, NO_2^-, O_3^-, O_2^-) into fluorinated ethylene propylene (FEP) surface. The surface charge density was modulated by adjusting the number of injection cycles. The maximum power density of reached approximately 315 W/m^2 [367]. It was over 20 times greater than power density of TENG device that was not modified with ion injecting. This effect was confirmed to be stable during five months and 400 thousands of operation cycles.

Wang and co-workers [368] developed a functionalization method of different surfaces (conducting an insulating) using self-assembled monolayers (SAM) of thiols and silanes. The gold surface was modified with self-assembled thiol monolayers. The silica surface was functionalized by applying silane molecule with amine as the head group. In this case, 4 fold increase of TENG output power was achieved. The SAM method was also reported by Song et al. [369] as a facile and efficient technique to boost the performance of TENG. The highly aligned molecular domains over a large area of the PDMS surface were created. The power density of PDMS/Al TENG device was enhanced by over 60 times after SAM functionalization of PDMS surface. Kwon et al. [370] constructed TENG from polyurethane acrylate (PUA) and perfluoropolyether (PFPE). The PUA was chemically functionalized by dip coating with poly(diallyldimethylammonium chloride) (PDDA). Such method led to rise of the output voltage from 430 V to 500 V and electric current density enhancement from 55 μA/cm^2 to 100 μA/cm^2. It corresponded to about 50 % increase of the TENG power density.

5.2.3. Synthesis of nanomaterials with desired surface properties

A novel method of TENG performance improvement was proposed by Potu et al. in Ref. [372]. The zeolitic imidazolate framework (ZIF)-8 particles were synthesized on surface of ZnO nanosheets in order to obtain ZIF-8@ZnO material with more complex morphology comparing to bare ZnO nanosheets. It was crucial for gaining the effective surface contact area of TENG device. It was revealed that ZIF-8@ZnO possessed lower work function (4.12 eV) than value of this parameter determined for pristine ZnO (4.40 eV). It indicated that ZIF-8@ZnO material was more beneficial for use in TENG since it had better tendency to lose electrons during triboelectrification. Therefore, the open-circuit voltage, short-circuit current, and output power density of ZIF-8@ZnO based TENG were respectively 1.39, 1.44, and 1.76 higher than those measured for TENG constructed from bare ZnO [372]. Jeon et al. [373] developed a solution process of ZnO nanoripples preparation. The shape of ZnO nanoripples and surface area of obtained ZnO film was easily adjusted by changing the conditions of the material synthesis. It allowed to optimize the contact area between the triboelectric layers. The open-circuit voltage of TENG constructed from ZnO nanoripples was three times higher than this parameter measured for TENG based on ZnO nanorods [373].

5.2.4. Defect engineering

The defect engineering is novel and interesting approach to modify fundamental physical and chemical properties of triboelectric surface. Zhou et al. [374] developed a method of formation of defects in graphene film via high temperature treatment at different annealing temperatures in the range from 500 °C to 3000 °C. This method allowed to successfully tune work function of graphene film from 4.49 eV up to 4.68 eV due to a change of oxygen concentration and carbon defects in the reduced graphene oxide (rGO). The voltage, current, and power density of rGO based TENG attained 190 V, 14 μA, and 5.04 W/m^2, respectively [374]. A construction of TENG device from perovskite $MAPbI_3$ film was reported in Ref. [375]. The surface of $MAPbI_3$ was processed with phenethyl ammonium iodide (PEAI) in order to create 2D/3D heterojunction and passivate defects existing in the material. An increase of output voltage from 33.3 to 40.1 V and current density from 9.1 to 10.1 mA/m^2 was observed after $MAPbI_3$ film treatment with PEAI.

5.3. Charge boosting methods

Teng working principle is based on triboelectrification, resulting in generation of electric charges. Thus, surface charge density and its maximization is considered one of the most important parameters to optimize during development of TENG. Since the invention of TENG in 2012, notable work has been done to improve their performance based on electric charge generation. Numerous investigations have been performed into ways of measuring and visualizing electric charge on the surface of triboelectric devices [376], and into electrification of particles useable in TENGs in varying conditions [377]. Obtaining energy from TENG is dependent on surface charge density. Therefore, optimization of TENGs in terms concerning electric charges can be divided into improvements in the three aspects: charge generation, charge storage, and charge decay [378,379], which are discussed below.

5.3.1. Charge generation improvement

Charge generation is often the first thing taken into consideration when thinking about increasing output of TENG, for an increase in surface charge density will directly improve achieved power density. Methods of increasing charge generation in triboelectric nanogenerators which can be roughly classified into structural/device layout modifications and materials engineering approaches. It is important to note that different methods need to be considered depending on the type of TENG, as devices intended for wind energy harvesting are going to use different solutions than ones used for recovering energy from human movement.

One of the most popular ways to increase charge generation, charge pumping is an approach using a supporting TENG in addition to the main generator, proven successful both in conventional triboelectric nanogenerators and hybrid systems employing other physical phenomena [380,381]. The charge pumping approach is based on employing additional triboelectric nanogenerator, which supports the main TENG by injecting charges into it. Investigation into wind energy harvesting TENGs charge generation improvement has yielded results such as the fluttering TENG developed by Chung et al. [382]. Device with charge supplying secondary TENG in addition to the main one (both based on flexible fluttering film made from Ni/Cu-plated conductive sheet) achieved power output of 38.16 mW at 6 m/s wind speed. Another device worth noting is charge pumping tubular-plate coupled structure TENG, with a dust clearance system [383], using integrated charge pumping TENG within its structure which can supply up to 103 μA of electrical current, with 184.9 mW of peak power output at 200 RPM. A foldable structure of the device can also provide an increase in performance, as shown in work by Li and coauthors in which a Miura folding structure TENG supplied by a charge excitation TENG achieved output charge of 1.54 μC and 5.17 mW at very low frequencies [384]. Another approach that can be considered a halfway between material and device layout approach, superlubric TENG, with thin liquid film decreasing friction coefficient between PTFE ball and ITO/glass triboelectric elements to extremely low levels, significantly decreasing device wear rate, while the oil is additionally working as a charge bridge, donor and reservoir [385]. Humidity effects for charge generation in TENGs have been investigated for the purpose of employing water molecule self-polarization by Wang et al., with the generator reaching charge density of 2.88 mC/m^2 [386]. Electrode design also plays an important role in TENG charge generation performance, which has been shown especially in water waves energy harvesting TENG examined by Hussain et al. [387], where it was presented that grid of interdigitated electrodes increased power output of TENG 140-fold in comparison to single electrodes approach used as a reference, which authors attribute to charge regeneration effects. Xu and coauthors reported an increase in generated voltage from 241 V to 4750 V by an addition of charge supplement channel into the device layout, in TENG intended for self-powered electroadhesion application [388]. Other considerations that have been tested include the application of pre-excitation boost, in which triboelectric elements of the nanogenerator are subjected to friction in open circuit, resulting in increased voltage and generated power in working mode, as reported by Ref. [389]. Finally, in the case of Liquid-Solid Triboelectric Nanogenerators (LSTENG), the external charge pumping approach was done while investigating Kapton-FEP nanoparticle system with conductive cloth electrodes, achieving power density of 231.8 W/m^2 [390].

Charge generation improvement based on materials approach uses modification of the composition of functional triboelectric layer in TENG, often applying composite materials with synergistic properties to maximize device performance. A common way to improve performance of TENG is to add functional filler into polymer triboelectric layer, examples of this approach being addition of rGO into PVDF matrix [391], introducing relaxor ferroelectric particles into triboelectric membrane

[392] and MXene and TiO_2 addition into MF and FME respectively [393]. High dielectric constant materials like $BaTiO_3$:La also improve the charge generation of TENG, as shown in the work by Xi et al. [355]. Composite materials can also be used in Liquid-Solid contact triboelectric generators, as shown in Ref. [394], where a cylindrical TENG using water as a charge generating medium displays a tenfold increase in charge density when using PCL-PI composite in comparison to neat PCL. As for further progress, a work building upon previously examined approach of using high-polarity materials, Yoon and coauthors describe a way forward based on development of new materials displaying superpolarity [395].

5.3.2. Methods of improving charge storage and transfer

Improving charge storage and their transfer from the triboelectric generator to supplied device is important for the efficiency of all developed TENGs. In terms of charge transfer and storage the device design once again determines viability of the approach.

Charge trapping and charge blocking strategies utilize layers, molecules and structures able to either contain charges to prevent them from dissipating or block them from recombination. Notable approaches to charge blocking used MoS_2 [396], SiO_2@Ag [397] and carbon nanoparticles [398], each achieving significant improvement in overall TENG performance. Cui and coauthors reported that addition of composite PS-CNT layer under negatively charged PVDF in a contact separation mode TENG resulted in 11-fold increase in the triboelectric charge density [399]. Deep charge trap construction by using (N, N-Dimethyl-3-aminopropyl) trimethoxysilane molecule at the interface of two PET molecules has been shown by Wang and coauthors [400]. This approach, with charge traps with higher Fermi levels, allowed for 5-fold increase in current density and 13-fold in power density of TENG. Surface modification of triboelectric layer by addition of air stable radicals has been also reported to improve stability of surface charges in triboelectric devices, Im et al. achieved remarkable charge stability, with TEMPOTES radicals hydrophilic layer retaining electrical charges for 12 h [401]. Hybrid devices also can be improved by incorporating additional layer influencing charge storage, as shown in Ref. [402] by Guo et al. PDMS/MWCNT composite in the PVTENG device served as negatively triboelectrified material and photogenerated hole collector, in tandem with positively charged $CsPbBr_3$ perovskite, reaching power density of 8.24 W/m^2.

Improving charge transfer can be done by providing a preferable transport way for electric charges by modification of the triboelectric layer as well as the electrodes. Lai et al. developed a method using longitudinal paths of electrostatic charges in contacting layers [403], increasing charge density to 168 $\mu C/m^2$, by providing gold ravine-like passageways for the generated charges in the near-surface of triboelectric layer. Wang and coauthors developed a solution using rolling mode MO-TENG (multi-tunnel opposite charge enhancement TENG) (Fig. 36) with grating electrodes for charge transfer acceleration [404]. The said device reached current output of 16 μA and transferred charge of 319.1 nC, a significant increase over comparative flat surface TENG (F-TENG), and standard multi-tunnel TENG (M-TENG), as seen in Fig. 36f.

5.3.3. Counteracting and suppressing charge decay

Charge loss and decay in TENGs occur due to charge drift and air breakdown mechanisms [405]. Charge drift and diffusion can be mitigated using methods described in section 8.3.2, utilizing either modifications of electrode or supporting functional layer addition. Air breakdown is a phenomenon unavoidable during triboelectric nanogenerator operation in air, resulting in TENG discharge and limiting maximum surface charge density [405].

Counteracting the air breakdown is the go-to approach to combat charge decay of triboelectric nanogenerators working in air conditions. The most basic strategy was presented by Cao et al., where the addition of a capacitor to the TENG circuit increased energy density output by a factor of 2.5 [406]. Other approaches include an addition of grounded shielding electrode on the slider's back and a blank tribo area on stationary part in rotating slidi [24], and by using a dual dielectric layer of PVDF and PI in contact separation mode TENG [407]. Charge decay suppression has also been achieved by incorporating ferromagnetic nanoparticles into the triboelectric layer of TENG [408], increasing the charge density by six times thanks to recombination suppression effects. Zheng and coauthors studied the influence of the addition of carbon nanotubes and polystyrene into PVDF triboelectric layer [409]. Their results show that charge decay rate can be manipulated by increasing

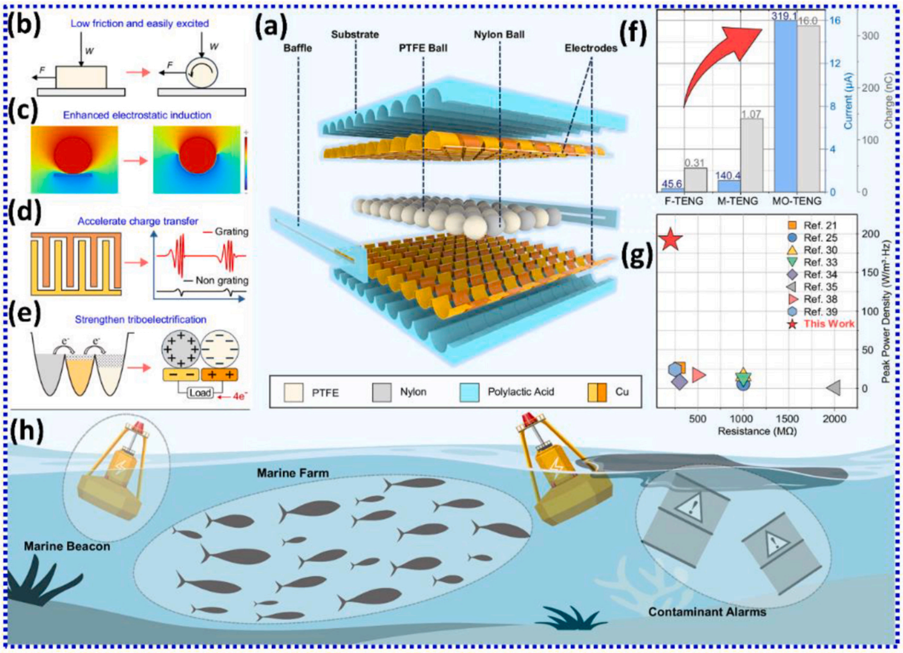

Fig. 36. (a) Structure of the MO-TENG, (b) the rolling mode, (c) tunnel-shaped electrode, (d) grating electrodes, (e) opposite charge enhancement strategies, (f) transferred charge and current generated by the F-TENG, M-TENG and MO-TENG, (g) parameter comparison with other referenced designs [404], and (h) proposed potential application scenarios. Reprinted from Wang et al. [404] under the terms of the Creative Commons Attribution 4.0 International License (CC BY 4.0). Copyright (2024) the Authors, published by Nature Springer.

certain filler amounts, with the findings reporting charge decay rate decrease for CNT, an improvement for TENGs, and charge decay rate increase for PS addition, which can be beneficial for triboelectric sensors. Other approach to combat charge decay has been shown by Xia and Zi [410] who utilized heat excitation to minimize thermoionic emission in sliding freestanding TENG. Increasing temperature of the positively charged triboelectric layer improved the performance of the device by charge promotion resulting from heat-excitation, as shown in Fig. 37.

5.4. Power management methods

Applying triboelectric nanogenerator as an energy source in existing devices necessitates utilization of power management system (PMS). Typical TENG working mode can often be characterized by irregularities or cycles of energy output, while most devices demand constant and stable energy supply. TENG can be modeled in an electrical circuit as an open-circuit voltage source in series with a time-varying capacitor, with its capacitance dependent on separation distance between triboelectric surfaces [411]. Due to varying capacitance, a simple solution of using a full wave rectifier to convert triboelectric nanogenerator's output into DC current is not viable. To answer this problem, several systems were developed, and among them the newer ones can be broadly categorized into two groups, firstly developed active switch PMS, with more recent advancements in passive switch PMS relying on power converter with electronic switches.

5.4.1. Active switches

Mechanical switch and active switching circuits were the first to be developed for TENG power management application. Active switches using MOSFETs can be applied in higher ambient energy conditions, due to their energy demands, thus often may not be a viable option for lower output TENGs. An example of TENG with an active switch with a flyback converter topology developed by Niu et al. [412] and its performance are shown in Fig. 38.

In the schematic shown above, TENG generates AC electric current, which is then rectified by a bridge rectifier, then DC current charges the capacitor C_{temp}. Once C_{temp} reaches impedance match condition the energy is transferred to final storage, C_{temp} is discharged, and cycle begins again. TENG with PMS investigated in Ref. [412] achieved 60% energy conversion efficiency and provided 7.34 W/m^3 of continuous energy from palm tapping. Besides flyback converter, buck converter topology is a common approach for TENG power management systems. Active switch topology using a buck converter has been used by Xi and coauthors [413] with an 85% TENG energy output released from the generator. A breathable, woven TENG using buck converter topology has also been investigated, displaying power output of 16.6 μW at 90 kΩ load resistance during harvesting human biomechanical energy [414]. Xia and coauthors proposed an inductor-free output multiplier topology based on Bennet's doubler for TENG output management, increasing charge output of TENG over 7 times [415].

5.4.2. Passive switches

Passive switch PMS topologies utilize programmable uni junction transistors (PUT), spark-switches and silicon controlled rectifiers (SCR) for triboelectric nanogenerator output control. In the passive power management circuit presented by Qin et al., consisting of an inductor, diode and capacitor, energy generated by TENG is converted to magnetic energy and stored in an inductor, and then converted back into electrical energy and stored in the capacitor [416]. Qin and coauthors' system achieved theoretical energy storage efficiency of 75.8%, with

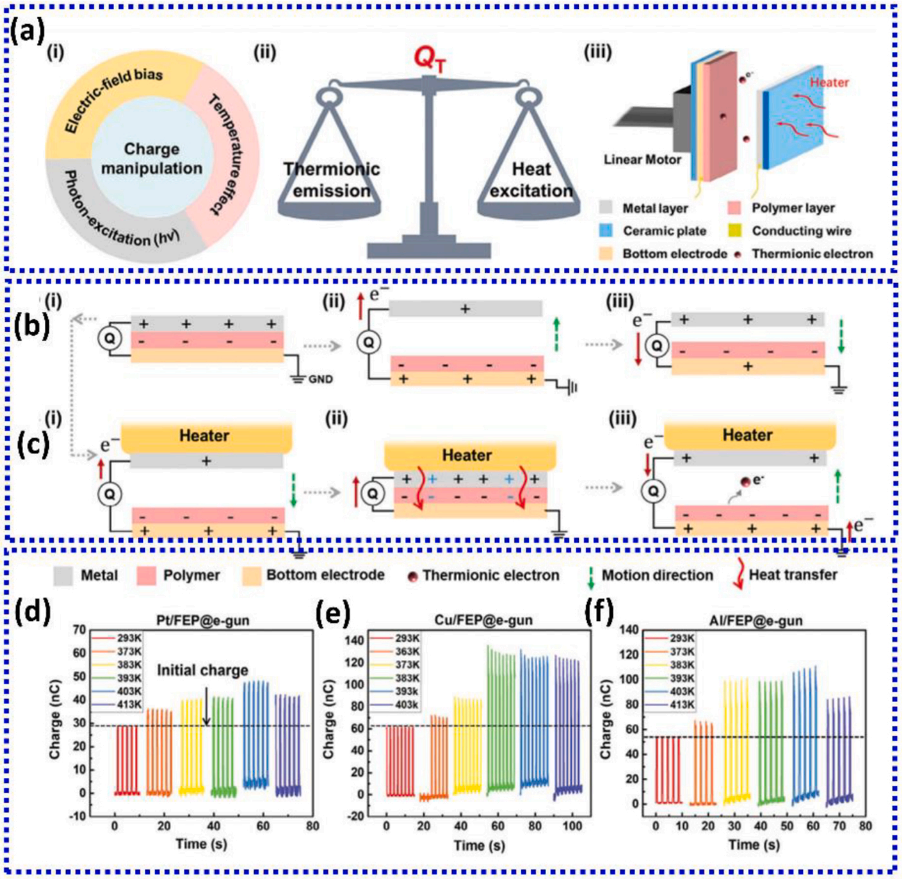

Fig. 37. Heat excitation effect. (a) Schematic of used heat excitation strategy. (b) Charge transfer process without heat excitation. (c) Charge transfer process with heat excitation of the positive side. (d–f) Charge variations in different temperatures for Pt, Cu, Al in contact with FEP. Reprinted from Xia et al. [410] under the terms of the Creative Commons Attribution 4.0 International License (CC BY 4.0). Copyright (2024) the Authors, published by Wiley-VCH GmbH.

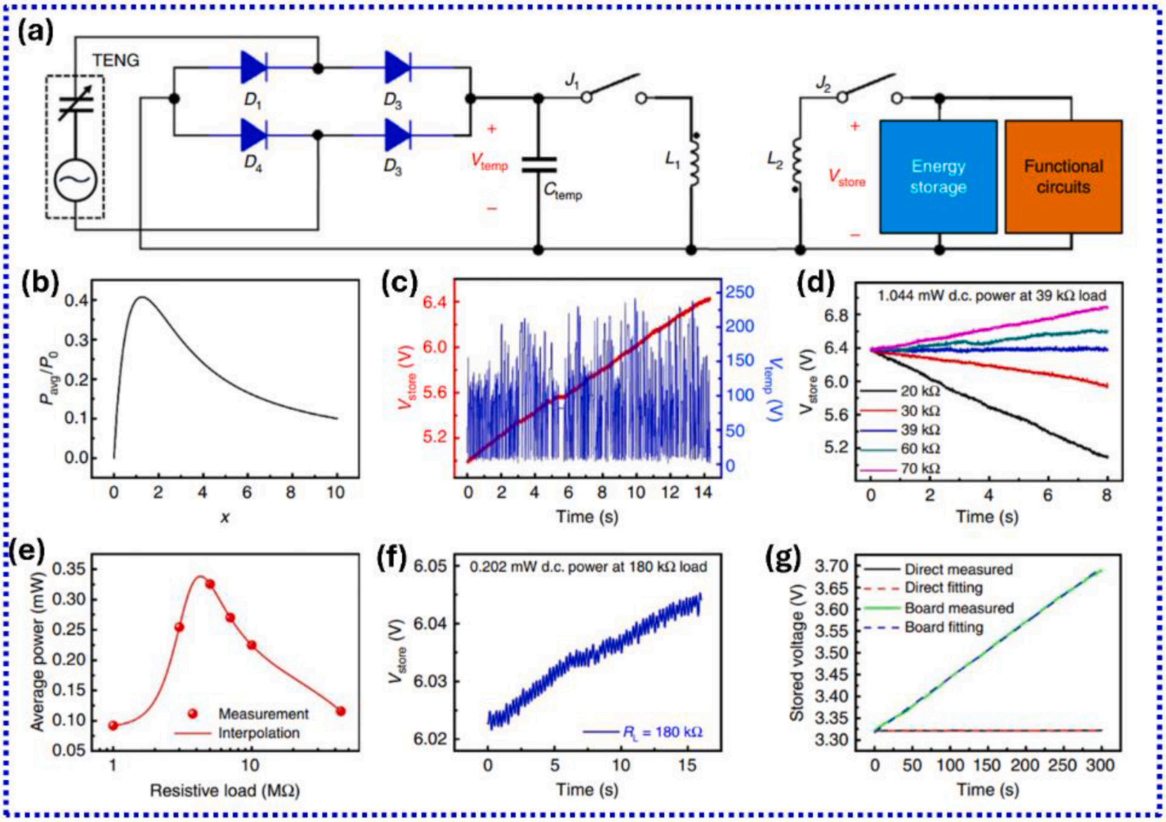

Fig. 38. Schematic and performance of TENG with an active switch topology based on a flyback converter. (a) Circuit diagram of the device. (b) Calculation of the optimized charging time. (c) Board efficiency measurements. (d) Maximum dc power obtained from human biomechanical energy. (e) Measurements of ac-harvested power from a resistor. (f) Total efficiency measurements. (g) Comparison of the charging current between direct charging and board charging. Reprinted from Niu et al. [412] under the terms of the Creative Commons Attribution 4.0 International License (CC BY 4.0). Copyright (2015) Springer Nature.

experimentally measured storage efficiency reaching 48%. The investigated system was able to supply power for an electronic watch and QLED. A simple version of PMS using passive switches has been made by Kawaguchi and coauthors, using PUT [417], achieving energy transfer efficiency of 89%. TENG operation loads capacitor C with voltage across it increasing up to 4 V, then the PUT turns on and transfers energy to resistor R_L, turning off again after C voltage falls to 0.5 V. Harmon et al. presented a fully self-powered PMS for triboelectric nanogenerator, with a passive switch topology using SCR and Zener diodes [418] with the PMS of sub 5 cm in size. The TENG supported by the PMS has reached output power of 251.9 μW from finger tapping with 3.3 Hz frequency, under 2 MΩ load.

6. TENG device structures

6.1. Advanced structural engineering of the TENGs

To improve the generation and collection of triboelectric charges as well as to reduce intrinsic charge loss during operation, inclusive structural designs and engineering approaches of TENGs—such as interlayer addition, instantaneous-discharge design, direct current design, flexible electrode design, and durable device design—are employed to alter the material properties of triboelectric layers and modify the behavior of charges. This ultimately leads to improved TENG outputs and stability compared to conventional designs.

6.2. Interlayer addition

One efficient approach to improving TENG's output performance is to introduce a functional interlayer, *i.e.*, charge trapping, to support the charge-generating and charge-collecting layers with a connection to a charge storage unit (Fig. 39a) [419]. This can effectively lower the charge dissipation of the triboelectric material and increase its charge storage capacity, which are critical points for TENG development. Various studies [332,399,420–422] have demonstrated the progress of boosting device performance using this strategy. For the initial work, as shown in Fig. 39b, Cui et al. [399] showed that adding polymeric layers containing aromatic rings in their chains, such as polystyrene (PS), could enhance charge generating ability (about 7-fold enhancement) due to the abundance of electron trap states of PS. They also embedded a charge transport layer, constructed with a conductive phase, between the frictional and dielectric layers. The results revealed an extended storage depth, which could further implement the high number of triboelectric charges. There could also be a substantial amount of electron traps from PS, which would prolong the electron retention duration in the triboelectric layer from 22 min to 44 h. A series of dielectric interlayers has expanded to polyvinylidene fluoride (PVDF), Nylon 6, polydimethylsiloxane (PDMS), polyoxymethylene (POM), Ecoflex, polytetrafluoroethylene (PTFE), polyethylene (PE), polyamide (PA), polypropylene (PP), and polyimide (PI) [332,420]. Kim et al. [332] found an excellent charge trap density in the stretchable PDMS layer, which could maximize and enhance the decay time of surface potential for the PVDF-based TENG. With the optimum conditions (2 μm and 46.4 μm, respectively, for PVDF and PDMS thicknesses), a 262 μA of current was achieved, which was a 17.5-fold increase when compared with the TENG using a single-layer PVDF (Fig. 39c). The same concept has been demonstrated by Lv et al., [420] using an PI interlayer underneath the frictional triboelectric material (Fig. 39d). With a great charge storage depth of PI, the fabric TENG could produce a transferred charge density of about 180 nC. In addition, Menge et al. [421] designed a highly

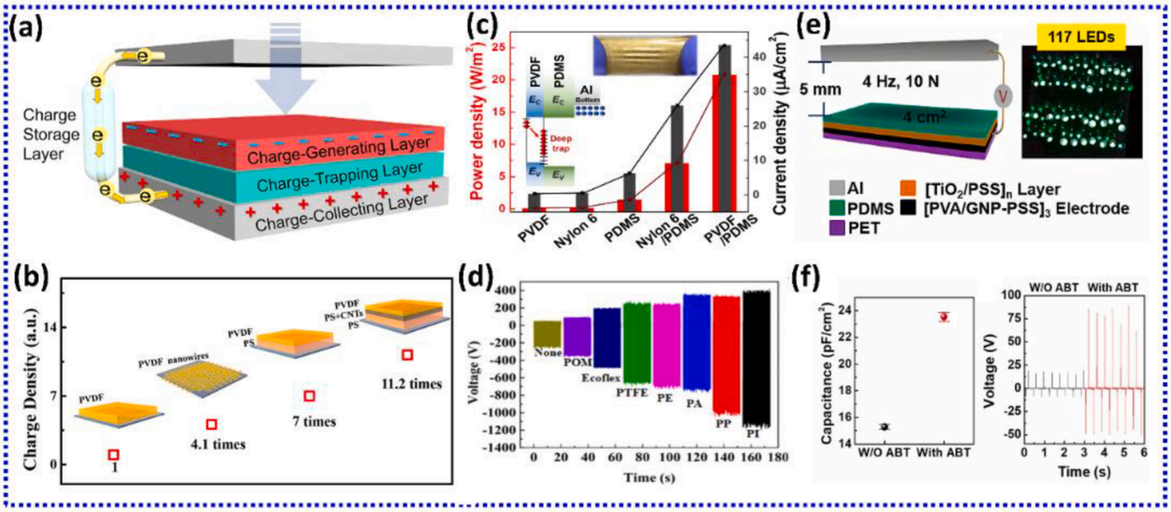

Fig. 39. Strategy to enhance the performance of TENG by embedding interlayers. (a) Conceptional design of efficient TENG including the charge-generating, charge-trapping, and charge-collecting layers. Reproduced with permission [419]. Copyright 2020, Springer Nature. (b) Enhanced charge density with different sublayers. Reproduced with permission [399]. Copyright 2016, American Chemical Society. (c) Comparative study of the output power and types of sublayers. Reproduced with permission [332]. Copyright 2018, Elsevier. (d) Transfer charges of TENGs with different dielectric sublayers. Reproduced with permission [420]. Copyright 2021, American Chemical Society. (e) LEDs driven by TENG based on a functional polymer nanocomposite interlayer. Reproduced with permission [421]. Copyright 2022, Elsevier. (f) Capacitance and output voltage of an interfacial-engineered TENG. Reproduced with permission [422]. Copyright 2022, Elsevier.

flexible TENG using bilayers of TiO_2/poly(4-styrene-sulfonic acid) (PSS) dielectric, and poly(vinyl alcohol) (PVA)/graphene nanoplatelet (GNP)-PSS electrode. As depicted in Fig. 39e, This TENG delivered the output voltage and current of approximately 3.8 and 5.7 times, respectively, higher than the device without sublayer addition, and could light up 117 LEDs. Another work from Kim et al. [422] presented an interfacial molecular layer to control the properties of a triboelectric layer (Fig. 39f). The findings revealed the use of a self-assembled aminothiophenol (ABT) monolayer as a barrier between the PDMS and electrode for improving the TENG output. Through the enhanced electrostatic induction and charge trap states, the triboelectric performance improved by a factor of 2.5.

These investigations demonstrate the key concept to effectively improve the triboelectric output by extending the depth of triboelectric charge storage, augmenting produced charges, and strengthening electron retention, which could be easily achieved by incorporating sublayers between the frictional and electrode layers. However, the challenge with interlayers in TENGs is that interlayer characteristics must be consistently controlled. This problem has been solved by using polymeric modifiers and self-assembled monolayers to enhance the triboelectric performance [422]. It is also important to balance output performance and durability when using interlayers in TENGs because, although thinner films with higher dielectric constants produce better output, they are not durable enough for real-world uses [423].

6.3. *Instantaneous-discharged design*

An abrupt electrical discharge, known as a spark discharge, happens when an electrically conductive channel is formed through a typically insulating material, such as air or other gases, by an ionized electric field that is sufficiently strong [424]. To create a spark discharge, generally, a high-voltage power supply is required. TENG can serve a very high output voltage with its simple structure and low cost of fabrication, leading to various applications in the high-voltage field [425], such as fluid and particle manipulators [426], electrospinning source [427], plasma excitation device [428], electrostatic air cleaner [429], and water splitter [430]. This section aims to summarize and discuss TENG designs based on instantaneous discharging, which is critical for nanogenerator development. The structures can be divided into two configurations: solid-solid (SS) and liquid-solid (LS) interfaces.

For the SS interface, there are many works demonstrating the TENG designs to achieve a high output power [431]. Cheng et al. [431] proposed the strategy to hugely improve the instantaneous output current of the TENG using a triggered switch design for instantaneous discharging (Fig. 40a). The instantaneous output current and power peak of a vertical contact-separation mode TENG reached up to 0.53 A and 142 W, respectively, when performing at a 500 Ω load. It's still challenging to design a switch without using an external trigger. As depicted in Fig. 40b, Cheng et al. [432] developed a self-powered air discharge switch using a controlled tip-electrode. They found that the switch changes from the arc discharge mode to the corona discharge mode as the distance between the two discharge electrodes increases. Given that the switch operated in an arc discharge mode, the instantaneous output power peak and total output energy were raised by 1600 and 31 times, respectively, in comparison to the similar TENG without a switch. The concept of the tip-discharging process was further developed to enhance the performance of nanogenerator. Kim et al. [433] demonstrated that the engineering of the tip electrode of the TENG could efficiently improve the power-generating performance. The microstructurally-serrated electrode produced a unique spark discharge intensity, resulting in numerous boosts to the output (Fig. 40c). Ultrahigh output voltage reached approximately 5 kV with a current density of 2 A/m^2. Moreover, a TENG with an ultrahigh instantaneous power density (more than 10 MW/m^2 at 1 Hz) was created by utilizing the opposite-charge enhancement effect and a transistor-like device architecture. As shown in Fig. 40d, concurrently, the transistor-like structure's design provides an output impedance that is nearly zero, which makes it potential for the amplified charges to be effectively released through the external load [434]. Recently, advancements in charge pumping technology have successfully overcome the limitation of increasing charge density. Yang et al. [381] therefore utilized the decoupled charge pump and discharge tube to maximize charge generation for the TENG. For the structural design (Fig. 40e), the main TENG is operated via a contact-separation mode, while the pump TENG is operated differently in a freestanding mode. With the addition of the discharge tube, the output current was boosted more than 1000 times (reaching 70 mA) with a calculated power density of 21.3 W/m^2.

The droplet-based electricity generation, which relies on a special interface between liquid and solid, has received considerable interest due to its ability to generate higher instantaneous electric power density

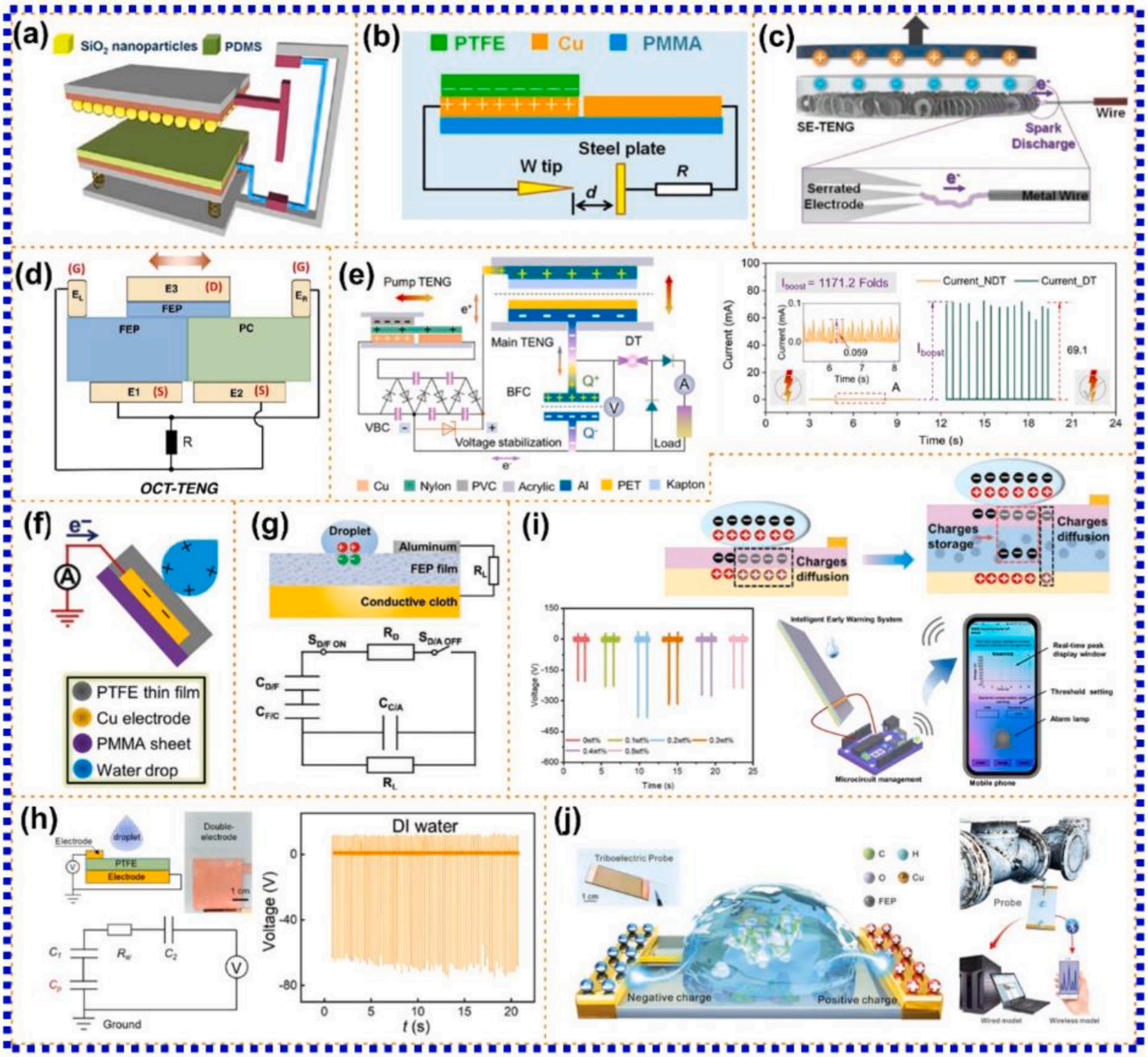

Fig. 40. Strategies to enhance the performance of TENG by instantaneous discharging with SS and LS interfaces. (a) Conceptional design of the instantaneous discharging TENG. Reproduced with permission [431]. Copyright 2013, American Chemical Society. (b) Device structure of the controlled tip-electrode air--discharging TENG. Reproduced with permission [432]. Copyright 2018, Elsevier. (c) Mechanism that causes spark discharge in the space between the metal wire and the serrated electrode. Reproduced with permission [433]. Copyright 2020, Wiley-VCH. (d) Schematic illustration of the opposite-charge-enhanced transistor-like triboelectric nanogenerator (OCT-TENG). Reproduced with permission [434]. Copyright 2020, Nature. (e) Working process and electrical output of the TENG utilized the decoupled charge pump and discharge tube for performance enhancement. Reproduced with permission [381]. Copyright 2022, Elsevier. (f) Structure of the basic TENG based on the LS interface. Reproduced with permission [435]. Copyright 2014, Wiley-VCH. (g) Schematic illustrations of the device structure and equivalent circuit model when the droplet is contacting on the FEP. Reproduced with permission [436]. Copyright 2021, Wiley-VCH. (h) Schematic diagram, equivalent circuit, and output voltage of the double-electrode DEG. Reproduced with permission [437]. Copyright 2022, Elsevier. (i) Mechanism, output, and feasibility for bacterial DNA sensing of the HP-DEG. Reproduced with permission [438]. Copyright 2024, Royal Society of Chemistry. (j) Triboelectric probe for sucrose detection and application. Reproduced with permission [439]. Copyright 2023, Wiley-VCH.

using a simple configuration [436,437,440]. By substituting liquid contacting material for one of the solid fraction layers, the SS contact can be changed to the LS interface. The fluidity of liquid creates a more effective contact area, which could lead to higher electrical output and the possibility of working in multimode [441,442]. Generally, the water droplet or the flow of water is compelling to move along the polymeric film. The water droplet will attract counterions from the negatively charged polymer film once it makes contact with it, creating an EDLand a positive electric potential differential. The mechanism is a key to producing numerous outputs through the accumulation of charges and instantly discharging them upon contact with the electrode [436]. For the initial work, Lin et al. [435] demonstrated the potential of harvesting water droplets using a single-electrode TENG by a sequential contact-electrification and electrostatic-induction process (Fig. 40f). With the continuous impingement of the droplet onto the polymer, interestingly, the generated outputs could reach a DC formation of about 9.3 V and 17 μA for voltage and current, respectively. To produce more electricity, a single-electrode mode is changed to a double-electrode configuration. Zhang et al. [436] constructed the electric-double-layer capacitor to solve the bottleneck of increasing the performance of the droplet electricity generator (DEG). As shown in Fig. 40g, the key structure of the double-electrode DEG consists of the polymeric film sandwiched between two electrodes. The equivalent circuit model is developed to explain the charge generation mechanism along the droplet motion of the DEG, which mainly comprises the equivalent resistance of the droplet, and three equivalent capacitances related to each interface: droplet-polymer, droplet-top electrode, and polymer-bottom electrode. For the engineered structure of the DEG, a single droplet could produce an output voltage over 100 V without pre-charging. For more investigation of the DEG's design, Li et al. [437] showed that different configurations and relevant parameters of the DEGs were highly influenced on the electricity generation. They also proved that the best design of the DEG should be the double-electrode configuration, as depicted in Fig. 40h. To boost more the performance of the DEG, Zhou et al. [438] suggested the technique of incorporating an intermediate layer composite, which has high dielectric and entropy properties, between the bottom electrode and the main frictional polymer (Fig. 40i). This concept is rather similar to the previously reported multilayer TENG [339,399]. Through the utilization, the polydimethylsiloxane doped high-entropy oxide materials for the DEG (HP-DEG) achieved the output voltage and current of approximately 420 V and 0.23 mA, respectively. Moreover, this work practically developed a novel sensing device for bacterial DNA detection with high sensitivity. The LS interface can also be utilized for real-time substance monitoring. As shown in Fig. 40j, Liu et al. [439] developed a triboelectric probe to detect sucrose as an issue for electrochemical reactions in industry. They reported that the fabricated probe has excellent linearity (0.966) and sensitivity ($-0.0038\%^{-1}$) for monitoring the sucrose concentration. Triboelectric probes are also employed as wireless smart nodes that provide real-time sucrose solution monitoring.

6.4. Direct current generator design

Our society is currently undergoing a significant technological trend with the exponential expansion of mobile electronic devices and sensor networks that are becoming ubiquitous and significantly enhancing the quality of life. To maintain sustained operation, most types of electronic equipment typically need a steady current input. The primary modern energy source for those electronics is batteries. But because of their limited lifespan, batteries require regular maintenance, prompt charging or replacement, high labor and material expenses, and environmental contamination.

As a result, the DC TENG has been developed to address the

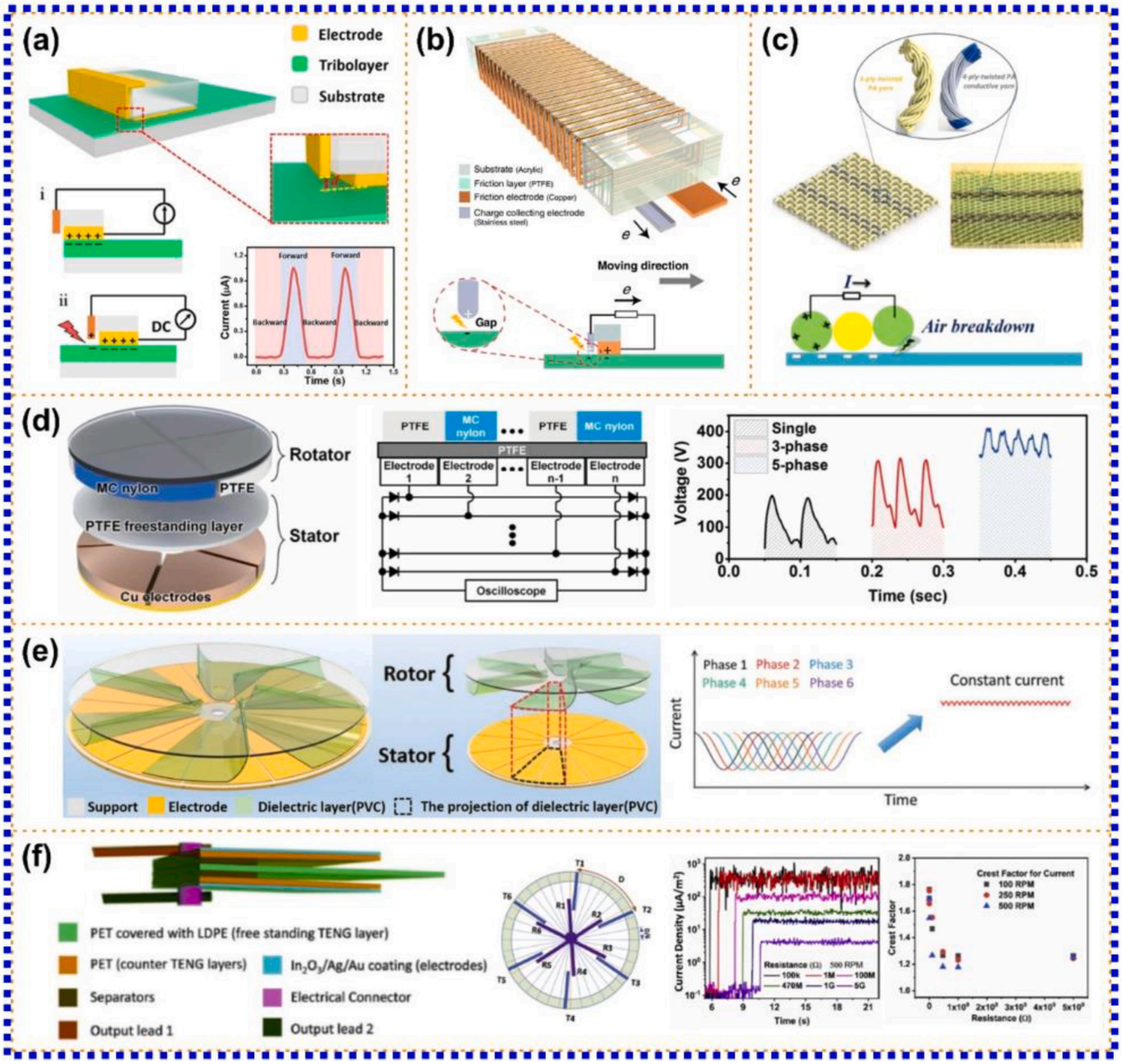

Fig. 41. Strategies to enhance the performance of TENG by dielectric breakdown and phase coupling. (a) Structure of the TENG operated in sliding mode based on the pair of copper and PTFE. Reproduced with permission [447]. Copyright 2019, American Association for the Advancement of Science. (b) Schematic illustration of the MDC-TENG. High electrical output was produced by an air breakdown. Reproduced with permission [448]. Copyright 2020, Springer Nature. (c) Design of the DC TENG based on the fabric and its working mechanism. Reproduced with permission [449]. Copyright 2020, American Chemical Society. (d) Structural design of the multi-phase TENG with an equivalent circuit. Reproduced with permission [450]. Copyright 2018, Royal Society of Chemistry. (e) Structure and output current of a rational phase-shift design-based CV TENG. Reproduced with permission [451]. Copyright 2022, Royal Society of Chemistry. (f) Schematic of the structure of the cantilever-based DC TENG with multiphase coupling. Reproduced with permission [452]. Copyright 2020, Elsevier.

limitation of AC type [254,443]. Even though DC TENG has evolved significantly [444,445], there are still issues to be resolved in order to simultaneously achieve high output and high stability. Various efficient approaches, *e.g.*, dielectric breakdown, phase coupling, and operation via a tribovoltaic effect, have been demonstrated to produce the DC signal. For the dielectric breakdown method, historically, the insulator-based DC TENG has been firstly proposed by Yang et al. [446] in 2014, using a sliding electrification with fluorinated ethylene propylene (FEP) as a main frictional layer. However, this work requires a complicated structure to gain the high electrical output. Liu et al. [447] presented a DC TENG with a simple contact-sliding structure by designing the coupling effect between the triboelectrification and electrostatic breakdown (Fig. 41a). The utilization of a small gap creates a very strong electric field between the collecting electrode and the negatively charged PTFE surface. The surrounding air may partially ionize and start conducting if it surpasses the dielectric strength of the air between them, which is determined by Paschen's law to be around 3 kV/mm [447]. The cyclic motion of PTFE and copper could produce a stable DC output with a charge density of 430 $\mu C/m^2$. This is much higher than a conventional TENG that does not use dielectric breakdown. In a similar concept, Zhao et al. [448] proposed the rationally patterned structure design of the TENG to significantly boost the surface charge density. The engineered structure contained the parallel connection of multiple outputs, which became the key role for achieving an ultrahigh charge density of 5.4 mC/m^2 (Fig. 41b). One can also utilize the concept of a dielectric breakdown into the textile-based TENG for biomedical monitoring. Chen et al. [449] designed the flexible DC fabric TENG using a pair of polyamide yarns (electrostatic breakdown and frictional yarns) and PTFE. The highlighted configuration could efficiently generate output signals of higher than 4.5 kV and 40 μA per motion cycle (Fig. 41c). Furthermore, there is an interesting structure that can directly produce the DC signal via phase shift design. In 2018, Ryu et al. [450] introduced a multi-phase-rotation-type TENG, which was able to overcome the limitations of low output and short duration of signal pulse. As shown in Fig. 41d, the TENG consists of multiple electrodes as a stator and mono-cast nylon/PTFE as a rotor. During operation, unlike conventional TENGs, the total output of the proposed TENG is nearly maintained DC signals (about 380 V and 3.6 mA/m^2), with rectified full wave and superimposed electrode outputs. To boost the output performance, Li et al. [451] presented a highly efficient DC TENG based on a complex phase-shift design (Fig. 41e). This device showed a low crest factor of 1.03 and served electrical outputs over 1200 V and 0.2 mA for output voltage and current, respectively. Through theoretical guidance in a dynamic process, the work also revealed the route to remarkably improve the energy-output efficiency of the proposed TENG. Furthermore, research attempted to use a phase-shift design in a cantilever-based generator to improve performance. Dharmasena et al. [452] designed a built-in phase shifting of multiple poles for the DC TENG. The presented poles in the TENG's structure were constructed in the formation of a cantilever (Fig. 41f). The contact-separation process of TENG between low density polyethylene-coated polyethylene terephthalate (PET) and pristine PET provided a nearly constant DC signal with the phase coupling.

To date, a tribovoltaic effect has attracted attention as a promising device for mechanical to DC electricity conversion [453]. For this phenomenon, the excited charges are produced in a certain direction via the junction-field effect, obeying the dynamic Schottky and p-n junctions in sliding motion [453–455]. Here are some examples of the literature that utilized the tribovoltaic effect in the TENG to produce DC electricity. Šutka et al. [456] demonstrated the influence of Schottky junction enabled by high-energy electrons during continuous sliding for producing a constant current. As shown in Fig. 42a, the sliding of WO_3 tip onto a tungsten plate generated a current density up to 1270 A/m^2 under 0.3 N and 0.7 cm/s of force and velocity, respectively. For investigating insight, Xu et al. [457] studied the relationship between interfacial properties and related outputs for the tribovoltaic nanogenerator (TVNG) (Fig. 42b). They found that the performance of the TVNG was consistent with the contact area (from the tailor of substrate types), force, and the surface state of the semiconductor. The TVNG, based on the Schottky junction, demonstrates the feasibility of scavenging multiple energies at the same time. Zhang et al. [458] demonstrated that the coupling between tribo-thermoelectric and tribovoltaic effects could boost the performance of the nanogenerator (Fig. 42c). A combination of frictional energy from the motion and heat formed at the junction served the DC signal, which contained two components: the stable and fluctuant parts. Faster velocities create a larger temperature gradient, resulting in a higher output. Generally, the electricity produced from a Schottky junction provides a large current with a low output voltage [453]. To gain more voltage, the TVNG requires to operate via a p-n junction. Xu et al. [459] initially presented a simple tribovoltaic effect by sliding p-Si onto n-Si. As illustrated in Fig. 42d–a direct current flows from the p-type to the n-type semiconductor in the direction of the internal electric field in the dynamic p-n homojunction. The increased performance depended on the sliding speed and acceleration, while the direction of sliding was contrary. In 2022, Wang et al. [460] developed a semiconductor DC TENG, which could generate an ultrahigh DC voltage up to 130 V (Fig. 42e). The role of heterojunction (using gallium nitride/silicon) yielded nearly 46 times enhancement of a peak power density, when compared with a traditional TVNG. The work is expected to be a high DC power supply, which can efficiently scavenge the environmental fictional energy. Similar to the previous mention, the TVNG is able to coupling with other energies for boosting more performance and constructing for multi-energy sources [455,461–463]. In the case of a p-n heterojunction, Ren et al. [463] investigated the coupling effect between tribovoltaic and photovoltaic effects for the TVNG based on sliding p-Si on the n-GaN wafer (Fig. 42f). The non-linear characteristic curves well confirmed the existence of a p-n junction. The bias under UV light resulted in a significant increase in output current, more than 13 times higher than those in the dark. Another clarification in the synergetic effect.

for the TVNG was realized by Worathat et al., [461] as shown in Fig. 42g. They studied the influence of the thermal-induced output of the nanogenerator based on the rubbing between n-Ag_2Se and aluminum and found the enhancement of performance during continuous sliding. The equivalent circuit was rather similar to a conventional semiconductor device, *e.g.*, solar cell, but the difference was the additional energy source from frictional energy. Operating through the tribovoltaic effect is also achieved in piezoelectric material. Sriphan et al. [462] demonstrated for the first time that a piezoelectric ceramic had a potential for the tribovoltaic material (Fig. 42h). By sliding metal onto a lead zirconate titanate ceramic, a DC output was produced. The synergistic effect of piezoelectric and tribovoltaic effects produced electron-hole pairs simultaneously during sliding. The proposed electronic band diagram, which elucidates the charge-generating mechanism of the harvester, is associated with the electrical performance outcome.

6.5. *Flexible electrode design*

In order to harvest mechanical energy in a variety of applications such as from soft biological energy from human, it is desirable to develop and implement flexible and stretchable TENGs [254,292,464,465]. Generally, the rigid materials are widely adopted in the current TENG device, which severely limits the application potential for corresponding devices in flexible and portable technologies. These problems could possibly be solved by mechanically flexible or stretchable electrodes by, *e.g.*, designing deformable structures [466–468], and using intrinsically soft materials [469,470]. Leng et al. [467] designed a highly flexible interdigital-electrodes-based TENG for scavenging the surrounding sliding and rotating energies (Fig. 43a). The proposed device showed various advantages, including light weight, high stretchability, multifunction of uses, and high output performance. Operating

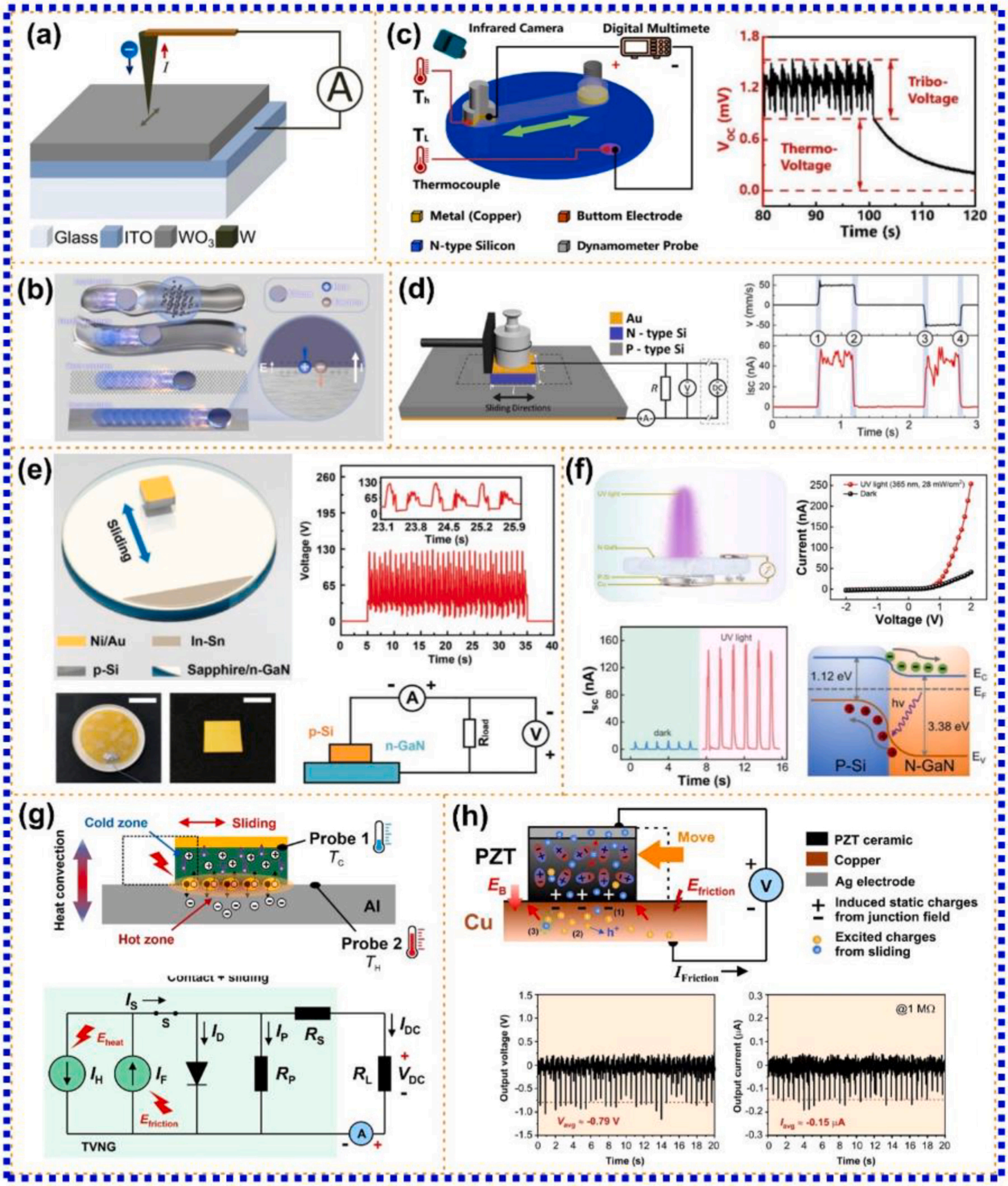

Fig. 42. Strategy to enhance the performance of TENG by tribovoltaic effect. (a) Simple sliding of the metal tip and WO_3 for the generation of a DC signal. Reproduced with permission [456]. Copyright 2021, American Chemical Society. (b) 3D structure of a DC TVNG in different substrates. Reproduced with permission [457]. Copyright 2022, Elsevier. (c) Role of the coupling effect between thermoelectric and tribovoltaic for boosting the nanogenerator performance. Reproduced with permission [458]. Copyright 2022, Elsevier. (d) 3D schematic of the experimental setup for the TVNG operated through a p-n junction. Reproduced with permission [459]. Copyright 2019, Elsevier. (e) Structure of the TVNG based on the sliding between n-GaN and p-Si. Reproduced with permission [460]. Copyright 2022, Royal Society of Chemistry. (f) Light-assisted DC TENG based on the tribovoltaic effect. Reproduced with permission [463]. Copyright 2021, American Chemical Society. (g) The TVNG based on the dynamic Schottky contact of Al/Ag_2Se. Reproduced with permission [461]. Copyright 2024, Elsevier. (h) Schematic diagram of the working mechanism of the TVNG operated in sliding state of PZT/Cu interface. Reproduced with permission [462]. Copyright 2024, Elsevier.

in sliding mode, this TENG served the peak current and power density up to 400 μA and 13 W/m^2, respectively. Guo et al. [466] presented a flexible single-electrode TENG based on a graphene oxide (GO) film, as shown in Fig. 43b. With an applied pressure of 125 kPa, the proposed TENG efficiently responded to the bare palm, achieving a short circuit current of over 56 μA. Due to the excellent inhibition property of GO, the TENG also showed a powerful sterilizing effect. Fig. 43c depicts the transparent and stretchable TENG designed for tactile sensors. Charoonsuk et al. [465] developed the abundant polyethylene plastic using a liquid phase electrolyte (LTE) as charge generating and electrode layers. Various types of LTEs, *e.g.*, acids, salts, and solvents, exhibited different output signals depending on liquid concentration. The presented film provided the optimal response of approximately 1.6 V, which could be applied wirelessly in tactile sensing systems. Self-powered wearable

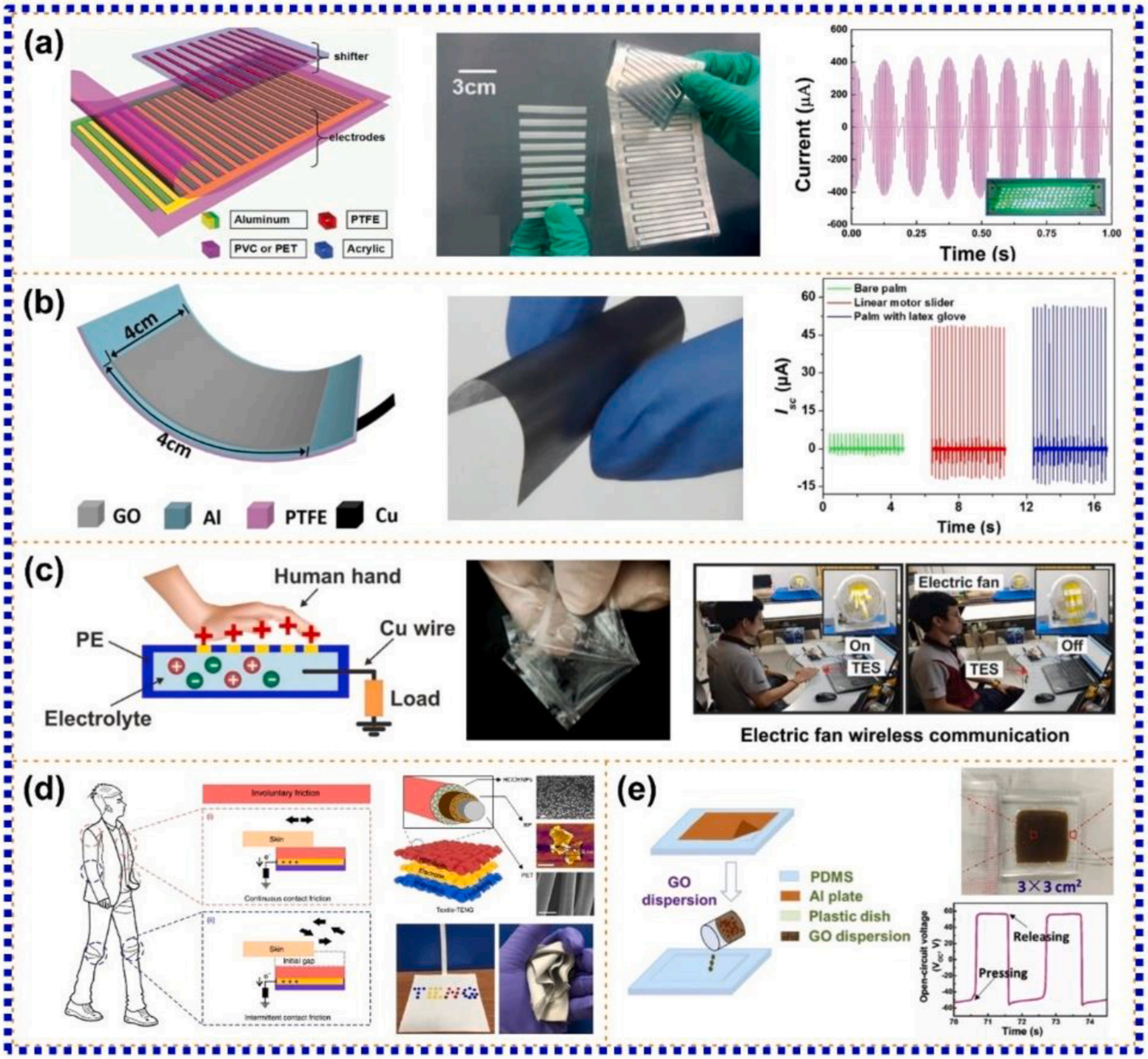

Fig. 43. Strategies to promote the TENGs for specific applications by flexible electrode design. (a) Flexible interdigital-electrodes-based TENG designed for sliding mode. Reproduced with permission [467]. Copyright 2014, Royal Society of Chemistry. (b) GO-enhanced flexible single-electrode TENG. Reproduced with permission [466]. Copyright 2017, American Chemical Society. (c) Transparent TENG based on liquid electrolyte for tactile sensor. Reproduced with permission [465]. Copyright 2021, Elsevier. (d) Feasibility of utilizing the fabric-based TENG for human motion sensing. Reproduced with permission [470]. Copyright 2018, Nature. (e) Flexible graphene oxide dispersion-based liquid single-electrode TENG. Reproduced with permission [469]. Copyright 2019, Elsevier.

electronics are interested in textiles that can capture biomechanical energy through the triboelectric effect. Xiong et al. [470] proposed the washable and durable textile-based TENG (Fig. 43d). The black phosphorus and hydrophobic cellulose oleoyl ester nanoparticles were encapsulated in the PET fabric as a main contacting layer. The Ag flake/PDMS-coated fabric was additionally designed for the flexible electrode. Interestingly, the advanced textile generator showed excellent water repellency and stability upon washing and served high peak-to-peak electrical outputs (approximately 880 V and 1.1. μA/cm^2). Liquid electrode is also utilized for the TENG in shape-adaptive electronics due to various advantages, for instance, high mobility of electron and high flexibility. Wu et al. [469] presented a conductive liquid, *i.e.*, GO, with super conformability as the electrode for the single-electrode TENG (see Fig. 43e). Even though a small amount of GO (10 mg/mL) was dispersed into the PDMS, the high output performance (123.1 V, 18.61 mA/m^2 and 1.99 mW), and high bio-sensitivity were achieved.

6.6. Durable device design

The lifetime of TENGs is hindered when employed in real applications since they primarily depend on friction to create surface charge on triboelectric materials. There are techniques to extend TENGs' restricted lifespan, for example, designing TENG in non-contact mode [471], utilizing lubrication [342,472], coating with a low-friction material [473], using a soft contact material [474], and advanced material selection [475]. The simplest way to extend the triboelectric material's frictional wear lifespan is to design the device in non-contact mode. Han et al. [471] demonstrated that the careful control gap distances (0.5 mm–2 mm) without making the contact could provide the electricity (Fig. 44a). The device performance was improved by using a giant dielectric ($CaCu_3Ti_4O_{12}$, CCTO) as a triboelectric material. From the perspective of mechanics, the use of lubricant reduces the frictional force between two surfaces in contact, resulting in less damage during operation [476]. From an electrical viewpoint, the lubricating liquid completely envelops the surface of triboelectric materials. This can obstruct escaped electrons due to higher breakdown strength [477]. Wu et al. [342] utilized the prominent points of lubrication for boosting the TENG performance. As depicted in Fig. 44b, adding liquid lubrication during sliding could form the sublayer inside the nanogap between two materials, and provide a super wear-resistive device. The

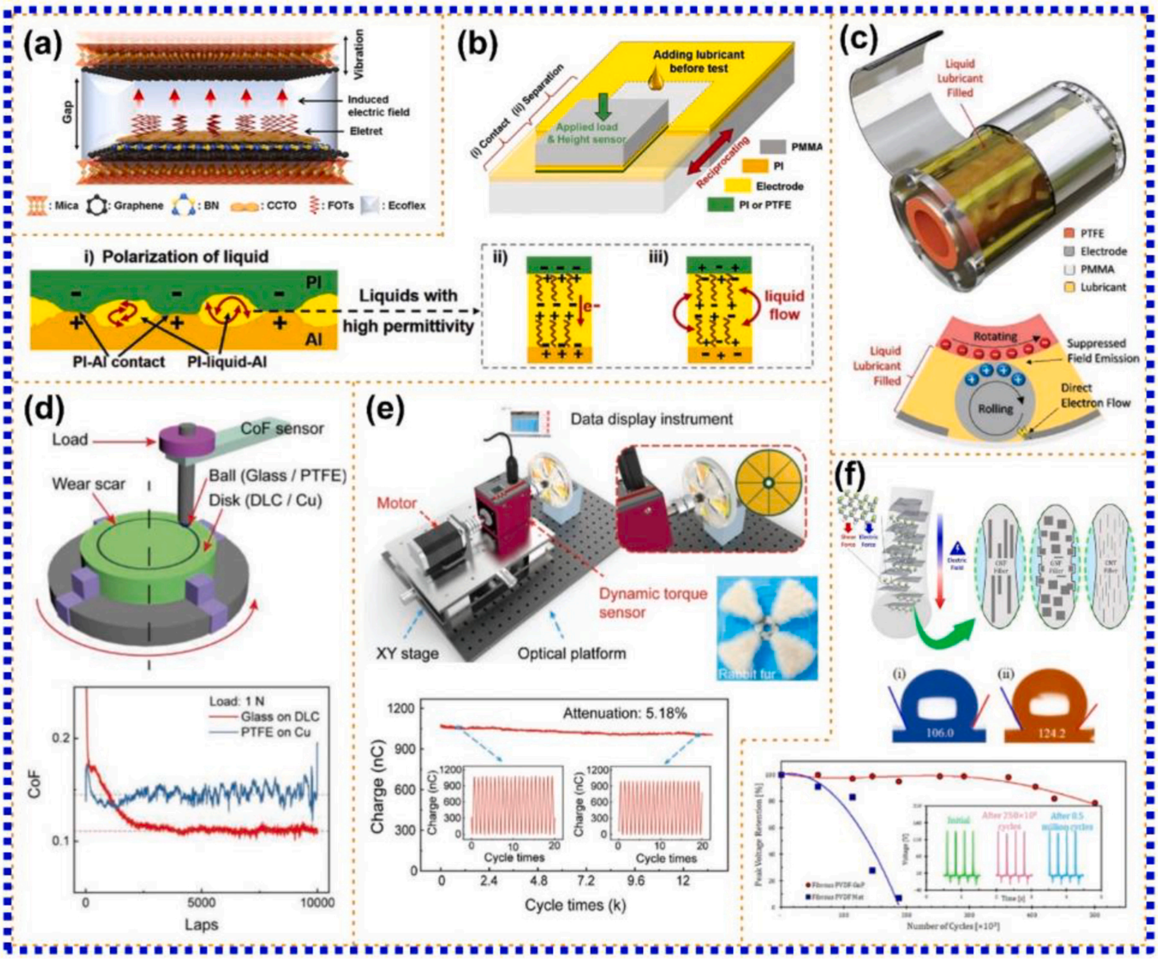

Fig. 44. Strategic designs to enhance the durability of TENGs. (a) Non-contact mode TENG based on a giant dielectric material. Reproduced with permission [471]. Copyright 2021, American Chemical Society. (b) Liquid-lubricated TENG operated in a simple sliding mode. Reproduced with permission [342]. Copyright 2020, Elsevier. (c) Liquid lubricant submerged TENG and direct electron flow. Reproduced with permission [472]. Copyright 2021, Wiley-VCH. (d) DLC-glass-based TENG with low-friction and high hardness. Reproduced with permission [473]. Copyright 2024, Wiley-VCH. (e) Soft fur-brush TENG for surrounding energy harvesting in smart agriculture. Reproduced with permission [474]. Copyright 2021, Wiley-VCH. (f) Fibrous fluoropolymer composite-based TENG. Reproduced with permission [475]. Copyright 2023, Elsevier.

squalane-lubricated TENG showed a great durability (>36,000 times) and generated electrical performance more than 3 times when compared with the unlubricated one. Furthermore, Chung et al. [472] designed a nonpolar liquid lubricant submerged TENG with the suppression of the air breakdown and field emission (Fig. 44c). The liquid lubricant TENG is capable of generating a significant electrical current, which enables it to effectively supply power to a total of 319 LEDs. Another strategy is using or coating a low-friction material, *e.g.*, diamond-like-carbon (DLC), onto the main contacting material. As proposed by Li et al., [473] the exceptionally high-power generation of the sliding-mode DLC-glass TENG is a result of the combination of its inherent superior triboelectrification performance and the extremely smooth interfaces between the DLC electrodes and the glass slider (Fig. 44d). The triboelectric pair exhibits a low coefficient of friction and minimal abrasion, resulting in a remarkable lifespan exceeding 500,000 cycles. For the TENG operated through a freestanding mode, there is a report by Chen et al. [474] showing a method to decrease a coefficient of friction of triboelectric material using a naturally available animal furs (Fig. 44e). The charge transferred by the fur-brush TENG only decreases by 5.6% after being used continuously for 300,000 cycles. Also, the generator maintains a high level of output performance even when the relative humidity increases to 90%. They utilized the concept for self-powered weather monitoring and wireless warning systems in smart agriculture. Besides physical modification, the design and selection of appropriate triboelectric materials are efficient routes to enhance the device's durability. The composite approach has the potential to develop high-performance TENGs due to its unique nanostructure assembly and high surface-to-volume ratio [478]. Rastegardoost et al. [475] proposed the effective method to design highly durable TENGs based on fibrous composite (Fig. 44f). They found that incorporating graphene nanoplatelets into the PVDF fibrous mats showed various significant characteristics, including boosting the performance (output voltage and current of 134.4 V and 12.9 μA, respectively), and high durability (operation over 350,000 cycles). The results pave the practical way for the further development of high performance and durable nanogenerators.

7. Diverse applications of TENGs

TENGs have evolved significantly since their inception in 2012 by Wang et al., initially focusing on energy harvesting from mechanical vibrations and motions. TENGs first explored applications such as powering LEDs, portable electronic devices, and self-powered sensing systems. Over time, TENG technology expanded into biomedical uses, including self-powered implantable medical devices, drug delivery systems, and real-time physiological monitoring [479–481]. Later, self-powered systems such as electroplating, hydrogen production, and self-powered electrospinning systems were reported. With the rise of the IoT, TENGs have been integrated into smart textiles, wireless sensor networks, and autonomous electronics, reducing dependency on conventional batteries. This section presents an overview of the diverse applications of TENGs reported so far in the literature, as classified in Fig. 45.

7.1. Self-powered sensing

Recently, scientists have been working to develop technologies that enable the creation of wireless sensors that are energy-autonomous or self-powered. There are two possible interpretations of the term "self-powered sensor." The first suggests that when mechanical force is applied, it generates an electric signal without needing external power. The second interpretation indicates that it can harness energy from the surrounding environment. Thus, self-powered technology that eliminates the need for batteries is becoming increasingly crucial for wireless sensing and the development of IoT. It is inevitable that self-powered, battery less technology will be utilized to achieve the trillion-node IoT mission. The future's extensive IoT deployment will rely on self-powered wireless sensors. This forthcoming data breakthrough will be propelled by battery less sensors, making it possible for billions of previously unmonitored physical assets to provide valuable data. Components for energy generation, energy storage, interaction, sensing, communication, and monitoring are assembled into a self-powered sensor system. Sensors that run on their own energy can capture energy from their surroundings. Energy harvesting is still difficult, though; solar energy, for instance, is highly influenced by weather, which reduces its viability and dependability for self-powered sensors. Energy sources like fluid and mechanical energy might be feasible. It is possible to examine the feasibility of producing electricity from waste heat from vehicles and industries. Reducing energy usage and related environmental effects can also be achieved by developing sophisticated waste energy recovery technologies. However, most energy-harvesting modules, including solar, thermoelectric/pyroelectric production, and radiofrequency, can only harvest a limited amount of power (about tens of microwatts of power per square centimeter). Still, battery less technology is starting to make sense as a low-power electronic system solution [482–485].

Zhang et al. reported on the fabrication of a high-sensitivity, lightweight, self-powered, and low-cost 3D acceleration sensor (AS) based on the liquid metal (LM) TENG [486]. Compared to the currently known self-powered AS, 3D AS maintains the smallest dimensions, lowest weight, and maximum integration due to the programmed approach of the electrodes. The fabricated acceleration sensor has a broad detection range (Horizontal direction: 0–100 m/s^2 and Vertical direction: 0–50 m/s^2) with 800 mV/g sensitivity. After running continuously for over 100,000 cycles, the open-circuit voltage barely decreases, demonstrating outstanding stability and robustness. Fig. 46a demonstrates many facets of the three-dimensional AS based on LM-TENG's layer-by-layer structure. A simulated collide experiment is used to demonstrate the three-dimensional AS based on the LM-TENG's capability as a component of vehicle restraint systems. The sensor determines whether and when to activate the airbag in a collision accident by measuring the impact acceleration. The car's integrated acceleration sensor effectively determines the position of the collision, as seen in Fig. 46 (b,c). The acceleration sensor is capable of measuring the force of the impact acceleration while determining the collision location so as to decide whether an airbag needs to be positioned to protect people inside. This is then evident in Fig. 46 (d,e), where a collision location is adjusted to the front while the acceleration changes from a low number to a high value. This LM-TENG-based 3D AS prototype demonstrates the possibility of developing an economic sensor for automobile head restraint systems that is both sensitive and efficient [486].

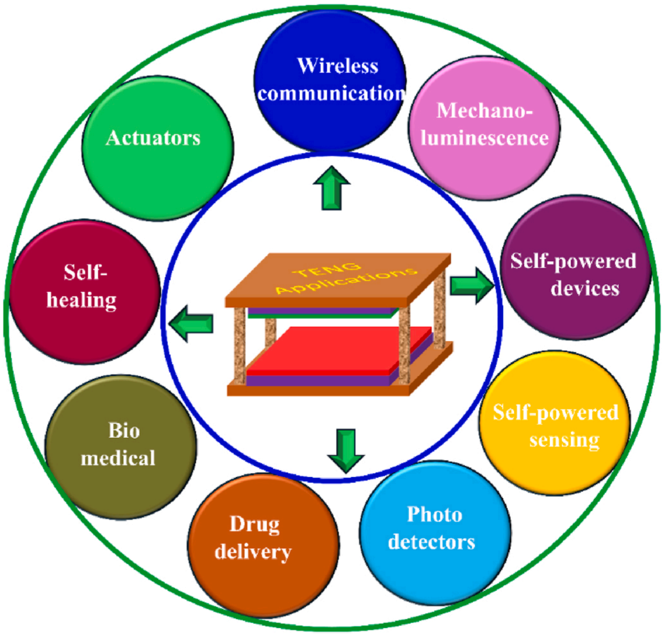

Fig. 45. Schematic outline of the applications of TENGs in the diverse fields.

Sun et al. present a novel technique called Accelerated Charge Transfer (ACT) TENG, which significantly improves TENG's performance [487]. Validate the viability of this method by means of methodical research, using bidirectional rotation mode and magnetic field modulation to confirm the gain impact of ACT-TENG. ACT-TENG is notable for achieving a stunning 14.6-fold increase in output power and a 4-fold improvement in transfer of charge rate when compared to ordinary free-standing TENG. This results in an outstanding 499.05 mW m-^{2} Hz-^{3} average power density, demonstrating better performance than previously documented FS-TENG systems. Moreover, ACT-TENG demonstrates remarkable performance in the water flow environment, producing 10.76 mW of electricity at a 180 L min^{-1} flow rate. Constructing underneath intelligent pipeline galleries is crucial for improving urban management that is intelligent. For underground passages to be safely controlled and operated effectively, a variety of sensors are required. However, regular manual maintenance is difficult and inconvenient because of the underground galleries' distinct spatial form and complex air composition. In order to guarantee the seamless functioning of sensor devices and reduce maintenance costs at the same time, implementing an autonomous IoT system powered by TENG technology appears to be a very effective solution. Environmental monitoring, fire protection, and intrusion alarm approaches are necessary for the underground pipeline galleries. In this esteem, WFEH-TENG was utilized to harvest the kinetic energy of the fluid passing through pipes, supplying an accurate source of electricity for the vital parts of these systems [487]. Fig. 46f provides a clear illustration of the application scenario. The WFEH-TENG, a vital tool for firefighting guidance, continually powers LED panels, as shown in Fig. 46g.

It guarantees emergency visibility in dire circumstances. Furthermore, WFEH-TENG's capacity to power wireless humidity and temperature sensors, both crucial for environmental monitoring, is shown in Fig. 46h. In about 265 s, WFEH-TENG effectively charges a capacitor (1500 μF) to 3.7 V. As shown in Fig. 46i, the humidity and temperature sensor is then powered by this stored energy, preventing the equipment from deteriorating more quickly as a result of harsh temperature and humidity conditions. The charge and discharge statistics are shown in Fig.s. 46 j and k, which also include pictures illustrating the WFEH-TENG's contribution to the underground smart pipe gallery's intrusion alarm system construction. The intrusion alarm system is triggered when a person comes inside the infrared induction module's monitoring range, reducing the possibility of serious mishaps or disturbances in the hallway. In this setup, the WFEH-TENG is essential since it charges a

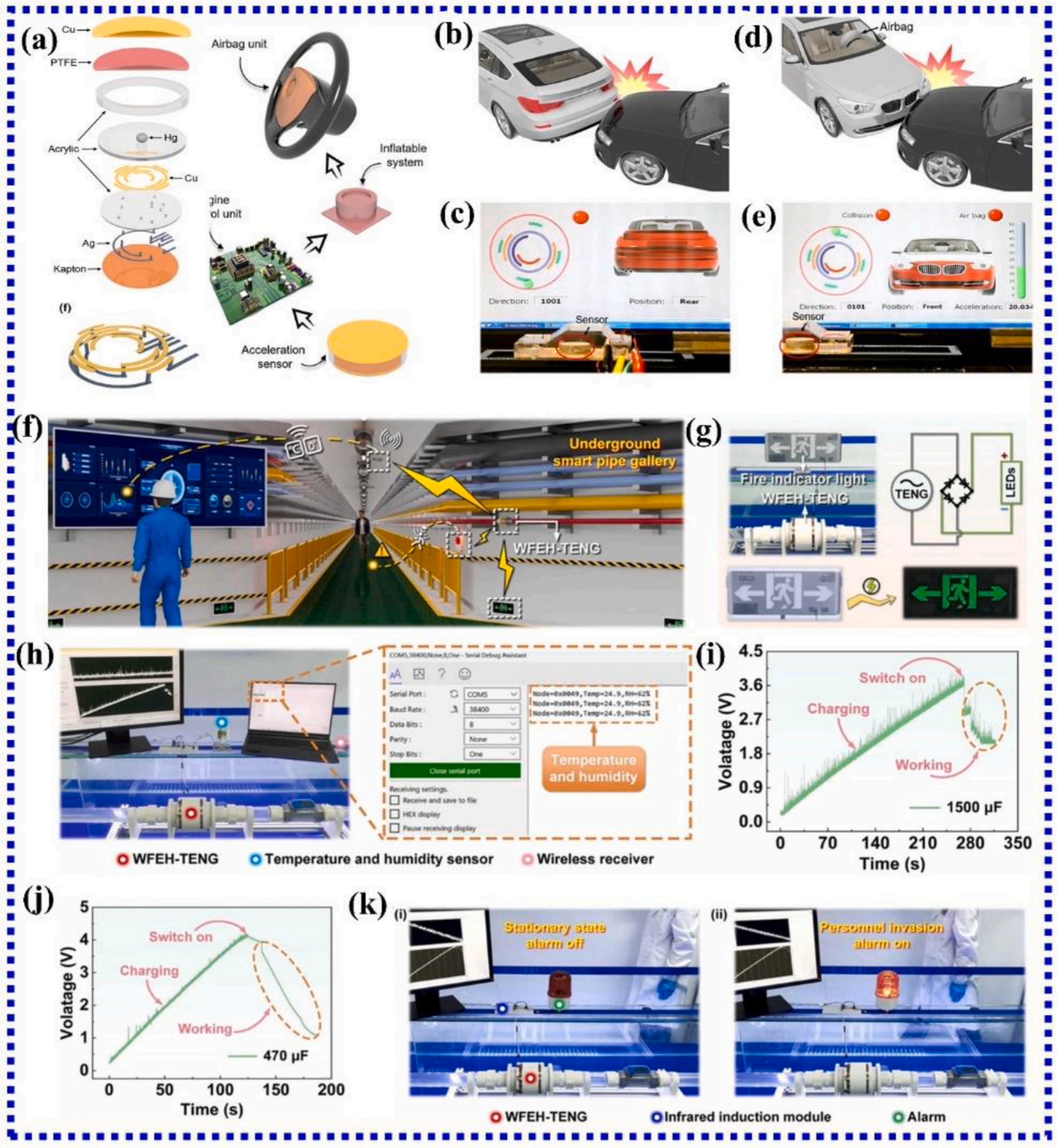

COM5,38400,None,8,One - Serial Debug Assistant

Serial Port : COM5
Baud Rate : 38400
Data Bits : 8
Parity : None
Stop Bits : One

Receiving settings.
☐ Receive and save to file
☐ HEX display
☐ Pause receiving display

```
Node=0x0049,Temp=24.9,RH=62%
Node=0x0049,Temp=24.9,RH=62%
Node=0x0049,Temp=24.9,RH=62%
```

Fig. 46. Acceleration analysis in the full space of 3D acceleration sensor, and its associated application in vehicle safety restraint method. (a) Schematic demonstration of 3D acceleration sensor and the working procedure of vehicle safety restraint method. (b,c) Collision spot of vehicle detected by 3D acceleration sensor. (d, e) Collision spot and the force detected by sensor, which can deliver data to vehicle safety restraint approach. Reproduced with permission [486]. Copyright 2021, Elsevier. Potential application of WFEH-TENG in an underground pipe gallery. (f) Schematic illustration of WFEH-TENG in the smart pipe gallery. (g) Presentation of WFEH-TENG powering LED panels for the guidance of fire safety. (h) WFEHTENG image operating wireless humidity and temperature sensors. (i) Charging and the discharging profiles of WFEH-TENG for a wireless humidity and temperature sensor. (j) Charging and the discharging process of WFEH-TENG power source for the infrared induction component. (k) Photograph of intrusion alarm system. Reproduced with permission [487]. Copyright 2024, Elsevier.

capacitor (470 μF) to 4.1 V in around 124 s. Together, these demonstrations offer strong proof of WFEH-TENG's potential for use in underwater smart pipe gallery. Additionally, it reaffirms ACT-TENG's superior output capabilities and the viability of its industrial use [487].

The ability of a perfluorinated polymer film to break from its adhesive when subjected to sonication is an intriguing phenomenon discovered by Guan et al. [488]. An easily constructed and compactly organized ultrasound-driven TENG (UDTENG) is suggested as a simple method of harvesting ultrasonic energy based on ultrasound-induced separation. Investigations are conducted into the mechanism of the coupling between ultra-high ultrasonic pressure and weak adhesion of the perfluorinated polymer film, which has been confirmed by simulation and experiment. By comparing various films, the connection between surface energy and the adhesive separation force of the film is ascertained. The impact of ultrasound parameters on the output performance of the UD-TENG is also revealed by the ultrasound's direction and intensity. After sonicating for 1 h, UD-TENG can attain a high charging rate (75 μC/s) and show outstanding stability with no discernible attenuation of voltage signal. There is a demonstration of a number of useful gadgets powered by the UD-TENG [488]. The practical use of the UD-TENG as a self-powered sensing system for underwater ultrasonic wave detecting and sound source localization is schematically illustrated in Fig. 47a. With signal towers on land and signal receiving terminals on the sea surface, a vast number of the UD-TENGs are dispersed throughout the ocean to build sensing network systems. With the benefits of low.

power consumption, self-driving, cheap cost, and quick response, UD-TENGs can sense the ultrasonic waves produced by the underwater sonar, instantly synthesize electrical signal peaks, and wirelessly communicate the observed data to terminal processing. A self-powered sound sensor featuring six nearby receptive surfaces is suggested in this study. Depending on the number of its signal-receiving surfaces, every sensor can separate the underwater space into matching portions (Fig. 47b). Fig. 47c presents the design concept. By gathering ultrasonic energy from various angles, the sensor's sides get varying voltage signals, utilizing the high directivity of ultrasonic transmission. The terminal is utilized to examine the voltage signal information from the sensor, and the printed circuit board is utilized to gather and send electrical signals produced by sound wave. The area of the maximum voltage signal, which indicates an area of maximum likelihood of the sound source, is derived by analyzing voltage patterns of all the receiving areas (Fig. 47d and e). When the highest probability of sound source areas identified by the UD-TENGs dispersed across various ocean locations converge, an overlapped zone will result (Fig. 47f). The

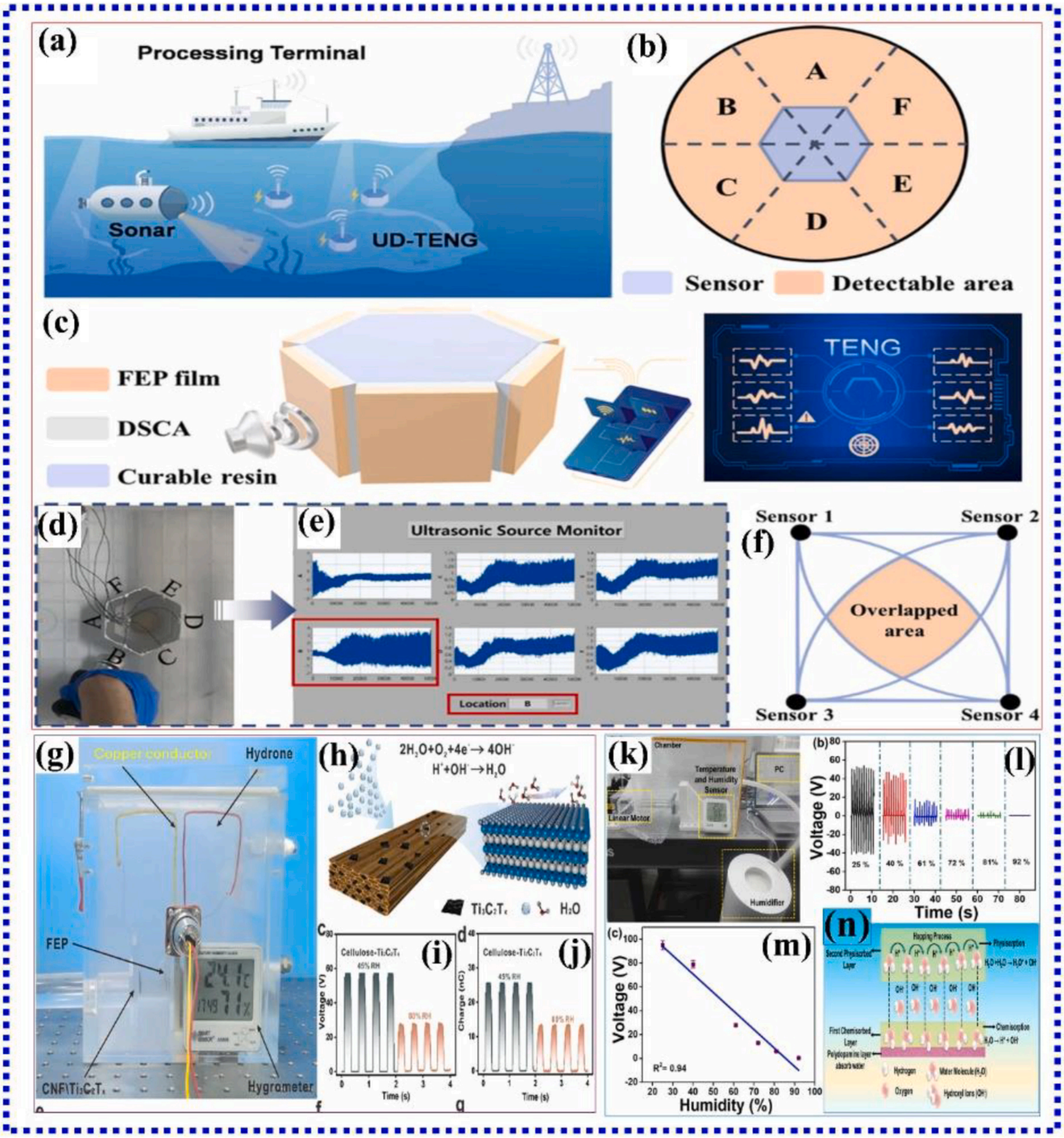

Fig. 47. (a) The practical use of the UD-TENG as a self-powered sensing system for underwater ultrasonic wave detecting and sound source localization. (b) Ultrasonic sensor detectable areas. (c) Ultrasonic sensor design concept. (d,e) Images of the (d) wide-angle test procedure and (e) terminal interface. (f) Schematic of sound source region location. Reproduced with permission [488]. Copyright 2022, Elsevier. Moisture-sensitive features of cellulose tribo materials. (g) Physical illustration of humidity testing device. (h) Schematic of the sensing mechanism of water molecules. (i) Voltage profiles without and with moisture. (j) Charge profiles without and with moisture. Reproduced with permission [489]. Copyright 2023, Elsevier. (k) Image of laboratory scale setup of the humidity chamber. (l) TENG voltage according to percentage of humidity. (m) Fitted data of voltage according to percentage of humidity. (n) illustration of the PDA mechanism demonstrating water molecules bonding and physiosorbed/chemisorbed layers formation along with the proton hopping. Reproduced with permission [490]. Copyright 2023, Elsevier.

overlapped zone is smaller, and the ultrasonic source location is more precisely positioned when the spatial distribution of UD-TENGs is denser [488].

Using natural cellulose as the template, Zhang et al. [489] created hydrophilic triboelectric materials that were then employed for self-powered sensing in extremely humid conditions. The intricate shape of material created in conjunction with the $Ti_3C_2T_x$ MXene during templating offers many places to adsorb water molecules because of interconnected structure of cellulose scaffold. Moisture-sensitive triboelectric material may maintain exceptional behavior in 150 s with excellent sensitivity (0.8%/1%) throughout the humidity range of 40%–90% RH. Self-powered sensing in high humidity conditions is made possible using cellulose template triboelectric material, which wirelessly sends electrical impulses to user interface. The cellulose/$Ti_3C_2T_x$ composite was evaluated as a TENG-positive triboelectric material in various humidity conditions to assess its moisture-sensitive characteristics (Fig. 47g). Numerous active sites are available for the entrance of water molecules thanks to the $Ti_3C_2T_x$ nanosheet units, the layered porosity structure, and the linkages between them. Absorption and activation of the defects and the functional groups on the water molecules are the primary components of the $Ti_3C_2T_x$ sensing process. In particular, –OH may absorb the water molecules and H bonds were formed between the surface functional groups (–OH and –O) and embedded water molecules. Water molecules were adsorbed on active sites of MXene nanosheets ($Ti_3C_2T_x$) primarily with diffusion by dispersion forces between the defects or partially charged functional groups. Water molecules can attach to functional groups on MXene surface, such as hydroxyl and oxygen, when it is exposed to the humid environment (Fig. 47h). Electrical output features are impacted by low conductivity of water, which raises resistance of $Ti_3C_2T_x$, once water molecules are embedded between the layers. The output efficiency of TENG is assessed at various humidity levels, as seen in Fig. 47i–j. The TENG's open-circuit voltage drops with 80% relative humidity of the surrounding air as opposed to 45% at the standard atmosphere. The trend of lowering short-circuit current values is also evident. The reason for this is that water molecules adsorb onto the $Ti_3C_2T_x$ nanosheets active sites, reducing the micro-capacitor network and lowering its charge storage capacity. This work encourages the investigation of self-powered sensing in high humidity conditions and offers a novel approach for the design and manufacture of high-performance triboelectric materials utilizing cellulose as a template [489].

Panda et al. [490] utilized biocompatible polydopamine (PDA) material and applied it for humidity sensing. PDA-integrated 3D-printed TENG for self-powered humidity sensing is demonstrated. The multi-unit TENG's current and output voltage are measured to be 2.4 μA and 90 V, respectively. Over the relative humidity range of 25%–92%. The humidity sensor's resistance drops with increasing humidity, which lowers the output of electial voltage. In essence, TENG-based humidity sensors are electrical humidity sensors. TENGs touch and separate triboelectric materials to produce electrical charges via the triboelectric effect. After that, these charges are gathered and utilized as a direct sensing mechanism or to power electronic gadgets. In a TENG-based humidity sensor, the active detecting component is the triboelectric layer (polydopamine). Humidity exposure alters the physical or electrical properties of humidity-sensitive layer on TENG surface, which influences the formation of triboelectric charges and modifies the TENG's electrical output. Variations in humidity levels were then associated with changes in the electrical impulses generated by TENG layer. A digital photograph of humidity chamber setup and the Z-TENG inside is shown in Fig. 47k. The change in RH% was tracked using the humidity sensor. However, battery-based sensors have problems with charging and have a short lifespan. Fig. 47l, illustrates how the Z-TENG's output gradually drops as the humidity level rises, and Fig. 47m shows that the fitting data was obtained (R_2=0.94). A schematic illustration of PDA is shown in Fig. 47n, where water molecules connect and chemisorbed/physisorbed layers occur in addition to proton hopping. In order to facilitate separation of the adsorbed water molecules, mechanism uses a water adsorption process in which oxygen is replaced by the water molecules or water vapor is chemisorbed on surface of PDA, creating oxygen vacancies in the PDA that serve as an adsorption site. The first chemisorbed layer forms when the relative humidity is low because there are very few water molecules present. Because of the formation of this uneven layer, water molecules are prevented from moving freely, and because protons are conductive, there is a greater electricity generated in the area with lower humidity. As the RH% rose, a layer of multiple water adsorption formed. Because of the Z-TENG's electrical field, which causes the creation of hydronium ions, and the numerous water adsorption layers, which cause proton to travel between hydrogen sites found in other water molecules, the water begins to ionize at greater relative humidity levels. In this manner, when the RH% rises, the voltage of the electrical output falls as the resistance of Z-TENG-based humidity sensor reduces [490].

Jiang et al. developed an Extremely Thin Eardrum-like Triboelectric Acoustic Sensor (ETAS) using Ag-coated nanofibers (40 μm thick) with a wide frequency response (20 Hz–5000 Hz) and high sensitivity (228.5 mV Pa^{-1} at 95 dB) [491]. Integrated with AI algorithms like DenseNet, the ETAS achieves 92.64% voice recognition accuracy, enabling real-time speech-to-text translation for individuals with hearing loss. Compared to ResNet (86%), DenseNet (93.25%) showed superior accuracy after training. The ETAS efficiently captures voice features, reduces power consumption, and provides high-quality voice recording and real-time text conversion, demonstrating its potential for advanced hearing aid technology and smart voice applications.

Qin et al. developed a humidity sensor using carbon nanodots (CDs) with high sensitivity (5318% at 94% RH) and long-term stability (11%–94% RH range) [492]. The sensor's hydrophilic functional groups enable efficient water molecule adsorption, making it highly responsive. Integrated with a breath-driven TENG, the self-powered sensor achieves a maximum output of 200 V and 9.2 μA, enabling real-time breath monitoring when attached to a mask. During exhalation, water adsorption increases sensor current, while inhalation desorbs water, restoring the baseline. The system effectively distinguishes deep, rapid, and normal breathing patterns, demonstrating its potential for real-time respiratory monitoring, though its reliance on an external power source limits portability.

Khan et al. developed a chitin nanopaper (CN)-based TENG by isolating chitin from king mushroom powder using a non-acidic method, significantly enhancing its triboelectric performance [493]. The CN-TENG achieved a maximum power density of 1.78 W/m^2, a current of 11.4 μA, and a voltage of 151 V, successfully powering 50 red LEDs and multiple capacitors. Additionally, CN was investigated as a self-powered humidity sensor, demonstrating a fast response (7s) and recovery time (10s) within a broad humidity range (21%–95% RH) due to hydrogen bonding with water molecules. The sensor exhibited high repeatability across multiple cycles and was effectively applied for hyperhidrosis detection and gait monitoring, showcasing its potential for sustainable, low-cost electronic applications.

7.2. Bio-medical applications

TENGs show great promise for use in the healthcare industry. Patients' pain levels can be considerably decreased and their recovery time greatly shortened when an active therapy schedule is paired with timely information feedback. Generally speaking, health rehabilitation is time-consuming, particularly for chronic conditions. Patients' financial and physical pain can be greatly reduced, and the recovery process can be shortened, when proactive treatment techniques are paired with timely information feedback. Thus, the development of effective and affordable technology for health monitoring and treatment is imperative. Personalized healthcare is made possible by the swift advancement of wearable and implantable technologies and IoTs. TENG can be used as a renewable source of electricity for medical equipment, as well as a sensor that is active for dynamic health information monitoring and electrical signal generation in response to stimuli of the human body. Furthermore, biological cells, neurons, tissues, and organs can be directly stimulated for stimulation with electricity therapy using the electrical impulses produced by TENG. Personalized medicine and mobile therapy will greatly benefit from the integration of TENG and TENG-based networked body areas with cloud computing, big data, and artificial intelligence technologies [494,495]. The current state of research on these three categories of self-powered, TENG-based health applications is very fragmented. Numerous functional prototypes for UV sterilization, plasma purification, air and water disinfection, mosquito killing, and plasma purification have been created in relation to TENG-based practical tools for environmental disinfection. Many prototypes with various functionalities, such as cancer therapy, bone fracture mending, muscle stimulation, tissue restoration, and cardiovascular activity monitoring, have been developed with regard to TENG-based, autonomous microsystems that carry out interventional therapeutic responsibilities. Therapeutic microsystems based on TENGs that require continuous in vivo operation require energy storage devices. Supercapacitors or batteries are typically energy storage devices in question. Two key concerns for these energy storage devices are miniaturization, which calls for on-chip energy storage devices to be small, and biocompatibility, which guarantees the security and eventual deterioration of these in vivo devices for storing energy [494,495].

Electrotherapy attained pronounced interest in the fields of tissue repair as an noninvasive, well-tolerated, and effective treatment. Because of the small Joule heating effect and peak output nature, TENG has demonstrated benefits in accelerating wound healing. However, because of its low antibacterial capacity, it has limited healing ability for infected wounds. Qin et al. [496] developed a wearable triboelectric stimulator (WTS) consisting flexible TENG and tribo responsive drug delivery hydrogel (TR-DDH) to heal bacterium contaminated wounds. F-TENG uses body movements to transform mechanical energy into pulsed electricity that may be applied to wounds. Under electrical

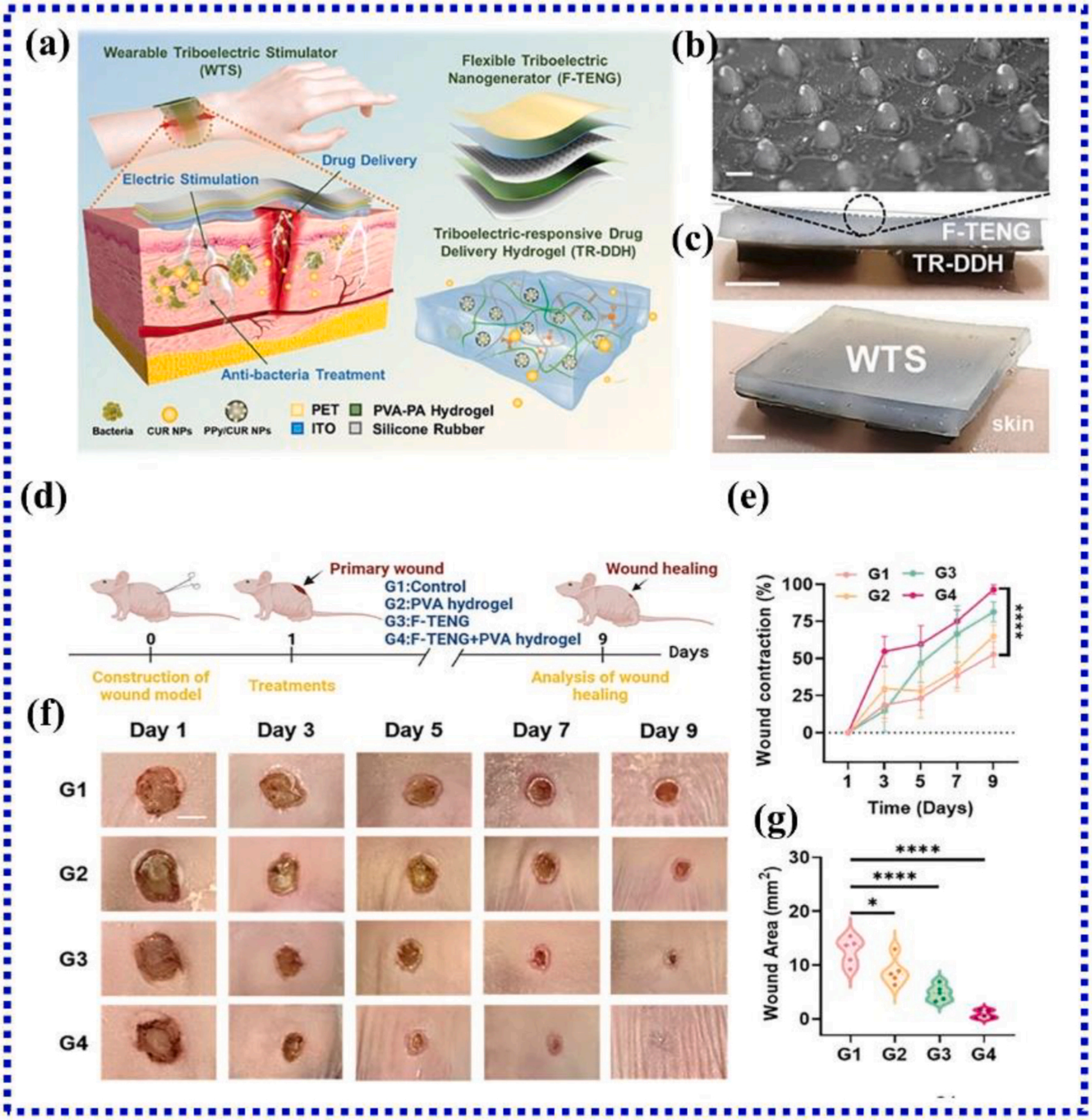

Fig. 48. Design of the WTS for the bacterially infected wound healing. (a) Schematic of WTS consisting of TR-DDH and F-TENG. (b) Photo of microstructure on silicone rubber film surface (300 μm scale). (c) WTS structure photographs (1 cm scale). (d) Full-layer wound models' validation. Schematic sketch of full-thickness wound model fabrication procedure. (e) Images of wounds; 4 groups over 9 days (4 mm scale). (f) 4 groups wound contraction (n=5) over 9 days. (g) Distribution of the wound areas in 4 groups of mice on day nine. Reproduced with permission [496]. Copyright 2024, Wiley-VCH.

stimulation, the polypyrrole is subject to reduction and volume contraction, which causes curcumin nanoparticles (CUR NPs) to desorb from the polypyrrole in TR-DDH. Thus, triboelectric stimulation can produce the extremely efficient and regulated release of CUR NPs. The F-TENG and the TR-DDH make up the WTS, as seen in Fig. 48a. Through the collection and conversion of mechanical energy, such as human movement, into the electrical energy, F-TENG makes self-powered electrical stimulation possible. The electric stimulation from the F-TENG can be used to transport curcumin NPs in the TR-DDH in a controlled and effective manner, enhancing the antibacterial impact and speeding up the healing of wounds infected with bacteria. A silicone film that has a conical microstructure was created, as seen in Fig. 48b, in order to enhance the contact area and charge the surface during the contact-separation process. An image illustrating the WTS is displayed in Fig. 48c. Because of the TR-DDH's excellent adherence, the WTS can be twisted and stuck to the skin in close proximity. By bending the joint area, the F-TENG may generate 15–20 V when it is fastened to the wrist, arm, or knee. By bending the joint area, the F-TENG may produce 15–20 V when it is fastened to the wrist, arm, or knee. The mice were randomly assigned to the four groups in order to test the benefits of the created PVA hydrogels over store-bought conductive tapes for maintaining transmission of signals stability during electrical stimulation. The control group, the PVA hydrogel group, the F-TENG group using commercially conductive tape as the contact electrodes, and the F-TENG group using PVA hydrogels as contact electrodes were represented by Groups 1 (G1), 2 (G2), 3 (G3), and.

4 (G4), respectively (Fig. 48d). The wound in G2 was scabbed, as seen in Fig. 48e, however the incision in G1 did not heal entirely on day 9. Compared to G1 and G2, wounds in the G3 and the G4 healed noticeably more quickly. According to Fig.s. 48f and g, the wounds in the G4 healed fastest and nearly entirely. Due to the conductive tape's inability to be stretched and the skin's significantly different Young's modulus, the mice in G3 were prone to falling off the skin when moving their bodies. This instability in signal transmission occurred during the electrically stimulating procedure. In contrast, hydrogels performed better as the electrodes when interacting with the skin due to their higher tensile strength and stickiness. When compared to treatments with electric stimulation or curcumin, WTS has the strongest antibacterial impact and promotes infected wound healing the quickest, according to both in vitro and in vivo investigations. With its many benefits, including self-powered and safe pulse electrical, the WTS has demonstrated potential in fostering infection by bacteria in wounds. Moreover, when developing the WTS, mobility and excellent electricity produced should be taken into account to achieve more effective treatments for chronic wound healing [496].

Wang et al. developed a multifunctional wound healing system by integrating aqueous-aqueous TENGs (AA-TENGs) with a conductive hydrogel loaded with min0ocycline [497]. The AA-TENGs generate a 100% contact area, significantly enhancing current output through efficient immiscible droplet interactions. The adhesive, self-healing hydrogel delivers electrical stimulation (ES) and antimicrobial therapy, accelerating infected wound healing. Compared to solid-solid TENGs, the M-H-A-A TENG system produces higher short-circuit current density, ensuring faster and more effective wound recovery. This innovation expands TENG applications in advanced medical treatments.

Implantable medical devices are helping thousands of patients thanks to advancements in biomedical technology, microelectronics, and precision manufacturing. The operational frequency and lifespan of medical devices that are implantable, such as vascular applicators, pacemakers, and neurostimulators, can be greatly increased by wireless power transfer. On the other hand, there are issues with the current transmission techniques, such poor power, discontinuity, or negative health effects. Herein, Liu et al. [498] create a flexible ultrasound (USD) generating system that can be implanted subcutaneously. It combines a power management circuit and a TENG transducer into a single flexible printed circuit board. By selecting an attached-electrode TENG with optimum structural characteristics, we maximize the performance of the TENG transducer. This TENG delivers reduced impedance and 66% superior output power. A system this adaptable has many uses in many contexts. It can effectively deliver a constant 1.8 V direct current voltage with an output power of more than 1 mW continuous DC and more than 10 mW instantaneous, which is enough to power micromotors, apply nerve stimulation, and continuously drive a variety of sensor systems. The device, which can power an implanted pacemaker, implantable chip, vascular robot, neurostimulator, or sensor, is intended to be inserted into subcutaneous tissue of human body. It does this by collecting mechanical energy carried by ultrasound that is transmitted through the skin (Fig. 49a). A TENG (4 × 4 cm) transducer and a power (2 × 4 cm) managing circuit make up the 6 × 4 cm USD-TENG system. Both are made on a flexible PCB (FPCB) that is built on polyimide (PI). Because of its outstanding flexibility and biocompatibility, this integrated design allows the device to be used in a variety of in vivo implantation situations (Fig. 49b). The FPCB is stacked with multiple layers to form the TENG transducer. FEP, which forms an attached-electrode structure when it is directly bonded to copper pad, is used to make the dielectric layer. FEP was selected due to its small weight, great stability, and extremely negative electron affinity. To create an air gap, a double-sided sticky spacer made of Kapton was then inserted. It is covered by a second layer of the FEP film that is deposited using an aluminum electrode to create a resonant cavity (Fig. 49c). PDMS, which exhibits great deformation and waterproof characteristics, is finally employed for packaging. These materials are biocompatible, nontoxic, and soft, which allows the gadget to function steadily in watery environments. The top membrane oscillates up and down when it is excited by ultrasound. Tribo-charges are created at interface and during periodic movement when top FEP membrane covered with Al layer comes into contact with bottom FEP dielectric layer. This results in production of a continuous stream of electricity. A rectifying bridge, DC-output component, and pulse-output module are components of the power control circuit (Fig. 9d). The internal energy management circuit (Fig. 49d) is capable of rectifying AC power produced by USD-TENG and supplying DC power to a range of load types. As mentioned, currently developed system may produce either a pulse or a fixed-amplitude DC voltage based on the requirements of various application scenarios. Combined the power management circuit and TENG transducer onto a single FPCB to maximize biocompatibility and enable the configuration of various power outputs to meet varying job needs. With respect to output behavior, biocompatibility, integration, and application scope, this suggested system has undergone a thorough improvement over the prior work. Ex vivo and in vivo characters, intermittently operating a micromotor, and activating a bullfrog sciatic nerve served as examples of application that demonstrated the efficacy of the system that was designed [498].

A vital component of the hip, knee, shoulder and ankle, joints, cartilage is essential for cushioning and lubricating these joints. Cartilage abnormalities can result from rheumatoid arthritis, age-related degeneration, and high-intensity mechanical exercise. These conditions can cause discomfort and movement difficulties in patients. Repair of defects in cartilage is a popular research subject worldwide because articular cartilage inhibits the ability of cartilage to self-repair when bone exposure occurs. Numerous therapy plans have been implemented thus far. Because allogeneic osteochondral transplantation can be used to treat severe cartilage defects, it is a viable treatment option because the necessary material sources are widely available. However, there are several challenges to overcome, including high transplant preservation costs, endogenous diseases, and strong immune system reactions triggered by allogeneic antigens. Future tissues trauma therapy with integrating bioelectronics, as proposed by Yue et al. [499] is motivated by electroactive properties of the living organisms and holds promise for producing the intended therapeutic outcomes. A multi-convex TENG based sensor and on-demand incorporation of smart scaffolds with the porous 3D structure were used to nanoengineer the tissue battery for the

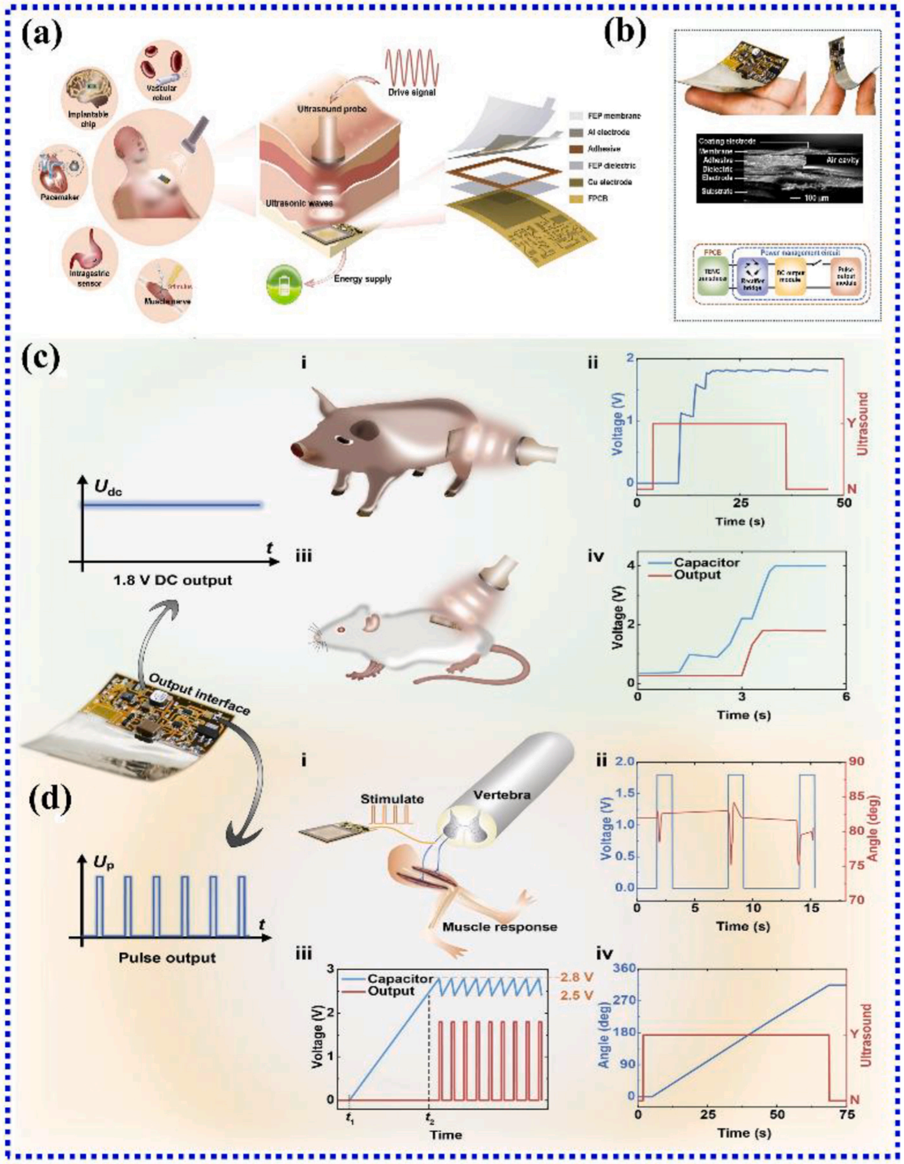

Fig. 49. Overview of USD-TENG. (a) USD-TENG device is implanted under skin, and it receives wireless energy from the ultrasound system to power implanted IMDs. (b) Images of USD-TENG flexibility, cross-section SEM image, and USD-TENG modular diagram. USD-TENG system has broad applications. (c) Working state of the DC output. (i,ii) Schematic of porcine ex vivo representation and output voltage curve. (iii,iv) Schematic of rat in vivo representation and output voltage curve. (d) Working state of pulse output. (i) Schematic representation of bullfrog sciatic nerve stimulation. (ii) Bullfrog hindlimb pulsate angle. (iii) Schematic representation of the voltage-controlled pulse output. (iv) micromotor rotation angle. Reproduced with permission [498]. Copyright 2022, Elsevier.

integrated cartilage therapy. Fig. 50a displays the macroscopic topology of tissue battery, allowing for the separation of the scaffold and sensor. The tissue battery used in this study is an artificial one that was created by combining tissue engineering, medical expertise, and electricity. It is made up of 2 components: (i) porous scaffold called PCL–PLGA–HA that is used to fill in cartilage defects, and (ii) TENG-based pressure sensor that is made up of PCL/PDMS/PCL–FA as the negative friction layer and CA–CS–HA as the positive friction layer. As demonstrated in Fig. 50b, TENG-based sensor transforms mechanical energy into electrical current when a tissue battery inserted in the cartilage of the joint is subjected to mechanical action as a result of body motion. This electrical current then encourages the growth of the chondrocytes. In addition, patients and physicians can assess the state of cartilage regeneration and promptly take appropriate medical action by wirelessly transmitting electrical signals produced by tissue batteries to computers, mobile phones, and even internet. The primary metrics that may be utilized to assess the tissue battery's performance are its sensitivity, anti-interference properties, and longevity. Comparing it to other published studies, it also performs better when utilized as the generator for tissue batteries for stimulating cartilage differentiation and cell proliferation through the ES. When sensor pixel was exposed to a rise in the pressure from 0.5 MPa to 1.8 MPa, voltage increased from 2.6 to 24.5 V. Furthermore, it was found that tissue batteries can react to the force at specific frequency. With signal processing, the frequency's impact on the pressure signals' strength can be eliminated, guaranteeing an accurate detection. 1.8 MPa of force has been applied to a sensor pixel that was chosen as the study's output terminal and coupled to exterior loads with varying resistances (0 MΩ–100 MΩ). As seen in Fig. 50c, the tissue battery was able to power the timer using the rectifier bridge when it was submerged in a solution of PBS and 1.8 MPa of pressure was exerted at a particular frequency (0.5 Hz). Investigations on rabbit cartilage in the knee have shown that ES stimulates dormant cells (100 mV mm^{-1}) (Fig. 50d). Furthermore, a significant issue with biomaterials for cartilage regeneration has always been their potential for infections of the body of humans because to their toxicity. The suggested tissue for cartilage battery is anti-interference, self-powered, extremely sensitive, degradable, and implantable. The tissue battery can in-situ monitor, current state of cartilage healing in "black box" thanks to the high sensitivity (52.5 V MPa^{-1}) of the sensors

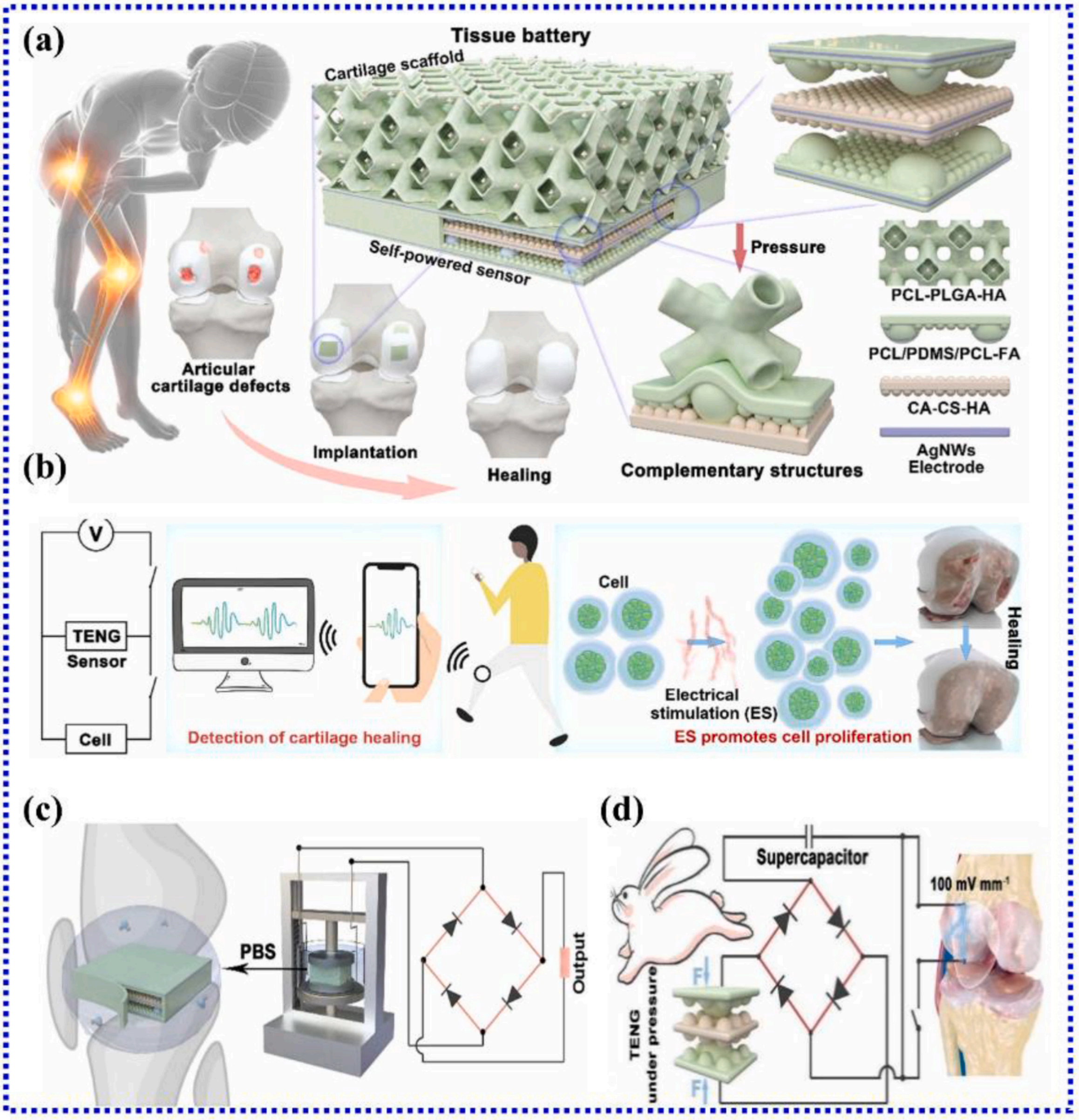

Fig. 50. (a,b) Schematic structure (a) and function (b) of designed tissue battery. (c) Photograph and schematic illustrating conversion of the mechanical energy into the electricity realized by sensor in PBS solution. (d) Schematic demonstrating the mechanism during which the electrical stimulation accelerates the repair of cartilage. Reproduced with permission [499]. Copyright 2023, Elsevier.

based on C-S TENG process within the joint movement pressure range (0–1.8 MPa). Moreover, research conducted both in vitro *and* in vivo showed that tissue battery speeds up healing process of cartilage by converting the mechanical energy into the electrical current that stimulates chondrocyte growth in scaffold. For patients with cartilage abnormalities, the suggested tissue battery for healing tissue under stimulation from electricity is helpful in lowering pain and treatment costs, and it is a viable approach for bioelectronic implants [499].

Recent advancements in self-powered medical technologies have led to innovative solutions for spinal cord injury, cancer therapy, and neuroglioma treatment. Zhong et al. developed an implanted MV-TENG diaphragm pacing device that converts micromechanical energy into nerve stimulation pulses, successfully inducing diaphragm contractions in rats, offering a promising approach for next-generation phrenic nerve stimulation [500]. Yao et al. introduced the TENG-CatSystem, a self-driven catalytic therapy that enhances ROS production for cancer treatment, using a wearable TENG, COF-CNT nanozyme, and conductive hydrogel to increase catalytic efficiency and effectively reduce malignant 4T1 breast cancer in mice [501]. Additionally, they developed a wirelessly controlled NO gas therapy system, where a self-powered TENG generates energy to release nitric oxide (NO) for glioma cell destruction, demonstrating effectiveness in rat glioblastoma and mouse breast cancer models [502].

Huo et al., developed an implantable TENG sensor for continuous ureteral peristalsis monitoring using shape-memory and biocompatible polymers, ensuring long-term stability and safety [503]. Zhang et al., designed a highly sensitive microcolumn-based TENG sensor for non-invasive, continuous blood pressure monitoring, capable of detecting subtle pulse wave signals with ECG-level accuracy [504]. Wu et al., introduced a stretchable, multimodal msw-TENG for biomechanical energy harvesting and physiological sensing, enabling real-time tracking of joint movements and pulse detection without an external power source [505]. Chu et al. explored TENG-based electrotherapy for cancer metastasis treatment, demonstrating its ability to inhibit tumor cell migration and prevent lung metastasis in vivo [506]. Yu et al., developed an asthma-preventive SS-TENG, utilizing respiratory motions for transdermal drug delivery and emergency alerts, enhancing real-time asthma management [507]. Xiong et al. developed a self-powered, stretchable TENG sensor for real-time monitoring of dry eye syndrome, detecting eye blinking patterns and providing user feedback via IoT-connected devices [508]. Wang et al. introduced triboelectric microneedle (MN) patches with controlled drug release and self-reporting capabilities for psoriasis treatment, using structural color hydrogel to track drug delivery in vivo [509]. Riaz et al. designed a ridge-structured TENG sensor for biomechanical movement detection, achieving high power output (490 mW/m^2) and stability (10,000 cycles), with applications in wearable gait, respiration, and pulse monitoring [510]. These developments highlight the growing potential of TENGs in personalized healthcare, diagnostics, and smart wearables.

7.3. Self-healing applications

Numerous electronic hydrogels with good self-healing properties have been produced. Hydrogels possessing the combined properties of adhesiveness, self-healing, deformability, and conductivity hold substantial potential for use in the next-generation soft robotics, energy, and electronic applications. Dong et al. [511] reported a dual-network PAAM/PAA/graphene/PEDOT:PSS (MAGP) conductive hydrogel consisting of dual-cross-linked PAA and PAAM as well as PEDOT:PSS and graphene as the conducting material that combines these characteristics. Fig. 51a demonstrate the robust adherence of the as-prepared MAGP hydrogels to a range of surfaces, such as wood, glass, ceramics, and iron. A commercially available LED bulb was used to link the MAGP hydrogel to a power source for the demonstration (Fig. 51b). Two sections of the MAGP hydrogel were cut and reattached. After the self-healing process, the wide fissure nearly vanished, demonstrating good repair capacity (inset of Fig. 51b). Furthermore, the ability to use the healed MAGP hydrogel as a conducting in the circuit that powers the LED bulb confirms the hydrogel's electrical function is healing. Moreover, in vitro proliferation and viability of cells revealed the MAGP hydrogel's strong cytocompatibility. The MAGP hydrogels are layered between the two dielectric CNTs/PDMS layers to create a wearable strain sensor that can track both gentle and forceful human action (Fig. 51c). Furthermore, hydrogel-based sensor can be used to gather mechanical energy by acting as a deformable TENG. Current and output voltage for the D-TENG are0.8 μA and 141 V, respectively. The D-TENG showed that it could power small electronics, including a thermometer and hygrometer, and it could readily illuminate 52 yellow LEDs at once. This work offers a possible method for creating self-powered strain sensors and malleable energy sources [511]. For TENGs to perform well in wearable electronic devices, a multifunctional hydrogel with mechanical toughness, self-healing capabilities, and conformal adherence to the interface is needed. Oh et al. [512] developed an adhesive, self-healing and stretchable, single electrode TENG with hydrogel elastomer double

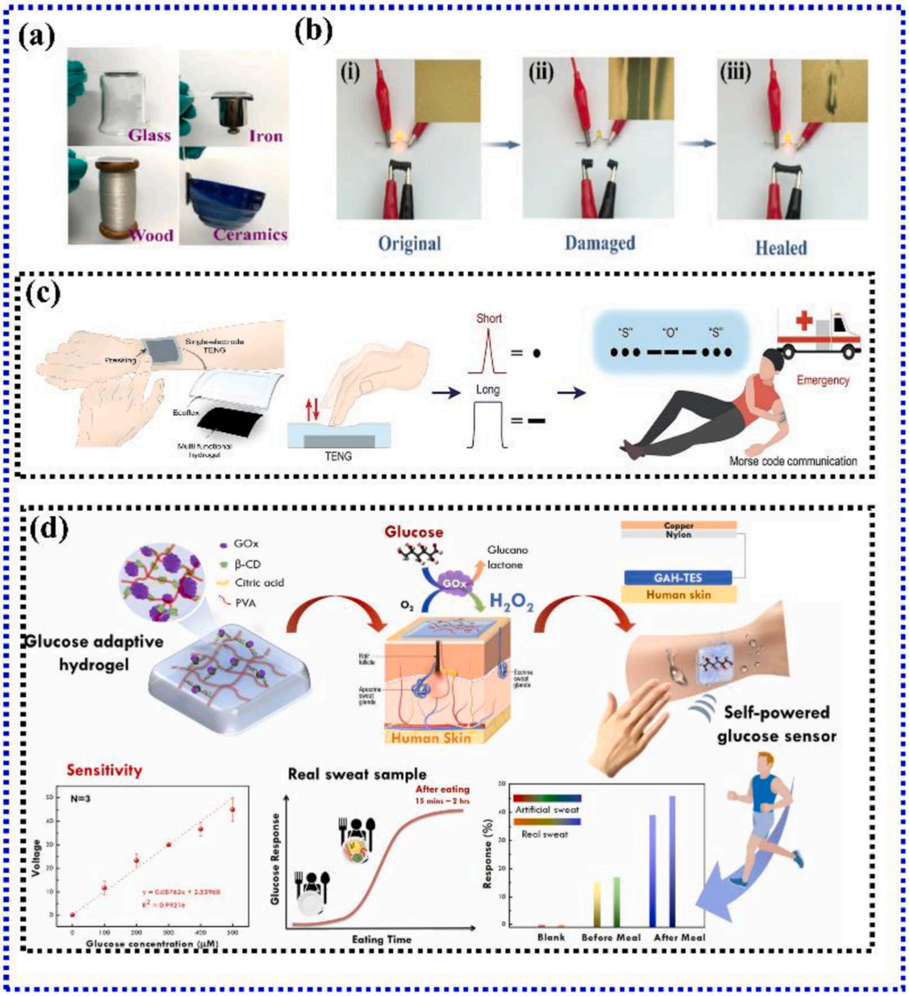

Fig. 51. (a) Photos of MAGP hydrogel adhered to various substrates. (b) Circuit containing MAGP hydrogel in series connection with yellow LED indicator (i) original state, (ii) bifurcated completely, and (iii) healed. (Inset represents the hydrogel optical microscopy image at each state). Reproduced with permission [511]. Copyright 2022, American Chemical Society. (c) Schematic explaining wearable TENG as the wearable touch sensor for the practical Morse code communication in emergency. Reproduced with permission [512] under the terms of the Creative Commons Attribution 4.0 International License (CC BY 4.0). Copyright (2024). (d) Self-healing GAH-TES perspiration monitoring. Reproduced with permission [273]. Copyright 2023, Elsevier.

layer. A multipurpose single-electrode TENG intended for wearable electronics is shown in Fig. 51d. Tannic acid (TA), polyvinyl alcohol (PVA), polyacrylic acid (PAA), and a carbon nanotube (CNT) make up the multifunctional hydrogel. PVA was chosen as the basis for construction because it is soft and biocompatible. TA was added to help PVA chains crosslink and produce weak, reversible H-bonds. Strong covalent bonds are formed upon the addition of PAA, which has carboxyl groups. Dual networking hydrogels with dynamic networks of polymers have the capacity to self-heal, conform to tissue, and are robust. With an energy dissipation of approximately 30 kPa, the hydrogel demonstrates exceptional toughness and conformal interface. Its Young's modulus is comparable to that of soft tissues. Because of the reversible and weak H-bonds, it can self-heal in 5 min at room temperature. Furthermore, stable adhesion ($\approx$250 Nm^{-1}) can be achieved by covalent bonding to a variety of surfaces with a straightforward chemical treatment. With a voltage of approximately 180 V and 0.8 of μA current, TENG devices with multifunctional hydrogel demonstrate good long-term stability, sustaining performance beyond 1000 cycles. Furthermore, even with manual tapping, it can produce 37.8 mW/m^2 of electricity and charge low-frequency energy using an extra power management circuit. The rectifier, DC buck converter, and switch are components of power management circuit. Using power management circuit, capacitors can be charged with the electrical output of TENG devices to power small electronic devices. A LED) was turned on after the capacitors were linearly charged to 5 V in 50 s. The capacitors got charged back to 5 V if TENGs were used continually after that. The LED can thus be powered continually by the energy that is being recharged. Additionally, by leveraging the stable properties of voltage peak during pressing, the suggested TENG modules may accomplish an interface between humans and machines application that produces Morse code signals. The TENG devices' voltage signals show consistent features that held constant when pushing. As a result, depending on how long the TENG devices are pressed, short- and long-voltage outputs are produced (Fig. 51c). Such signals can be used to create "dot" and "dash" signals, which are used in the Morse code communication protocol. In an emergency, a wearable TENG sensor can be tapped to transmit a phrase or message. These findings collectively imply that the TENG devices may find use in wearable electronics for touch sensors and energy harvesting. Human-machine interfaces and flexible wearable power supply have a lot of possibilities thanks to this study [512].

One of the main sources of energy for the activity of cells in living things is glucose. The most prevalent feature of diabetes is high glucose concentration, which is brought on by an inability to control blood glucose levels. In order to provide continuous glucose monitoring of concentrations ranging from 0 to 500 μM in human sweat, Kanokpaka et al., proposed the design and development of a self-healable glucose adaptable hydrogel-based triboelectric-induced sensor (GAH-TES) for monitoring perspiration, as shown in Fig. 51d [273]. The β-cyclodextrin (β-CD) encapsulated glucose oxidase (GO_x) enzyme was added to the PVA matrix because of its high selectivity, non-toxicity, and stretchability. With the help of GO_x enzymatic mechanism, that oxidizes glucose to make gluconic acid and H_2O_2, the GAH functions when glucose is present. Conductivity in the hydrogel matrix is further increased by osmotic swelling caused by mechanochemical bond breaking brought on by an increase in strength of the ions when the concentration of glucose has increased. Triboelectrification on the TENG system is facilitated by the change in conductivity in hydrogel that is based on the enzymatic process. GAH has considerable polarization effect during contact electrification in addition to being a flexible electrical conductor. As the glucose concentration increased from 0 μM to 500 μM, the higher TENG output performance was examined. GAH-TES effectively implemented continuous, self-driven glucose monitoring with superior repeatability, stability, selectivity, and reproducibility. Along with its stretchability and self-healing capabilities, GAH-TES offers an intriguing medical platform for diagnosing diabetes patients. When the levels of glucose exceed the threshold of normal health, LEDs are used to visualize the condition. For wearable electronics, the hydrogel is a well-known flexible conductive material that can preserve its structural integrity and TENG-based sensing capabilities even during mechanical deformation. The GAH was used as conductor in circuit that connected meter to the LED light in order to visibly illustrate intermolecular reversible network design of the GAH toward the self-healing capability in wearable technology. In its initial state, GAH was able to illuminate an LED in a closed circuit. There is an open circuit that causes the LED to dim after dividing the GAH in half. Because the PVA chains in the GAH were rearranged on same surface, their OH groups were able to establish interchain hydrogen bonds to reduce the surface energy, which further allowed GAH to repair itself into one piece. Consequently, the self-healing GAH was able to relight the LED. Additionally, when GAH stretched, an LED gradually lost brightness; nevertheless, when the external force was removed, the LED's brightness returned. For GAH-TES, GAH showed a good capacity for healing. The exceptional mechanical durability and self-healing capabilities of GAH-TES combine with dependable self-powered glucose monitoring to provide a practically medical diagnostic. In the end, GAH-TES only confirms that the use of painless, self-healing, self-powered glucose sensors is achievable using actual volunteer sweat at various meal consumption times. Through continuous, non-invasive examination of human perspiration, the proposed self-sustaining GAH-TES may offer an alternative medical option for the diagnosis and treatment of diabetes [273].

Conductive hydrogels have enormous significance in the formation of flexible strain sensors and significant TENGs, due to their adjustable and stretchability properties. Nonetheless, how to instantaneously attain self-healing, high transparency, antibacterial, adhesion, anti-drying, biocompatibility, and antifreezing, properties through a simple approach remains a challenge. Zhao et al. [513] synthesized and fabricated multifunctional organohydrogel with features of self-healing (25/-24 °C), good transparency, adhesiveness (on pig skin), conductivity, anti-freezing (−24 °C), skin barrier (−45 °C), flexible sensor, antibacterial property, environmental stability and self-powered device (Fig. 52a). The potential self-healing strategy of PAOAM-PDO is depicted in Fig. 52b. Using oxide sodium alginate, aminated gelatin, acrylic acid, and $AlCl_3$ as raw materials, a free radical polymerization process in water/1,3-propanediol (PDO) binary solvent system produced a freezing-tolerant, multifunctional, and transparent, organo-hydrogel (PAOAM-PDO) that can be used as an electrode for the TENGs and strain sensors. The resulting PAOAM-PDO demonstrated excellent conductivity (1.13 S/m), self-healing, adhesiveness, antibacterial properties, transparency (>90%), and long-term environmental stability. With a freezing temperature of −60 °C, PAOAM-PDO was given freezing resistance with the addition of PDO, and at low temperatures, it might act as a protecting skin barrier to avoid frostbite. With a gauge factor of 7.05 and strain = 233%, PAOAM-PDO might be built as strain detectors to detect diverse human movements. In the interim, PAOAM-PDO might be produced in the single electrode mode as a TENG with a "sandwich" shape. Additionally, the resultant TENG functioned as a self-powered tool to LEDs and produced electrical outputs with only a simple hand touch. This work presents a workable method for creating multipurpose, environment-tolerant organo hydrogels that may find use in self-powered gadgets and wearable electronics [513].

TENGs and self-healing piezoresistive sensors were built by Li et al. [514]. An innovative all-weather self-powered intelligent traffic monitoring system is built using a novel PVA, polyacrylamide (PAM), and tannic acid modified cellulose nanocrystal dual-network hydrogel (referred to as PPC). This system monitors the vehicle's state using the triboelectrification effect and detects the driver's state using the piezoresistive effect. The self-healing feature of PPC-based strain sensor, which enhances long-term functionality of intelligent traffic supervising system, is caused by a significant quantity of hydrogen bonds and dynamic boron ester bonding. By inserting the PPC in PDMS with an elevated matrix on its surface, a single electrode TENG sensor that can measure a vehicle's weight and speed in real time is created. The

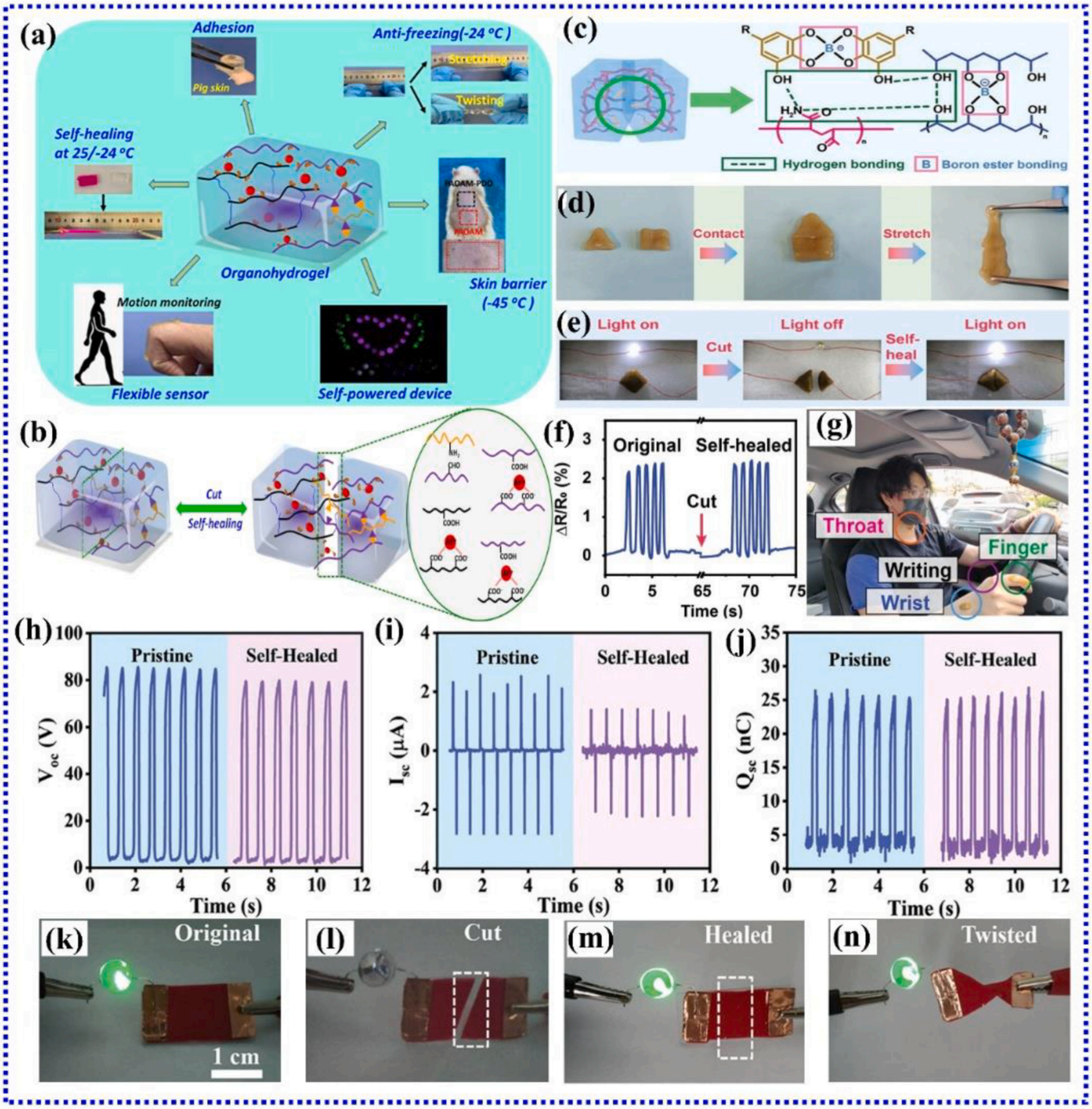

Fig. 52. (a) Multifunctional PAOAM-PDO organo hydrogel showing features of self-healing (25/-24 °C), good transparency, adhesiveness (on pig skin), conductivity, anti-freezing (−24 °C), skin barrier (−45 °C), flexible sensor, antibacterial property, environmental stability and self-powered device. (b) Probable PAOAM-PDO (organo hydrogel) self-healing mechanism. Reproduced with permission [513]. Copyright 2023, American Chemical Society. (c) PPC self-healing mechanism with combined impacts of dynamic hydrogen bonding and boron ester bonding. (d) PPC (2 pieces) with unique shapes self-healed into one piece, and they are stretchable. (e) PPC digital photos in a conductive loop with an LED. (f) $\Delta R/R_0$ plot of the original and the self-healed PPC strain sensor at the wrist within 1 min. (g) Photo of PPC sensor attached to the throat, wrist, and finger. Reproduced with permission [514]. Copyright 2023, Wiley-VCH. (h–j) M-TENG anti-freezing and self-healing performances. V_{oc}, I_{sc}, and Q_{sc} outputs of self-healed M-TENG in comparison with the pristine one. (k–n) TSA-ionogel self-healing process. Reproduced with permission [515]. Copyright 2023, Wiley-VCH.

resulting PPC-based strain sensor has a 97.4% self-healing efficiency and can quickly self-heal, regaining its sensing capability in about 1 min thanks to hydrogen and boron ester bonds. Ions in sodium alginate give the PPC-based strain sensor a relatively large gauge factor (8.39), which is based on piezoresistive effect and allows it to track driver fatigue and motion. In order to create dynamic boron ester bonding, the $B(OH)_4$ can readily engage with the two hydroxyl groups that are next to the PVA chains' cis-diol site. Concurrently, the $B(OH)_4$ can also effectively cross-link with tannic acid's catechol groups to create boron ester connecting, which enhances the PPC's capacity for quick self-healing (Fig. 52c). In order to illustrate the PPC's quick self-healing capability, square and triangular parts are touched together. As shown in Fig. 52d, the two PPC parts can be extended without shattering after 1 min of self-healing. The PPC can be utilized as a flexible wire for electricity for circuit maintenance thanks to SA. A sequence of circuits put together by the PPC and an LED bulb is depicted in Fig. 52e. An LED bulb illuminates when two chopped PPCs are connected, demonstrating the PPC's satisfactory conductive and self-healing qualities. By putting PPC-based strain sensor on a wrist and cutting it off, the strain sensor's capacity for self-healing is assessed. The PPC-based strain sensor remains able to precisely identify the wrist's 90° bending after 1 min of self-healing (Fig. 52f). Fig. 52g shows the photo of PPC sensor attached to throat, wrist and finger. By integrating several TENG sensors, it is possible to evaluate the average speed of cars, assign blame for traffic accidents, and avoid accidents caused by sleepy drivers without the need for monitoring cameras. Additionally, the PPC's all-weather operation is made possible by the partial substitution of glycerin for water. Intelligent traffic monitoring approach, which consists of wearable flexible

PPC-based strain sensors and the PPC based TENG sensors, creatively makes it possible to simultaneously monitor the condition of drivers and vehicles in order to maintain traffic safety and enable effective accident handling. This has important ramifications for the future development of smart urban transportation [514].

The advent of AI and IOTs era necessitates the progression of the self-powered wearable electronics. Stacked layers, rigid electrodes, and external sources of power continue to be major obstacles for common multifunctional electronics, which limits the advancement of flexible electronics. Xia et al. [515] proposed a transparent, antifreezing and self-healing ionogel (TSA ionogel) to design M-TENG and electromagnetic energy touch panel. TSA-ionogel is composed of amorphous PVDF-HFP (high-dipole-moment elastomer) and EMITFSI ionic liquid. Additionally, the TSA ionogel has excellent qualities such as 90% optical clarity, strain (greater than 600%), 120 kPa tensile stress, stability over a year, freezing endurance (253 K), and self-healing capacity. The resulting M-TENG based on TSA-ionogel exhibits a high output power density (200 mW/m^2) and a highly dependable electrical output at air conditions for a year. It functions as both a conductive electrode and a triboelectric material. Meanwhile, self-healing procedure of damaged M-TENG was easily accomplished in the ambient temperature (293 K for 24 h) without the need for unnecessary solvents, materials, or a thermal source because of the extremely reversible ion–dipole interactions among EMITFSI and P(VDF-HFP) polymeric chains. It is highly anticipated that M-TENG's self-healing capacity in an atmospheric environment will restore its electrical outputs, extending its lifespan. As seen in Fig. 52h–j, the damaged M-TENG's stable electrical outputs (Voc, Isc, and Qsc) are equivalent to the pristine one following self-healing in an atmospheric environment. A DC power source and LED a were linked in series with red ink dyed TSA-ionogel cable to further assess its electrical conductivity and self-healing potential. The LED could be illuminated at a driving voltage of 3 V, demonstrating the TSA-ionogel's exceptional conductivity (Fig. 52k). The LED was extinguished when TSA ionogel film was fully sliced with scissors into two pieces, as illustrated in Fig. 52l. After two TSA-ionogel pieces were separated and exposed to an atmospheric environment for 24 h, they completely self-healed to create a closed circuit, which allowed the LEDs to light up once more. (Fig. 52m and n). Additionally, compared to the pristine one, the conducting capacity of self-healed TSA-ionogel (60 wt% EMITFSI concentration) showed a little decrease (7.5%), going from 0.93×10^{-2} to 0.86×10^{-2} S cm^{-1}. Additionally, a microcontroller unit and arrayed M-TENG-based wearable self-powered control interface has been successfully investigated for wirelessly controlled smart home applications. More intriguingly, the electromagnetic energy from stray magnetic fields can be transformed into electrical energy using the human body as an antenna in accordance with Faraday's induction law. This electrical energy can then be used as self-powered power source to create a multifunctional TSA-ionogel-based epidermal touch panel that uses a surface-capacitive sensing mechanism. Concurrently, the self-powered EME-based epidermal touch panel built on TSA-ionogel has accomplished outstanding input capabilities, including playing Chinese Go and writing words. Thus, the created TSA-ionogel exhibits great promise in smart electronics, energy harvesting, and human–machine interface [515].

Wearable and flexible electronics have several uses in both human machine interaction and personal health monitoring. Zhang et al. developed an organo-hydrogel-based O-TENG with self-healing, antibacterial, stretchable, and antifreezing properties for biomechanical energy harvesting and self-powered sensing [277]. The Ag@rGO-PVA-PAAm hydrogel, integrating silver nanoparticles (AgNPs) on reduced graphene oxide (rGO) sheets, exhibits excellent stretchability, high conductivity, and cytocompatibility while effectively inhibiting gram-negative and gram-positive bacteria. The organo-hydrogel maintains flexibility at −30 °C, stretching up to 700% strain, and demonstrates superior antifreezing properties with no exothermic peak in the −90 to 25 °C range. Its dynamic borate crosslinking enables 72.5% mechanical self-healing efficiency within 12 h at 25 °C, retaining electrical functionality, as evidenced by its ability to power an LED post-repair. Even after damage, the O-TENG maintains stable output at ambient and subzero temperatures, making it a promising self-powered sensor for detecting handwriting and wrist movements while efficiently harvesting mechanical energy.

Hydrogel-based H-TENGs are gaining traction for wearable electronics due to their conductivity and flexibility, but challenges like complex polymerization and freezing limit their practicality. To overcome these issues, Feng et al. developed a transparent, anti-freezing, stretchable, and self-healing eutectogel-based TENG (E-TENG) using sulfonated lignin (SL) and Fe^{3+} coordination in a deep eutectic solvent (DES) [516]. The resulting eutectogel exhibits high stretchability (~450%), excellent ionic conductivity (8.70 mS cm^{-1}), and 93.5% transparency while withstanding temperatures as low as −80 °C. E-TENGs demonstrate stable electrical output with a power density of 53 mW/m^2, an open-circuit voltage of 105 V, and the ability to self-charge, lighting up 20 LEDs and powering commercial devices. Its self-healing capability, confirmed through LED circuit restoration after 6 h, further enhances durability. The amazing advancements in IoT technology for POC diagnostics have the potential to completely transform telemedicine and customized healthcare. By facilitating the early detection and prevention of numerous medical diseases, wearable biosensors that target a variety of physiological markers have significantly improved people's quality of life [273,517–519]. Tian et al. developed a self-healing, anti-freezing, and antibacterial nanocomposite hydrogel (PAGCA) by in-situ polymerizing acrylamide with gelatin and Ag NPs on tannic acid-modified CNTs (CNT-TA-Ag) [520]. This cost-effective modification improves CNT dispersion and conductivity (0.11 S/m), making PAGCA suitable for wearable piezoresistive detectors in athlete monitoring. Embedded in PDMS, the PAGCA-based TENG sensor effectively detects infractions, curling stone speed, and crashes, maintaining functionality at −30 °C by replacing water with glycerol. With a self-healing efficiency of 92%, it can be mechanically stretched and used as a wire to power an LED. This smart sensor system enhances athlete training and ensures fair decision-making in curling events.

The suggested violation detection system may be used as a next-generation smart sport supervision and assistance tool and might have a significant impact on the world of international sporting events. Bagchi et al., introduced a flexible, self-healing, and highly efficient hydrogel-based TENG for next-generation smart sports supervision and wearable electronics [521]. Using a semi-transparent hydrogel doped with AuNPs as the electrode and Ecoflex as the triboelectric layer, the device exhibits exceptional conductivity, 900% stretchability, and rapid self-healing within 2 min. The hydrogel, strengthened by hydrogen bonding and dynamic crosslinking, achieves 100% self-healing over 50 cycles and remains semi-transparent, making it suitable for energy harvesting on glass surfaces. Despite occasional breakage after 8000 cycles at 45 N force, the gel fully recovers within 10 min inside its Ecoflex packaging. With a record-high power density of 1680 mWm^{-2} and 26% energy conversion efficiency, this moldable TENG enables self-powered wearable and implanted devices, efficiently harnessing energy from body movements for diverse electronic applications.

He et al., developed a flexible sandwich-structured NBR/MXene/NBR film that self-heals within 5 s when heated and functions as a triboelectric sensor for tracking sports movements [522]. Zhao et al., introduced a self-healing triboelectric film using the DNCQ method, demonstrating exceptional mechanical recovery and suitability for intelligent robotics and human-computer interaction [523]. Zhang et al., synthesized a highly stretchable (4600%) ionic hydrogel with MXene nanosheets, enhancing energy harvesting efficiency in PTSM-TENGs [524]. Qin et al., fabricated a triboelectric self-powered sweat sensor from nanocellulose-based hydrogels, enabling real-time electrolyte monitoring with wireless data transmission [525]. Chou et al., developed a zwitterion-based elastomeric TENG with muscle-like flexibility, maintaining reliable performance in extreme temperatures (−30 to

60 °C) [526]. Shen et al., created a biodegradable polyurethane elastomer TENG (Cu-POU TENG) with self-healing efficiency of 77.5 % and stable electrical output, making it ideal for implantable and on-skin electronics [527]. These advancements highlight the transformative potential of self-healing TENGs in health monitoring, smart wearables, and human-machine interfaces.

7.4. Drug delivery applications

The advancement of precision medicine has led to increased demands on drug delivery systems (DDS). Low bioavailability, blood concentration fluctuations, first-pass action, and adaptability of constant rate delivery are some of the drawbacks of the conventional DDS that will increase side effects and decrease therapeutic efficacy. Controlled methods of delivering drugs on demand that improve safety, therapeutic impact, and adherence among patients are crucial, especially for some diseases that need long-term administration. The quick development and comprehensive investigation of DDS for time and space specific release has been facilitated by advancements in materials, micromechanical, and electronics technology. Drug delivery on demand can be accomplished by using internal stimulating signals like pH and glucose as well as external stimulating signals like magnetic, temperature, optical, electrical, and ultrasonic to initiate or regulate drug release. Because electrical impulses are simple to manipulate and can enable consistent and dependable drug release for therapeutic requirements, the electrically stimulated system has garnered a lot of interest among them. In addition, it is simple to integrate sensors or microchips to regulate medication administration and feedback. It establishes the groundwork for on-demand precision medicine and remote diagnosis and treatment [528]. Wound healing processes could be significantly accelerated by combining on-demand treatment with real-time monitoring. For effective wound care in this regard, Wang et al**.,** created a TENG and a multifunctional bilayer microneedle (MNs) as a theranostic platform [529]. Controlling infection, encouraging proliferation and cell migration, and having biochemical sensing capabilities are some advantages of this platform. The bilayer MNs consist of conductive stainless-steel MN (sMN) attached to a solvable polyvinylpyrrolidone MN (pMN). While the pMN, which is loaded with

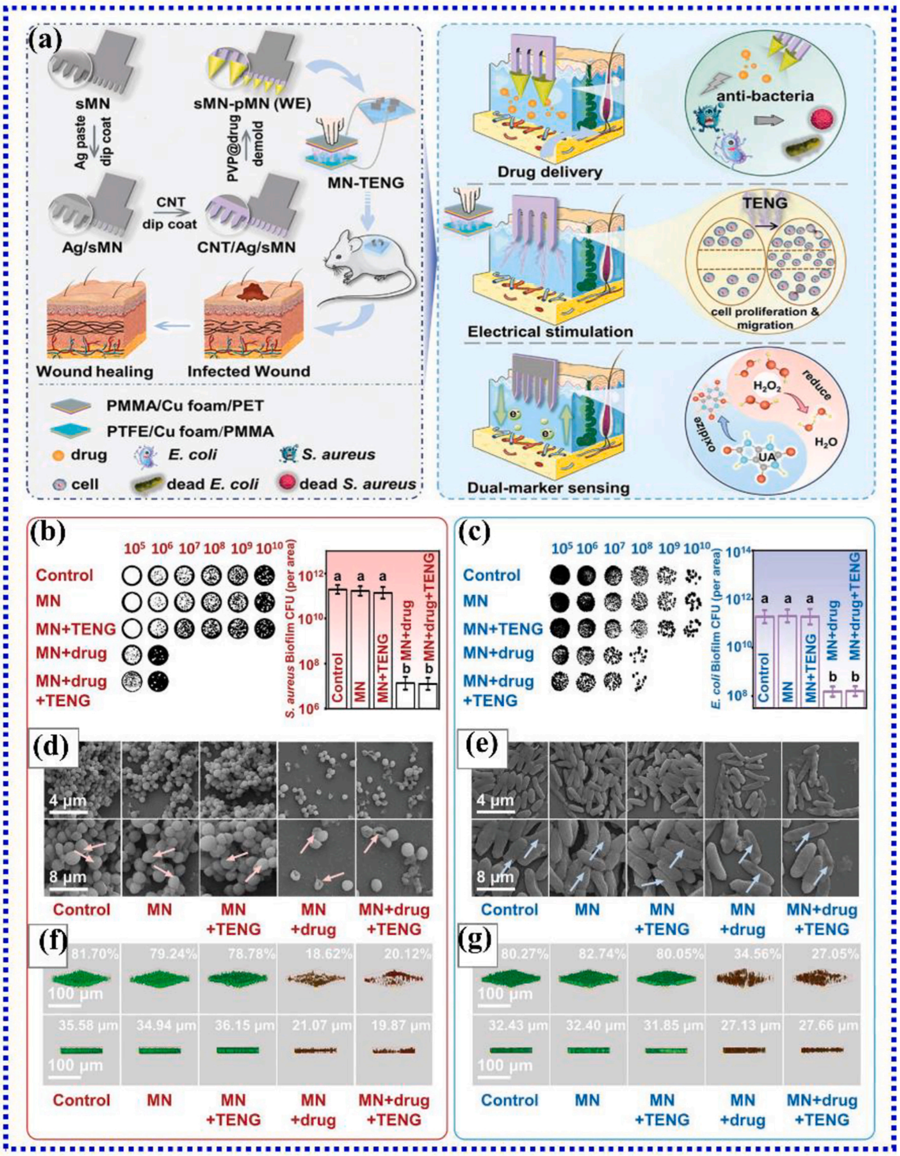

Fig. 53. (a) The schematic image for the MN-TENG-based theranostic platform's construction process (left) and operating principles (right). (b,c) Antibacterial effects on *S. aureus* and *E. coli* biofilm formation: CFU counts of *S. aureus* and *E. coli* biofilm formation. SEM images of (d) *S. aureus* biofilm. (e) *E. coli* biofilm. (f,g) 3D images of developed biofilms for *S. aureus* and *E. coli*. Reproduced with permission [529]. Copyright 2024, Wiley-VCH.

antibiotics, guarantees prolonged drug release upon dissolving in interstitial fluids, sturdy sMN penetrates the necessary skin depth. At the same time, the TENG produces electrical stimulation that is sent to wound site via conductive sMN, hastening the healing process. Additionally, by detecting uric acid and hydrogen peroxide, the silver and carbon nanotube-coated sMN (CNT-Ag-sMN) acts as a transdermal electrochemical sensor to evaluate the wound status. It is noteworthy that in vivo animal studies have shown that MN-TENG device is useful in enhancing the recovery from infected wounds since it not only efficiently suppresses bacterial growth and speeds up wound healing, but it also tracks wound biomarkers. The schematic image for the MN-TENG-based theranostic platform's construction process (left) and operating principles (right) is displayed in Fig. 53a. Antibacterial effects on *S. aureus* and *E. coli* biofilm formation: CFU counts of *S. aureus* and *E. coli* biofilm formation (Fig. 53b and c) (n=3, p<0.01, error bars show means ± standard deviations; bars with different alphabets (a,b) show statistically noteworthy variations between the two groups). 3D views of developed biofilms for *S. aureus* (Fig. 53f) and *E. coli* (Fig. 53g) with the information for dead/live bacteria ratio and the average thickness; microscopy images for (Fig. 53d) *S. aureus* and (Fig. 53e) *E. coli* biofilms, with arrows indicating bacterial deformation or destruction. Thus, this transdermal approach based on MN-TENG promotes improvements in therapeutic and diagnostic technologies in the fields of wound care and associated biomedical fields [529].

A self-powered wearable transdermal MN patch with a flexible TENG that can transform individual mechanical movements into electrical energy was created by Wang et al. [530]. This innovation greatly enhances drug penetration into deeper tissues by guaranteeing continuous gadget operation independent of an external supply. Water-soluble polymers combined with $CaCO_3$ NPs loaded with doxorubicin (DOX) and chlorin e6 (Ce6) make up the MNs. The dissolvable MNs quickly dissolved when the FTENG-integrated MN patch (also known as F-MN patch) was inserted into skin, allowing the drug-loaded negative-charged NPs to be delivered to the skin quickly. The F-TENG then produced iontophoresis, which forced these NPs into deeper skin sites. The acidic milieu in the tumor caused the pH-responsive NPs to rapidly dissociate once they reached the deep-seated melanoma. As a result, loaded DOX and Ce6 are directly released into the tumor, resulting in a synergistic impact for the deep-seated tumor through photodynamic and chemotherapies. One application of the F-MN patch was more effective than using the MN patch alone in preventing the formation of deep-seated tumors and extending the lifespan of tumor-bearing mouse in an animal model of deep-seated melanoma. This illustrates the wearable self-powered Minnesota patch's significant potential for effectively treating solid tumors in remote settings. The construction and actual images of the flexible triboelectric layer, which was made of silicone rubber and conductive fabric, are displayed in Fig. 54a further demonstrated the wearable proof-of-concept as a self-powered F-MN system. As seen in Fig. 54b, the patient's arm was fitted with a single side of MN patch which had MN arrays for the transdermal drug administration, while other side which included a conductive layer was fitted with an F-TENG to enable deep-tissue drug delivery. Because the manufactured F-MN device is small (about 0.5 cm^2), it can be worn on any area of the body with ease (Fig. 54c and d). The wearable self-powered F-MN device for treating deep-seated melanoma is schematically illustrated in Fig. 54e and f. The F-MN device, which is made up of F-TENG and a dissolving MN patch, operates as illustrated in Fig. 54e. A schematic of an MN patch that enables transdermal medication delivery to deeply lodged tumors is shown in Fig. 54f. This study is the first to use externally applied MN patches incorporated with F-TENG to promote

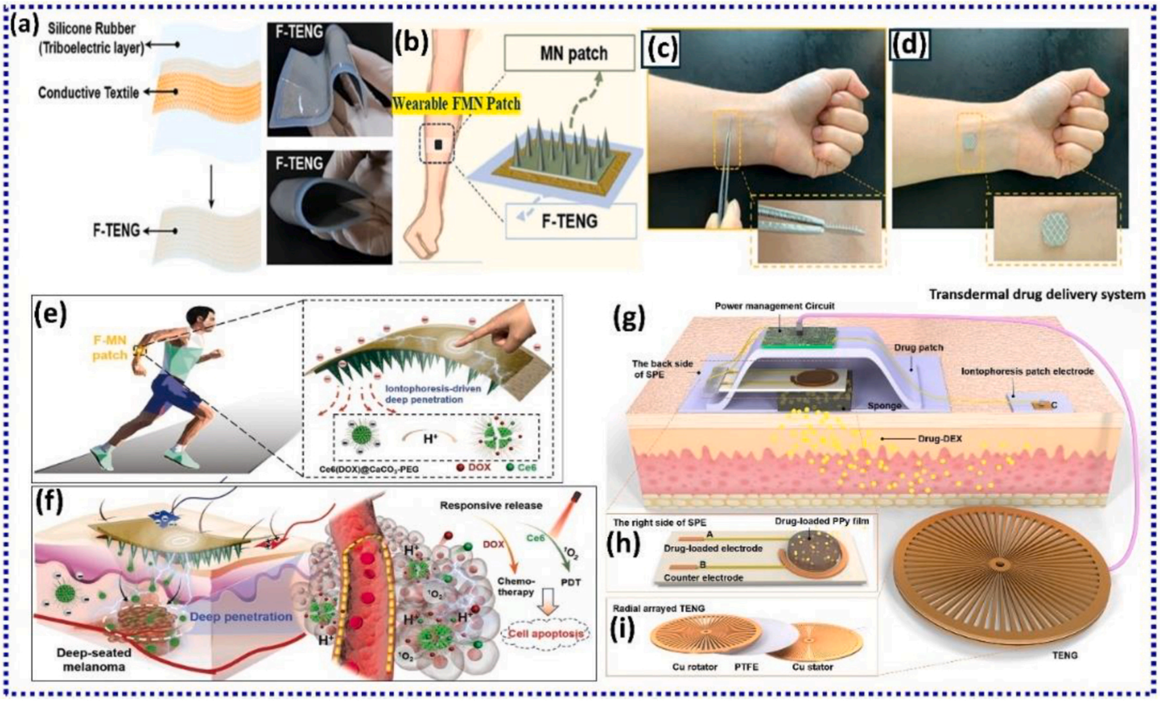

Fig. 54. Working mechanism of F-TENG in the contact separation mode. (a) F-TENG photographs (right) and schematic diagram (left). (b) Wearable F-MN patch schematic. (c,d) Photographs demonstration of wearable F-MN patch (c) before and (d) after attaching on human arm without puncture of skin. (e) Schematic of wearable self-powered F-MN for the treatment of deep-seated melanoma. (f) Schematic showing MN patch to facilitate TDD to deep seated tumors. Reproduced with permission [530]. Copyright 2023, Wiley-VCH. Schematic of self-powered, on-demand TDD system: (g) System contains transdermal patches (iontophoresis and drug patch electrode), power management circuit and TENG. (h) Right side of SPE. DEX-P loaded PPy porous films electrodeposited on drug-loaded electrode A of SPE, which serves as the reservoir of drug. The DEX-P- can release from PPy film into PBS-soaked sponge when the TENG is operated to power SPE. After electric-stimulated release, TENG is utilized further for the iontophoresis activation by powering electrode A, and iontophoresis patch electrode C to improve efficiency of drug delivery in skin. (i) TENG radial-arrayed rotary contains one PTFE layer and two copper layers. Reproduced with permission [531]. Copyright 2019, Elsevier.

deep-seated tumor therapy and facilitate drug penetration without the need for surgery, even though numerous implantable TENG-based devices have been successfully previously reported and investigated for cancer therapy via delivery of various therapeutic drugs. For improved transdermal medication delivery, certain systems that utilize a combination of MNs and iontophoresis have been developed; however, these systems often require an external power source and lack the self-powered capability. By delivering macromolecules of biology or therapeutic NPs to deep skin areas for local or systemic use, this study will also be beneficial and reliable for treating other disorders, like diabetes [530].

An on-demand, self-powered, transdermal medication delivery system powered by TENG was introduced by Ouyang et al. [531]. To activate iontophoresis therapy for improved drug delivery efficiency and to activate the electric-responsive drug carrier for regulated drug release, a miniature TENG and a custom power management circuit were developed. Fig. 54g–i schematically represents the on-demand self-powered transdermal drug delivery approach. Power management circuit of system can store, modify, and stabilize electricity for the on-demand release of drug activities, while the TENG can generate electricity from biomechanical energy. Obtained findings ascertain that TENG can be easily operated to achieve the on-demand medication release. 3 μg/cm^2 dosage of medication can be released by manually spinning the TENG (30–40 rpm) for 1.5 min. Additionally, by adjusting the power management circuit resistance or the length of time that TENG charges, the system has accomplished a tunable rate of drug release for transdermal drug delivery, which can be adjusted from 0.05 μg/cm^2 to 0.25 μg/cm^2 per minute. Effectiveness of this TENG-based drug delivery device is further confirmed by ex vivo tests conducted on pig skin, which show a roughly 50% improvement over traditional transdermal patches. The goal of the suggested method is to give patients a simple way to obtain a personalized medicine release rate and dosage [531]. For in situ treatment of hepatocellular carcinoma (HCC), Zhao et al. [532] created an intelligent DDS based on implantable TENG and red blood cell. In order to make the transition from oral formulation to injection preparation, apatinib, an oral anticancer medication that can block the production of the vascular endothelial growth factor receptor-2 (VEGFR2), is loaded into red blood cells. Effective biomechanical energy harvesting is possible with multishape iTENG that is tailored for various implant locations and conditions. The DDS is very controllable since the electric field produced by the iTENG can accelerate the release of APA, and the release will rapidly reduce when the electric field stops. With a remarkably lower APA dosage, the controlled DDS exhibits an interesting capacity to destroy HCC cells both in vitro and in vivo. The self-powered DDS has a noticeable therapeutic impact on rabbits with HCC after implantation, and clinical medicine is anticipated to use it [532]. The special benefits of ease, self-administration, and safety have drawn a lot of research and clinical interest in transdermal drug delivery (TDD) systems with control via feedback. For the closed-loop detection of motion and therapy, self-powered, a wearable, iontophoretic TDD system that may be controlled and driven by energy extracted from biomechanical movements is suggested. A hydrogel-based soft patch with side-by-side electrodes is intended to enable noninvasive iontophoretic TDD, while a wearable TENG serves as an energy harvester and motion sensor that may transform biomechanical movements into electricity for iontophoresis without the need for stored power energy sources. Proof-of-concept tests using dyes as model pharmaceuticals on pig skin effectively show that the suggested approach is feasible. This approach may offer a financially viable option for noninvasive, electronically assisted TDD and closed loop sensing and therapy, in addition to expanding the use of TENG in the biomedical industry [533].

Therapeutic intracellular drug/biomacromolecule administration that is nondestructive, highly effective, and on-demand is still exceedingly difficult. In vitro and in vivo, Liu et al. [534] created a bio-mechanical energy-powered TENG driven electroporation device for the intracellular delivery of drug that is very effective and causes little cell damage. A self-powered TENG acting as a steady voltage pulse source in the integrated system causes the membrane permeability and plasma membrane potential to rise. By improving the localized field of electricity at nanoneedle cell interface and reducing plasma membrane fluidity to increase molecular inflow, the silicon nanoneedle-array electrode works in tandem to reduce cellular damage during electroporation. With 90% of delivery efficiency and cell survival of over 94%, the integrated system effectively delivers exogenous components (macromolecules, siRNA, and small molecules) into various cell types, containing primary cells that are difficult to transfect. It effectively achieves a transdermal biomolecule distribution with a depth augmentation of more than three times in mice through straightforward hand slapping or finger friction with the wearable TENGs. Wearable medicine and self-tuning drug administration have a lot of potential thanks to this incorporated, self-powered active electroporation drug delivery system [534]. It is still very difficult to help patients with a curative impact because cancer chemotherapy has been shown to have serious adverse reactions and low therapeutic performance. A self-powered DDS was devised by Chen et al. [535] and included two Au electrodes and a current source that was obtained from disk TENG (D-TENG). Thus, the current followed by D-TENG's action could trigger cells seeded within electrode's gap. The D-TENG obtained 2.8 μA of average output current and a peak output voltage and current of 135 V and 3.7 μA under a rotation frequency of approximately 7.4 Hz. Additionally, under long-term conditions, the D-TENG demonstrated good stability in producing a consistent current. When this self-powered drug delivery system applied electric stimulation, cancer cells significantly absorbed the chemotherapeutic medication doxorubicin (DOX). Thus, using a new TENG device in chemotherapy would open up new possibilities for the treatment of diseases in the future [535]. Myopia poses a significant challenge, particularly in youngsters, for whom atropine and 7-methylxanthine are used in therapeutic care. This requires many doses, has significant side effects, and results in inadequate compliance because of the resistance of the children. To address these problems, a self-generated electricity-driven DDS (EDDDS) for the treatment of precision myopia was proposed by Jiang et al. [536]. In order to efficiently slow down the growth of myopia, the EDDDS uses drug-coated nanogenerators to intelligently release therapeutic medications, including atropine, at ocular tissues. This system achieves regulated and reactive drug administration by combining nanotechnology with intelligent drug delivery technologies. Targeted treatment is provided by the nanogenerators built into the EDDDS, which produce electric fields that cause drug release in response to ocular problems. Concurrently, a small voltage can efficiently relax the ciliary muscle, providing further advantages for the treatment of myopia. Experiments both in vitro and in vivo have shown how effective and promising the EDDDS is at accurately controlling the course of myopia. The suggested EDDDS has a lot of potential as a cutting-edge, highly accurate therapeutic strategy for the treatment of myopia. It is a promising direction for further study and clinical applications because of its capacity to solve the drawbacks of existing treatments [536]. A hypertension emergency is a medical emergency in which a patient's blood pressure suddenly and significantly rises as a result of certain triggers, with potentially fatal results. Sodium nitroprusside is frequently injected intravenously to quickly reduce blood pressure. Its specialized nature, however, restricts its use for self-help or first aid in emergency scenarios. In order to solve this problem, Chen et al. [537] designed a simple, self-powered, controlled microneedle drug delivery device that effectively lowers blood pressure. The system is primarily constituted of two components: a drug delivery module consisting of PLA-gold microneedles and polylactic acid-gold-polypyrrole MNs, and a piezoelectric thin film self powered module built of CNTs and PVDF. The findings demonstrate that varying pressures imparted to the self-powered modules produce varying voltages, which regulates the microneedles' drug release efficiency. It is more effective and has a higher rate of medication release than traditional active devices. Additionally, the technique was effectively used to lower and regulate blood pressure in rats who developed spontaneous hypertension. This technique has been shown to be biologically safe and is more successful in lowering and controlling blood pressure levels than sodium nitroprusside injections. With significant therapeutic application potential, this work offers a manageable and user-friendly fast blood pressure reduction device appropriate for hypertensive emergencies [537].

7.5. Photodetector applications

Self-powered nanosystems and nanosensors have attracted substantial attention over the past few decades. Moreover, they have progressively developed as the most promising and desirable prototype for the environmental detection/protection because battery is not required to power the device. In 2014, Lin [538] and his coworkers reported the first photodetector based on TENG. A simple and economical method to produce PANI-PPY conducting nanoflakes with the self-healing properties was shown by Singh et al. [539]. A contact separation mode TENG-based self-powered photosensor with 149 V of maximum voltage, maximum current 16 mA of, 0.56 mAcm^{-2} of current density, and 83.56 mWcm^{-2} of power density was constructed using these PANI-PPY NFs. A thorough review of the literature demonstrates how PANI-PPY NFs are compared to other photo-sensing materials. This study emphasizes PANI-PPY's amazing capacity for self-repair and its incredibly quick self-powering nature. Moreover, it also shows how temperature-assisted polymerization, which requires only stirrer with a hot plate, can be used to create polymeric nanomaterials in a very simple and economical manner. When the molecules number in polymer chains under study is enhanced, theoretical analysis (DFT calculations employing Gauss view 05 and Gaussian 09) consistently demonstrates an improvement in stability. Prior to and following healing, the self-healing TENG demonstrated consistent performance [539]. The compact UV photodetector serves as a timely reminder to people about excessive UV radiation exposure. Nevertheless, the conventional UV photodetector is unable to satisfy the practical requirements, and the issue with the power supply prevents it from being developed further. Zhang et al. [540] showed how to combine triboelectric and photoelectric phenomena to create flexible, transparent, and self-powered UV photodetector. The apparatus incorporates LEDs on PET film, a flexible and transparent film based TENG (TFFTENG), a flexible ZnO nanoparticle UV photodetector, and commercial chip resistors. Fig. 55(a–f) demonstrates self-powered photodetector for the UV surveillance application. In order to enable self-powered detection, TFF-TENG may capture mechanical energy from the finger sliding and tapping action and use it to power ZnO NP UV photodetector. As the power intensities increase from 0.46 to 21.8 mW/cm^2, the voltage of constant resistors connected in series with UV photodetector varies from 0.5 to 19 V. The number of LEDs directly

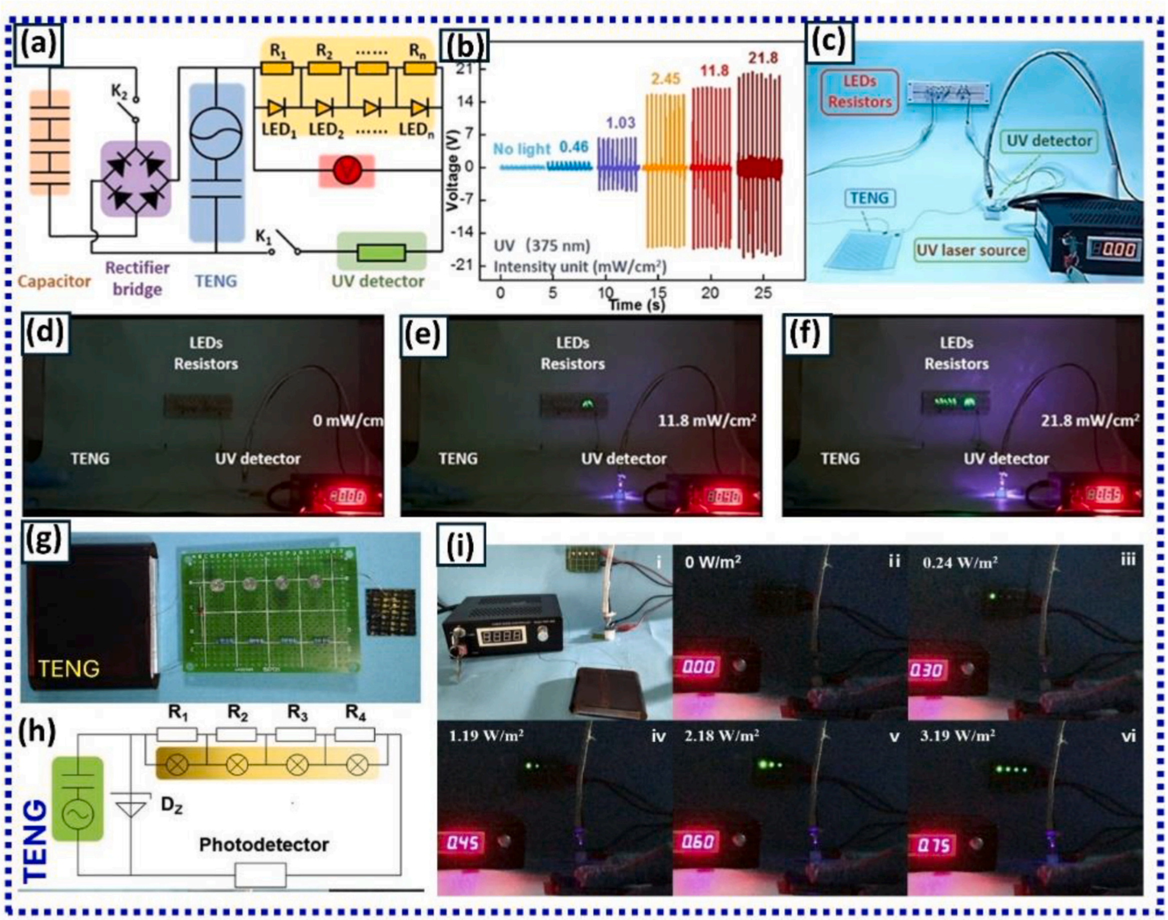

Fig. 55. Demonstrations of self-powered photodetector for UV surveillance application. (a) Self-powered semiquantitative UV photodetection system circuit diagram. (b) Voltage across constant resistor under various intensities of UV light for the tapping mode (2 Hz frequency). (c) Photo of designed self-powered quantifiable UV photodetection system. (d) Without UV light LEDs cannot be lit, (e) one part of the LEDs can be lit under 375 nm UV with 11.8 mW/cm^2 power intensity irradiance, and (f) two parts of the LEDs can be lit under 375 nm UV with 21.8 mW/cm^2 power intensity irradiance. Reproduced with permission [540]. Copyright 2020, American Chemical Society. (g) Representation of self-driven photodetection based on impedance matching impact between MoS_2 and photodetector TENG. (h) Self-driven photodetection system equivalent circuit. (i) Images of self-driven photodetection under test, and optical images of LEDs at in dark and light intensities of 0.24 W/m^2, 1.19 W/m^2, 2.18 W/m^2, 3.19 W/m^2 (405 nm). Reproduced with permission [541]. Copyright 2019, Elsevier.

reflects this voltage variation. The device's exceptional flexibility and transparency may expand its range of applications; for instance, a portable device of this kind may be employed to monitor UV radiation in real time and alert people to strong UV light [540].

It is critically necessary to build electronic systems that does not need an external power source to achieve self-powered photodetection. Using a vertical CS-TENG as power supply, a MoS_2 nanosheet photodetector as light intensity sensor, and multiple LEDs as an alarm, Han et al. [541] suggested a self-driven photodetection system. Self-driving photodetection system based on the impedance match effect between the MoS_2 and TENG photodetectors is shown in Fig. 55(g–i). The MoS_2-based planar photodetector was created using a lift-off procedure and a traditional photolithography technique. It has outstanding repeatability properties under light on-off switching, a high current on-off ratio, and a high sensitivity for visible light illumination. When these functional devices are combined, the photodetector's load resistance, which reacts to light intensity, adjusts the CS-TENG's induced output voltage. The mechanism can be attributed to matching impedance effect between the photodetector's operational state and certain TENG output characteristics. The self-driven device's current and voltage vary between 0.06 and 4.78 μA and 1.58–20.60 V (0–3.19 W/m^2 light intensity range), respectively, thanks to the addition of a Zener diode, which functions as a voltage regulator. With an extreme current on-off ratio and outstanding repeatability properties under light on-off switching, the device is extremely sensitive to visible light illumination. The recuperation time was 0.36 s, and the response time was 0.32 s. After that, the circuit is adjusted to use the arch TENG as the source of voltage to generate a steady voltage output. Lastly, it is shown that the CS-TENG's output fluctuates in response to the MoS_2 photodetector's changing operating states before precisely reflecting on the number of LEDs that are illuminated [541]. The creation of a piezo-triboelectric hybrid nanogenerator (STPHNG) based on a ZnO- $CsPbBr_3$-PVDFHFP system for the photodetection in ultraviolet to visible range was documented by Baro et al. [542]. It has been demonstrated that encapsulating chemically produced $CsPbBr_3$ nanoparticles (about 10 nm) in the PVDF-HFP polymers is a great way to achieve STPHNG with long-term stability. When $CsPbBr_3$-PVDF-HFP comes into contact with ZnO nanorods that have an average diameter of about 55 nm, it not only encapsulates the $CsPbBr_3$ nanoparticles from the surrounding environment but also provides a suitable piezoelectric behavior to increase triboelectric characteristics by five times. Once more, changes in the STPHNG output under either visible or ultraviolet light were used to realize the hybrid nanogenerator's photodetection capabilities. Tribo-charges' screening action, which alters the nanogenerator's intrinsic capacitance in addition to lowering the open-circuit voltage, is what causes the light-induced change in the output. The exceptional optical absorption qualities and tribo-charge shielding in the active materials are the sources of the excellent photoresponsivity values of approximately 6.59 × 104 and 3.67 × 104 V/W for visible and UV light, respectively. Furthermore, after the STPHNG was attached to the human body, the real-time photodetection capabilities was examined. The STPHNG may be controlled by the normal motions of the human body, including knee, finger, and wrist bending. For experimental demonstration, the STPHNG connected to a user's index finger for use with basic biomechanical movements like finger bending or movement. As shown in Fig. 56a, the measurement was carried out using an Arduino UNO with a Bluetooth module. An illustration of the photodetection process during movement of the finger under UV illumination is shown in Fig. 56b. The connected PC can be used to monitor the output production under both light and dark illumination circumstances, as illustrated in Fig. 56c. The output voltage drops in light illumination conditions as opposed to dark ones. Additionally, an end-user can get the output voltage data that is created

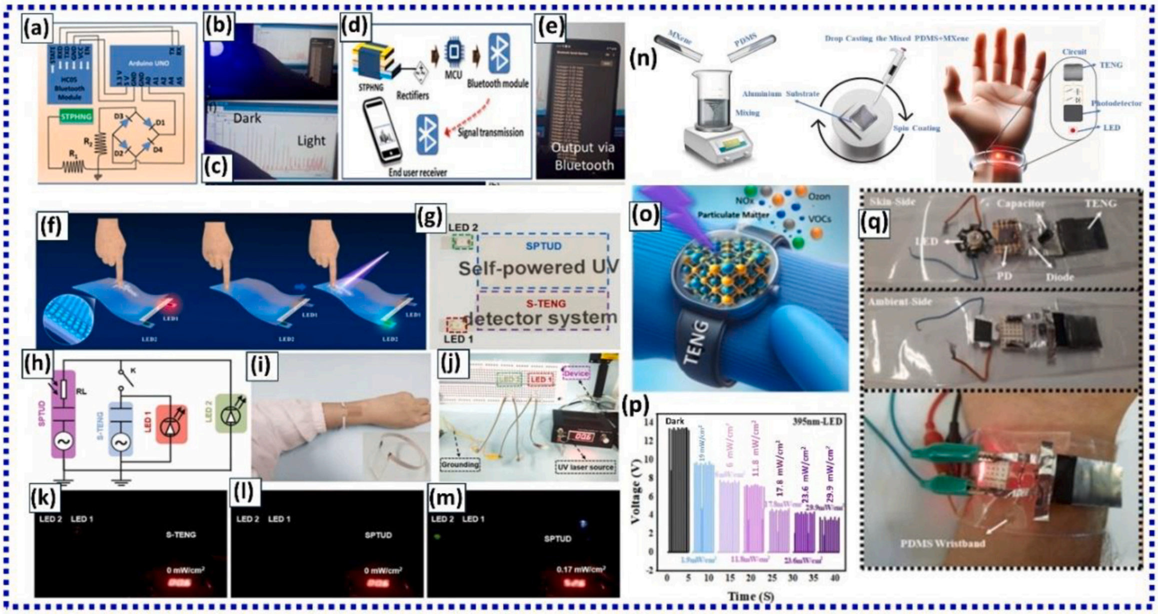

Fig. 56. (a) Circuit diagram schematic used for transmission of data. (b) Photodetection image during light and dark illumination situation. (c) Harvested voltage peaks at the PC during light and dark illumination situations. (d) Schematic of transmission of data for photodetection of as-designed STPHNG. (e) Harvested output voltage data in the mobile phone. Reproduced with permission [542]. Copyright 2024, American Chemical Society. (f–m) Representation of SPTUD wearable system for practical self-powered UV photodetection: (f) Systematic configuration, (g) photo and (h) circuit diagram of self-powered wearable UV photodetection, (i) photo of tester wearing bracelet with self-powered wearable UV photodetection system (inset represents the bracelet photo), (j) photo of simulated scenario test the self-powered UV photodetection approach, (k) illustration of LED1 can be glown without UV light when triggering the S-TENG, (l) LED cannot lit without the UV light when only triggering SPTUD, and (m) LED2 can lit under 0.17 mW/cm^2 of 375 nm UV light when triggering SPTUD. Reproduced with permission [543]. Copyright 2023, Elsevier. (n) Schematic of mixing procedure of MXene and PDMS, coating mixed MXene + PDMS on Al substrate, PDMS wristband with the LED + photodetector + TENG, and a circuit on it. (o) Schematic of self-powered UV detectors coupled with the TENG as wearable electronic. (p) time vs voltage for the self-powered photodetector under UV LED illumination in various intensities. (q) Device physical demonstration. Reproduced with permission [544]. Copyright 2024, Elsevier.

under both light and dark illumination circumstances (Fig. 56d). The Arduino UNO's HC05 Bluetooth module allows a smartphone to remotely monitor the photodetection data, as seen in Fig. 56e. As a result, UV exposure can be remotely monitored using the manufactured STPHNG. The development of flexible/wearable photodetectors may be facilitated by the improved photodetection demonstrated by the ZnO and CsPbBr3/PVDF-HFP-based STPHNG. The ZnO-CsPbBr3/PVDF-HFP system's output modification, outstanding photodetection, and stability over the long term could provide the groundwork for wearable, futuristic, reasonably priced photodetectors with exceptional longevity and efficiency [542].

Self-powered photodetectors can meet IoTs development requirements for intelligence, multifunctionality, integration, and reduction. The design and development of a self-powered triboelectric UV photodetector (SPTUD) based on the photoresistive effect and coupling impedance matching was documented by Peng et al. [543]. By substituting a ZnO nanoparticle layer for the conventional electrode in single electrode mode TENG, a sensing-electrode model is verified. The resistance variability range of the ZnO film, which functions as both an electrode and a photo resistive material, closely resembles resistance dependence of the S-TENG. Impedance matching phenomenon causes the ZnO film's variable resistances to change in response to UV light intensity, which has a substantial impact on the output voltage. Under 375 nm ultraviolet illumination, the voltage signal of the self-powered UV photodetector SPTUD rises from 0.5 V to 1.1 V as the light intensity increases from 0 to 0.61 mW/cm^2 at a voltage responsiveness of 2.66 V (mW cm^{-2})$^{-1}$, it can effectively detect UV light at a low intensity of 0.17 mW/cm^2. Fig. 56f-m demonstrates SPTUD wearable device for the real-time self-powered UV photodetector application. A self-powered wearable UV photodetection system relying on the S-TENG and SPTUD is combined into a bracelet for demonstration purposes (Fig. 56l). Sensing and reference electrodes are made to be connected to chip LEDs for visible UV light photodetection, which serves as a reminder to individuals to take preventative steps against hazardous UV light outside. This work may open up new possibilities for development of self-powered triboelectric sensors in the future [543].

Mirsepah et al. [544] reported an effective and sustainable wearable technology for environmental sensing and health monitoring. To facilitate convenient and effective comprehensive health monitoring, a self-powered wearable sensor that can simultaneously measure heart rate and UV exposure was created. Users can get real-time information into how the environment affects their health (UV exposure) and physical well-being (heart rate) by combining these features into a single gadget. Semiconducting MoS_2 crystal was mechanically exfoliated between the two gold electrodes in a horizontal arrangement to create the MoS_2 photodetector. In order to generate electricity, the photodetector was coupled with a MXene + PDMS based TENG. A diode was integrated to stabilize peak voltages. Fig. 56n exhibits a schematic illustration of the procedure of combining PDMS and MXene, then applying a spin coating onto a 1 × 1 cm sheet of Al foil. As shown in Fig. 56n, the assembly which consists of TENG, LED, and the photodetector is next put onto PDMS wristband. This all-encompassing strategy combines multiple elements to enable the photodetector to self-power, increasing its usefulness and adaptability in real-world applications. The voltage response of the photodetector to the UV light intensity may be precisely measured in AC mode when photodetector is exposed to the UV light and key “1” is closed while key “2” is open. This mechanism is demonstrated in Fig. 56o and p, which shows how the voltage of the photodetector changes in response to varying UV intensity levels. Under 395 nm-LED illumination, the responsivity and specific detectivity are 1.5 × 1014 Jones and 4.7 × 107 V/W, respectively. This feature increases the photodetector's usefulness beyond merely detecting visible light, making it an important instrument for uses involving UV sensing, like biological research, industrial operations, and environmental monitoring. The experimental measuring procedure and the actual physical presentation are shown in Fig. 56q. The diastolic and systolic phases of heart are represented by the current peaks in an “I-t” diagram caused by LED light reflected off fingertip onto photodetector's active area. The heart rate was computed by the device and compared to data acquired from clinical settings. This self-powered, flexible, and lightweight photodetector holds promise for wearable sensors that don't require batteries. According to this invention, the 2D photodetector may be able to operate without the need for additional power sources or traditional batteries, which would make it perfect for flexible and energy-efficient wearable technology. By encouraging a thorough awareness of one's general health, this integrated approach enables people to take preventative action to lower risks and enhance their well-being [544].

A TENG has been proposed as a power source for self-powered sensor networks based on impedance matching effect, which has garnered a lot of interest in the Internet of Things community. However, in real-world working situations with unpredictable mechanical stimuli, the conventional TENG's current, and voltage are influenced by both working frequency of TENG and load impedance. This results in erroneous sensing data. Wang et al., introduced a self-powered sensing system using a Pulsed-TENG with a synchronized trigger switch, ensuring that its current and voltage remain independent of operating frequency [545]. This approach enables consistent photodetection results regardless of rotation speed. Two detection modes were developed: current mode (0–1 W/m^2), where output current increases linearly with light intensity, and voltage mode (9–403 W/m^2), where output voltage is inversely proportional to light intensity. A self-powered photodetection device with a visual LED display was created, using LEDs to indicate light intensity. The system, powered by an RF Pulsed-TENG, operates effectively under unpredictable mechanical stimuli, making it suitable for real-world applications.

Recently, there has been interest in wearable UV photodetectors for detecting excessive UV radiation exposure of the skin. Even though there have been many advancements in this area, there are still many obstacles to overcome, especially when it comes to the device's self-powering and reliability under simultaneous high mechanical deformations. Using kirigami-inspired honeycomb-patterned Zno NWs and a TENG, Kumaresan et al. [546] demonstrate a self-powered stretchable photodetector. Following a thorough investigation of the effects of the metal-ZnO NWs contacts and the ZnO NWs dispersion medium, a unique fabrication technique utilizing structural engineering on the NWs-elastomer composite is utilized to attain high stretchability. With a dark/photo current ratio of 5 × 105, a responsivity of 54 A W^{-1}, and a quick recovery time of 100 ms, the synthesized ZnO NWs based UV photodetectors, implanted inside a kirigami-inspired honeycomb-patterned elastomeric substrate, demonstrate unparalleled stretchability of 125% and great performance. Additionally, a self-powered system for possible use in actual time UV radiation monitoring utilizing cutting-edge wearable healthcare technology is demonstrated by the stretchy PD in conjunction with flexible TENGs [546].

Wang et al., proposed a self-powered photo-detection system using a paper-based contact-separation TENG to power a silicon PIN photodetector, eliminating the need for an external power supply [547]. The photodetector, based on scalable silicon processing, is connected to the TENG via a rectifier bridge circuit. When exposed to light, the detector's resistance decreases, altering the TENG's output voltage due to the internal photoelectric effect and impedance matching. The system's performance was analyzed under varying lighting conditions, with a circuit model developed to study current influence on detection range. Light intensity detection was demonstrated using LEDs as display devices, highlighting the potential of TENG-based self-powered sensors for large-scale IoT applications.

7.6. *Artificial intelligence and machine learning*

To accomplish highly effective gathering of energy from linear movement of a stick used for walking with ultralow frequency, Guo et al. [548] constructed a linear to rotary structure. To give motion-impaired individuals a healthcare monitoring platform, a walking stick with deep learning-enabled sophisticated sensing characteristics was created and driven by ultra-low-frequency human motion. Additionally, two different types of the self-powered triboelectric sensors are suggested and combined to extract walking stick's motion characteristics. Deep learning-based data analysis has made it possible to perform augmented sensing functions with high accuracy, such as motion status differentiating, disability evaluation, and identity recognition. It also yields a self-sustaining Internet of Things system that includes humidity and temperature amenity sensing capabilities and global positioning system tracing. When used in conjunction with the previously mentioned features, this walking stick is shown in a variety of circumstances as a caregiver for monitoring activity and well-being in real time. The caring walking stick has the potential to be a clever tool that helps people with motion impairments live their lives safely and independently. More gadgets and systems have been combined with AI as a result of the technology's quick development, enabling automation control, status recognition, and intelligent decision-making. Devices can learn more representative aspects of raw signal data by training an end-to-end artificial neural network, which opens the door to more sophisticated functionality. Therefore, implemented the deep-learning technique to examine and extract every element of five-channel P-TENG output to create a caring walking stick with sophisticated tracking features. A particular output profile for 5 electrode P-TENG can be generated in an ongoing procedure of a walking stick touching and leaving ground show in Fig. 57a and b. Different output profiles from various users and movements can be produced during a full gait cycle using the walking stick due to the different contact spots, contact series, and contact force.

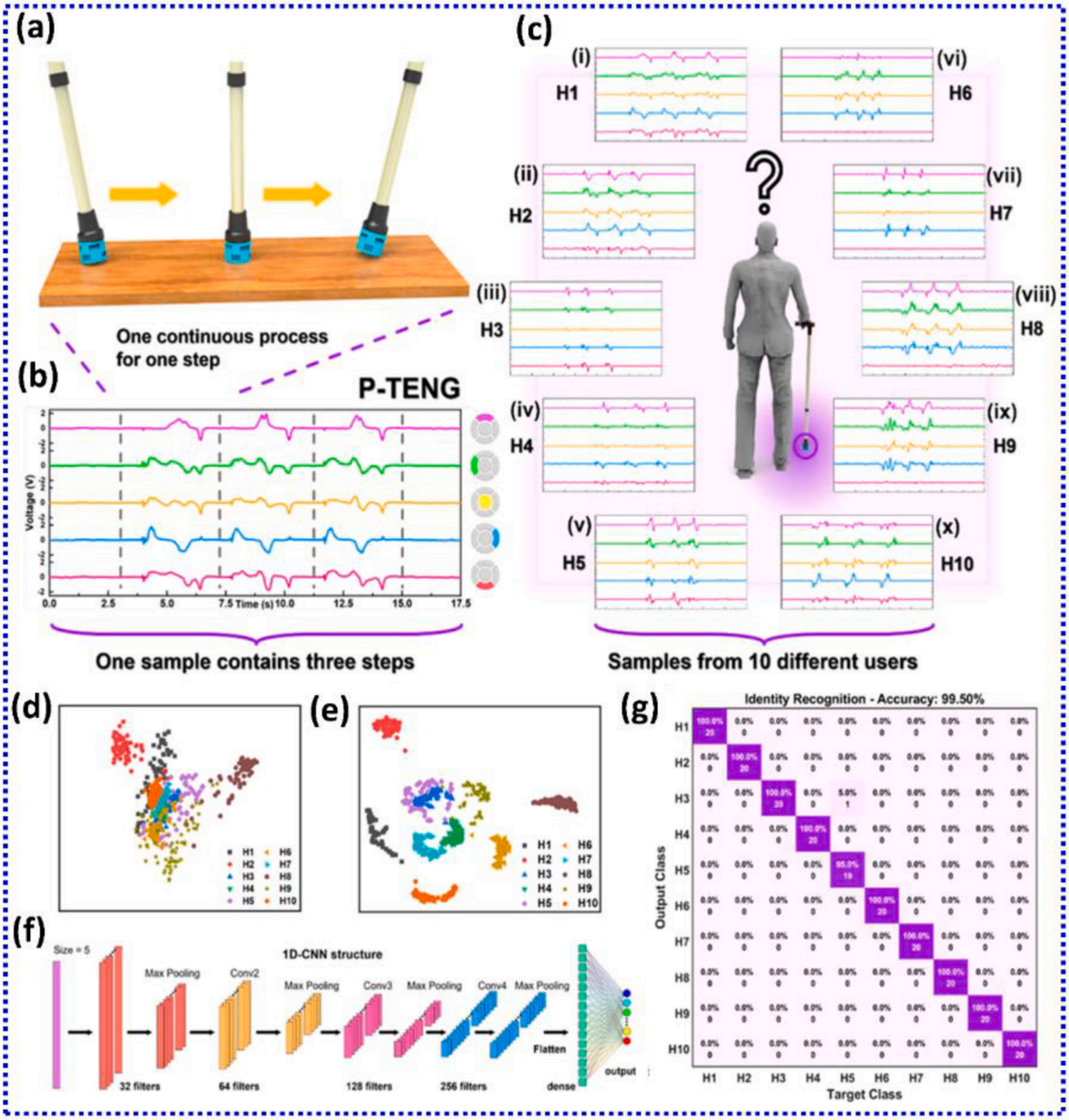

Fig. 57. (a) Schematic representation of the contact and leaving procedure of the walking stick for one step. (b) Subsequent output profiles were produced from 3 steps of the user. (c) Output profiles collected from ten distinct users. All curves have the same x and y-axis as (b). (d) PCA from ten distinct users. (e) t-SNE curve from a data set attained from ten distinct users. Separation of the clusters after each user demonstrates the discriminative ability of P-TENG. (f) A comprehensive structure of an employed 1D-CNN model for deep learning. (g) Confusion matrix for identity recognition for ten distinct users. Reproduced with permission [548]. Copyright 2021, American Chemical Society.

The P-TENG's real-time output signals for ten distinct users, designated H1 through H10, are displayed in Fig. 57c (i–x), which was obtained by using Arduino MEGA 2560 microcontroller. One sample includes output signals for 3 consecutive steps, totaling 3500 points of data for every channel. Eighty samples were gathered for each user in order to construct the entire data set. Of the 80 samples, 20 sets are selected at random for testing and 60 sets are selected at random for training. As illustrated.

in Fig. 57d and e, highly dimensional sensations have been envisioned into the 2D space using t-distributed stochastic neighbor embedding (t-SNE) and PCA (principal component analysis) in order to instinctively demonstrate the discriminative ability of P-TENG. It is evident that the data gathered from various users spontaneously creates unique clusters, demonstrating the walking stick's effectiveness as a tool for identifying people. Although it is possible to identify differences in the signals under various settings, it is nearly impossible to manually extract enough characteristics to differentiate between these testing conditions. To achieve sophisticated data analytics, a deep-learning model was constructed using 1D convolutional neural network (CNN) structure shown in Fig. 57f. Fig. 57g displays the associated confusion map for the 10 users' identity recognition, demonstrating an excellent accuracy of 99.5%. Although this phenomenon has rarely been studied and addressed, the high accuracy of recognition has further confirmed that the motion characteristics and gait patterns of sensory information gathered from walking stick employed by different users are distinct. Additionally, it shows that the P-TENG's five electrode sensor architecture is useful for detecting tiny motion variations, as it is sufficiently sensitive to differentiate between ten movement patterns from various

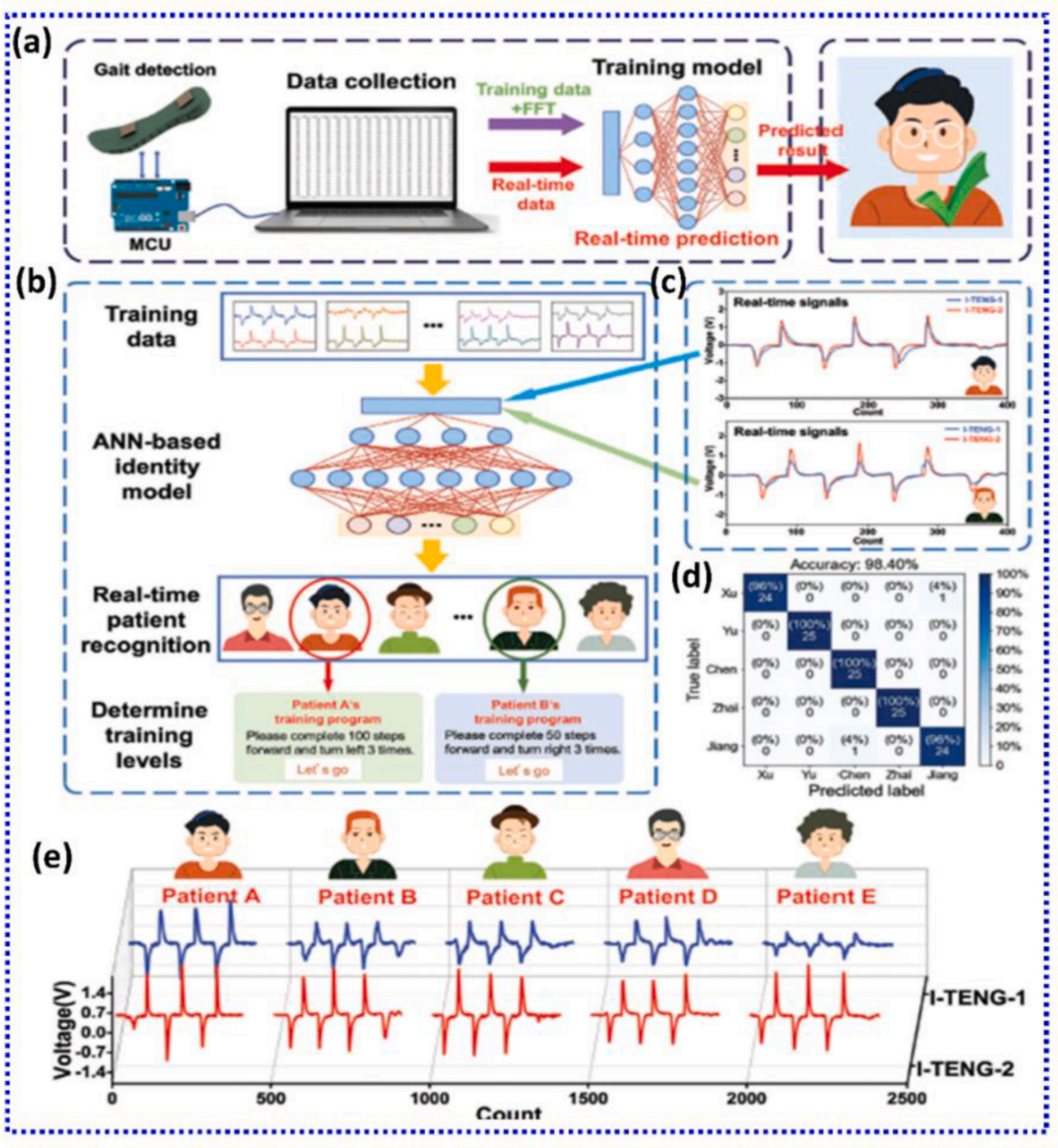

Fig. 58. (a) Schematic of recognition based on smart insole and ML. (b) Recognition system overview. (c) Different patients' real-time signals. (d) Confusion map of ML training result. (e) 3D plots of I-TENG sensor outputs subsequent to 5 patients. Reproduced with permission [549], under the terms of the Creative Commons Attribution 4.0 International License (CC BY 4.0). Copyright (2021). Where five people in (e) were marked as patient "A" to patient "E". Self-powered hybrid sensor-driven keystroke dynamics-based biometric validation utilizing a neural network.

individuals [548].

In order to improve intelligence and effectiveness of the lower-limb and waist rehabilitation Zhang et al. [549] created wearable TENG-based devices for analysis of gait and waist motion recording. To improve waist training, a virtual game and real-time robotic manipulation are made possible by four triboelectric sensors that are evenly spaced on a fabric belt. The two TENG sensors in the insole are intended to identify walking state, and by using machine learning software to additionally analyze the signals, a 98.4% accuracy in identifying for five distinct persons is attained with the goal of selecting a rehabilitation strategy. The authors exhibit the sensory system's capability in connected to the internet of smart healthcare applications by using a lower-limb rehabilitation robotic to show how well it performs in motion monitoring, user recognition, and robot and gaming-aided training. In order to achieve patient recognition for the purpose of choosing a rehabilitation plan, ANNs were used with fast Fourier transform (FFT) to obtain characteristics from triboelectric signal (Fig. 58 a,b). Five volunteers, each weighing between 55 and 75 kg, are asked to perform the same walking motion while wearing shoes with smart insoles in order to strengthen the machine learning model. The hardware circuit, which consists of an MCU and ADC, initially gathers and processes the analog voltage signals produced in the TENG-based intelligent insole during the test. In order to obtain the dataset, the signals from I-TENG-1 and I-TENG-2 sensors are then recorded for a total of 150 instances of tests (3 steps each). To guarantee the efficacy of the data collected, a particular window is used to visualize 400-point length signals, meaning that every sample should include sensory data for 3 continuous steps, as illustrated in Fig. 58c. In the end, 5 FCL ANN-based models are confirmed to have a high true positive rate and positive predictive value for patient recognition; as Fig. 58d illustrates, the overall recognition accuracy approaches 98.4%. Regarding the healthcare system, costly medical devices like rehabilitation robots are often shared by several patients, and privacy concerns are common because training data, containing personal information, is always stored in machines. This encourages patient identification and the creation of readily available private accounts in a practical and user-friendly way. By extending recognition of identities into the rehabilitation system based on the model of machine learning, the personalized training plan may be matched with various patients through an IoT-based remote setting. It should be noted that an excellent recognition rate was achieved using only 100-sample training data, demonstrating the need and potential for the impaired patient to follow this up with recognition. Notably, gathered the sensory input for the right foot in order to reduce the amount of data and simplify the system, demonstrating trade-off between size of sample and accuracy, even if a bigger set of data usually indicates additional characteristics for a greater rate of recognition. Next, each row of voltage records of 2 channels directly as sample features. This means that each sample has $400 \times 2 = 800$ features, each of which represents a single data point at time series during stepping, which includes stepping speed, contact force, contact duration, and some other data. The typical sensor outputs from five different participants are shown in Fig. 58e. Each participant's 150 samples are processed using FFT to remove time-domain information while preserving frequency characteristics. The samples are then randomly divided into three groups at a 4:1:1 ratio (100 samples for training, 25 samples for testing, and 25 samples for validation). In order to create the forecasting model, the ANNs framework is then directly fed all 100 of the chosen samples. Notably, trained models were optimized under assessment of cross-entropy loss function using the suggested network architecture with various fully connected layers [549].

The handwriting recognition system developed by Liu et al. [550] can be used as an encryptor for private data as well as a written text recognizer. This adaptable and clever handwriting recognition device combines hydrogel sensors based on graphene oxide with a printed circuit board. It provides high-precision handwritten content detection, ranging from an individual letter to words and signatures, and it responds quickly and sensitively. Through the analysis of 690 handwritten signatures collected from seven people, we are able to show a high recognition rate (about 91.30%) and a quick identification time (less than 1 s). Advanced interactions between humans and machines, wearable devices for communication, soft robotics manipulative devices, and augmented virtual reality are all promising applications for our designed handwriting recognition system. Additionally, it functions as an encryptor, leveraging the BiLSTM model's ability to analyze sequential data for secure information storage and processing. The system's adaptability allows for advanced interactions, offering significant advancements in soft electronics, secure authentication, and encrypted data communication.

Mao et al., developed a flexible silicone composite layer (SCL@(GCN-PVA)) for TENG applications by sequentially spin-coating Ecoflex-PVA and Ecoflex-GCN layers onto a cotton yarn substrate [551]. The SCL-TENG, optimized with 10% PVA and 1.6% GCN, achieved high output performance (720 V, 0.255 mW/cm^2, 134 μA) under 5 kPa pressure and 8 Hz frequency. In single-electrode mode, it was integrated into an intelligent recognition system for IoT-based monitoring and control of electronic devices. Utilizing deep-learning models like Convolutional Neural Networks (CNN) and Gate Recurrent Units (GRU), the SCL-TENG demonstrated high accuracy in detecting and differentiating mechanical contacts from various materials. Specifically, it was used in a robotic manipulator to classify different spherical objects baseball, tennis ball, hockey ball, and bouncing ball by analyzing voltage signal variations generated from contact interactions.

Zhu et al., developed a machine learning (ML)-enhanced ion mobility analyzer incorporating a triboelectric-based ionizer (SM-TENG), offering a compact design and adaptable functionality for VOC detection [552]. The system generates a stable DC bias through charge accumulation, enabling a distinct and repeatable plasma discharge pattern specific to different VOCs. By leveraging ML algorithms, the analyzer automatically extracts key features from ion mobility spectrometry profiles, significantly improving VOC detection accuracy and selectivity. This approach presents a real-time, low-power, and portable solution for VOC monitoring in IoT-based environmental applications, addressing the challenge of detecting multiple VOCs in dynamic conditions. The ion mobility mechanism, based on drift time analysis, effectively distinguishes VOCs by their molecular weight and volume, making it particularly useful in research labs and industrial settings where solvent evaporation poses health risks.

The ML-enhanced detection system accurately differentiates VOCs such as methanol, ethanol, and acetone by analyzing ion drift time variations under different concentrations. For example, ethanol's drift time increases from 0.5 ms at low concentration to 3 ms at high concentration, while isopropyl alcohol (IPA) shows a drift range from 1 ms to 6 ms. The system achieves an ML recognition accuracy of over 48.3% by training on 50 samples per category, with 42 used for training and 8 for testing, eliminating the need for manual interpretation and reducing computational expenses. The analyzer effectively distinguishes between VOCs with similar carbon structures, such as acetone and IPA, demonstrating its capability for precise gas identification. This ML-driven ion mobility analysis approach offers a scalable and efficient solution for real-time VOC monitoring in environmental safety, industrial applications, and chemical research facilities.

Maharjan et al., introduced a hybrid nanogenerator-based biometric verification system that integrates AI with keystroke dynamics, leveraging a combination of electromagnetic-TENG sensors and artificial neural networks (ANNs) for enhanced authentication security [553]. The system converts keystroke mechanical energy into electrical signals, which are then processed to extract keystroke features such as hold time, signal magnitude, and flight time. These features are analyzed by an ANN model, which classifies users based on their typing behavior with an accuracy of 99%. The system utilizes the "Softmax" activation function for multi-class prediction and optimizes classification using the "Adam" gradient descent algorithm. During testing, four users entered the password "1356″ 500 times, with 400 samples used for training and the rest for evaluation. The ANN model successfully identified users with 98%–99% accuracy using hybrid sensors, outperforming single-sensor models (93%–97% for EMG or TENG alone). The findings highlight the system's robustness, demonstrating its potential as an additional security layer against password vulnerabilities.

Further comparisons revealed that hybrid sensors provided superior authentication accuracy over individual EMG and TENG sensors, achieving a 99% accuracy rate for "User 2″ versus 96% (EMG) and 97% (TENG). Unlike conventional machine learning methods such as support vector machines (SVM), ANN proved more effective, particularly for hybrid sensors, due to its ability to capture time-variant keystroke behavioral patterns and update algorithms dynamically. The system's real-time implementation was demonstrated using hybrid sensors mounted on a commercial keyboard, with processed signals displayed through an analogue circuit. These results emphasize the potential of self-powered hybrid sensors in securing user authentication, reducing reliance on traditional passwords, and mitigating cybersecurity risks through AI-driven biometric verification.

In addition to the above studies, Luo et al., developed a voice and gesture signal translator (VGST) utilizing TENG technology to enhance human–machine interaction by converting natural motions into electrical signals [554]. The VGST, coated with silk protein over copper, achieves a wide frequency range (20–2000 Hz) with high sensitivity (167 mV/dB) and 0.1 Hz resolution. It effectively recognizes voices with 97% accuracy, even in noisy environments, and serves as a high-fidelity platform for sound recovery and machine learning-based voice authentication. The device also detects hand movements using electrostatic induction, demonstrating potential applications in accessibility tools for individuals with hearing impairments, smart security systems, and information encryption. Using a random forest algorithm, VGST was tested on speech data from four participants, achieving accurate speaker recognition. The system effectively differentiates voice signals by tracking frequency variations, as confirmed by high accuracy rates after multiple training cycles. This innovation highlights the VGST's role in secure authentication and enhanced voice-based human-machine interaction.

Shrestha et al., proposed a rotational energy harvesting system using a circular Halbach array (HA-REH) with arc magnets to improve power generation efficiency and flux focusing [555]. The system, designed for self-powered IoT-based environmental monitoring, achieves a power density of 603.2 W/m^3 and charges a 30 mAh battery to sustain wireless sensor networks. A TENG-based self-powered wind speed sensor was integrated into the system, demonstrating a strong correlation between wind speed and harvester output with a linear sensitivity of 13.6 $\mu A\ m^{-1}s^{-1}$. Utilizing artificial intelligence, an ANN-based prediction model was trained on 10,000 wind speed data points, incorporating meteorological factors like temperature, pressure, and humidity. Initially achieving 89% accuracy without weather inputs, the model improved to 99% when additional environmental factors were considered. The HA-REH system successfully powered an environmental monitoring network, collecting real-time data on air quality, temperature, and pressure, transmitting it wirelessly to mobile devices. This innovation demonstrates the potential of self-powered energy harvesters for sustainable environmental surveillance and smart IoT applications.

7.7. Underwater communication

Underwater communication plays a crucial role in marine exploration, underwater sensor networks, and autonomous vehicles. However, conventional methods such as acoustic, optical, and electromagnetic communication face significant limitations. Acoustic communication, though widely used, suffers from transmission delays and is affected by environmental factors like temperature, salinity, and pressure variations. Optical communication, despite offering high data rates, is limited by absorption, scattering, and interference from ambient light. Electromagnetic waves, particularly at high frequencies, are strongly attenuated in water, while low-frequency signals require large antennas, making them impractical for many applications. To address these challenges, recent studies have explored the potential of TENGs as an innovative solution for underwater communication and energy harvesting. Zhao et al. proposed a novel underwater wireless communication system based on Maxwell's displacement current generated by a TENG, offering an alternative to traditional electromagnetic wave-based communication [556]. This system exploits the second term of Maxwell's displacement current, ∂_P/∂_t, rather than the time variation of the electric field, allowing efficient underwater communication without direct charge transfer. The communication system comprises a sound-driven TENG connected to a transmitting electrode that generates an alternating electric field in water (Fig. 59a). A receiving electrode detects the induced current signals, making the transmission process purely dependent on the electric field. The researchers modeled the system using a capacitance-based approach, where water acts as a dielectric, and the electrodes function as capacitor plates, facilitating signal transmission as shown in Fig. 59b. Experimental results demonstrated that the TENG-based system ensured reliable signal transmission through a 100-m-long saltwater pipe while maintaining waveform integrity. Unlike acoustic and optical methods, this system was unaffected by water turbidity, obstacles, temperature variations, and ambient light, proving its robustness in complex underwater environments. On-Off Keying (OOK) modulation was employed for data transmission, achieving a transmission rate of 16 bits per second, with successful text and image transmission and no errors detected after transmitting approximately 20,000 bits. Additionally, the study showcased real-time underwater control applications, where a voice-driven TENG wirelessly controlled underwater lighting systems as shown in Fig. 59c. A large-scale experiment in a 50m × 30m × 5m water basin confirmed that a sandwich-like TENG effectively transmitted signals over a distance of 5 m, demonstrating the practical application of TENG-based underwater communication in marine exploration, underwater robotics, and pipeline monitoring.

Xi et al. reported underwater ultrasonic wave energy harvesting, presenting a TENG designed to capture ultrasonic wave energy efficiently [559]. A TENG featuring PTFE pellets that undergo contact-separation motions when exposed to ultrasonic waves, effectively converting vibrations into electrical energy. The device achieved an energy conversion efficiency of 13.1%, with an impressive output power of 0.362 W/cm^2 at 80 kHz, making it one of the most efficient underwater energy harvesters reported to date. The structure consisted of cubic acrylic plates with cylindrical holes containing PTFE pellets, and copper-coated Kapton films as electrodes. The waterproofed system demonstrated a peak output voltage of 170 V and a peak output current of 0.12 An under ultrasonic wave excitation. Different structural configurations were tested, revealing that optimizing the fill ratio and pellet size improved energy harvesting efficiency. The TENG successfully powered multiple electronic devices, including LED lamps, a temperature-humidity meter, and a health monitor, while integration with a supercapacitor enabled self-charging capabilities. These results highlight the potential of TENG-based energy harvesters in marine sensor networks and autonomous underwater systems, providing a sustainable solution for long-term underwater monitoring.

Guan et al. further expanded the applicability of TENGs for underwater ultrasonic signal monitoring and localization [557]. Their study presented a UD-TENG utilizing ultrasound-induced separation of a perfluorinated polymer film from its adhesive, generating electrical signals in response to ultrasonic waves (shown in Fig. 59d). Unlike conventional film-based ultrasonic TENGs, which require precise structural design and suffer from mechanical wear, this approach leveraged a simple and compact structure to ensure stable energy harvesting. The UD-TENG exhibited high stability, maintaining an output voltage of 1.5 V and a short-circuit current of 75 nA even after prolonged operation. The study also explored the impact of different environmental factors, including sound propagation distance, ultrasonic power

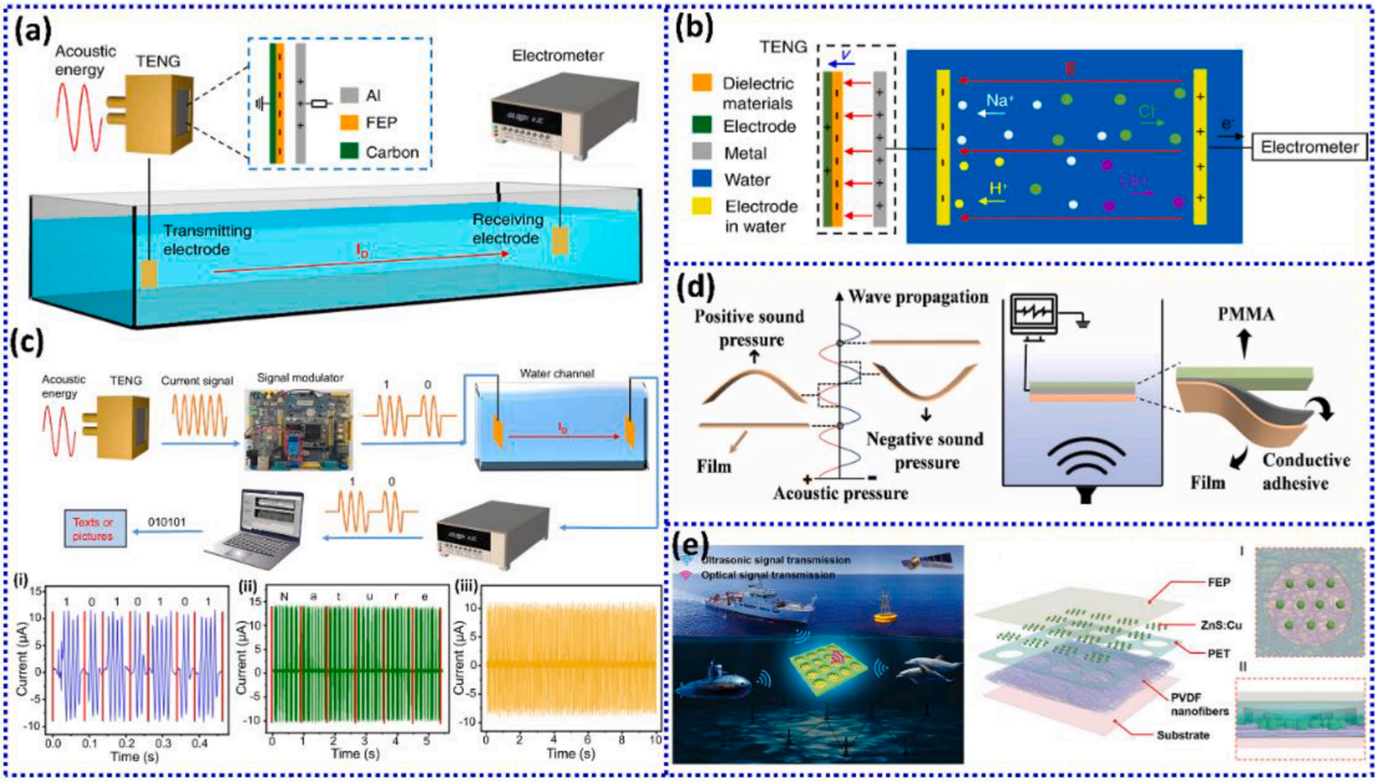

Fig. 59. (a) Schematic diagram of the experimental process. I_D represents displacement current in all Fig.s. (b) Schematic diagram of the working principle. *E* is the underwater electric field, and *v* is the speed of the TENG for contact and separation. (c) Schematic diagram of the modulation and demodulation process. Reproduced with permission [556] Creative Commons CC BY license Copyright © 2022 Springer Nature. (d) Schematic diagram of acoustic wave propagation and the vibration of the film, and experimental setup of underwater sonicating, and the structural scheme of a UD-TENG. Reproduced with permission [557]. Copyright © 2022 Elsevier. (e) Conceptual diagram of the SAWS capable of converting ultrasonic wave energy into visible light signals for sensing, positioning, and communication, structure diagram of the SAWS constructed layer by layer (I top and II side views of one cavity unit). Reproduced with permission [558]. Copyright © 2021 Wiley-VCH.

density, and liquid type, revealing that UD-TENGs perform consistently across various underwater conditions. Additionally, a self-powered acoustic sensor network was developed, integrating multiple UD-TENGs to form a large-scale sensing system for real-time underwater sound source localization. This system demonstrated its ability to accurately detect and locate ultrasonic signals in a marine environment, further solidifying the role of TENG-based sensors in underwater surveillance, military reconnaissance, and marine research.

Tian and colleagues introduced a self-powered all-optical wireless ultrasonic sensor (SAWS) utilizing triboelectrification-induced electroluminescence (TIEL) for underwater sensing and communication as shown in Fig. 59e [558]. Traditional ultrasonic sensors, which rely on piezoelectric materials, require wired communication and are limited by high costs and environmental constraints. The SAWS system eliminates the need for electrical wiring by leveraging TIEL-based luminescence, where triboelectric charges generated by ultrasonic waves excite electroluminescent phosphors, producing optical signals that can be detected remotely. The sensor consists of a layered composite structure featuring a PVDF nanofiber layer, fluorinated ethylene propylene (FEP) film, and ZnS:Cu phosphors enclosed within a cylindrical cavity. Experimental results demonstrated that the SAWS achieved high positioning accuracy with an error of less than 4.6%, an ultrafast response time of below 50 ms, and a high signal-to-noise ratio of 26.02 dB. Furthermore, the device maintained stable performance in different liquid environments, showing no significant degradation in luminescence intensity after prolonged immersion in saltwater. The SAWS enabled real-time optical communication by transmitting binary optical data, with successful transmission of text messages using ASCII encoding. A customized LabVIEW interface processed and visualized the received data, demonstrating the feasibility of self-powered optical communication systems for underwater applications.

TENG-based underwater communication and energy harvesting face challenges including mechanical wear, environmental sensitivity, structural complexity, and limited energy conversion efficiency. Prolonged exposure to high-frequency vibrations degrades device performance, while factors like salinity, pressure, and turbulence affect signal stability. Current designs struggle with long-distance transmission and seamless integration into existing sensor networks. To address these issues, future research should focus on advanced materials for durability, AI-driven signal processing for optimized data transmission, and multimodal energy harvesting for enhanced power generation. Lightweight, flexible TENG designs and integration with autonomous underwater vehicles will expand applications in marine exploration and defense. Hybrid optical-acoustic communication using electroluminescence could further improve underwater data transfer. Advancements in these areas will enhance the reliability and sustainability of TENG-based underwater systems.

7.8. *Triboelectric mechanoluminescence*

The integration of mechanoluminescence (ML) and TENG creates a multifunctional platform capable of simultaneously harvesting mechanical energy and providing real-time visual feedback. ML materials emit light when subjected to mechanical stress, while TENGs convert mechanical motion into electrical energy through contact electrification and electrostatic induction. By combining these two phenomena, the resulting system not only generates power from mechanical operations but also offers an immediate optical indication of stress or deformation, making it particularly useful for self-powered sensing, safety monitoring, and emergency signalling applications.

Hajra et al. present an innovative integration of ML and TENGs, creating a self-powered system capable of both mechanical energy harvesting and real-time optical feedback [560]. ML materials emit light upon mechanical stress, while TENGs convert mechanical energy into electrical signals via contact electrification. The combination of these mechanisms allows for applications in safety monitoring, structural health assessment, and emergency signalling by providing simultaneous electrical output and visible light emission. Fig. 60a illustrates the experimental setup used to measure the ML intensity of the PDMS-ZnS:Cu composite under mechanical stretching. The schematic depicts how the composite is subjected to tensile stress while an electrode is used to capture the emitted light. This setup enables the quantification of ML intensity variations at different stretching rates, demonstrating the composite's ability to provide real-time stress detection and monitoring.

The authors presented the practical application of the integrated TENG-ML device for Morse code signalling, showcasing its potential in self-powered communication. The Fig. depicts how single and dual voltage pulses generated by the TENG are mapped to Morse code representations of "dot" and "dash," allowing for message transmission, including "SOS" and "DGIST." The Fig. also includes digital images of the wearable device, illustrating its feasibility for real-world use. The voltage output graphs confirm the device's capability to generate distinguishable electrical signals for encoding Morse code. Additionally, an OR gate circuit design is shown, demonstrating the use of TENG voltage pulses in logic-based electronic circuits. This integration of ML and TENG ensures energy-independent emergency signalling, particularly in challenging environments such as underwater or low-light conditions, reinforcing its suitability for safety monitoring and distress communication.

The self-powered wind flow monitoring system described by Hajra et al. integrates TENG and ML technologies to create a hybrid energy-harvesting and sensing platform [561]. This system utilizes PDMS/ZnS:Cu composite materials, which generate both electrical and optical signals when subjected to mechanical stress (shown in Fig. 60b). The TENG operates in a single-electrode mode, allowing energy generation through wind-driven vibrations, while the ML component provides a visual indicator of mechanical deformation. The study demonstrates the system's ability to monitor low-pressure wind flow using a nitrogen gas-driven setup that simulates real-world wind conditions. A specially designed TENG-ML device was affixed to a wind flow pipe, and electrical as well as ML signals were recorded at different wind flow rates. Results show that higher wind speeds, particularly at 50 LPM (liters per minute), produce stronger electrical output due to increased contact and separation between triboelectric layers. The mechanoluminescence intensity also correlates with wind-induced deformation, confirming the system's potential for real-time wind flow monitoring. To enhance signal processing and classification, computational techniques such as Fast Fourier Transform (FFT) and Artificial Neural Networks (ANN) were employed. FFT helped extract frequency components from complex wind flow signals, allowing differentiation between various flow rates. The ANN model, trained with 150 datasets covering different wind speeds (30 LPM, 40 LPM, and 50 LPM), achieved an impressive classification accuracy of 96.7%, demonstrating its reliability for wind monitoring applications. This self-powered wind monitoring system has significant potential in various fields, including environmental sensing, cleanroom airflow monitoring, and industrial ventilation control. Its ability to provide both electrical and optical feedback without requiring external power makes it a promising solution for sustainable and real-time wind flow monitoring applications.

Zhang et al. present a self-powered triboelectric-mechanoluminescent electronic skin (STMES) that integrates TENG and ML for dual-mode sensing of mechanical stimuli [562]. Fig. 60c illustrates the STMES structure and working principles, where a layered design consisting of silver nanowires (AgNWs) embedded in polydimethylsiloxane (PDMS) enables both electrical and optical signal generation. The mechanoluminescent spacer layer, composed of ZnS:Cu/PDMS, not only facilitates contact separation for the TENG mechanism but also emits visible light in response to strain. The Fig. further explains how different mechanical stimuli—pressing, bending, and stretching—generate distinct signal responses: pressing induces only electrical signals, stretching activates only optical signals, and bending results in both, making STMES capable of distinguishing multiple stimuli. Further, the

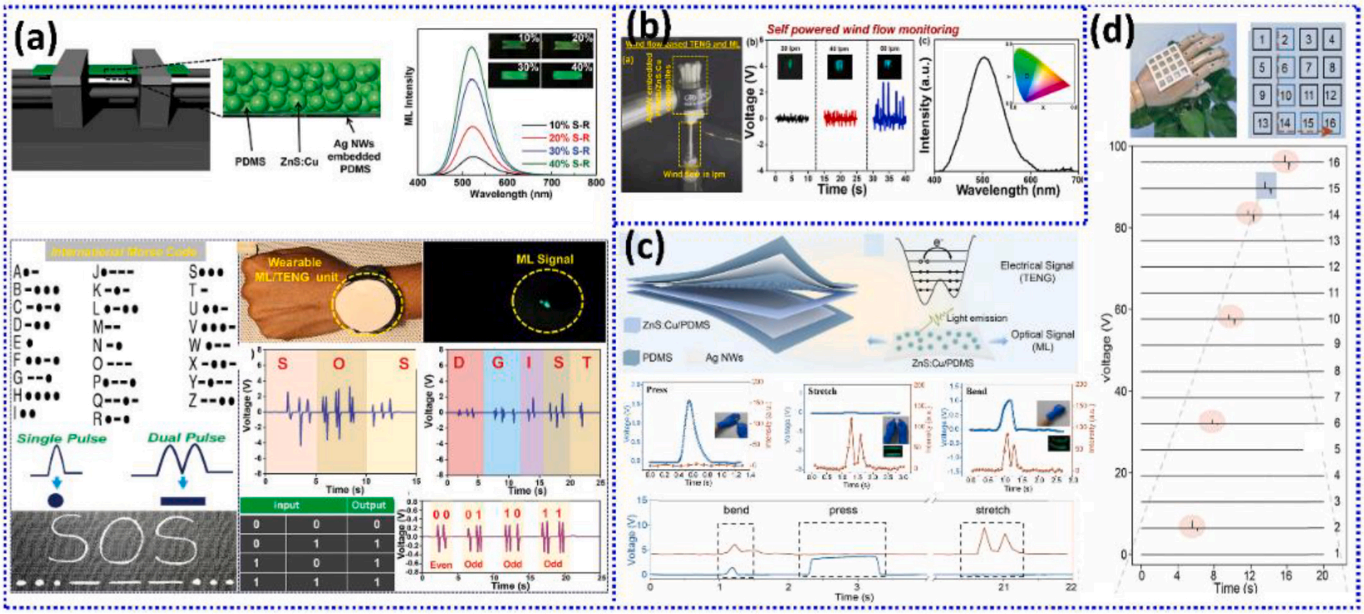

Fig. 60. (a) Experimental setup for measurement of ML intensity of composite using stretching and illustration of composite with the electrode and Wearable integrated TENG and Device for Morse code signalling and digital image. Reprinted with permission [560]. Copyright ©2024 Wiley-VCH. (b) Digital image of the partially sliced PDMS/ZnS:Cu composites-based device wrapped upon a ring holder, voltage and ML intensity of the device during different wind flow, and ML spectra and CIE coordinate of the intensity of ML light produced during 50 LPM wind flow. Reprinted with permission [561]. Copyright © 2023 Elsevier. (c,d) Schematic depiction of the STMES, Mechanism of electrical signal and optical signal generation. Application of STMES for monitoring of various stimuli as well as position sensing. Reprinted with permission [562]. Copyright © 2022 Elsevier.

authors presented the practical applications of STMES in wearable sensing and spatial position detection. When attached to a finger, the device successfully detects and differentiates pressing, stretching, and bending movements based on unique electrical and optical response patterns. A 4 × 4 STMES sensor array is also demonstrated for position sensing, where specific pixels generate electrical signals upon being pressed, allowing real-time tracking of touch locations. The pressing sequence forming the letter "L" further validates the accuracy of the device in spatial mapping, as shown in Fig. 60d. These findings establish STMES as a promising platform for applications in soft robotics, human-machine interaction, and wearable electronics, offering a self-powered and highly sensitive approach to real-time mechanical sensing.

To present a more cohesive view of the extensive range of TENGs, it is essential to connect the materials and engineering approaches studied with their relevant practical and real-world applications. The development of TENG technology can be understood through a comprehensive framework of "materials-methods-applications." “Materials” are the core components that influence the triboelectric behavior, mechanical properties, degradability, biocompatibility, and scalability of TENG devices. In this comprehensive review, we examine a broad selection of materials, including 2D materials, MOFs, carbon, perovskites, polymers, metal oxides, biodegradable, and plant-based materials, each offering unique benefits for specific applications. "Methods” involve chemical and physical modifications, device architecture, and charge-enhancement techniques. Surface functionalization, micro/nano structuring, defect engineering, doping, power management strategies, and multilayer device design all enable precise control over device durability and triboelectric output. These methods are commonly used to tailor material properties and improve the overall performance of TENG devices. “Applications” refer to the strategic and synergistic translation of material and device improvements into functional platforms for sustainable energy harvesting and self-powered sensing systems. These applications include self-powered illumination, triboelectric mechanoluminescence, self-powered devices, sensing, photodetectors, drug delivery, biomedical uses, self-healing systems, actuators, underwater communication, wearable electronics, smart textiles, IoT, and energy storage solutions. Each application has specific requirements, such as environmental resistance, flexibility, miniaturization, or biocompatibility, which influence the choice of materials and methods. By adopting this holistic perspective, we can clearly understand the intricate relationships among materials, engineering approaches, and application requirements. This comprehensive viewpoint not only enhances the consistency of the study but also serves as a vital guide for future research, helping material scientists, device engineers, and technologists systematically design next-generation TENGs.

8. Multifaceted energy harvesting methods of TENG

Due to climate policy, it is necessary to introduce a large number of renewable sources. This was forced by the departure from fossil fuel energy [563,564]. For commercial use of TENG, the profitability and efficiency of the solution is very important. This makes production costs and power density important. These parameters depend on the load of the TENG device and their number [565,566], TENG networks are developed [567–570]. TENGs network are referred to as Multifaceted energy harvesting due to their multiple energy harvesting surfaces. These are options being considered for use around the world due to the amounts of power required in the energy system. Parallel [567,568,570] or spatial [571,572] connection is possible. Parallel connection increases the size of the energy collecting surface. Spatial connection increases the axes of space in which mechanical energy is converted into electrical energy. The most popular application of multi-faceted energy harvesting is the conversion of energy from air or water into mechanical energy, which is converted into electrical energy in TENG. In the case of air energy conversion, two main applications can be distinguished: wind, acoustics. In the first case, it is an alternative to wind turbines [573]. In the case of acoustics, it is possible to use flexible electronics to collect energy surrounding a person [574]. In the case of using energy from water, we can divide it into: raindrop, blue energy. Using rain involves changing the energy of water droplets hitting the surface of TENG [575]. In the case of blue energy, the energy of the wave at sea is changed [576]. The division of Multifaceted energy harvesting methods of TENG are illustrated in Fig. 61. This section will discuss the different types of Multifaceted energy harvesting and provide examples. The topic of Multifaceted energy harvesting has been developed mainly in recent years, which results from the desire to use developed TENG systems as alternatives to already used alternative energy sources. The applications of the discussed TENGs have been described in works [577,578] that focus on the applications themselves.

8.1. *Wind energy*

The development of renewable energy sources forces the search for other methods of obtaining energy. One of them is changing the wind to electricity. TENG's offer a simple design and high voltage. This can be an alternative to classic methods of obtaining energy from wind [581]. Two main design options are considered: rotational [573,582–588] and vibration [579,589–594]. Systems of this type are being considered for home applications [586]. The issue of TENG lifts is discussed in more detail in the works [595,596].

8.1.1. *Rotational TENG*

These solutions are among the first to appear. Their great advantage is their incredible simplicity and relatively high generated voltage [573]. The voltage can be as high as 1 kV [582]. Work is currently underway to adapt the generated voltage for home use [586]. This will simplify the transmission and storage of energy, and the entire TENG system. The simplest solution is two discs rolling on each other, powered by the wind [582,583]. This solution consists in sliding a polymer circle over metal electrodes arranged on the circle [582]. This solution is shown in Fig. 62 (a,d). Solution (a) differs from solution (d) only in design details. The comparison is intended to show how different results can be achieved by designing the same device. While the devices generate similar currents of about 60 μA. The Long et al. [582] solution generates about 7 times greater voltage. The results are shown in Fig. 62b,c,e, f. Mu et al. [584] used such a TENG device to power 3840 green LEDs. This illustrates how much energy can be generated using wind. An often-overlooked aspect is machine operation. He et al. [585] have proven that TENGs can survive over a million cycles and maintain an efficiency of 87%. Ahmed, A. et al. [588] suggest the need to create entire farms of TENGs.

8.1.2. *Vibration TENG*

Devices of this type use flexible vibrating elements that swing freely and rub against electrodes [590]. This simplifies the construction of the device as much as possible. Wang. et al. [594] proposed three independently vibrating elastic materials at a small distance from each other, which allowed them to rub. Such a simple solution allowed to generate 36 V and 8 μA. Sun. et al. [590] proposed an identical solution in terms of structure but used a better Ag-FEP triboelectric pair. This allowed to generate 4 mW. Cui. et al. [591] used this kind of TENGs to power the electrochemical reaction. Choi, J. et al. [585] presented the application of such a TENG at home. They used TENG to create blinds. Feng et al. [589] noticed that solutions of this type resemble nature and leaves. For this reason, they can be described as biomorphic [579]. A slightly different approach to this topic was presented by Shin et al. [593]. They developed a layered system suspended on flexible spacers. The system consisted of spacers and two surfaces with electrodes and friction elements. Airflow between the surfaces sets them in motion. The device is shown in Fig. 63a-c. It collected energy from the wind regardless of its direction. This device generates 120 V and very high currents of 200 μA.

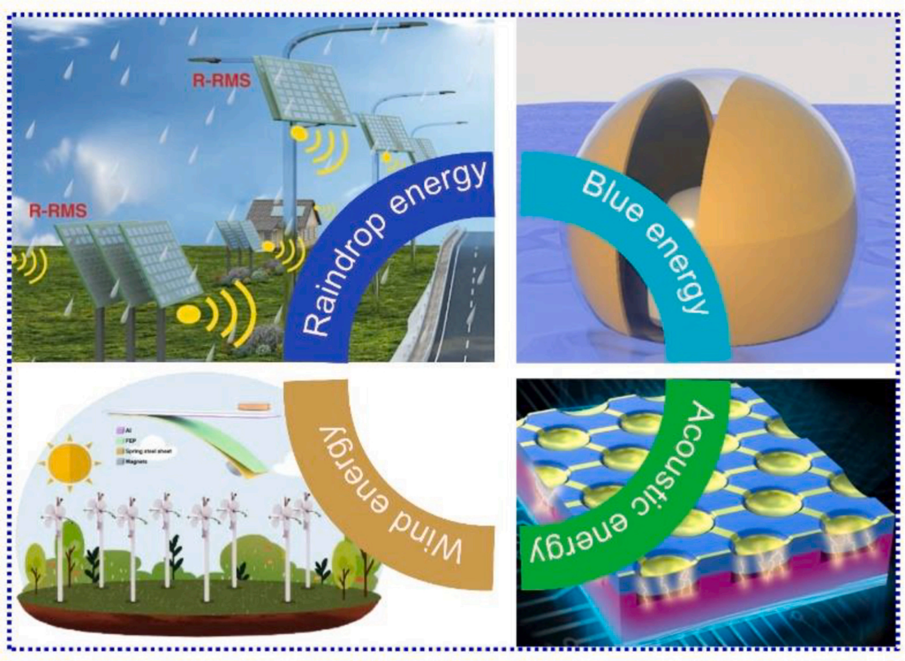

Fig. 61. Schematic illustration of: raindrop energy TENG. Reprinted from Xu, C. et al. [575] under the terms of the Creative Commons Attribution 4.0 International License (CC BY 4.0). Copyright (2022) Springer Nature. Blue energy TENG. Reprinted from Liu, W. et al. [570] under the terms of the Creative Commons Attribution 4.0 International License (CC BY 4.0). Copyright (2020) Elsevier. Wing energy TENG. Reprinted from Zhang, Y. et al. [579] under the terms of the Creative Commons Attribution 4.0 International License (CC BY 4.0). Copyright (2020) Springer Nature. Acoustic energy TENG. Reprinted from Chen, C. et al. [580] under the terms of the Creative Commons Attribution 4.0 International License (CC BY 4.0). Copyright (2020) Springer Nature.

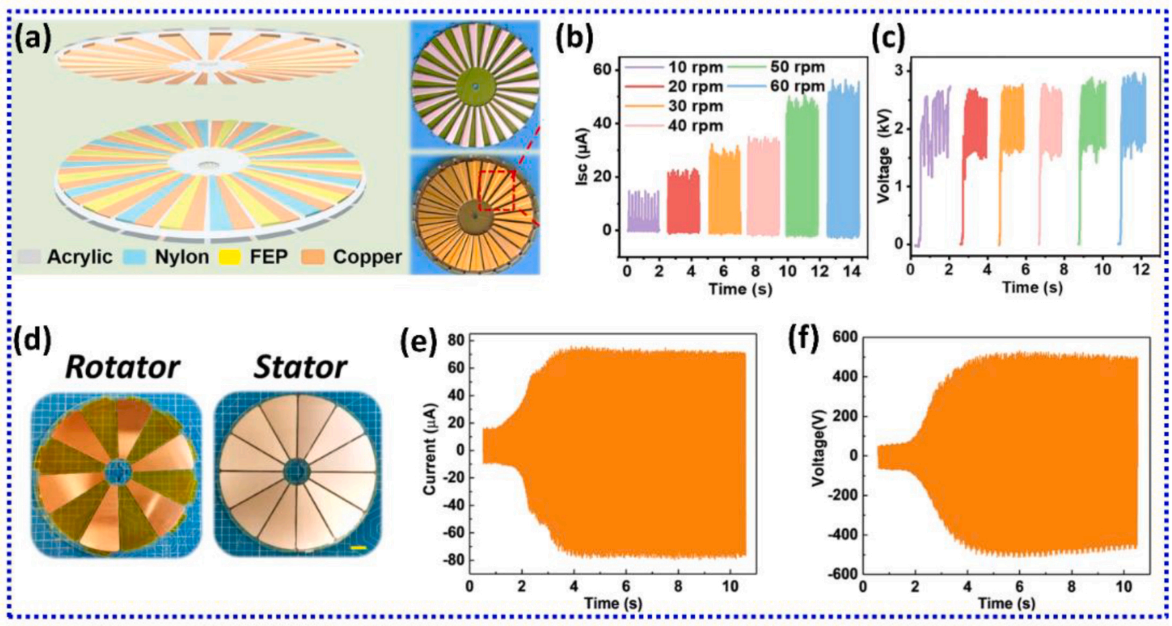

Fig. 62. (a,d) Device TENG's. (b,e) Current response, (c,f) Voltage response. (a–c) Rotational TENG. Reprinted from Long, L. et al. [582] under the terms of the Creative Commons Attribution 4.0 International License (CC BY 4.0). Copyright (2021) Springer-Nature. (d–f) Reprinted from Fu, S. et al. [583] under the terms of the Creative Commons Attribution 4.0 International License (CC BY 4.0). Copyright (2022) Springer.

TENG was used to power 25 LEDs.

8.1.3. The future of development

For future activities, mainly less classical kinematic systems [581, 597] and integration with existing electromagnetic turbines are considered [598,599]. Smaller structures than traditional wind turbines are being considered due to their application potential. It is possible to extract small amounts of energy from a device resembling a whistle. Yong et al. [581] proposed such a device (Fig. 64a). The device worked through a closed chamber with an air inlet and outlet in which there is a polymer ball. The ball moved freely inside. The walls of the chamber are lined with electrodes. Movement caused free charges to move and generated power. The operation of the device is illustrated in Fig. 64b. In this way, it was possible to obtain 11.2 V and 1.86 μA [581]. The method of generating current and voltage is shown in Fig. 64c, d. Another possibility is to use changes in wind direction. This will allow for the acquisition of small amounts of energy at high voltage, which will help with the integration of such solutions with the power grid. Liu et al.

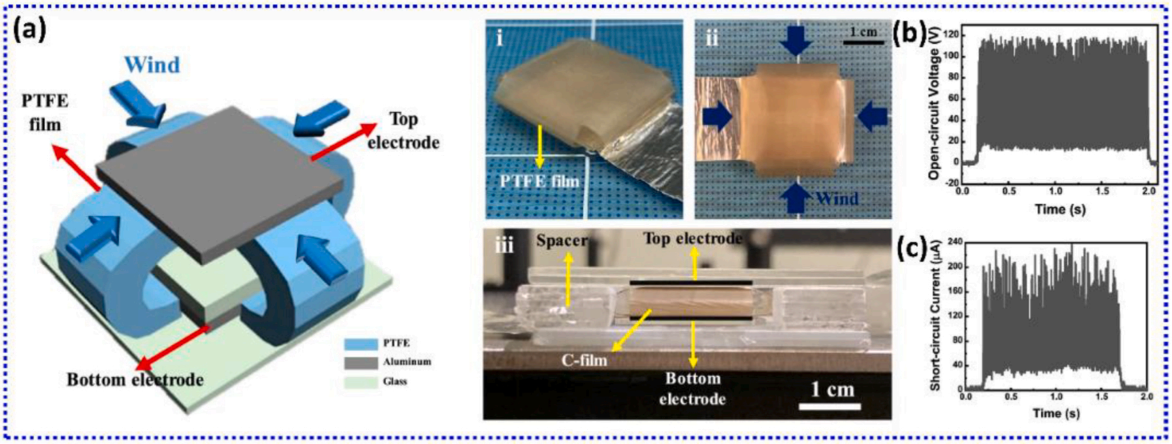

Fig. 63. (a) Device TENG's. (b) Voltage response. (c) Current response. (a–c) Rotational TENG. Reprinted from Shin, Y. et al. [593] under the terms of the Creative Commons Attribution 4.0 International License (CC BY 4.0). Copyright (2021) Springer.

[597] generated 374.97 V, 84.77 μA in this way. Due to the different efficiency, a combination of electromagnetic and triboelectric generator is planned [598,599]. This will allow the load of the system and the generated power to be adjusted to the current wind conditions. This is extremely important due to the nature of the energy coming from the wind. This will allow you to obtain up to 410 V, 18 μA and 4.82 mW [598].

8.2. Raindrop energy

Raindrop TENGs are one of the latest triboelectric devices to be invented. The operating principle is incredibly simple. Electrically charged water droplets strike the surface of the device, transferring charges between the electrodes and flowing down it [575]. This is illustrated in Fig. 65a. These devices operate at the liquid-solid interface [575,600,601]. Various numbers of.

electrodes are possible, from 1 [575], through two [603–607], to 4 [602,608] for a single device, and many more for a network (Fig. 65b,c). Fig. 65d,e shows the current and voltage results with different numbers of connected TENGs. This shows a linear relationship between the connected devices and the increase in output parameters. This allows devices to be connected in large arrays, which can result in high output power. He et al. [602] investigated various connection configurations of TENG's. The differences are shown in Fig. 65f. There are visible differences in both voltage and current values. This confirms that the type and number of connected devices are important for TENGs. Due to contact with water, surfaces must have appropriate hydrophobic and hydrophilic properties [601,604,606,609]. In this way, Hu et al. [606] make possible to increase the voltage twice. Currently, the main application is considered to be roofs of buildings [605,608,610,611]. Roof tiles [608,610,611] are mainly used for this purpose, but there are also proposals to use glass [605]. Dang. et al. [610] used energy from a VO_2 TENG to force a phase transition in the material. This allowed for a change in optical properties. This allows for the creation of self-regulating windows, depending on the weather. Interaction with sensors for self-powering is also being considered [612]. For optical applications, Jang et al. proposed TENGs which are flexible and have 92 % light transmittance [607]. In the future application, integration with solar panels is currently planned [613–615]. This will allow continuous collection of energy from the environment (on sunny days from light and on cloudy and rainy days from raindrop.). This may be helped by the high integration proposed by Liu et al. [616].

8.3. Blue energy

Blue energy involves using ocean waves as a source of mechanical energy and converting it into electrical energy using TENG [617–620]. It is one of the most accessible types of energy coming from the ocean [576,621]. A serious problem is the small use of ocean energy in the world's energy sector [622]. The major challenge in obtaining energy from sea waves is their multidirectionality [623]. Currently, 3 main device configurations are being developed: Rolling [570,576,624],

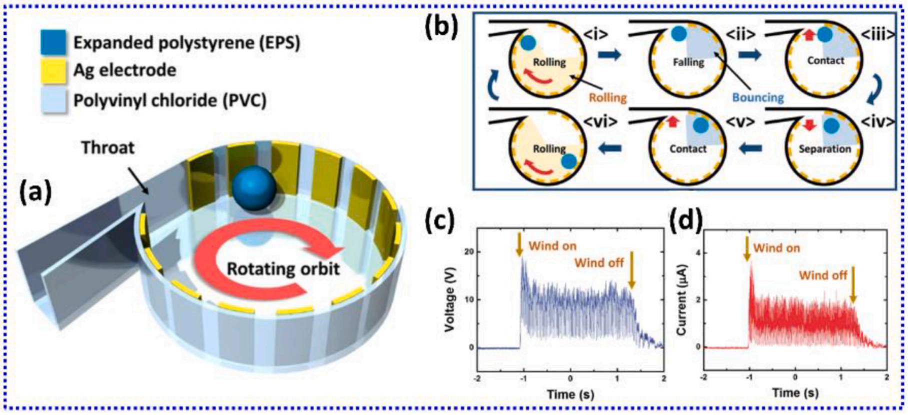

Fig. 64. (a) Schema of device TENG's. (b) Operating diagram. (c) Voltage response. (d) Current response. (a–d) Rotational TENG. Reprinted from Yong, H. et al. [581] under the terms of the Creative Commons Attribution 4.0 International License (CC BY 4.0). Copyright (2016) Springer-Nature.

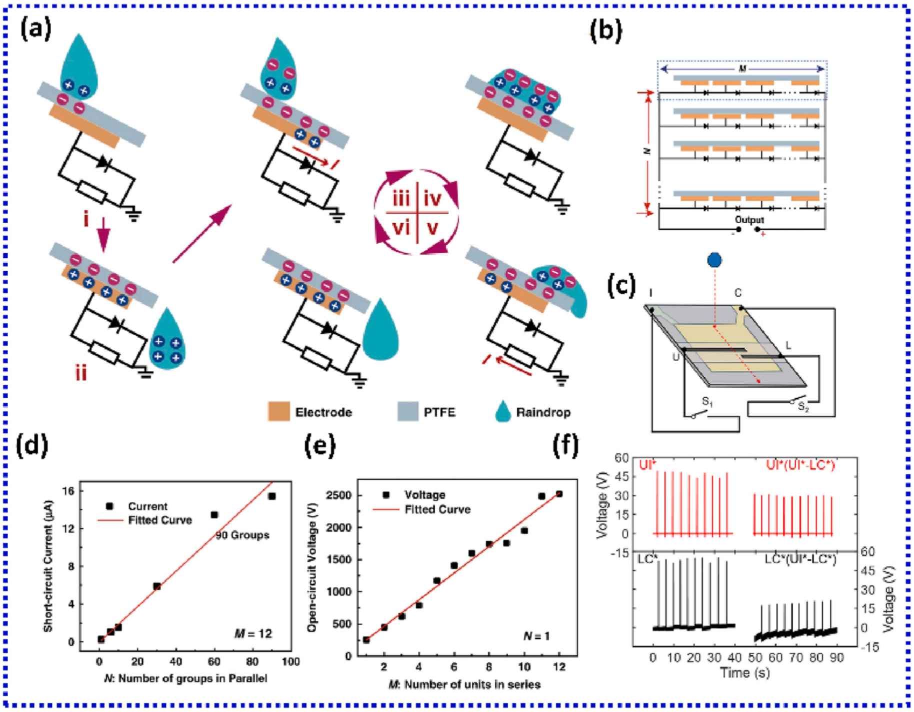

Fig. 65. (a) Operation diagram of raindrop TENG's. (b) Possible connection schemes. (c) Sample TENG. (d) Current depending on the number of devices. (e) Voltage depending on the number of devices. (f) Voltage response for different load configurations. (a, d,e) Raindrop TENG. Reprinted from Xu, C. et al. [575] under the terms of the Creative Commons Attribution 4.0 International License (CC BY 4.0). Copyright (2022) Springer-Nature.). (b,c,f) Raindrop TENG. Reprinted from He, P. et al. [602] under the terms of the Creative Commons Attribution 4.0 International License (CC BY 4.0). Copyright (2024) Elsevier.

Spring-like [567,571,572,625], rotory [569,626–629] TENG's. In this section, each of them will be discussed. The materials and methods of transmitting energy are also very important aspects [630–633]. This is due to the potential deployment of TENGs in the middle of the ocean. Materials must be resistant to water. For this reason, hydrophobic materials are suggested [576,634–636]. Which will ensure the operation of TENG's for a long time without power interruptions. This aspect was discussed in more detail in Wu et al. [637]. Due to the location of TENG's blue energy, it is also necessary to process and/or store the energy within the device itself. Appropriate connection of TENGs allows to increase the energy obtained from devices by reducing losses [570]. A very important aspect is the adaptation of voltage and current to DC values [638]. This will allow for energy storage. Energy storage from blue energy TENGs can be done using capacitors [568] or supercapacitors [639].

8.3.1. *Rolling TENG*

There are two main approaches to creating rolling TENG's. The first one involves multi-directional energy collection by basing the design solution on balls as a friction element [404,570,576,624,640–643]. The method consists of placing one or more polymer balls on a surface (usually a semicircle). The ball moves freely on the surface with the appearance of waves. Electrodes are placed on the surface (placed on each of the semicircle halves) [576]. The second option is to base the solution on a roller [644–647]. This causes the device to roll in only 2 directions. The method involves placing a roller between two surfaces. An electrode is placed on each surface. The TENG's movement, resembling that of a buoy on the water, causes the roller to move between the surfaces, generating electrical charges [645]. Fig. 66 shows sample solutions for each design option.

The solution using a ball as a friction element allows the use of water wave vibrations in any direction [624]. A single ball rolling TENG cell generates a small amount of energy. Combining 15 modules allowed Yuan et al. [572] to increase the charge from 21 *n*C to 820 *n*C relative to a single module. This allowed to achieve a power density of 20.57 W/m^3 at 5.9 Hz. For this reason, various connections are considered. It is possible to connect: independent [570,640,643], vertical stack [576,624], Box-like [404,641,642]. Liu et al. [570] connected independent buoys in different configurations. They connected from 2 to 16 modules. This allowed to increase the power about 8 times, while at the same time reducing the resistance of system 10 times. They also pointed out the importance of the connection topology, which turned out to be more important than the number of modules. For 2.0×10^6 modules, the difference in power for the two topologies was 15 times [570]. The results of the work are shown in Fig. 66a-c. A photograph of the device is presented in Fig. 66a. It worked on the principle of a buoy. The scheme of operation and the materials used for its construction are described in Fig. 66b. It shows the movement of the ball between the electrodes. The device generated a large voltage (Fig. 66c). Vertical connection of several TENGs allowed the increase from 1.03 W/m^3 to 10.6 W/m^3 by Xu et al. [576]. With a box-like connection Duan, Y. et al. [642] achieved as much as 80.29 W/m^3 maximum power density.

Roller rolling TENG's focus on the solutions of two surfaces rolling on each other. The main solutions are the roller [644,645] and the flat surface [646,647]. The roller forces the surface to be unidirectional. The movement of the device resembles the movement of a buoy on the water. Kim et al. [645]managed to generate 69.34 μW m^{-2} at 200 MΩ in this way. They used 2 rollers of different sizes. This allowed them to move at different forces, which allowed for more efficient energy collection. Using 2 versus 1 roller allowed the voltage to be increased from 4.27 V to 21.9 V. Their device is presented in Fig. 66d,f. The operating scheme and the materials used for its construction are shown in Fig. 66f. As depicted in Fig. 66e, it generates a much lower voltage than the ball generator. Miao. et al. [647] fabricated a columnar multi-layer sliding TENG (CMLS-TENG), which, despite having a roller structure, was multi-axial. It allowed to generate 730 mW/m^3. Lin et al. [646] and Zhang et al. [648] also proposed an interesting multi-axis solution. The device operated on the principle of a pendulum. One surface was suspended on an elastic element that swung.

8.3.2. *Spring-like TENG*

Spring is one of the simplest mechanical elements that can store

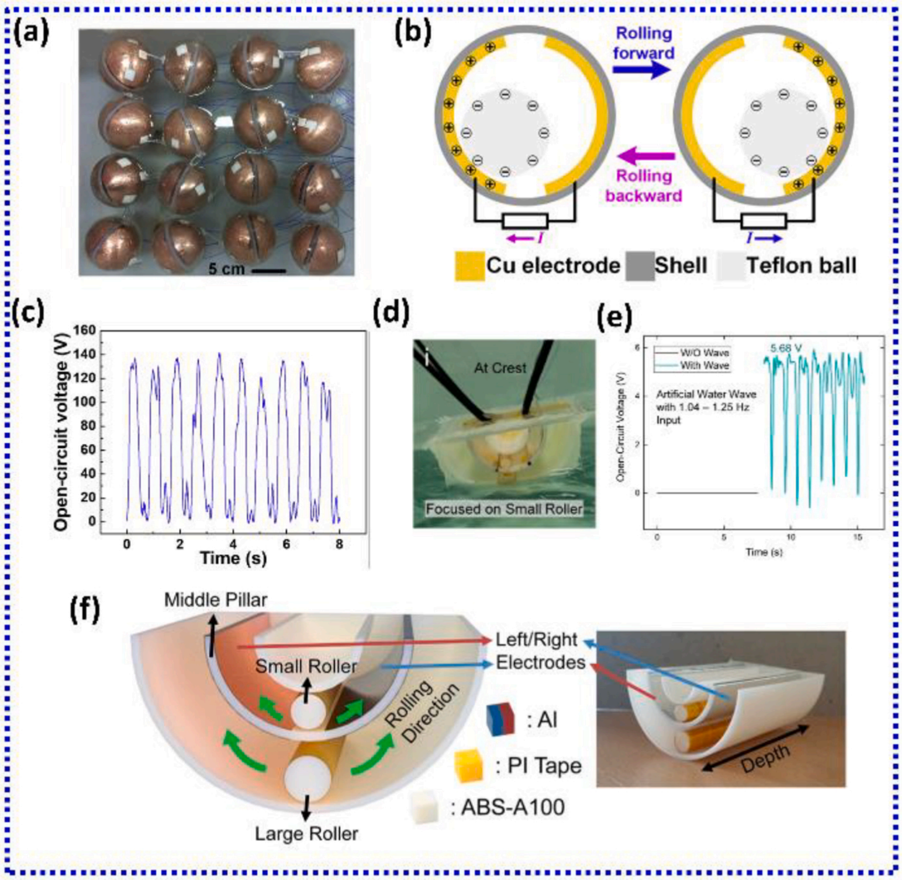

Fig. 66. (a,d) Photo of TENG's. (b,f) Operation Scheme. (c) Voltage response at a frequency of 1.25 Hz of water vibrations. (e) Open circuit voltage response. (a–c) Ball rolling TENG. Reprinted from Liu, W. et al. [570] under the terms of the Creative Commons Attribution 4.0 International License (CC BY 4.0). Copyright (2020) Elsevier. (d–f) Roller rolling TENG. Reprinted from Kim, I. et al. [645] under the terms of the Creative Commons Attribution 4.0 International License (CC BY 4.0). Copyright (2021) MDPI.

energy. TENG's using its operating principle cause the deformation of the support material to set the friction surfaces in motion. There are many types of construction of such elements [567,571,572,625,629,649,650]. Jiang et al. [650] used a spring to support the TENG. This allowed them to generate 7.22 mW. They used Cu-PTFE-covered acrylic. A more complex TENG was proposed by Wen et al. [649] who created an

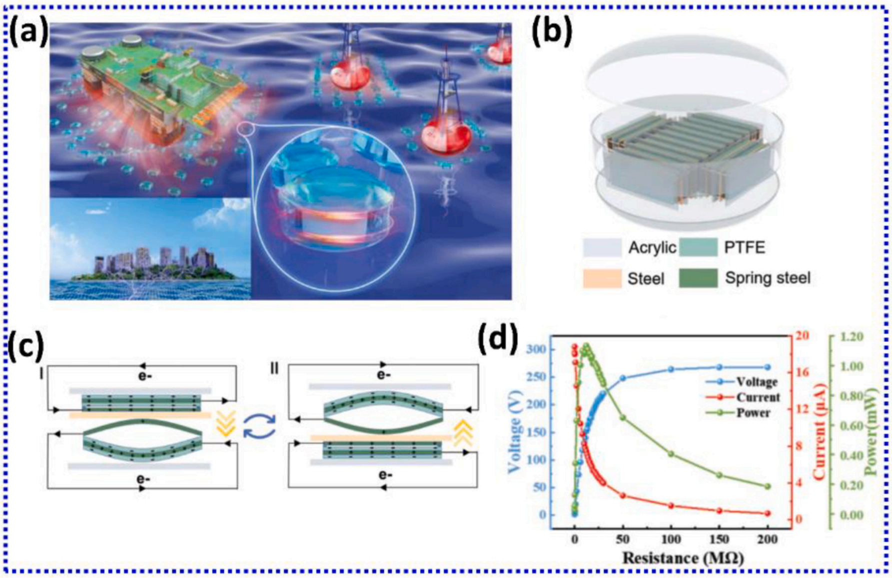

Fig. 67. (a) Idea of application TENG's. (b) Build schema. (c) Operation scheme. (d) Output voltage and current, and output power under different external loads. Spring-like TENG's reprinted from Feng, J. et al. [625] under the terms of the Creative Commons Attribution 4.0 International License (CC BY 4.0). Copyright (2022) Wiley.

origami spring using PLA and iron and PTFE as friction surfaces. This allowed to generate a much higher power of 15.4 W/m^3. It is possible to make a bent element on which the friction element will be supported [571,572,625]. Feng et al. [625] proposed systems using microporosity of PTFE as rubbing surfaces of spiring like TENGs. It is shown in Fig. 67. The idea of the device is based on self-powered platforms, which is illustrated in Fig. 67a. The device consisted of an acrylic container, steel springs to which PTFE surfaces were attached. The PTFE surfaces rubbed against steel electrodes. The operation and construction of the device are shown in Fig. 67b,c. With an appropriate load of the device, it was possible to obtain even about voltage of 275 V and power of 1.2 mW (Fig. 67d).

8.3.3. Rotory TENG

TENG's rotating systems were inspired by the water wheel that has been used for centuries [628]. The principle of the device is extremely simple. The flow of water generates the movement of the wheel, to which a friction element is attached that generates electricity [627]. This will allow for slightly different applications than the previously discussed TENGs, as it can be used in rivers. Mainly, paddles pushed by the water are used for this purpose [626–628]. This solution was proposed by Hu et al. [627] who created a system of PTFE and aluminum. It allowed to generate 1.29 mW. Another solution was proposed by Gao et al. [569] who created a sphere in which there was an independent ball. The device worked on the gyroscopic principle. This allowed to generate 0.8–3.2 μA and 160 V [569].

8.3.4. The future of development

An alternative to classical TENGs operating on solid-solid contact, Zhang et al. [568] proposed a TENG that used water flow over electrodes to generate energy. They created PTFE containers covered with a copper electrode. Inside the containers was distilled water (DI). These systems were connected to form buoys. The movement of the ocean caused water to flow inside the container, which generated triboelectric charges. During the tests, it was possible to achieve a peak open-circuit voltage of over 150 V and a peak short-circuit current of over 0.1 μA [568]. A similar solution was proposed by Munirathinam et al. [651]. Zhang et al. are also plans for TENG-powered water farms in the middle of the ocean. The energy generated by the TENG was stored in capacitors, which powered electrochemical cells placed next to the TENG farm. The energy generated by the TENG was stored in capacitors, and they powered electrochemical cells placed next to the TENG farm. The developed TENGs generated 30 μA at 2.5 Hz. This allowed the production of 64.5 μL min^{-1} hydrogen [621]. The great potential of electrochemical cells was also noticed by Leung et al. [639] who proposed CO$_2$ conversion to liquid fuel using energy from TENG. They used TENG to charge a supercapacitor that powered a two-electrode electrochemical cell. They analyzed the cell's operation at different supply voltages. They managed to generate maximum 2.798 μmol carbon-based liquid fuel [639].

8.4. Acoustic energy

Piezoelectric nanogenerators are most commonly used for acoustic values. This is due to their high efficiency at these forces and frequencies [652]. Despite this, research on acoustic TENGs has enjoyed great popularity. This is due to many problems related to the nonlinearity of piezoelectric materials [653]. We can distinguish two main approaches. One of them uses relatively cost-effective polymeric materials [654–660]. The second solution focuses on nanotechnology and increasing performance through surface engineering [484,661–664]. Due to the high energy specificity of ultrasonic waves, it is worth distinguishing them as a separate device [317,488,559,665–667]. These three aspects will be discussed in this chapter. The aspects related to acoustic TENGs are discussed in detail in Ref. [652]. Typically, TENGs are used only for energy harvesting. What is unique about acoustic applications is the possibility of using TENGs to measure sound as well, in self-powered applications [488,574,580,654,658,660,662,663]. In large cities, noise is a nuisance. Correct measurements are very important for improving the quality of life. TENGs can be used for such purposes as self-powered sensors [574,658,660,663]. Yang et al. [658] fabricated TENG with a resonator for such applications. They succeeded in generating 60.2 mW/m^2 of energy to power such a device. This made it possible to power 17 LEDs. A high-performance device was developed by Zhao et al. [657] using a Helmholtz resonator. This allowed the generation of 1.82 WPa^{-1} m^{-2}. The most interesting solution was proposed by Zhu, G. et al. [654] in which they used TENGs for intelligent sound recognition. By using a resonator (a suitable container for the TENG that adjusted the signal) and machine learning algorithms, the research group managed to recognize patterns. The solution of underwater localization using TENG's was proposed by Guan et al. [488], who fabricated TENG from PMMA and adhesive film with conductive properties. The use of such sensor array allowed imaging with accuracy of one TENG module.

8.4.1. Membrane base TENG

Membrane solutions are based on the system known from the loudspeaker. However, the electromagnetic system is replaced by a triboelectric system. The operation of this type of device consists in placing a flexible polymer membrane that rubs against a metal electrode [655,656]. The operation of the system is shown in Fig. 68a, c. This solution was proposed by Refs. [654–660]. Classical membrane systems were made in the works [655,656,658,660]. Xiao et al. [656] and Yuan et al. [655] proposed a system that was very similar in construction. Both teams used aluminum electrodes and a carbon-based material as friction material. A comparison of the voltage responses is presented in Fig. 68b, d. Generated voltage is similar; the difference is the linearity of the response with increasing excitation dB. This confirms that the type of microstructure of the friction surface is very important. Zhao et al. [657] developed a solution based on the Helmholtz resonator principle. This allowed for an increase in acoustic sensitivity per unit area by 60 % and power density per unit sound pressure by 20% compared to the literature data [657]. A similar device based on a resonator was used by Zhu et al. [654]. The multi-hole resonator solution allowed achieving an open circuit voltage of 347 V.

8.4.2. Micro/nano structured TENG

Micro/Nano structured solution allows to customize the surface for TENG's applications. There are three main options for fabricating the systems: membrane modification [661,663], micro-device fabrication [580], increasing surface roughness [574,662]. Surface roughening involves depositing/etching material onto the TENG's friction surface. In this way, Yang et al. [662] fabricated PTFE nanowire, which is usually used in the form of a film. Chen et al. [580] constructed a microdevice consisting of 50 μm-sized diaphragms assembled into arrays. This solution allowed to generate only 16.8 mV. However, its advantage is its small size and the possibility of use in micro-devices as a power source. A popular solution is to use electrospun to produce the membrane [661,663]. This causes the membrane to take on a micro-surface pattern, which increases the response of the TENG's. Sun et al. [661] proposed a device based on an electrospun membrane. The construction and operating principle of this device are presented in Fig. 69a, b. This type of device is extremely interesting due to its low weight. It was possible to obtain a power density of 2.25 W/m^2 and a power reached 259 μW/g. It was possible to obtain a generated voltage of approximately 120 V while maintaining an extremely low mass (Fig. 69c). The tests of different materials proved to be very interesting. The highest responses were obtained for 1% MWCNT addition (Fig. 69d) [484,664]. also used CNTs in the device as a membrane element. Rani et al. [484] allowed for the currents flowing in the TENG's system to be increased by 2 times.

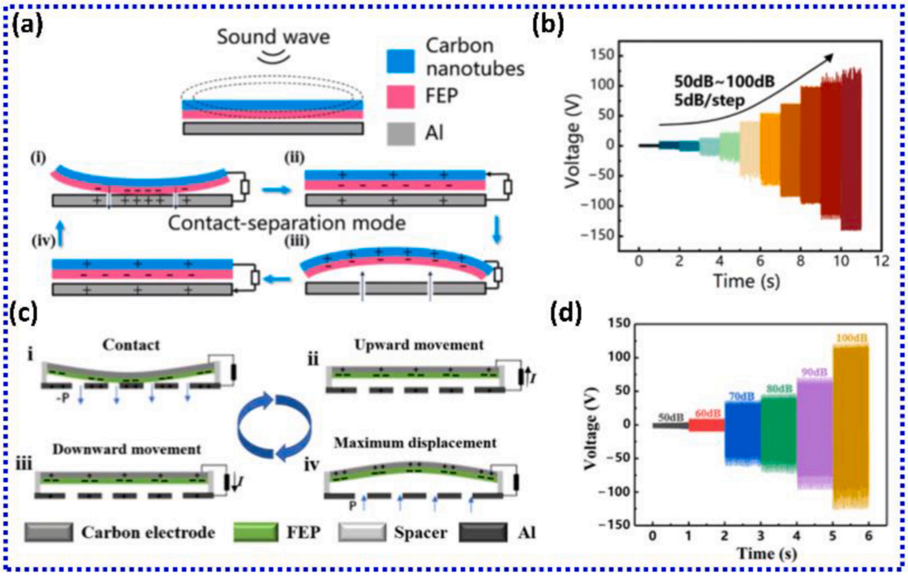

Fig. 68. (a,c) Construction and principle of operation. (b,d) Voltage response at different excitation power. (a, b) Membrane base TENG's reprinted from Xiao, X. et al. [656] under the terms of the Creative Commons Attribution 4.0 International License (CC BY 4.0). Copyright (2023) MDPI.). (c, d) Membrane base TENG's reprinted from Yuan, H. et al. [655] under the terms of the Creative Commons Attribution 4.0 International License (CC BY 4.0). Copyright (2021) MDPI.).

8.4.3. *Ultrasound-driven TENG*

The last type of acoustic TENG discussed is the one using ultrasound. The construction is similar to both blue energy [317,559] and acoustic [488,665,666] TENGs. This is largely due to the use of water ultrasound and its propagation under water. Nowacki et al. [317] proposed a solution of small polymer beads placed between metal electrodes. The low mass of the beads allowed them to be excited by ultrasound. The device is shown in Fig. 70 (a, b). A voltage of 10 mV was obtained (Fig. 70c). Another underwater application was proposed by Lee et al. [667] which, however, was modeled on membrane acoustic devices. The device is shown in Fig. 70d. A voltage of 1.33 V_{rms} was obtained (Fig. 70e). Ultrasound has been used in underwater technology for years. TENG's solutions are also proposed for this application area. Zhao et al. [488] used TENG's for object localization. Another underwater application is communication, which is extremely difficult in media such as salt water [666]. Kim et al. [665] attempted to use the device in medicine. They

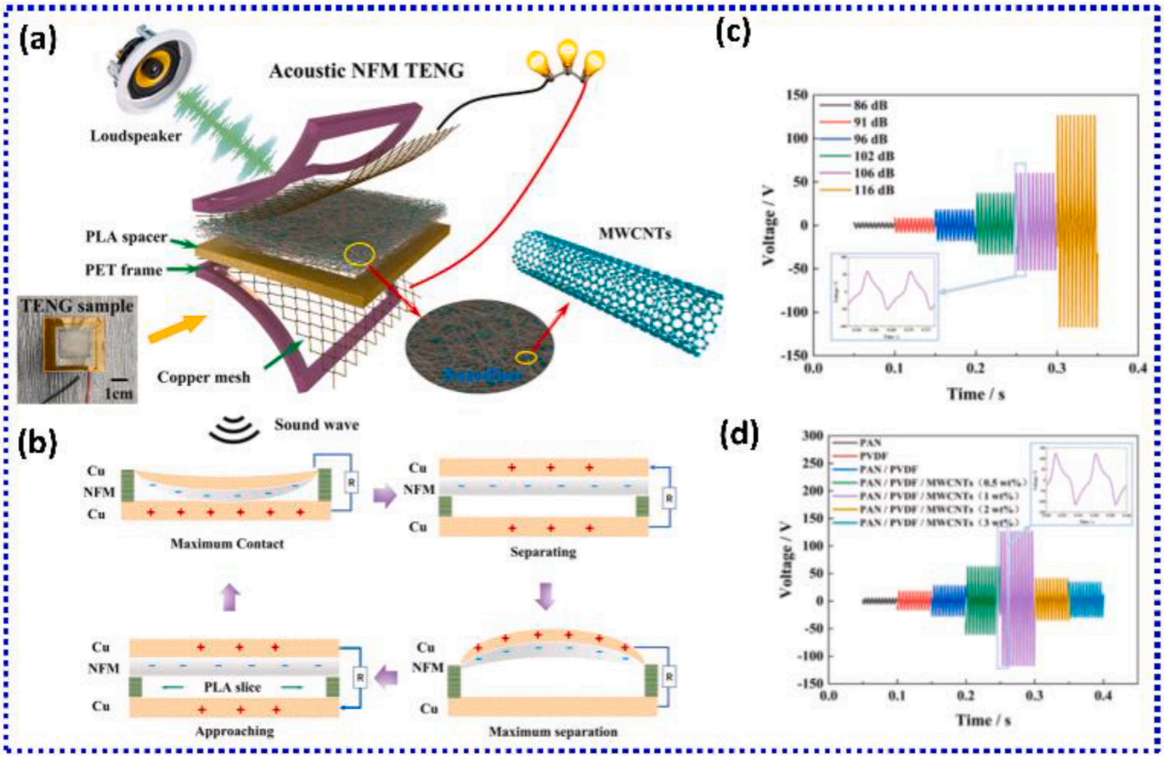

Fig. 69. (a) Diagram of the device. (b) Principle of operation. (c) Responses for different excitation conditions. (d) Voltage responses for different membrane materials. Nanomaterial base TENG's reprinted from Sun, W. et al. [661] under the terms of the Creative Commons Attribution 4.0 International License (CC BY 4.0). Copyright (2023) Elsevier.

developed a power supply device under the skin. It could be charged using an ultrasonic sonotrode placed on the skin.

9. Summary & prospects

In this review, we have consolidated the rapid progress in triboelectric nanogenerators into a comprehensive and integrative framework. Our discussion spans from fundamental charge-transfer mechanisms and triboelectric measurement methods to the classification of diverse material families, device architectures, and strategies for performance enhancement. The work offers a comprehensive perspective that integrates theory, materials, fabrication strategies, and applications into a unified roadmap.

A distinctive contribution of this review is the establishment of a materials classification framework that systematically positions polymers, MOFs/COFs, perovskites, 2D layered systems, textiles, and biodegradable materials within the triboelectric series. By correlating triboelectric polarity with intrinsic descriptors such as work function, Lewis's acidity/basicity, and surface wettability, the review offers predictive insights that enable rational material design. This approach transforms the triboelectric series from an empirical list into a quantitative design tool for researchers. In addition, the review highlights sustainability aspects often overlooked in earlier studies, including PFAS-free alternatives, biodegradability, and recyclability, ensuring relevance to future regulatory and environmental demands.

The adoption of TENGs in real-world applications has grown significantly, with successful implementations in self-powered sensors for environmental monitoring, human-machine interfaces, wearable health monitoring systems, and energy-efficient IoT networks. The development of fire-resistant and stretchable triboelectric fabrics further expands their potential in safety applications, while advances in charge storage and energy management solutions are addressing limitations related to energy intermittency. As TENGs transition from laboratory research to practical deployment, ongoing work focuses on improving material durability, optimizing charge transfer efficiency, and developing scalable fabrication techniques for widespread commercialization.

9.1. Future prospects

The future of TENGs lies in addressing existing limitations and expanding their real-world applications through targeted technological advancements. One of the primary areas of focus is improving charge retention and energy conversion efficiency. Current TENGs suffer from charge dissipation due to environmental influences, such as humidity and air breakdown effects. Efforts to develop encapsulated or vacuum-sealed TENGs, along with the use of advanced dielectric coatings, will help mitigate these issues and enhance long-term stability.

Another critical advancement will be scaling up TENG fabrication for industrial applications. While TENGs have demonstrated potential in wearable electronics and small-scale energy harvesting, the challenge remains in developing cost-effective, high-throughput manufacturing processes. Roll-to-roll fabrication techniques and printed electronics offer promising solutions for producing large-area TENG devices suitable for smart textiles, industrial monitoring, and urban infrastructure.

DC-TENG Advancements: Overcoming rectification losses to achieve direct current output without external circuits. Energy Storage & Power Management: Developing self-charging supercapacitors and microbatteries for efficient energy storage.

Integration with energy storage systems is also crucial for ensuring that TENG-generated energy can be efficiently utilized. Current research is focusing on directly coupling TENGs with supercapacitors, lithium-ion batteries, and flexible power storage solutions, enabling continuous operation of self-powered devices. This development is particularly relevant for IoT applications, where autonomous, battery-free operation is a key requirement.

In the biomedical field, TENGs will continue to evolve for health monitoring and therapeutic applications. Flexible, biocompatible TENGs have already demonstrated the ability to power small implantable devices and monitor physiological signals. Future efforts will refine these designs for real-world medical applications, such as non-invasive biosensors, self-powered prosthetics, and wearable rehabilitation systems.

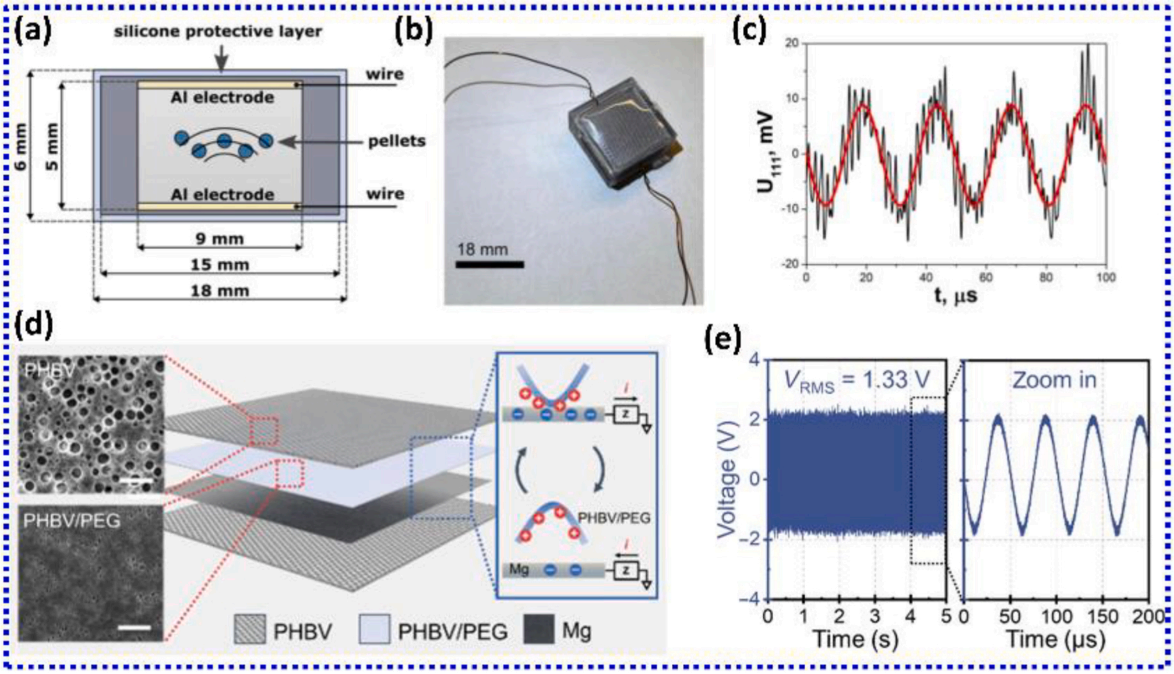

Fig. 70. (a,d) Schema of devices. (b) Device photo. (c,e) Voltage response of device. (a,b,c) Ultrasounds TENG's reprinted from Nowacki, B. et al. [317] under the terms of the Creative Commons Attribution 4.0 International License (CC BY 4.0). Copyright (2023) Elsevier). (d,e) Ultrasounds TENG's reprinted from Lee, D.M. et al. [667] under the terms of the Creative Commons Attribution 4.0 International License (CC BY 4.0). Copyright (2023) Springer-Nature).

Finally, environmental sustainability will play a significant role in the future of TENG research. The push toward biodegradable and recyclable materials will drive the development of eco-friendly TENGs that can be used for disposable health monitors, environmental sensors, and sustainable energy solutions. Research into naturally derived polymers and biodegradable conductors will ensure that TENGs contribute to energy efficiency without adding to electronic waste concerns.

While TENGs are unlikely to replace conventional energy sources, their role as complementary power solutions for small-scale, distributed energy needs is becoming increasingly clear. With ongoing improvements in material engineering, charge management, and large-scale manufacturing, TENGs are set to become a vital component of next-generation smart devices, self-sustaining electronics, and energy-harvesting systems for industrial and environmental applications.

In conclusion, this review presents a comprehensive, multidisciplinary perspective on TENG advancements, addressing material innovations, charge retention challenges, application-specific optimizations, and future integration possibilities. As the field continues to expand into AI-enhanced, bio-integrated, and large-scale energy systems, TENGs will reshape energy harvesting paradigms, leading to self-sufficient, intelligent, and sustainable power solutions. AI and machine learning offer strong potential for advancing TENG research, but significant challenges remain. These include the scarcity of large, high-quality datasets and inconsistent triboelectric measurement methods that hinder reproducibility. Many AI models operate as black boxes, offering limited mechanistic insight, and a gap often exists between computational predictions and experimental feasibility. With further research in quantum-driven material discovery, AI-assisted triboelectric optimization, and large-scale integration, TENGs will transition from specialized nanogenerators to mainstream, industrial-scale power solutions, driving the future of smart electronics, green energy, and autonomous self-powered systems.

CRediT authorship contribution statement

Uday Kumar Khanapurarm: Writing – review & editing, Writing – original draft, Visualization, Formal analysis, Data curation, Conceptualization. **Gokana Mohana Rani:** Writing – original draft, Visualization, Methodology, Formal analysis, Data curation. **Swati Panda:** Writing – original draft, Visualization, Methodology, Formal analysis, Data curation. **Thitirat Charoonsuk:** Writing – original draft, Visualization, Formal analysis, Data curation. **Krystian Mistewicz:** Writing – original draft, Visualization, Formal analysis, Data curation. **Sugato Hajra:** Writing – original draft, Visualization, Formal analysis, Data curation. **Kushal Ruthvik Kaja:** Writing – original draft, Visualization, Formal analysis, Data curation. **Reddicherla Umapathi:** Writing – original draft, Visualization, Formal analysis, Data curation. **Saichon Sriphan:** Writing – original draft, Visualization, Formal analysis, Data curation. **Jakub Jała:** Writing – original draft, Visualization, Formal analysis, Data curation. **Haranath Divi:** Writing – review & editing, Visualization, Validation. **Albert Smalcerz:** Writing – original draft, Visualization, Formal analysis, Data curation. **Mohamed Belal:** Writing – original draft, Visualization, Formal analysis, Data curation. **Pannur Jaahnavi:** Writing – original draft, Visualization, Formal analysis, Data curation. **Moein Safarkhani:** Writing – original draft, Visualization, Formal analysis, Data curation. **Hanseung Kim:** Writing – original draft, Visualization, Formal analysis, Data curation. **Yogendra Kumar Mishra:** Writing – review & editing, Visualization, Validation. **Hoe Joon Kim:** Writing – review & editing, Writing – original draft, Visualization, Supervision, Formal analysis, Data curation, Conceptualization. **Yun Suk Huh:** Writing – review & editing, Writing – original draft, Visualization, Validation, Formal analysis, Conceptualization. **Naratip Vittayakorn:** Writing – review & editing, Writing – original draft, Validation, Supervision, Formal analysis, Conceptualization. **Bartłomiej Nowacki:** Writing – review & editing, Writing – original draft, Validation, Supervision, Formal analysis, Conceptualization. **Sai Kishore Ravi:** Writing – review & editing, Visualization, Validation. **Stephen James Eichhorn:** Writing – review & editing, Visualization, Validation, Data curation. **Monica F. Craciun:** Writing – review & editing, Visualization, Validation. **Ana Borras:** Writing – review & editing, Visualization, Validation. **Hamideh Khanbareh:** Writing – review & editing, Visualization, Validation. **Jiaqian Qin:** Writing – review & editing, Validation, Supervision, Resources, Formal analysis, Data curation, Conceptualization. **Rakesh Kumar Rajaboina:** Writing – review & editing, Writing – original draft, Visualization, Supervision, Project administration, Formal analysis, Data curation, Conceptualization.

Declaration of generative AI and AI-assisted technologies in scientific writing

During the preparation of this work, the authors used ChatGPT to improve the language of this paper. After using this tool, the authors reviewed and edited the content as needed. The authors take full responsibility for the content of the published article.

Data availability

No data was used for the research described in the article.

Declaration of competing interest

Jiaqian Qin is an editorial board member for Advanced Powder Materials and was not involved in the editorial review or the decision to publish this article. All authors declare that there are no competing interests.

Acknowledgements

HJK acknowledges the support by the National Research Foundation of Korea, funded by the Ministry of Science and ICT of Korea (RS-2024-00346135, RS-2024-00406674**). SH & SP** acknowledge this work was supported by the InnoCORE program of the Ministry of Science and ICT (25-InnoCORE-01). **BN** acknowledges this study was partially supported by Silesian University of Technology (Gliwice, Poland) through the statutory research grants No. BK-227/RM4/2025 (11/040/BK_25/0040), BK-208/RIF1/2025, statutory research project for young scientists BKM-748/RM4/2024 (11/040/BKM24/0038) and pro-quality Rector's grant No. 14/010/RGJ25/0018. **YSH** acknowledges the support by the Korea Institute of Energy Technology Evaluation and Planning (KETEP) grant funded by the Korea government (MOTIE) (RS-2024-00420434) **NV** acknowledges the research was funded by National Science, Research and Innovation Fund (NSRF), and King Mongkut's University of Technology North Bangkok (Project no. KMUTNB-FF-68-B-28) and also supported by King Mongkut's Institute of Technology Ladkrabang under Grant No. 2569-02-05-001.

References

[1] J. Lowell, A.C. Rose-Innes, Contact electrification, Adv. Phys. 29 (1980) 947–1023.
[2] D.J. Lacks, R.M. Sankaran, Contact electrification of insulating materials, J. Phys. D Appl. Phys. 44 (2011) 453001.
[3] W.G. Kim, D.W. Kim, I.W. Tcho, J.K. Kim, M.S. Kim, Y.K. Choi, Triboelectric nanogenerator: structure, mechanism, and applications, ACS Nano 15 (2021) 258–287.
[4] S. Potu, A. Kulandaivel, B. Gollapelli, U.K. Khanapuram, R.K. Rajaboina, Oxide based triboelectric nanogenerators: recent advances and future prospects in energy harvesting, Mater. Sci. Eng. R Rep. 161 (2024) 100866.
[5] R.K. Rajaboina, U.K. Khanapuram, A. Kulandaivel, 2D layered materials based triboelectric self-powered sensors, Advanced Sensor Research 3 (2024) 2400045.
[6] D.J. Lacks, T. Shinbrot, Long-standing and unresolved issues in triboelectric charging, Nat. Rev. Chem 3:8 (3) (2019) 465–476, 2019.
[7] M. Seol, S. Kim, Y. Cho, K. Byun, H. Kim, J. Kim, S.K. Kim, S. Kim, H. Shin, S. Park, Triboelectric series of 2d layered materials, Adv. Mater. 30 (2018) e1801210.

[8] D.M. Pai, B.E. Springett, Physics of electrophotography, Rev. Mod. Phys. 65 (1993) 163–211.

[9] J. Wang, C. Wu, Y. Dai, Z. Zhao, A. Wang, T. Zhang, Z.L. Wang, Achieving ultrahigh triboelectric charge density for efficient energy harvesting, Nat. Commun. 88 (2017) 1–8.

[10] F.R. Fan, Z.Q. Tian, Z. Lin Wang, Flexible triboelectric generator, Nano Energy 1 (2012) 328–334.

[11] G.M. Rani, C.M. Wu, K.G. Motora, R. Umapathi, C.R.M. Jose, Acoustic-electric conversion and triboelectric properties of nature-driven cf-cnt based triboelectric nanogenerator for mechanical and sound energy harvesting, Nano Energy 108 (2023) 108211.

[12] L. Qi, L. Kong, Y. Wang, J. Song, A. Azam, Z. Zhang, J. Yan, Recent progress in application-oriented self-powered microelectronics, Adv. Energy Mater. 13 (2023) 2302699.

[13] K.U. Kumar, S. Hajra, G.M. Rani, S. Panda, R. Umapathi, S. Venkateswarlu, H. J. Kim, Y.K. Mishra, R.R. Kumar, Revolutionizing waste-to-energy: harnessing the power of triboelectric nanogenerators, Adv. Compos. Hybrid Mater. 7 (2024) 91.

[14] X.S. Zhang, M. Di Han, B. Meng, H.X. Zhang, High performance triboelectric nanogenerators based on large-scale mass-fabrication technologies, Nano Energy 11 (2015) 304–322.

[15] T. Sanislav, G.D. Mois, S. Zeadally, S.C. Folea, Energy harvesting techniques for internet of things (IoT), IEEE Access 9 (2021) 39530–39549.

[16] A. Ali, H. Shaukat, S. Bibi, W.A. Altabey, M. Noori, S.A. Kouritem, Recent progress in energy harvesting systems for wearable technology, Energy Strategy Rev. 49 (2023) 101124.

[17] F. Jean, M.U. Khan, A. Alazzam, B. Mohammad, Harnessing ambient sound: different approaches to acoustic energy harvesting using triboelectric nanogenerators, J. Sci. Adv. Mater. Devices 9 (2024) 100805.

[18] D. Choi, Y. Lee, Z.H. Lin, S. Cho, M. Kim, C.K. Ao, S. Soh, C. Sohn, C.K. Jeong, J. Lee, M. Lee, S. Lee, J. Ryu, P. Parashar, Y. Cho, J. Ahn, I.D. Kim, F. Jiang, P. S. Lee, G. Khandelwal, S.J. Kim, H.S. Kim, H.C. Song, M. Kim, J. Nah, W. Kim, H. G. Menge, Y.T. Park, W. Xu, J. Hao, H. Park, J.H. Lee, D.M. Lee, S.W. Kim, J. Y. Park, H. Zhang, Y. Zi, R. Guo, J. Cheng, Z. Yang, Y. Xie, S. Lee, J. Chung, I. K. Oh, J.S. Kim, T. Cheng, Q. Gao, G. Cheng, G. Gu, M. Shim, J. Jung, C. Yun, C. Zhang, G. Liu, Y. Chen, S. Kim, X. Chen, J. Hu, X. Pu, Z.H. Guo, X. Wang, J. Chen, X. Xiao, X. Xie, M. Jarin, H. Zhang, Y.C. Lai, T. He, H. Kim, I. Park, J. Ahn, N.D. Huynh, Y. Yang, Z.L. Wang, J.M. Baik, D. Choi, Recent advances in triboelectric nanogenerators: from technological progress to commercial applications, ACS Nano 17 (2023) 11087–11219.

[19] T. Aziz, A. Farid, F. Haq, M. Kiran, A. Ullah, K. Zhang, C. Li, S. Ghazanfar, H. Sun, R. Ullah, A. Ali, M. Muzammal, M. Shah, N. Akhtar, S. Selim, N. Hagagy, M. Samy, S.K. Al Jaouni, A review on the modification of cellulose and its applications, Polymers 14 (2022) 3206.

[20] X. Tao, X. Chen, Z.L. Wang, Design and synthesis of triboelectric polymers for high performance triboelectric nanogenerators, Energy Environ. Sci. 16 (2023) 3654–3678.

[21] Y. Mi, Y. Lu, Y. Shi, Z. Zhao, X. Wang, J. Meng, X. Cao, N. Wang, Biodegradable polymers in triboelectric nanogenerators, Polymers (Basel) 15 (2022) 222.

[22] R.K. Rajaboina, U.K. Khanapuram, V. Vivekananthan, G. Khandelwal, S. Potu, A. Babu, N. Madathil, M. Velpula, P. Kodali, Crystalline porous material-based nanogenerators: recent progress, applications, challenges, and opportunities, Small 20 (2023) 2306209.

[23] S. Ghorbanzadeh, W. Zhang, Advances in mxene-based triboelectric nanogenerators, Nano Energy 125 (2024) 109558.

[24] Q. Chen, W. Akram, Y. Cao, C. Ge, T. Lin, J. Fang, Recent progress in the fabrication and processing of triboelectric yarns, Carbon Neutralization 2 (2023) 63–89.

[25] S. Kim, M.K. Gupta, K.Y. Lee, A. Sohn, T.Y. Kim, K. Shin, D. Kim, S.K. Kim, K. H. Lee, H. Shin, D. Kim, S. Kim, Transparent flexible graphene triboelectric nanogenerators, Adv. Mater. 26 (2014) 3918–3925.

[26] Y. Li, Y. Luo, H. Deng, S. Shi, S. Tian, H. Wu, J. Tang, C. Zhang, X. Zhang, J. W. Zha, S. Xiao, Advanced dielectric materials for triboelectric nanogenerators: principles, methods, and applications, Adv. Mater. 36 (2024) 2314380.

[27] S. Hajra, S. Panda, H. Khanberh, V. Vivekananthan, E. Chamanehpour, Y. K. Mishra, H.J. Kim, Revolutionizing self-powered robotic systems with triboelectric nanogenerators, Nano Energy 115 (2023) 108729.

[28] Q. Zhang, T. Jin, J. Cai, L. Xu, T. He, T. Wang, Y. Tian, L. Li, Y. Peng, C. Lee, Wearable triboelectric sensors enabled gait analysis and waist motion capture for iot-based smart healthcare applications, Adv. Sci. (Weinh.) 9 (2022) e2103694–e2103694.

[29] P. Munirathinam, A. Anna Mathew, V. Shanmugasundaram, V. Vivekananthan, Y. Purusothaman, S.J. Kim, A. Chandrasekhar, A comprehensive review on triboelectric nanogenerators based on real-time applications in energy harvesting and self-powered sensing, Mater. Sci. Eng., B 297 (2023) 116762.

[30] Y. Gai, Y. Jiang, Z. Li, Advances in health rehabilitation devices based on triboelectric nanogenerators, Nano Energy 116 (2023) 108787.

[31] L. Xu, Y. Yang, Y. Mao, Z. Li, Self-Powerbility in electrical stimulation drug delivery system, Adv. Mater. Technol. 7 (2021).

[32] C. Song, N. Xuan, X. Du, P. Chang, B. Yue, M. Zheng, Y. Jia, G. Cheng, Self-powered electrocatalytic integrated system based on teng for high-yield bipolar hydrogen production, Nano Energy 136 (2025) 110707.

[33] S. Zhu, Y. Xia, Y. Zhu, M. Wu, C. Jia, X. Wang, High-performance triboelectric nanogenerator powered flexible electroluminescence devices based on patterned laser-induced copper electrodes for visualized information interaction, Nano Energy 96 (2022) 107116.

[34] Z. Zhao, L. Zhou, S. Li, D. Liu, Y. Li, Y. Gao, Y. Liu, Y. Dai, J. Wang, Z.L. Wang, Selection rules of triboelectric materials for direct-current triboelectric nanogenerator, Nat. Commun. 12 (2021).

[35] A. Šutka, K. Mālnieks, L. Lapčinskis, M. Timusk, K. Kalniņš, A. Kovaļovs, J. Bitenieks, M. Knite, D. Stevens, J. Grunlan, Contact electrification between identical polymers as the basis for triboelectric/flexoelectric materials, Phys. Chem. Chem. Phys. 22 (2020) 13299–13305.

[36] L. Lapčinskis, A. Linarts, K. Mālnieks, H. Kim, K. Rubenis, K. Pudzs, K. Smits, A. Kovaļovs, K. Kalniņš, A. Tamm, C.K. Jeong, A. Šutka, Triboelectrification of nanocomposites using identical polymer matrixes with different concentrations of nanoparticle fillers, J Mater Chem A Mater 9 (2021) 8984–8990.

[37] H. Feng, Q. Li, Z. Peng, D. Ren, X. Li, H. Yang, X. Zhang, Y. Xi, Non-uniform surface charge distribution of tribodielectric material by edge effect, Nano Energy 130 (2024) 110116.

[38] D. Liu, L. Zhou, S. Cui, Y. Gao, S. Li, Z. Zhao, Z. Yi, H. Zou, Y. Fan, J. Wang, Z. L. Wang, Standardized measurement of dielectric materials' intrinsic triboelectric charge density through the suppression of air breakdown, Nat. Commun. 13 (2022) 6019.

[39] C. Zhang, L. Zhou, P. Cheng, X. Yin, D. Liu, X. Li, H. Guo, Z.L. Wang, J. Wang, Surface charge density of triboelectric nanogenerators: theoretical boundary and optimization methodology, Appl. Mater. Today 18 (2020) 100496.

[40] H. Zou, Y. Zhang, L. Guo, P. Wang, X. He, G. Dai, H. Zheng, C. Chen, A.C. Wang, C. Xu, Z.L. Wang, Quantifying the triboelectric series, Nat. Commun. 10:1 (10) (2019) 1–9, 2019.

[41] Y. Zi, S. Niu, J. Wang, Z. Wen, W. Tang, Z.L. Wang, Standards and Fig.-of-merits for quantifying the performance of triboelectric nanogenerators, Nat. Commun. 6 (2015) 8376.

[42] H. Wang, J. Wang, K. Yao, J. Fu, X. Xia, R. Zhang, J. Li, G. Xu, L. Wang, J. Yang, J. Lai, Y. Dai, Z. Zhang, A. Li, Y. Zhu, X. Yu, Z.L. Wang, Y. Zi, A paradigm shift fully self-powered long-distance wireless sensing solution enabled by discharge-induced displacement current, Sci. Adv. 7 (2021) 6751–6773.

[43] R.D. Cruise, S.O. Starr, K. Hadler, J.J. Cilliers, Triboelectric charge saturation on single and multiple insulating particles in air and vacuum, Sci. Rep. 13 (2023) 1–12.

[44] Q. Chen, H. Shang, B. Cheng, C. Lu, Y. Wang, Y. Zhang, T. Shao, Quantifying triboelectric series of polymers based on the measurement of triboelectrification with nacl solution, Chem. Eng. J. 488 (2024) 150871.

[45] S. Chen, R.T. Leon, R. Qambari, Y. Yan, M. Chen, P.C. Sherrell, A.V. Ellis, J. D. Berry, Irreversible charging caused by energy dissipation from depinning of droplets on polymer surfaces, Phys. Rev. Lett. 134 (2025) 104002.

[46] N. Madathil, A. Babu, M. Velupula, A. Kulandaivel, R.K. Rajaboina, U. K. Khanapuram, K.C. Devarayapalli, D.S. Lee, A layered double hydroxides/mxene composite based triboelectric nanogenerator for energy harvesting and self-powered electroplating applications, Sustain. Energy Fuels 9 (2025) 4364–4374.

[47] L. Shi, Y. Wang, T. Guo, Y. Lei, J.K. El-Demellawi, Z. Zhao, H.N. Alshareef, Triboelectric series of two-dimensional metal carbide mxenes, Adv. Funct. Mater. 34 (2024) 2408538.

[48] B. Slater, J.C. Tan, Triboelectric behaviour of selected zeolitic-imidazolate frameworks: exploring chemical, morphological and topological influences, Chem. Sci. 15 (2024) 10056–10064.

[49] N. Pk, A. Chandrasekhar, Marriage between metal-organic frameworks/covalent-organic frameworks and triboelectric nanogenerator for energy harvesting —a review, Mater. Today Energy 37 (2023) 101393.

[50] V.P. Kallupadi, H. Varghese, U.N.S. Hareesh, A. Chandran, Modulating contact electrification with metal-organic frameworks in flexible triboelectric nanogenerators for kinetic energy harvesting and self-powered humidity sensing applications, Adv. Funct. Mater. 35 (2025) 2411855.

[51] X. Li, C. Jiang, Y. Yao, Q. Zhang, S. Dai, Y. Ying, J. Ping, Growth-controllable triboelectric nanogenerator based on surface-attached metal-organic framework layer on living leaf, Small 17 (2021).

[52] Y. Wang, X. Yang, X. Yu, J. Duan, Q. Yang, Y. Duan, Q. Tang, Triboelectric charging behaviors and photoinduced enhancement of alkaline earth ions doped inorganic perovskite triboelectric nanogenerators, Nano Energy 77 (2020) 105280.

[53] X. Yu, Y. Wang, J. Zhang, J. Duan, X. Yang, L. Liu, Q. Tang, Halogen regulation of inorganic perovskites toward robust triboelectric nanogenerators and charging polarity series, J Mater Chem A Mater 8 (2020) 14299–14307.

[54] Y. Wang, X. Yang, W. Xu, X. Yu, J. Duan, Y. Duan, Q. Tang, Triboelectric behaviors of inorganic Cs$_{1-x}A_x$PbBr$_3$ halide perovskites toward enriching the triboelectric series, J Mater Chem A Mater 8 (2020) 25696–25705.

[55] Y.J. Kim, J. Lee, S. Park, C. Park, C. Park, H.J. Choi, Effect of the relative permittivity of oxides on the performance of triboelectric nanogenerators, RSC Adv. 7 (2017) 49368–49373.

[56] R. Zhang, C. Dahlström, H. Zou, J. Jonzon, M. Hummelgård, J. Örtegren, N. Blomquist, Y. Yang, H. Andersson, M. Olsen, M. Norgren, H. Olin, Z. Lin Wang, H.Y. Zou, Z.L. Wang, Y. Yang, H. Andersson, R.Y. Zhang, J. Jonzon, M. Hummelgård, J. Örtegren, N. Blomquist, M. Olsen, H. Olin, C. Dahlström, M. Norgren, Cellulose-based fully green triboelectric nanogenerators with output power density of 300 w m^{-2}, Adv. Mater. 32 (2020) 2002824.

[57] H. Meng, Q. Yu, Z. Liu, Y. Gai, J. Xue, Y. Bai, X. Qu, P. Tan, D. Luo, W. Huang, K. Nie, W. Bai, Z. Hou, R. Tang, H. Xu, Y. Zhang, Q. Cai, X. Yang, Z.L. Wang, Z. Li, Triboelectric performances of biodegradable polymers, Matter 6 (2023) 4274–4290.

[58] N.D. Tyrrell, A proposal that would ban manufacture, supply, and use of all fluoropolymers and most fluorinated reagents within the entire eu, Org. Process Res. Dev. 27 (2023) 1422–1426.
[59] P.C. Sherrell, A. Šutka, M. Timusk, A. Šutka, Alternatives to fluoropolymers for motion-based energy harvesting: perspectives on piezoelectricity, triboelectricity, ferroelectrets, and flexoelectricity, Small 20 (2024) 2311570.
[60] X. Zhang, L. Chen, Y. Jiang, W. Lim, S. Soh, Rationalizing the triboelectric series of polymers, Chem. Mater. 31 (2019) 1473–1478.
[61] H. Zou, L. Guo, H. Xue, Y. Zhang, X. Shen, X. Liu, P. Wang, X. He, G. Dai, P. Jiang, H. Zheng, B. Zhang, C. Xu, Z.L. Wang, Quantifying and understanding the triboelectric series of inorganic non-metallic materials, Nat. Commun. 11 (2020) 1–7.
[62] S. Niu, Z.L. Wang, Theoretical systems of triboelectric nanogenerators, Nano Energy 14 (2015) 161–192.
[63] Z.L. Wang, From contact electrification to triboelectric nanogenerators, Rep. Prog. Phys. 84 (2021) 096502.
[64] Z.L. Wang, L. Lin, J. Chen, S. Niu, Y. Zi, Vertical contact-separation Mode, Triboelectric Nanogenerator, Springer, New York, 2016, pp. 23–47.
[65] Z.L. Wang, L. Lin, J. Chen, S. Niu, Y. Zi, Lateral sliding mode. Triboelectric Nanogenerator, Springer, New York, 2016, pp. 49–90.
[66] Z. Li, Y. Yu, Y. Wang, H. Li, J. Wang, H. Jin, T. Cheng, Z.L. Wang, X. Cheng, Crossing lateral-sliding type triboelectric nanogenerator, Nano Energy 139 (2025) 110952.
[67] Z.L. Wang, L. Lin, J. Chen, S. Niu, Y. Zi, Single-electrode mode. Triboelectric Nanogenerator, Springer, New York, 2016, pp. 91–107.
[68] J. Chen, Z.L. Wang, Reviving vibration energy harvesting and self-powered sensing by a triboelectric nanogenerator, Joule 1 (2017) 480–521.
[69] Z.L. Wang, L. Lin, J. Chen, S. Niu, Y. Zi, Triboelectric Nanogenerator: Freestanding triboelectric-layer Mode, Green Energy and Technology, 2016, pp. 109–153.
[70] O. Cakir, D. Doganay, M. Cugunlular, M.O. Cicek, O. Demircioglu, S. Coskun, H. E. Unalan, Post-treatment optimization for silver nanowire networks in transparent droplet-based teng sensors, Nano Energy 128 (2024) 109940.
[71] X. Bi, Z. Huang, M. Yao, Z. Wang, P. Yu, C. Jiang, Highly conductive rubber-based electrode with a robust wrinkled mesh-like copper coating for stretchable triboelectric nanogenerator, Colloids Surf. A Physicochem. Eng. Asp. 700 (2024) 134786.
[72] K. Shi, B. Chai, H. Zou, Z. Wen, Y. Liu, M. He, J. Chen, P. Jiang, X. Huang, Direct-Current triboelectric nanogenerators based on contact–separation mode and conductive–adhesive interface, Adv. Funct. Mater. 34 (2024).
[73] Q. Sun, G. Ren, S. He, B. Tang, Y. Li, Y. Wei, X. Shi, S. Tan, R. Yan, K. Wang, L. Yu, J. Wang, K. Gao, C. Zhu, Y. Song, Z. Gong, G. Lu, W. Huang, H. Yu, Charge dispersion strategy for high-performance and rain-proof triboelectric nanogenerator, Adv. Mater. 36 (2023).
[74] J. Yang, L. Chang, H. Deng, Z. Cao, Zwitterionic eutectogels with high ionic conductivity for environmentally tolerant and self-healing triboelectric nanogenerators, ACS Nano 18 (2024) 18980–18991.
[75] S. Amini, R.F.S. Muktar Ahmed, S. Madanahalli Ankanathappa, M. H. Chandrashekara Shastry, M. Shivanna, K. Sannathammegowda, Investigating the annealing effects on the performance of polyvinyl alcohol-graphite-based triboelectric nanogenerator, Sens Actuators A Phys 372 (2024) 115309.
[76] X. Sun, L. Dong, J. Liu, T. Hou, S. Chen, Multi-scale modified PVDF/Ag@C layer based on dielectric doping and plasma treatment for high-performance triboelectric nanogenerators and self-powered water sterilization, Nano Energy 124 (2024) 109511.
[77] P. Manchi, S.A. Graham, M.V. Paranjape, A. Kurakula, V.S. Kavarthapu, J.S. Yu, Calcium copper titanate incorporated polydimethylsiloxane flexible composite film-based triboelectric nanogenerator for energy harvesting and self-powered sensing applications, J. Mater. Sci. Technol. 190 (2024) 56–66.
[78] K.G. Motora, C.M. Wu, C.R.M. Jose, Boosting the triboelectric performances of biowaste chitosan keratin triboelectric nanogenerator using carbon composite film as charge storage and charge recombination blocking intermediate layer, Chem. Eng. J. 492 (2024) 152413.
[79] X. Liang, T. Zhao, W. Jiang, X. Yu, Y. Hu, P. Zhu, H. Zheng, R. Sun, C.P. Wong, Highly transparent triboelectric nanogenerator utilizing in-situ chemically welded silver nanowire network as electrode for mechanical energy harvesting and body motion monitoring, Nano Energy 59 (2019) 508–516.
[80] D. Kim, S. Lee, Y. Ko, C.H. Kwon, J. Cho, Layer-by-layer assembly-induced triboelectric nanogenerators with high and stable electric outputs in humid environments, Nano Energy 44 (2018) 228–239.
[81] H. Phan, P.N. Hoa, H.A. Tam, P.D. Thang, N.H. Duc, Multi-directional triboelectric nanogenerator based on industrial Q-switched pulsed laser etched aluminum film, Extreme Mech. Lett. 40 (2020) 100886.
[82] Y. Yang, J. Qian, Y. Dong, M.A. Nikitina, U. Zafari, X. Xiao, Parameter optimization for enhancing teng by UV nanosecond laser direct writing and coupling, Results Eng. 14 (2022) 100482.
[83] H. Yi, L. Xiong, The effect of the electric field on the output performance of triboelectric nanogenerators, J. Comput. Electron. 19 (2020) 1670–1677.
[84] S.J. Shetty, N.T.K., S. Amini, S.M. Rumana Farheen, M.A. Sangamesha, S. Krishnaveni, G. S.C, Exploring the potential of one-dimensional functionalized multi-walled carbon nanotubes in triboelectric nanogenerator for self-powered applications, J. Alloys Compd. 1041 (2025) 183837.
[85] X. Wang, B. Yang, J. Liu, Y. Zhu, C. Yang, Q. He, A flexible triboelectric-piezoelectric hybrid nanogenerator based on P(VDF-TrFE) nanofibers and PDMS/MWCNT for wearable devices, Sci. Rep. 6 (2016) 36409.
[86] I.W. Tcho, W.G. Kim, S.B. Jeon, S.J. Park, B.J. Lee, H.K. Bae, D. Kim, Y.K. Choi, Surface structural analysis of a friction layer for a triboelectric nanogenerator, Nano Energy 42 (2017) 34–42.
[87] M. Su, J. Brugger, B. Kim, Simply structured wearable triboelectric nanogenerator based on a hybrid composition of carbon nanotubes and polymer layer, International Journal of Precision Engineering and Manufacturing-Green Technology 7 (2020) 683–698.
[88] H. Wu, J. Wang, S. Fu, C. Shan, Q. Zhao, K. Li, G. Li, Q. Mu, X. Wang, C. Hu, A constant current triboelectric nanogenerator achieved by hysteretic and ordered charge migration in dielectric polymers, Energy Environ. Sci. 16 (2023) 5144–5153.
[89] J. Zheng, S. Xu, M. Chen, K. Li, Z. Wang, H. Feng, S. Wang, H. Yu, Z. Li, Recyclable high-performance triboelectric nanogenerator enabled by dynamic covalently crosslinked polymers, Nano Energy 122 (2024) 109288.
[90] C. Li, R. Luo, Y. Bai, J. Shao, J. Ji, E. Wang, Z. Li, H. Meng, Z. Li, Molecular doped biodegradable triboelectric nanogenerator with optimal output performance, Adv. Funct. Mater. 34 (2024).
[91] T. Mudgal, M. Tiwari, D. Bharti, Polymer-composite triboelectric nanogenerators with hook-shaped electrode for wind energy harvesting, Mater. Today Commun. 40 (2024) 109616.
[92] S. Hajra, P. In-na, C. Janpum, S. Panda, H.J. Kim, Triboelectric nanogenerators based on immobilized living microalgae for biomechanical energy harvesting, Electron. Mater. Lett. 19 (2023) 367–373.
[93] N. Meng, Y. Zhang, W. Liu, Q. Chen, N. Soykeabkaew, Y. Liao, Monolithic conjugated microporous polymer aerogel for triboelectric nanogenerator, Adv. Funct. Mater. 34 (2024).
[94] K. Ruthvik, A. Babu, P. Supraja, M. Navaneeth, V. Mahesh, K. Uday Kumar, R. Rakesh Kumar, B. Manmada Rao, D. Haranath, K. Prakash, High-performance triboelectric nanogenerator based on 2d graphitic carbon nitride for self-powered electronic devices, Mater. Lett. 350 (2023) 134947.
[95] V. Mohan, P. Pazhamalai, K. Krishnamoorthy, S.J. Kim, Free-standing graphene oxide/carboxymethyl cellulose paper-based triboelectric nanogenerator for self-powered motion sensor, Surf. Interfaces 51 (2024) 104553.
[96] P. Hajara, M.R. Shijeesh, K.V. Vijoy, T.P. Rose, K.J. Saji, Harnessing energy through ZnO-based triboelectric nanogenerator: a comparative analysis of polymer materials, with emphasis on pvdf nanofibers, J. Electron. Mater. 53 (2024) 5617–5628.
[97] Y. Zhou, J.H. Zhang, S. Li, H. Qiu, Y. Shi, L. Pan, Triboelectric nanogenerators based on 2d materials: from materials and devices to applications, Micromachines 14 (2023) 1043.
[98] S. Pramanik, C. Sengupta, S. Sharma, S. Mondal, D.K. Goswami, T. Mondal, Advancement of 2d material-based moisture-enabled nanogenerators, ACS Appl. Electron. Mater. 6 (2024) 8689–8702.
[99] T. Sun, C. Yao, Z. Liu, S. Huang, X. Huang, S. Zheng, J. Liu, P. Shi, T. Zhang, H. Chen, H. Chen, X. Xie, Machine learning-coupled vertical graphene triboelectric pressure sensors array as artificial tactile receptor for finger action recognition, Nano Energy 123 (2024) 109395.
[100] M.S. Bin Sadeque, M. Rahman, M.M. Hasan, M. Ordu, Graphene nanoplatelet integrated thermally drawn PVDF triboelectric nanocomposite fibers for extreme environmental conditions, Adv. Electron. Mater. 10 (2024).
[101] K. Sharma, N.K. Puri, B. Singh, Hexagonal boron nitride in sensing and biosensing applications. Hexagonal Boron Nitride: Synthesis, Properties, and Applications, 2024, pp. 511–552.
[102] L. Pang, Z. Li, Y. Zhao, X. Zhang, W. Du, L. Chen, A. Yu, J. Zhai, Triboelectric nanogenerator based on polyimide/boron nitride nanosheets/polyimide nanocomposite film with enhanced electrical performance, ACS Appl. Electron. Mater. 4 (2022) 3027–3035.
[103] K. Zhao, Z. Gao, J. Zhang, J. Zhou, F. Zhan, L. Qiang, M.J. Liu, R.H. Cyu, Y. L. Chueh, Design of strong-performance, high-heat dissipation rate, and long-lifetime triboelectric nanogenerator based on robust hexagonal boron nitride (hBN) nanosheets/polyvinyl chloride (PVC) composite films for rotational energy harvesting, J. Power Sources 614 (2024) 234997.
[104] B. Das, R. Paul, R. Karmakar, A.K. Meikap, A. Kumar, S. Krishnamurthy, R. Ghosh, A triboelectric nanogenerator based on waste plastic and layered materials via modulation of the electrical and dielectric properties, ACS Appl. Energy Mater. 7 (2024) 7025–7036.
[105] B.G. Hyun, Y.S. Jun, J.H. Lee, M. Hamidinejad, Z. Saadatnia, S. Ghaffari-Mosanenzadeh, H.E. Naguib, C.B. Park, Incorporation of hexagonal boron nitride and multi-walled carbon nanotube for motion sensing triboelectric nanogenerators, Compos. B Eng. 272 (2024) 111193.
[106] A.S. Bhavya, H. Varghese, A. Chandran, K.P. Surendran, Two-dimensional hexagonal boron nitride nanosheet–polycarbonate composite ink-based printed flexible triboelectric nanogenerator for scavenging mechanical energy, ACS Appl. Electron. Mater. 5 (2023) 5483–5493.
[107] S. Nuthalapati, A. Chakraborthy, I. Arief, K.K. Meena, K. Ruthvik, R. Rakesh Kumar, K. Uday Kumar, A. Das, M. Ercan Altinsoy, A. Nag, Wearable high-performance mwcnts/pdms nanocomposite based triboelectric nanogenerators for haptic applications, IEEE Journal on Flexible Electronics 3 (2024) 393–400.
[108] N. Madathil, S. Potu, J. Pani, L. Bochu, A. Babu, H. Borkar, P. Kodali, U. K. Khanapuram, R.K. Rajaboina, Enhancing triboelectric nanogenerators performance with MXene–silicone nanocomposites: a leap forward in energy harvesting and touch-sensitive technologies, ACS Appl. Electron. Mater. 6 (2024) 5574.
[109] J. Fan, R. Yang, Y. Du, F. Wang, L. Wang, J. Yang, A. Zhou, A triboelectric nanogenerator based on MXene/TPU composite films with excellent stretchability for self-powered flexible sensing, Nano Energy 129 (2024) 109999.

[110] J.A. Ajani Lakmini Jayarathna, S. Hajra, S. Panda, E. Chamanehpour, I. Sulania, M. Singh Goyat, S.H. Hsu, H. Joon Kim, T. Treeratanaphitak, Y. Kumar Mishra, Exploring potential of MXenes in smart sensing and energy harvesting, Mater. Lett. 363 (2024) 136252.

[111] Y. Tao, H. Xiang, X. Cao, N. Wang, Spring design of triboelectric nanogenerator with MXene-modified interface for fluid energy harvesting and water level monitoring, ACS Appl. Mater. Interfaces 16 (2024) 3406–3415.

[112] M. Mao, J. Kong, X. Ge, Y. Sun, H. Yu, J. Liu, W. Huang, D.Y. Wang, Y. Wang, MXene-based wearable self-powered and photothermal triboelectric nanogenerator patches for wound healing acceleration and tactile sensing, Chem. Eng. J. 482 (2024) 148949.

[113] G. Khandelwal, S. Deswal, D. Shakthivel, R. Dahiya, Recent developments in 2d materials for energy harvesting applications, J. Phys.: Energy 5 (2023) 032001.

[114] M. Baraily, B. Baro, R. Boruah, S. Bayan, PVDF-HFP encapsulated ws$_2$ nanosheets in droplet-based triboelectric nanogenerators for possible detection of human na $^+$/k$^+$ ion concentration, Nanotechnology 35 (2024) 365502.

[115] Y. Liu, D. Zhang, X. Ji, Z. Xu, H. Zhang, R. Mao, W. Liu, J. Wang, Y. Sun, Rotational contact triboelectric nanogenerator driven by water flows inspired by waterwheels and their applications for lead ion removal, Nano Energy 128 (2024) 109800.

[116] J. Zhou, J. Zhang, Y. Deng, J. Guo, H. Zhao, C. Li, S. Dang, H. Yu, D. Liu, D. Wang, C. Song, Y. Zhao, Z. Yan, J. Chen, H. Li, X. Xu, Atomic-crystal transition metal dichalcogenides schottky triboelectricity nanogenerator with ultrahigh direct-current density, Nano Energy 128 (2024) 109936.

[117] T. Chekke, R. Narzary, S. Ngadong, B. Satpati, S. Bayan, U. Das, Cotton based self-powered temperature sensor based on au-augmented WS$_2$ triboelectric nanogenerator, J. Electron. Mater. 53 (2024) 238–249.

[118] Y. Zheng, X. Li, M. Zheng, G. Cheng, Y. Zi, S. Cheng, H. Cui, X. Li, MoSe$_2$ enhanced raindrop triboelectric nanogenerators and its energy conversion analysis, Adv. Funct. Mater. 34 (2024).

[119] S. Jo, N. Kitchamsetti, H. Cho, D. Kim, Microwave-assisted hierarchically grown flake-like nico layered double hydroxide nanosheets on transitioned polystyrene towards triboelectricity-driven self-charging hybrid supercapacitors, Polymers 15 (2023) 454.

[120] S. Ippili, V. Jella, A.M. Thomas, C. Yoon, J.S. Jung, S.G. Yoon, ZnAl–LDH-induced electroactive β-phase and controlled dielectrics of PVDF for a high-performance triboelectric nanogenerator for humidity and pressure sensing applications, J Mater Chem A Mater 9 (2021) 15993–16005.

[121] P. Cui, J. Wang, J. Xiong, S. Li, W. Zhang, X. Liu, G. Gu, J. Guo, B. Zhang, G. Cheng, Z. Du, Meter-scale fabrication of water-driven triboelectric nanogenerator based on in-situ grown layered double hydroxides through a bottom-up approach, Nano Energy 71 (2020) 104646.

[122] G. Arrabito, R. Pezzilli, G. Prestopino, P.G. Medaglia, Layered double hydroxides in bioinspired nanotechnology, Crystals 10 (2020) 602.

[123] S. Badatya Ritu, M.K. Patel, M.K. Gupta, Unveiling a robust and high-temperature-stable two-dimensional ZnAl layered double hydroxide nanosheet based flexible triboelectric nanogenerator, Nanoscale 16 (2024) 4176–4188.

[124] Y. Dong, S.S.K. Mallineni, K. Maleski, H. Behlow, V.N. Mochalin, A.M. Rao, Y. Gogotsi, R. Podila, Metallic MXenes: a new family of materials for flexible triboelectric nanogenerators, Nano Energy 44 (2018) 103–110.

[125] T. Chekke, R. Narzary, S. Ngadong, B. Satpati, S. Bayan, U. Das, 2D WS$_2$-based single-electrode triboelectric nanogenerator for power generation and motion sensing, J. Electron. Mater. 52 (2023) 2685–2694.

[126] T.I. Kim, I.J. Park, S. Kang, T.S. Kim, S.Y. Choi, Enhanced triboelectric nanogenerator based on tungsten disulfide via thiolated ligand conjugation, ACS Appl. Mater. Interfaces 13 (2021) 21299–21309.

[127] V. Singh, B. Singh, PDMS/PVDF- MoS$_2$ based flexible triboelectric nanogenerator for mechanical energy harvesting, Polyme 274 (2023) 125910.

[128] A. Mahapatra, R.S. Ajimsha, D. Deepak, Sumit, R. Aggarwal, S. Kumar, R. Venkatesh, S.S. Roy, P. Misra, Textile-integrated MoS$_2$-pdms single electrode triboelectric nanogenerator for vibrational energy harvesting and biomechanical motion sensing, Nano Energy 116 (2023) 108829.

[129] R. Wen, J. Guo, A. Yu, J. Zhai, Z. lin Wang, Humidity-resistive triboelectric nanogenerator fabricated using metal organic framework composite, Adv. Funct. Mater. 29 (2019).

[130] Z. Abbas, M. Anithkumar, A.P.S. Prasanna, N. Hussain, S.J. Kim, S.M. Mobin, Triboelectric nanogenerators enhanced by a metal–organic framework for sustainable power generation and air mouse technology, J Mater Chem A Mater 11 (2023) 26531–26542.

[131] S. Hajra, M. Sahu, A.M. Padhan, I.S. Lee, D.K. Yi, P. Alagarsamy, S.S. Nanda, H. J. Kim, A green metal–organic framework-cyclodextrin MOF: a novel multifunctional material based triboelectric nanogenerator for highly efficient mechanical energy harvesting, Adv. Funct. Mater. 31 (2021).

[132] C. Altintas, I. Erucar, S. Keskin, MOF/COF hybrids as next generation materials for energy and biomedical applications, CrystEngComm 24 (2022) 7360–7371.

[133] A. Babu, K. Ruthvik, P. Supraja, M. Navaneeth, K.U. Kumar, R.R. Kumar, K. Prakash, N. Raju, High-performance triboelectric nanogenerator using ZIF-67/PVDF hybrid film for energy harvesting, J. Mater. Sci. Mater. Electron. 34 (2023).

[134] M. Velpula, N. Madathil, S. Potu, L. Bochu, K. Chithari, J. Vallamkondu, P. Kodali, U.K. Khanapuram, R.K. Rajaboina, High-performance mof-303-based triboelectric nanogenerators for self-powered electronics and road safety applications, ACS Appl. Electron. Mater. 6 (2024) 7890–7897.

[135] A. Babu, S. Gupta, R. Katru, N. Madathil, A. Kulandaivel, P. Kodali, H. Divi, H. Borkar, U.K. Khanapuram, R.K. Rajaboina, From acoustic to electric: advanced triboelectric nanogenerators with Fe-based metal–organic frameworks, Energy Technol. 12 (2024) 2400796.

[136] S. Barsiwal, A. Babu, U.K. Khanapuram, S. Potu, N. Madathil, R.K. Rajaboina, S. Mishra, H. Divi, P. Kodali, R. Nagapuri, T. Chinthakuntla, ZIF-67-metal–organic-framework-based triboelectric nanogenerator for self-powered devices, Nanoenergy Advances 2 (2022) 291–302.

[137] Z. Shao, J. Chen, Q. Xie, L. Mi, Functional metal/covalent organic framework materials for triboelectric nanogenerator, Coord. Chem. Rev. 486 (2023) 215118.

[138] J. Swain, S. Hajra, N. Das, P. Parhi, S. Panda, A. Priyadarshini, J. Panda, A. K. Sahu, P. Alagarsamy, V. Vivekananthan, H.J. Kim, R. Sahu, Spent catalyst-derived Mo-MOF: triboelectric nanogenerators and energy harvesting, Energy Technol. 11 (2023) 2300498.

[139] B.C. Dhal, S. Hajra, A. Priyadarshini, S. Panda, V. Vivekananthan, J. Swain, S. Swain, N. Das, R. Samantray, H.J. Kim, R. Sahu, Innovative synthesis of zeolitic imidazolate framework by a stovetop kitchen pressure cook pot for triboelectric nanogenerator, Energy Technol. 12 (2024).

[140] A. Kakim, A. Nurkesh, B. Sarsembayev, D. Dauletiya, A. Balapan, Z. Bakenov, A. Yeshmukhametov, G. Kalimuldina, A. Kakim, A. Nurkesh, B. Sarsembayev, D. Dauletiya, A. Balapan, Z. Bakenov, A. Yeshmukhametov, G. Kalimuldina, Incorporating MIL-125 metal-organic framework for flexible triboelectric nanogenerators and self-powered sensors for robotic grippers, Advanced Sensor Research (2024) 2300163.

[141] M.N. Liu, T. Chen, F. Yin, W.Z. Song, L.X. Wu, J. Zhang, S. Ramakrishna, Y. Z. Long, Smart bandage based on a ZIF-8 triboelectric nanogenerator for in situ real-time monitoring of drug concentration, ACS Appl. Mater. Interfaces 16 (2024) 39079–39089.

[142] A. Babu, L. Bochu, S. Potu, R. Kaja, N. Madathil, M. Velpula, A. Kulandaivel, U. K. Khanapuram, R.K. Rajaboina, H. Divi, P. Kodali, B. Ketharachapalli, R. Ammanabrolu, Facile direct growth of ZIF-67 metal–organic framework for triboelectric nanogenerators and their application in the internet of vehicles, ACS Sustain. Chem. Eng. 11 (2023) 16806–16817.

[143] N. P K, A. Chandrasekhar, Fingerprint-mimicking, ZIF -67 decorated, triboelectric nanogenerator for iot cloud-supported self-powered smart glove for paralyzed patient care, ACS Appl. Electron. Mater. 6 (2024) 5314–5327.

[144] X. Feng, X. Ding, D. Jiang, Covalent organic frameworks, Chem. Soc. Rev. 41 (2012) 6010–6022.

[145] J. Dong, X. Han, Y. Liu, H. Li, Y. Cui, Metal–covalent organic frameworks (MCOFs): a bridge between metal–organic frameworks and covalent organic frameworks, Angew. Chem. Int. Ed. 59 (2020) 13722–13733.

[146] H. Qiao, K. Zhao, X. Xu, M. Jiao, P. Li, L. Yang, X. Kong, L. Zhai, Synergistic effects of coordinated metals and fluoridation in metal-covalent organic framework for efficient triboelectric nanogenerator, Nano Energy 126 (2024) 109700.

[147] P. Sathiyanathan, D. Saatchi, Y. Boo, M. Mahato, B. Wicklein, J. Kim, H. Yoo, T. Song, A.K. Taseer, W.J. Kim, I. Oh, Nitrogen and sulfur rich covalent organic framework-chitosan triboelectric nanogenerator for disposable urination evaluation tool, Adv. Mater. Technol. 9 (2023).

[148] L. Shi, V.S. Kale, Z. Tian, X. Xu, Y. Lei, S. Kandambeth, Y. Wang, P.T. Parvatkar, O. Shekhah, M. Eddaoudi, H.N. Alshareef, Fluorinated covalent organic framework as a positive tribo-material for high-performance triboelectric nanogenerators, Adv. Funct. Mater. (2023) 2212891.

[149] L. Zhai, W. Wei, B. Ma, W. Ye, J. Wang, W. Chen, X. Yang, S. Cui, Z. Wu, C. Soutis, G. Zhu, L. Mi, Cationic covalent organic frameworks for fabricating an efficient triboelectric nanogenerator, ACS Mater. Lett. 2 (2020) 1691–1697.

[150] K. Saichompoo, W. Kingkam, S. Issarapanacheewin, S. Ukasi, S. Pongampai, P. Pakawanit, P. Limsuwan, N. Vittayakorn, T. Charoonsuk, Effective rare-earth dielectric addition and gamma ray irradiation for achieving highly efficient PDMS triboelectric nanogenerator, Radiat. Phys. Chem. 227 (2025) 112330.

[151] S.A. Behera, S. Hajra, S. Panda, A.K. Sahu, P. Alagarsamy, Y.K. Mishra, H.J. Kim, P.G.R. Achary, Synergistic energy harvesting and humidity sensing with single electrode triboelectric nanogenerator, Ceram. Int. 50 (2024) 37193–37200.

[152] N. Kim, S. Hwang, S. Panda, S. Hajra, J. Jo, H. Song, M.A. Belal, V. Vivekananthan, B.K. Panigrahi, P.G.R. Achary, H.J. Kim, A sustainable free-standing triboelectric nanogenerator made of flexible composite film for brake pattern recognition in automobiles, Macromol. Rapid Commun. 45 (2024) 2400431.

[153] Z. Wei, L. Ding, N. Sun, L.Y. Dang, H.R. Sun, J.C. Han, J.Q. Zhu, G.G. Wang, Lead-free CsBi$_3$I$_{10}$ perovskite based photo-enhanced triboelectric nanogenerator, Nano Energy 108 (2023) 108209.

[154] M. Sahu, S. Hajra, J. Bijelic, D. Oh, I. Djerdj, H.J. Kim, Triple perovskite-based triboelectric nanogenerator: a facile method of energy harvesting and self-powered information generator, Mater. Today Energy 20 (2021) 100639.

[155] S.A. Behera, H.G. Kim, I.R. Jang, S. Hajra, S. Panda, N. Vittayakorn, H.J. Kim, P.G. R. Achary, Triboelectric nanogenerator for self-powered traffic monitoring, Mater. Sci. Eng., B 303 (2024) 117277.

[156] G. Khandelwal, A. Chandrasekhar, N.P. Maria Joseph Raj, S.J. Kim, Metal–organic framework: a novel material for triboelectric nanogenerator–based self-powered sensors and systems, Adv. Energy Mater. 9 (2019).

[157] G. Khandelwal, N.P. Maria Joseph Raj, S.J. Kim, Zeolitic imidazole framework: metal–organic framework subfamily members for triboelectric nanogenerators, Adv. Funct. Mater. 30 (2020).

[158] G. Khandelwal, N.P. Maria Joseph Raj, S.J. Kim, ZIF-62: a mixed linker metal-organic framework for triboelectric nanogenerators, J Mater Chem A Mater 8 (2020) 17817–17825.

[159] G. Khandelwal, N.P. Maria Joseph Raj, V. Vivekananthan, S.J. Kim, Biodegradable metal-organic framework MIL-88A for triboelectric nanogenerator, iScience 24 (2021) 102064.

[160] Z. Shao, J. Chen, K. Gao, Q. Xie, X. Xue, S. Zhou, C. Huang, L. Mi, H. Hou, A double-helix metal-chain metal-organic framework as a high-output triboelectric nanogenerator material for self-powered anticorrosion, Angewandte Chemie - International Edition 61 (2022) e202208994.

[161] Y.M. Wang, X. Zhang, D. Yang, L. Wu, J. Zhang, T. Lei, R. Yang, Highly stable metal-organic framework UiO-66-NH_2 for high-performance triboelectric nanogenerators, Nanotechnology 33 (2022) 065402.

[162] S. Hajra, M. Sahu, R. Sahu, A.M. Padhan, P. Alagarsamy, H.G. Kim, H. Lee, S. Oh, Y. Yamauchi, H.J. Kim, Significant effect of synthesis methodologies of metal-organic frameworks upon the additively manufactured dual-mode triboelectric nanogenerator towards self-powered applications, Nano Energy 98 (2022) 107253.

[163] R.A. Shaukat, Q.M. Saqib, J. Kim, H. Song, M.U. Khan, M.Y. Chougale, J. Bae, M. J. Choi, Ultra-robust tribo- and piezo-electric nanogenerator based on metal organic frameworks (MOF-5) with high environmental stability, Nano Energy 96 (2022) 107128.

[164] N. Jayababu, D. Kim, Co/Zn bimetal organic framework elliptical nanosheets on flexible conductive fabric for energy harvesting and environmental monitoring via triboelectricity, Nano Energy 89 (2021) 106355.

[165] N. Papadopoulos, Q. Li, X. An, X. Qian, Methyl orange-doped polypyrrole promoting growth of ZIF-8 on cellulose fiber with tunable tribopolarity for triboelectric nanogenerator, Polymers 14 (2022) 332.

[166] J. Chen, Z. Shao, Y. Zhao, X. Xue, H. Song, Z. Wu, S. Cui, L. Zhang, C. Huang, L. Mi, H. Hou, Metal-ion coupling in metal-organic framework materials regulating the output performance of a triboelectric nanogenerator, Inorg. Chem. 61 (2022) 2490–2498.

[167] T. Wang, Q. Zhu, Q. Zhu, Q. Yang, S. Wang, L. Luo, A highly stable bimetallic organic framework for enhanced electrical performance of cellulose nanofiber-based triboelectric nanogenerators, Nanoscale Adv. 4 (2022) 4314–4320.

[168] P. Pandey, K. Thapa, G.P. Ojha, M.K. Seo, K.H. Shin, S.W. Kim, J.I. Sohn, Metal-organic frameworks-based triboelectric nanogenerator powered visible light communication system for wireless human-machine interactions, Chem. Eng. J. 452 (2023) 139209.

[169] J.A.A.L. Jayarathna, K.R. Kaja, Energy-harvesting device based on lead-free perovskite, AI, Comput. Sci. Robotics Technol. 3 (2024) 1–9.

[170] H. Dong, C. Ran, W. Gao, M. Li, Y. Xia, W. Huang, Metal halide perovskite for next-generation optoelectronics: progresses and prospects, eLight 3 (2023) 1–16.

[171] H. Zhu, S. Teale, M.N. Lintangpradipto, S. Mahesh, B. Chen, M.D. McGehee, E. H. Sargent, O.M. Bakr, Long-term operating stability in perovskite photovoltaics, Nat. Rev. Mater. 8 (2023) 569–586.

[172] T. Charoonsuk, S. Ukasi, P. Mokthaisong, P. Khuntakaew, S. Hajra, H.J. Kim, R. Muanghlua, W. Vittayakorn, S. Pongampai, N. Vittayakorn, Acidic dynamics: unveiling mechanistic insights for improved performance in chitosan triboelectric nanogenerators, Cellulose 31 (2024) 6453–6470.

[173] T. Charoonsuk, S. Supansomboon, P. Pakawanit, W. Vittayakorn, S. Pongampai, S. Woramongkolchai, N. Vittayakorn, Simple enhanced charge density of chitosan film by the embedded ion method for the flexible triboelectric nanogenerator, Carbohydr. Polym. 297 (2022) 120070.

[174] M.S. Kwak, Y.J. Park, M.P. Kim, H. Ko, Interfacial polarization for high-performance triboelectric devices: principles, strategies, and applications, ACS Appl. Mater. Interfaces 17 (2025) 37336–37352.

[175] L. Zhu, Exploring strategies for high dielectric constant and low loss polymer dielectrics, J. Phys. Chem. Lett. 5 (2014) 3677–3687.

[176] Ling An, S.A. Boggs, J.P. Calame, Energy storage in polymer films with high dielectric constant filler, IEEE Electr. Insul. Mag. 24 (2008) 5–10.

[177] J. Wang, F. Guan, L. Cui, J. Pan, Q. Wang, L. Zhu, Achieving high electric energy storage in a polymer nanocomposite at low filling ratios using a highly polarizable phthalocyanine interphase, J. Polym. Sci. B Polym. Phys. 52 (2014) 1669–1680.

[178] M.P. Kim, D.S. Um, Y.E. Shin, H. Ko, High-performance triboelectric devices via dielectric polarization: a review, Nanoscale Res. Lett. 16 (2021) 35.

[179] S. Panda, S. Hajra, H. Jeong, B.K. Panigrahi, P. Pakawanit, D. Dubal, S. Hong, H. J. Kim, Biocompatible $CaTiO_3$-PVDF composite-based piezoelectric nanogenerator for exercise evaluation and energy harvesting, Nano Energy 102 (2022) 107682.

[180] R. Sumang, T. Charoonsuk, N. Vittayakorn, P. Panpho, High-performance flexible lead-free piezo-antiferroelectric based on $NaNbO_3$/PDMS composites for energy harvesting application, Ceram. Int. 50 (2024) 51952–51963.

[181] T. Charoonsuk, S. Sriphan, C. Nawanil, N. Chanlek, W. Vittayakorn, N. Vittayakorn, Tetragonal $BaTiO_3$ nanowires: a template-free salt-flux-assisted synthesis and its piezoelectric response based on mechanical energy harvesting, J Mater Chem C Mater 7 (2019) 8277–8286.

[182] S. Pongampai, T. Charoonsuk, N. Pinpru, P. Pulphol, W. Vittayakorn, P. Pakawanit, N. Vittayakorn, Triboelectric-piezoelectric hybrid nanogenerator based on $BaTiO_3$-nanorods/chitosan enhanced output performance with self-charge-pumping system, Compos. B Eng. 208 (2021) 108602.

[183] M.V. Paranjape, J. Kim, Y. Kim, E. Jo, S.A. Graham, P. Manchi, J.K. Lee, J.S. Yu, Perovskite ν–$NaNbO_3$ embedded pdms composite film-based robust hybrid nanogenerator for efficient mechanical energy harvesting, Compos. Sci. Technol. 242 (2023) 110195.

[184] X. Meng, D. Hui, S. Ge, S. Zhou, X. Hu, D. Lin, W. Liu, Nanopillar- and nanocone-structured $SrTiO_3$/PDMS films for triboelectric nanogenerators, ACS Appl. Nano Mater. 7 (2024) 14193–14202.

[185] P. Pandey, D.H. Jung, G.J. Choi, M.K. Seo, S. Lee, J.M. Kim, I.K. Park, J.I. Sohn, Nafion-mediated barium titanate-polymer composite nanofibers-based triboelectric nanogenerator for self-powered smart street and home control system, Nano Energy 107 (2023) 108134.

[186] M.V. Paranjape, S.A. Graham, P. Manchi, A. Kurakula, J.S. Yu, Multistage $SrBaTiO_3$/PDMS composite film-based hybrid nanogenerator for efficient floor energy harvesting applications, Small 19 (2023) 2300535.

[187] J. Zhang, Y. Hu, X. Lin, X. Qian, L. Zhang, J. Zhou, A. Lu, High-performance triboelectric nanogenerator based on chitin for mechanical-energy harvesting and self-powered sensing, Carbohydr. Polym. 291 (2022) 119586.

[188] S. Park, K.N. Kim, J.M. Kim, W. Song, S. Myung, S.S. Lee, K.S. An, Deacetylation-controlled chitin derivative imbedded wpu nanocomposite for highly powered and robust triboelectric nanogenerator, Compos. B Eng. 265 (2023) 110948.

[189] S. Ukasi, P. Jutapukti, C. Ninthub, N. Pinpru, P. Pakawanit, W. Vittayakorn, S. Pongampai, N. Vittayakorn, T. Charoonsuk, Gamma glycine enhances efficiency of organic hybrid piezoelectric-triboelectric nanogenerators, Nano Energy 119 (2024) 109045.

[190] T. Charoonsuk, S. Pongampai, P. Pakawanit, N. Vittayakorn, Achieving a highly efficient chitosan-based triboelectric nanogenerator via adding organic proteins: influence of morphology and molecular structure, Nano Energy 89 (2021) 106430.

[191] C. Gao, W. Tong, S. Liu, X. Wang, Y. Zhang, Fully degradable chitosan–based triboelectric nanogenerators applying in disposable medical products for information transfer, Nano Energy 117 (2023) 108876.

[192] C. Gao, W. Tong, X. Wang, Y. Zhang, Y. Zhang, Degradable triboelectric nanogenerators based on chitosan fibers for smart sensing, ACS Appl. Electron. Mater. 5 (2023) 3865–3874.

[193] A. Mondal, M. Faraz, M. Dahiya, N. Khare, Double-layer electronegative structure-based triboelectric nanogenerator for enhanced performance using combined effect of enhanced charge generation and improved charge trapping, ACS Appl. Mater. Interfaces 16 (2024) 50659–50670.

[194] K. Lee, H.S. Han, J.H. Ryu, S. Kang, K. Jung, Y.K. Kim, T. Song, S. Mhin, K.M. Kim, Laser-driven formation of $ZnSnO_3$/CNT heterostructure and its critical role in boosting performance of the triboelectric nanogenerator, Carbo 212 (2023) 118120.

[195] W. Li, Y. Xiang, W. Zhang, K. Loos, Y. Pei, Ordered mesoporous SiO_2 nanoparticles as charge storage sites for enhanced triboelectric nanogenerators, Nano Energy 113 (2023) 108539.

[196] N. Rafiefard, S. Fardindoost, M. Karimi Kisomi, L. Shooshtari, A. Irajizad, S. Seddighi, R. Mohammadpour, D. Vashaee, High-performance flexible and stretchable self-powered surface engineered PDMS-TiO_2 nanocomposite based humidity sensors driven by triboelectric nanogenerator with full sensing range, Sensor. Actuator. B Chem. 378 (2023) 133105.

[197] S. Das, M. Mallik, K. Parida, N. Bej, J. Baral, Flexible PMN-PT/rGO/PVDF-TrFE based composites for triboelectric and piezoelectric energy harvesting, Appl. Surf. Sci. Adv. 23 (2024) 100626.

[198] V. Singh, B. Singh, MoS_2-PVDF/PDMS based flexible hybrid piezo-triboelectric nanogenerator for harvesting mechanical energy, J. Alloys Compd. 941 (2023) 168850.

[199] I.S.S. Vamsi, N.K. Das, S. Badhulika, $FeNbO_4$ nanoparticles-PDMS based triboelectric nanogenerator as self-powered sensor for human motion and artefact position tracking applications, Mater. Sci. Semicond. Process. 169 (2024) 107945.

[200] Q. Zhou, R. Takita, T. Ikuno, Improving the performance of a triboelectric nanogenerator by using an asymmetric TiO_2/PDMS composite layer, Nanomaterials 13 (2023) 832.

[201] K. Zhao, X. Zhang, H. Lv, W. Sun, M. Zhong, M. Liu, H. Liu, D. Zhang, Boosting performance of triboelectric nanogenerator via polydimethylsiloxane modified with perovskite $BiFeO_3$ nanoparticles, Mater. Technol. 37 (2022) 3212–3221.

[202] S.R. Gopal, T.S. Velayutham, W.C. Gan, J.Y. Cheong, A.E. Soh, A hybrid piezoelectric and triboelectric nanogenerator with lead-free BZT–BCT/PDMS composite and PVA film for scavenging mechanical energy, RSC Adv. 13 (2023) 7921–7928.

[203] K. Zhao, W. Sun, S. Li, Z. Song, M. Zhong, D. Zhang, B.N. Gu, M.J. Liu, H. Fu, H. Liu, C. Meng, Y.L. Chueh, Rational design on high-performance triboelectric nanogenerator consisting of silicon carbide@silicon dioxide nanowhiskers/polydimethylsiloxane (SiC@SiO_2/PDMS) nanocomposite films, Discover Nano 18 (2023) 1–12.

[204] J. Wang, X. Dai, L. Qi, F. Ning, P. Yang, J. Chen, Y. Li, J. Chen, Y. Zhao, X. Zhang, Ferroelectric $BaTiO_3$@ZnO core-shell heterojunction triboelectric nanogenerators for electrochemical degradation of Mo, Ceram. Int. 50 (2024) 4841–4850.

[205] A. Thakur, M. Jangra, S. Dam, S. Hussain, Enhanced dielectric constant with addition of a low amount of SnO_2 nanoparticles as fillers in a PVDF matrix with low dielectric loss, Nano-Struct. Nano-Objects 34 (2023) 100978.

[206] M.V. Paranjape, S.A. Graham, H. Patnam, P. Manchi, J.S. Yu, Dopamine treated SnO_2/PVDF composite films for hybrid mechanical energy harvester, Compos. Sci. Technol. 221 (2022) 109323.

[207] S. S, A.M. Chandran, S. Varun, M.V.P. Kumar, P.K.S. Mural, Chitosan nanocomposite-based triboelectric nanogenerators with enhanced electrical performance: an opportunity for bioelectronics, ACS Appl. Electron. Mater. 6 (2024) 887–900.

[208] X.S. Zhang, J. Brugger, B. Kim, A silk-fibroin-based transparent triboelectric generator suitable for autonomous sensor network, Nano Energy 20 (2016) 37–47.

[209] C. Liu, J. Li, L. Che, S. Chen, Z. Wang, X. Zhou, Toward large-scale fabrication of triboelectric nanogenerator (TENG) with silk-fibroin patches film via spray-coating process, Nano Energy 41 (2017) 359–366.

[210] Y. Luo, Y. Li, X. Feng, Y. Pei, Z. Zhang, L. Wang, Y. Zhao, B. Lu, B. Zhu, Triboelectric nanogenerators with porous and hierarchically structured silk fibroin films via water electrospray-etching technology, Nano Energy 75 (2020) 104974.

[211] Z. Li, S. Xu, Z. Xu, S. Shu, G. Liu, J. Zhou, D. Lin, W. Tang, Enhancing cellular behavior in repaired tissue via silk fibroin-integrated triboelectric nanogenerators, Microsyst Nanoeng 10 (2024) 68.

[212] Q. Wang, B. Xu, D. Tan, X. Hu, Y. Yang, J. Huang, Y. Gao, X. Liu, Nature-inspired scalable high-performance triboelectric nanogenerators for energy harvesting and sensing, Nano Energy 121 (2024) 109217.

[213] R. Pan, W. Xuan, J. Chen, S. Dong, H. Jin, X. Wang, H. Li, J. Luo, Fully biodegradable triboelectric nanogenerators based on electrospun polylactic acid and nanostructured gelatin films, Nano Energy 45 (2018) 193–202.

[214] J. Ma, J. Zhu, P. Ma, Y. Jie, Z.L. Wang, X. Cao, Fish bladder film-based triboelectric nanogenerator for noncontact position monitoring, ACS Energy Lett. 5 (2020) 3005–3011.

[215] Y. Han, Y. Han, X. Zhang, L. Li, C. Zhang, J. Liu, G. Lu, H.D. Yu, W. Huang, Fish gelatin based triboelectric nanogenerator for harvesting biomechanical energy and self-powered sensing of human physiological signals, ACS Appl. Mater. Interfaces 12 (2020) 16442–16450.

[216] Y. Pang, F. Xi, J. Luo, G. Liu, T. Guo, C. Zhang, An alginate film-based degradable triboelectric nanogenerator, RSC Adv. 8 (2018) 6719–6726.

[217] Q.M. Saqib, M.Y. Chougale, M.U. Khan, R.A. Shaukat, J. Kim, K.S. Bhat, J. Bae, Triboelectric nanogenerator based on lignocellulosic waste fruit shell tribopositive material: comparative analysis, Mater. Today Sustain. 18 (2022) 100146.

[218] C.M. Veerabhadraswamy, S.N. Rashmi, S.M. Mizba Tazleem, S. Puneeth, S. M. Rumana Farheen, M.A. Sangamesha, S. Krishnaveni, Novel approach to bio-inspired triboelectric nanogenerators employing recycled natural fibres for sustainable energy harvesting, Sens Actuators A Phys 377 (2024) 115678.

[219] Z. Xu, Y. Chang, Z. Zhu, A triboelectric nanogenerator based on bamboo leaf for biomechanical energy harvesting and self-powered touch sensing, Electronics 13 (2024) 766.

[220] Z. Ding, M. Zou, P. Yao, Z. Zhu, L. Fan, A novel triboelectric material based on deciduous leaf for energy harvesting, Micromachines 12 (2021) 1314.

[221] Y. Chen, Y. Jie, J. Wang, J. Ma, X. Jia, W. Dou, X. Cao, Triboelectrification on natural rose petal for harvesting environmental mechanical energy, Nano Energy 50 (2018) 441–447.

[222] S.R. Patil, M.Y. Chougale, J. Kim, R.A. Shaukat, M. Noman, Q.M. Saqib, M. U. Khan, T.D. Dongale, J. Bae, Triboelectric nanogenerator based on biowaste tribopositive delonix regia flowers powder, Energy Technol. 10 (2022) 2200876.

[223] J. Heo, H. Ahn, J. Won, J.G. Son, H.K. Shon, T.G. Lee, S.W. Han, M.H. Baik, Electro-inductive effect: electrodes as functional groups with tunable electronic properties, Science (1979) 370 (2020) 214–219.

[224] Z. Lin, J. Chen, J. Yang, Recent progress in triboelectric nanogenerators as a renewable and sustainable power source, J. Nanomater. 2016 (2016) 1–24.

[225] H.Y. Mi, H. Li, X. Jing, P. He, P.Y. Feng, X. Tao, Y. Liu, C. Liu, C. Shen, Silk and silk composite aerogel-based biocompatible triboelectric nanogenerators for efficient energy harvesting, Ind. Eng. Chem. Res. 59 (2020) 12399–12408.

[226] A. Babu, D. Rakesh, P. Supraja, S. Mishra, K.U. Kumar, R.R. Kumar, D. Haranath, E. Mamidala, R. Nagapuri, Plant-based triboelectric nanogenerator for biomechanical energy harvesting, Results Surf. Interfaces 8 (2022) 100075.

[227] K.Y. Lee, D.J. Mooney, Alginate: properties and biomedical applications, Prog. Polym. Sci. 37 (2012) 106–126.

[228] K. Xia, D. Wu, J. Fu, N.A. Hoque, Y. Ye, Z. Xu, Tunable output performance of triboelectric nanogenerator based on alginate metal complex for sustainable operation of intelligent keyboard sensing system, Nano Energy 78 (2020) 105263.

[229] N. Zheng, J. Xue, Y. Jie, X. Cao, Z.L. Wang, Wearable and humidity-resistant biomaterials-based triboelectric nanogenerator for high entropy energy harvesting and self-powered sensing, Nano Res. 15 (2022) 6213–6219.

[230] H. Hu, A corn leaf based-strain sensor and triboelectric nanogenerator for running monitoring and energy harvesting, Heliyon 10 (2024) e29025.

[231] J. Kaur, R.S. Sawhney, H. Singh, M. Sandhu, R.S. Sohal, A. Singh, M. Singh, S. Kaur, Comparative analysis of triboelectric behavior of natural waste biomaterials and green energy harvesting, Energy & Environment 36 (3) (2023) 1309–1320.

[232] R. Ccorahua, J. Huaroto, C. Luyo, M. Quintana, E.A. Vela, Enhanced-performance bio-triboelectric nanogenerator based on starch polymer electrolyte obtained by a cleanroom-free processing method, Nano Energy 59 (2019) 610–618.

[233] F. Meder, A. Mondini, B. Mazzolai, Measuring triboelectric energy conversion in leaves of living plants, IEEE Instrum. Meas. Mag. 25 (2022) 4–9.

[234] R.F.S.M. Ahmed, S.K.K. Swamy, G.S. Chandrasekhar, S.M. Ankanathappa, A. Chandrasekhar, K. Sannathammegowda, Clitoria ternatea flower extract: biopolymer composite-based triboelectric nanogenerator as a self-powered smart counter, Surf. Interfaces 42 (2023) 103369.

[235] M. Madhushree, P. Vairavel, G.T. Mahesha, K.S. Bhat, A comprehensive review of cellulose and cellulose-based materials: extraction, modification, and sustainable applications, J. Nat. Fibers 21 (2024) 2418357.

[236] R. Kullmann, M. Delbianco, C. Roth, T.R. Weikl, Role of van der Waals, electrostatic, and hydrogen-bond interactions for the relative stability of cellulose Iβ and II crystals, J. Phys. Chem. B 128 (2024) 12114–12121.

[237] Z. Wang, X. Zou, T. Liu, Y. Zhu, D. Wu, Y. Bai, G. Du, B. Luo, S. Zhang, M. Chi, Y. Liu, Y. Shao, J. Wang, S. Wang, S. Nie, Directional moisture-wicking triboelectric materials enabled by laplace pressure differences, Nano Lett. 24 (2024) 7125–7133.

[238] J. Zhao, W. Zhang, T. Liu, B. Luo, Y. Qin, C. Gao, J. Yuan, S. Wang, S. Nie, Multiscale structural triboelectric aerogels enabled by self-assembly driven supramolecular winding, Adv. Funct. Mater. 34 (2024) 2400476.

[239] T. Liu, Z. Zhao, R. Liang, H. He, Y. Liu, K. Yu, M. Chi, B. Luo, J. Wang, S. Zhang, C. Cai, S. Wang, S. Nie, Tough and elastic anisotropic triboelectric materials enabled by layer-by-layer assembly, Adv. Funct. Mater. 35 (2025) 2500207.

[240] P. Lu, Y. Yang, B. Luo, C. Cai, T. Liu, S. Zhang, M. Chi, T. Zhao, J. Wang, X. Meng, Y. Bai, Y. Shao, G. Du, S. Wang, S. Nie, Multiscale structural strong yet tough triboelectric materials enabled by in situ microphase separation, Adv. Funct. Mater. 35 (2025) 2418336.

[241] X. Wang, T. Liu, J. Wang, Y. Liu, M. Chi, S. Zhang, C. Cai, Y. Shao, G. Du, S. Wang, B. Luo, S. Nie, Wearable strain insensitive triboelectric materials enabled by structure-induced self-orientation, Nano Energy 134 (2025) 110569.

[242] E. Fukada, Piezoelectricity of wood, J Physical Soc Japan 10 (1955) 149–154.

[243] F.L. Dri, S. Shang, L.G. Hector, P. Saxe, Z.K. Liu, R.J. Moon, P.D. Zavattieri, Anisotropy and temperature dependence of structural, thermodynamic, and elastic properties of crystalline cellulose Iβ: a *first-principles investigation*, Model. Simulat. Mater. Sci. Eng. 22 (2014) 085012.

[244] L. Csoka, I.C. Hoeger, O.J. Rojas, I. Peszlen, J.J. Pawlak, P.N. Peralta, Piezoelectric effect of cellulose nanocrystals thin films, ACS Macro Lett. 1 (2012) 867–870.

[245] X.S. Zhang, M. Su, J. Brugger, B. Kim, Penciling a triboelectric nanogenerator on paper for autonomous power mems applications, Nano Energy 33 (2017) 393–401.

[246] S. Sriphan, T. Charoonsuk, T. Maluangnont, P. Pakawanit, C. Rojviriya, N. Vittayakorn, Multifunctional nanomaterials modification of cellulose paper for efficient triboelectric nanogenerators, Adv. Mater. Technol. 5 (2020) 2000001.

[247] C. Lin, H. Huang, H. Zhao, S. Cao, X. Ma, Acid- and alkali-resistant and high-performance cellulose paper-based triboelectric nanogenerator by controlling the surface hydrophobicity, ACS Sustain. Chem. Eng. 10 (2022) 13669–13679.

[248] M. Li, Y. Pan, L. Wan, X. Hao, T. Huang, K. Zhang, W. Mai, S. Chen, A. Qin, Sisal cellulose paper based triboelectric nanogenerator with high performance for detection of chemical group substitution degree, Nano Energy 104 (2022) 107937.

[249] C. Lin, H. Zhao, H. Huang, X. Ma, S. Cao, PEO/cellulose composite paper based triboelectric nanogenerator and its application in human-health detection, Int. J. Biol. Macromol. 228 (2023) 251–260.

[250] M. Yang, X. Tian, T. Hua, Green and recyclable cellulose based teng for sustainable energy and human-machine interactive system, Chem. Eng. J. 442 (2022) 136150.

[251] K. Xia, Z. Zhu, H. Zhang, C. Du, Z. Xu, R. Wang, Painting a high-output triboelectric nanogenerator on paper for harvesting energy from human body motion, Nano Energy 50 (2018) 571–580.

[252] B. Fatma, S.M. Andrabi, S. Gupta, V. Verma, A. Kumar, C. Pitsalidis, A. Garg, Biocompatible, breathable and degradable microbial cellulose based triboelectric nanogenerator for wearable transient electronics, Nano Energy 114 (2023) 108628.

[253] L. Feng, X. Cao, Z.L. Wang, L. Zhang, A transparent and degradable bacterial cellulose-based film for triboelectric nanogenerator: efficient biomechanical energy harvesting and human health monitoring, Nano Energy 120 (2024) 109068.

[254] S. Pongampai, P. Pakawanit, T. Charoonsuk, S. Hajra, H.J. Kim, N. Vittayakorn, Design and optimization of miura-origami-inspired structure for high-performance self-charging hybrid nanogenerator, J. Sci. Adv. Mater. Devices 8 (2023) 100618.

[255] C. Jin, C. Zhang, P. Yan, M. Jiang, R. Yin, K. Li, W. Zhao, Z. Bai, A superhuman sensing triboelectric nanogenerator with boosted power density and durability via a bio-inspired IJanus structure, Adv. Funct. Mater. 34 (2024) 2402233.

[256] J. Peng, H. Zhang, Q. Zheng, C.M. Clemons, R.C. Sabo, S. Gong, Z. Ma, L.S. Turng, A composite generator film impregnated with cellulose nanocrystals for enhanced triboelectric performance, Nanoscale 9 (2017) 1428–1433.

[257] A. Chandrasekhar, N.R. Alluri, B. Saravanakumar, S. Selvarajan, S.J. Kim, A microcrystalline cellulose ingrained polydimethylsiloxane triboelectric nanogenerator as a self-powered locomotion detector, J Mater Chem C Mater 5 (2017) 1810–1815.

[258] C. Luo, Y. Shao, H. Yu, H. Ma, Y. Zhang, B. Yin, M. Yang, Improving the output performance of bacterial cellulose-based triboelectric nanogenerators by modulating the surface potential in a simple method, ACS Sustain. Chem. Eng. 10 (2022) 13050–13058.

[259] N. Wang, D. Yang, W. Zhang, M. Feng, Z. Li, E. Ye, X.J. Loh, D. Wang, Deep trap boosted ultrahigh triboelectric charge density in nanofibrous cellulose-based triboelectric nanogenerators, ACS Appl. Mater. Interfaces 15 (2023) 997–1009.

[260] S. Parandeh, M. Kharaziha, F. Karimzadeh, An eco-friendly triboelectric hybrid nanogenerators based on graphene oxide incorporated polycaprolactone fibers and cellulose paper, Nano Energy 59 (2019) 412–421.

[261] H. Seddiqi, E. Oliaei, H. Honarkar, J. Jin, L.C. Geonzon, R.G. Bacabac, J. Klein-Nulend, Cellulose and its derivatives: towards biomedical applications, Cellulose 28:4 (28) (2021) 1893–1931, 2021.

[262] H.J. Kim, E.C. Yim, J.H. Kim, S.J. Kim, J.Y. Park, I.K. Oh, Bacterial nano-cellulose triboelectric nanogenerator, Nano Energy 33 (2017) 130–137.

[263] S. Sriphan, U. Pharino, T. Charoonsuk, P. Pulphol, P. Pakawanit, O. Khamman, W. Vittayakorn, N. Vittayakorn, T. Maluangnont, Tailoring charge affinity, dielectric property, and band gap of bacterial cellulose paper by multifunctional Ti_2NbO_7 nanosheets for improving triboelectric nanogenerator performance, Nano Res. 16 (2023) 3168–3179.

[264] A. Mensah, S. Liao, J. Amesimeku, J. Li, Y. Chen, Y. Hao, J. Yang, Q. Wang, F. Huang, Y. Liu, Q. Wei, P. Lv, Therapeutic smart insole technology with Archimedean algorithmic spiral triboelectric nanogenerator-based power system and sensors, Adv. Fiber Mater. 6 (2024) 1746–1764.

[265] J. Zhou, H. Wang, C. Du, D. Zhang, H. Lin, Y. Chen, J. Xiong, Cellulose for sustainable triboelectric nanogenerators, Adv. Energy Sustain. Res. 3 (2022) 2100161.

[266] S. Hu, J. Han, Z. Shi, K. Chen, N. Xu, Y. Wang, R. Zheng, Y. Tao, Q. Sun, Z. L. Wang, G. Yang, Biodegradable, super-strong, and conductive cellulose macrofibers for fabric-based triboelectric nanogenerator, Nano-Micro Lett. 14 (2022) 1–20.

[267] C. Xing, Y. Tian, Z. Yu, Z. Li, B. Meng, Z. Peng, Cellulose nanofiber-reinforced MXene membranes as stable friction layers and effective electrodes for high-performance triboelectric nanogenerators, ACS Appl. Mater. Interfaces 14 (2022) 36741–36752.

[268] J. González, A. Ghaffarinejad, M. Ivanov, P. Ferreira, P.M. Vilarinho, A. Borrás, H. Amorín, B. Wicklein, Advanced cellulose–nanocarbon composite films for high-performance triboelectric and piezoelectric nanogenerators, Nanomaterials 13 (2023) 1206.

[269] C. Luo, H. Ma, H. Yu, Y. Zhang, Y. Shao, B. Yin, K. Ke, L. Zhou, K. Zhang, M. B. Yang, Enhanced triboelectric nanogenerator based on a hybrid cellulose aerogel for energy harvesting and self-powered sensing, ACS Sustain. Chem. Eng. 11 (2023) 9424–9432.

[270] X. Bu, B. Zhou, J. Li, C. Gao, J. Guo, Orange peel-like triboelectric nanogenerators with multiscale micro-nano structure for energy harvesting and touch sensing applications, Nano Energy 122 (2024) 109280.

[271] B. Song, X. Fan, J. Shen, H. Gu, Ultra-stable and self-healing coordinated collagen-based multifunctional double-network organohydrogel e-skin for multimodal sensing monitoring of strain-resistance, bioelectrode, and self-powered triboelectric nanogenerator, Chem. Eng. J. 474 (2023) 145780.

[272] C. Li, P. Wang, D. Zhang, Self-healable, stretchable triboelectric nanogenerators based on flexible polyimide for energy harvesting and self-powered sensors, Nano Energy 109 (2023) 108285.

[273] P. Kanokpaka, Y.H. Chang, C.C. Chang, M. Rinawati, P.C. Wang, L.Y. Chang, M. H. Yeh, Enabling glucose adaptive self-healing hydrogel based triboelectric biosensor for tracking a human perspiration, Nano Energy 112 (2023) 108513.

[274] J. Oh, M. Kang, J. Park, T.Y. Kim, K. Park, J. Seo, Autonomously self-healing, adhesive, and stretchable triboelectric nanogenerator using multifunctional hydrogel-elastomer double layer with a power management circuit, Adv. Electron. Mater. 10 (2024) 2400013.

[275] Y. Qin, J. Mo, Y. Liu, S. Zhang, J. Wang, Q. Fu, S. Wang, S. Nie, Y. Qin, J. Mo, Y. Liu, S. Zhang, J. Wang, Q. Fu, S. Wang, S. Nie, Stretchable triboelectric self-powered sweat sensor fabricated from self-healing nanocellulose hydrogels, Adv. Funct. Mater. 32 (2022) 2201846.

[276] X. Qin, H. Shi, Z. Wen, B. Chu, H. Li, H. Wang, Y. He, X. Sun, Triboelectric-responsive drug delivery hydrogel for accelerating infected wound healing, Adv. Healthcare Mater. 13 (2024) 2303474.

[277] J. Zhang, X. Zhao, Z. Wang, Z. Liu, S. Yao, L. Li, Antibacterial, antifreezing, stretchable, and self-healing organohydrogel electrode based triboelectric nanogenerator for self-powered biomechanical sensing, Adv. Mater. Interfac. 9 (2022).

[278] H. Park, S.J. Oh, D. Kim, M. Kim, C. Lee, H. Joo, I. Woo, J. Woo Bae, J.H. Lee, H. Park, D. Kim, M. Kim, C. Lee, H. Joo, J.H. Lee, S.J. Oh, I. Woo, J.W. Bae, Plasticized PVC-gel single layer-based stretchable triboelectric nanogenerator for harvesting mechanical energy and tactile sensing, Adv. Sci. 9 (2022) 2201070.

[279] L. Dong, M. Wang, J. Wu, C. Zhu, J. Shi, H. Morikawa, Stretchable, adhesive, self-healable, and conductive hydrogel-based deformable triboelectric nanogenerator for energy harvesting and human motion sensing, ACS Appl. Mater. Interfaces 14 (2022) 9126–9137.

[280] Y. Liu, F. Zhuo, J. Zhou, L. Kuang, K. Tan, H. Lu, J. Cai, Y. Guo, R. Cao, Y. Fu, H. Duan, Machine-learning assisted handwriting recognition using graphene oxide-based hydrogel, ACS Appl. Mater. Interfaces 14 (2022) 54276–54286.

[281] H. Patnam, S.A. Graham, P. Manchi, M.V. Paranjape, J.S. Yu, Single-electrode triboelectric nanogenerators based on ionic conductive hydrogel for mechanical energy harvester and smart touch sensor applications, ACS Appl. Mater. Interfaces 15 (2023) 16768–16777.

[282] H. Zhang, D. Zhang, Z. Wang, G. Xi, R. Mao, Y. Ma, D. Wang, M. Tang, Z. Xu, H. Luan, Ultrastretchable, self-healing conductive hydrogel-based triboelectric nanogenerators for human–computer interaction, ACS Appl. Mater. Interfaces 15 (2023) 5128–5138.

[283] L. Zhao, Q. Ling, X. Fan, H. Gu, Self-healable, adhesive, anti-drying, freezing-tolerant, and transparent conductive organohydrogel as flexible strain sensor, triboelectric nanogenerator, and skin barrier, ACS Appl. Mater. Interfaces 15 (2023) 40975–40990.

[284] G. Du, Y. Shao, B. Luo, T. Liu, J. Zhao, Y. Qin, J. Wang, S. Zhang, M. Chi, C. Gao, Y. Liu, C. Cai, S. Wang, S. Nie, Compliant iontronic triboelectric gels with phase-locked structure enabled by competitive hydrogen bonding, Nano-Micro Lett. 16 (2024) 170.

[285] Z. Yu, Z. Zhu, Y. Zhang, X. Li, X. Liu, Y. Qin, Z. Zheng, L. Zhang, H. He, Biodegradable and flame-retardant cellulose-based wearable triboelectric nanogenerator for mechanical energy harvesting in firefighting clothing, Carbohydr. Polym. 334 (2024) 122040.

[286] F. Peng, D. Liu, W. Zhao, G. Zheng, Y. Ji, K. Dai, L. Mi, D. Zhang, C. Liu, C. Shen, Facile fabrication of triboelectric nanogenerator based on low-cost thermoplastic polymeric fabrics for large-area energy harvesting and self-powered sensing, Nano Energy 65 (2019) 104068.

[287] Z. Li, G. Jin, Y. Ma, X. Zhou, Y. Gao, X. Xiong, K. Dong, L. Lyu, Preparation and performance of 3-d woven triboelectric nanogenerators with integrated friction and spacer layers, Compos. Struct. 322 (2023) 117430.

[288] W.J. Kim, S. Cho, J. Hong, J.P. Hong, Geometrically versatile triboelectric yarn-based harvesters via carbon nanotubes-elastomer composites, Compos. Sci. Technol. 219 (2022) 109247.

[289] Y. Pang, X. Zhu, Y. Jin, Z. Yang, S. Liu, L. Shen, X. Li, C. Lee, Textile-inspired triboelectric nanogenerator as intelligent pavement energy harvester and self-powered skid resistance sensor, Appl. Energy 348 (2023) 121515.

[290] N.U.H.L. Ali, P. Pazhamalai, A. Sathyaseelan, T.D. Dongale, S.J. Kim, A self-integration via dual-active mode structural-SC-TENG energy device for electrochemical energy storage and triboelectric energy harvesting, Appl. Energy 376 (2024) 124265.

[291] T. Zhao, Y. Fu, C. Sun, X. Zhao, C. Jiao, A. Du, Q. Wang, Y. Mao, B. Liu, Wearable biosensors for real-time sweat analysis and body motion capture based on stretchable fiber-based triboelectric nanogenerators, Biosens. Bioelectron. 205 (2022) 114115.

[292] S. Dong, F. Xu, Y. Sheng, Z. Guo, X. Pu, Y. Liu, Seamlessly knitted stretchable comfortable textile triboelectric nanogenerators for e-textile power sources, Nano Energy 78 (2020) 105327.

[293] W. Wang, J. Zhou, S. Wang, F. Yuan, S. Liu, J. Zhang, X. Gong, Enhanced Kevlar-based triboelectric nanogenerator with anti-impact and sensing performance towards wireless alarm system, Nano Energy 91 (2022) 106657.

[294] E. Kovalska, H.T. Lam, Z. Saadi, R. Mastria, A.I.S. Neves, S. Russo, M.F. Craciun, Textile beeswax triboelectric nanogenerator as self-powered sound detectors and mechano-acoustic energy harvesters, Nano Energy 120 (2024) 109109.

[295] A.K. Aliyana, S. Bairagi, C. Kumar, D.M. Mulvihill, G.K. Stylios, Investigating superior performance by configuring bimetallic electrodes on fabric triboelectric nanogenerators (f-TENGs) for IoT enabled touch sensor applications, Nano Energy 130 (2024) 110125.

[296] P. Zhang, W. Zhang, H. Zhang, A high-performance textile-based triboelectric nanogenerator manufactured by a novel brush method for self-powered human motion pattern detector, Sustain. Energy Technol. Assessments 46 (2021) 101290.

[297] T.D. Khanh, J.S. Meena, S. Bin Choi, J.W. Kim, Breathable, self-healable, washable and durable all-fibrous triboelectric nanogenerator for wearable electronics, Mater Today Adv 20 (2023) 100427.

[298] Y. Chen, Y. Ling, Y. Yang, Z. Wang, Y. Liu, W. Gao, B. Yang, X. Tao, R. Yin, A clickable embroidered triboelectric sensor for smart fabric, Device 2 (2024) 100355.

[299] R. Khwanming, S. Pongampai, N. Vittayakorn, T. Charoonsuk, Cellulose-based fabrics triboelectric nanogenerator: effect of fabric microstructure on its electrical output, Journal of Metals, Materials and Minerals 33 (2023) 1673.

[300] J. Hu, M. Iwamoto, X. Chen, A review of contact electrification at diversified interfaces and related applications on triboelectric nanogenerator, Nano-Micro Lett. 16 (2023) 7.

[301] N. Wang, Y. Liu, E. Ye, Z. Li, D. Wang, Control methods and applications of interface contact electrification of triboelectric nanogenerators: a review, Mater. Res. Lett. 10 (2022) 97–123.

[302] S.A. Lone, K.C. Lim, K. Kaswan, S. Chatterjee, K.P. Fan, D. Choi, S. Lee, H. Zhang, J. Cheng, Z.H. Lin, Recent advancements for improving the performance of triboelectric nanogenerator devices, Nano Energy 99 (2022) 107318.

[303] J.M. Baik, J.P. Lee, Strategies for ultrahigh outputs generation in triboelectric energy harvesting technologies: from fundamentals to devices, Sci. Technol. Adv. Mater. 20 (2019) 927–936.

[304] C. Li, Y. Bai, J. Shao, H. Meng, Z. Li, Strategies to improve the output performance of triboelectric nanogenerators, Small Methods (2024) 2301682.

[305] D. Liu, Y. Gao, L. Zhou, J. Wang, Z.L. Wang, Recent advances in high-performance triboelectric nanogenerators, Nano Res. 16 (2023) 11698–11717.

[306] T. Liu, X. Cui, Z. Ye, X. Li, Y. Liu, B. Luo, S. Zhang, M. Chi, J. Wang, C. Cai, Y. Bai, S. Wang, S. Nie, A pulsed bubble-driven efficient liquid-solid triboelectric nanogenerator, Adv. Funct. Mater. 35 (2025) 2415483.

[307] W. Peng, J. Zhao, Q. Li, Y. Sun, G. Du, F. Tang, Y. Liu, Q. Hu, X. Li, S. Nie, A strong and tough ion-gel enabled by hierarchical meshing and ion hybridizations collaboration, Adv. Funct. Mater. 35 (2025) 2414682.

[308] S. Zhang, M. Chi, J. Mo, T. Liu, Y. Liu, Q. Fu, J. Wang, B. Luo, Y. Qin, S. Wang, S. Nie, Bioinspired asymmetric amphiphilic surface for triboelectric enhanced efficient water harvesting, Nat. Commun. 13 (2022) 4168.

[309] D. Kim, I.W. Tcho, I.K. Jin, S.J. Park, S.B. Jeon, W.G. Kim, H.S. Cho, H.S. Lee, S. C. Jeoung, Y.K. Choi, Direct-laser-patterned friction layer for the output enhancement of a triboelectric nanogenerator, Nano Energy 35 (2017) 379–386.

[310] M. Muthu, R. Pandey, X. Wang, A. Chandrasekhar, I.A. Palani, V. Singh, Enhancement of triboelectric nanogenerator output performance by laser 3d-surface pattern method for energy harvesting application, Nano Energy 78 (2020) 105205.

[311] M. Wajahat, A.Z. Kouzani, S.Y. Khoo, M.A.P. Mahmud, Output enhancement of a 3d-printed triboelectric nanogenerator using laser surface 3d patterning, Adv. Eng. Mater. 26 (2024) 2400199.

[312] K. P S, P. Gupta, D. J, A.S. Tripathi, S.S. Joshi, I.A. Palani, Investigation of laser-textured triboelectric nanogenerator for vibration sensing of machine tools, Smart Mater. Struct. 32 (2023) 85028.

[313] D. Kim, S.B. Jeon, J.Y. Kim, M.L. Seol, S.O. Kim, Y.K. Choi, High-performance nanopattern triboelectric generator by block copolymer lithography, Nano Energy 12 (2015) 331–338.

[314] M.A.P. Mahmud, J. Lee, G. Kim, H. Lim, K.B. Choi, Improving the surface charge density of a contact-separation-based triboelectric nanogenerator by modifying the surface morphology, Microelectron. Eng. 159 (2016) 102–107.

[315] B. Chen, W. Tang, Z.L. Wang, Advanced 3d printing-based triboelectric nanogenerator for mechanical energy harvesting and self-powered sensing, Mater. Today 50 (2021) 224–238.

[316] H. Li, R. Li, X. Fang, H. Jiang, X. Ding, B. Tang, G. Zhou, R. Zhou, Y. Tang, 3D printed flexible triboelectric nanogenerator with viscoelastic inks for mechanical energy harvesting, Nano Energy 58 (2019) 447–454.

[317] B. Nowacki, K. Mistewicz, S. Hajra, H. Joon Kim, 3D printed triboelectric nanogenerator for underwater ultrasonic sensing, Ultrasonics 133 (2023) 107045.

[318] L. Zhao, Q. Zheng, H. Ouyang, H. Li, L. Yan, B. Shi, Z. Li, A size-unlimited surface microstructure modification method for achieving high performance triboelectric nanogenerator, Nano Energy 28 (2016) 172–178.

[319] J.G. Sun, T.N. Yang, I.S. Kuo, J.M. Wu, C.Y. Wang, L.J. Chen, A leaf-molded transparent triboelectric nanogenerator for smart multifunctional applications, Nano Energy 32 (2017) 180–186.

[320] Q. Li, A. Peer, I.H. Cho, R. Biswas, J. Kim, Replica molding-based nanopatterning of tribocharge on elastomer with application to electrohydrodynamic nanolithography, Nat. Commun. 9 (2018) 974.

[321] H.J. Choi, J.H. Lee, J. Jun, T.Y. Kim, S.W. Kim, H. Lee, High-performance triboelectric nanogenerators with artificially well-tailored interlocked interfaces, Nano Energy 27 (2016) 595–601.

[322] J.H. Lee, I. Yu, S. Hyun, J.K. Kim, U. Jeong, Remarkable increase in triboelectrification by enhancing the conformable contact and adhesion energy with a film-covered pillar structure, Nano Energy 34 (2017) 233–241.

[323] I.W. Tcho, W.G. Kim, S.B. Jeon, S.J. Park, B.J. Lee, H.K. Bae, D. Kim, Y.K. Choi, Surface structural analysis of a friction layer for a triboelectric nanogenerator, Nano Energy 42 (2017) 34–42.

[324] T. Zhang, Z. Wen, H. Lei, Z. Gao, Y. Chen, Y. Zhang, J. Liu, Y. Xie, X. Sun, Surface-microengineering for high-performance triboelectric tactile sensor via dynamically assembled ferrofluid template, Nano Energy 87 (2021) 106215.

[325] Y. Wu, X. Wang, Y. Wang, Y. Nan, H. Xu, H. Zhou, M. Ren, J. Duan, Y. Huang, B. Hou, Enhancing the performance of triboelectric nanogenerator via facile pdms surface modification, Adv. Eng. Mater. 25 (2023) 2201442.

[326] D. Tan, B. Xu, Y. Gao, Y. Tang, Y. Liu, Y. Yang, Z. Li, Breathable fabric-based triboelectric nanogenerators with open-porous architected polydimethylsiloxane coating for wearable applications, Nano Energy 104 (2022) 107873.

[327] S. Mishra, P. Supraja, D. Haranath, R.R. Kumar, S. Pola, Effect of surface and contact points modification on the output performance of triboelectric nanogenerator, Nano Energy 104 (2022) 107964.

[328] H. Chen, Y. Xu, J. Zhang, W. Wu, G. Song, Enhanced stretchable graphene-based triboelectric nanogenerator via control of surface nanostructure, Nano Energy 58 (2019) 304–311.

[329] C. Lin, J. Lan, J. Yu, Z. Hua, H. Huang, X. Ma, S. Cao, Cocklebur-structured design of plant fibers for high-performance triboelectric nanogenerators and pressure sensors, Mater. Today Commun. 30 (2022) 103208.

[330] Y. Feng, Y. Zheng, G. Zhang, D. Wang, F. Zhou, W. Liu, A new protocol toward high output teng with polyimide as charge storage layer, Nano Energy 38 (2017) 467–476.

[331] S. Mishra, S. Potu, R.S. Puppala, R.K. Rajaboina, P. Kodali, H. Divi, A novel zns nanosheets-based triboelectric nanogenerator and its applications in sensing, self-powered electronics, and digital systems, Mater. Today Commun. 31 (2022) 103292.

[332] D.W. Kim, J.H. Lee, I. You, J.K. Kim, U. Jeong, Adding a stretchable deep-trap interlayer for high-performance stretchable triboelectric nanogenerators, Nano Energy 50 (2018) 192–200.

[333] J.-H. Zhang, Y. Zhang, N. Sun, Y. Li, J. Du, L. Zhu, X. Hao, Enhancing output performance of triboelectric nanogenerator via large polarization difference effect, Nano Energy 84 (2021) 105892.

[334] V.A. Cao, S. Lee, M. Kim, M.M. Alam, P. Park, J. Nah, Output power density enhancement of triboelectric nanogenerators via ferroelectric polymer composite interfacial layers, Nano Energy 67 (2020) 104300.

[335] A.A. Narasimulu, P. Zhao, N. Soin, K. Prashanthi, P. Ding, J. Chen, S. Dong, L. Chen, E. Zhou, C.D. Montemagno, J. Luo, Significant triboelectric enhancement using interfacial piezoelectric ZnO nanosheet layer, Nano Energy 40 (2017) 471–480.

[336] H.W. Park, N.D. Huynh, W. Kim, C. Lee, Y. Nam, S. Lee, K.B. Chung, D. Choi, Electron blocking layer-based interfacial design for highly-enhanced triboelectric nanogenerators, Nano Energy 50 (2018) 9–15.

[337] H. Jiang, H. Lei, Z. Wen, J. Shi, D. Bao, C. Chen, J. Jiang, Q. Guan, X. Sun, S. T. Lee, Charge-trapping-blocking layer for enhanced triboelectric nanogenerators, Nano Energy 75 (2020) 105011.

[338] L. Cheng, Q. Xu, Y. Zheng, X. Jia, Y. Qin, A self-improving triboelectric nanogenerator with improved charge density and increased charge accumulation speed, Nat. Commun. 9 (2018) 3773.

[339] Z. Li, M. Zhu, Q. Qiu, J. Yu, B. Ding, Multilayered fiber-based triboelectric nanogenerator with high performance for biomechanical energy harvesting, Nano Energy 53 (2018) 726–733.

[340] X. Liu, J. Zhang, L. Zhang, Y. Feng, M. Feng, N. Luo, D. Wang, Influence of interface liquid lubrication on triboelectrification of point contact friction pair, Tribol. Int. 165 (2022) 107323.

[341] W. He, W. Liu, S. Fu, H. Wu, C. Shan, Z. Wang, Y. Xi, X. Wang, H. Guo, H. Liu, C. Hu, Ultrahigh performance triboelectric nanogenerator enabled by charge transmission in interfacial lubrication and potential decentralization design, Research2022 (2022) 1–11.

[342] J. Wu, Y. Xi, Y. Shi, Toward wear-resistive, highly durable and high performance triboelectric nanogenerator through interface liquid lubrication, Nano Energy 72 (2020) 104659.

[343] S.H. Chung, J. Chung, M. Song, S. Kim, D. Shin, Z.H. Lin, B. Koo, D. Kim, J. Hong, S. Lee, Nonpolar liquid lubricant submerged triboelectric nanogenerator for current amplification via direct electron flow, Adv. Energy Mater. 11 (2021) 2100936.

[344] L. Zhou, D. Liu, Z. Zhao, S. Li, Y. Liu, L. Liu, Y. Gao, Z.L. Wang, J. Wang, Simultaneously enhancing power density and durability of sliding-mode triboelectric nanogenerator via interface liquid lubrication, Adv. Energy Mater. 10 (2020) 2002920.

[345] P. Wang, S. Zhang, L. Zhang, L. Wang, H. Xue, Z.L. Wang, Non-contact and liquid–liquid interfacing triboelectric nanogenerator for self-powered water/liquid level sensing, Nano Energy 72 (2020) 104703.

[346] B. Yang, X. Tao, Z. Peng, Upper limits for output performance of contact-mode triboelectric nanogenerator systems, Nano Energy 57 (2019) 66–73.

[347] X. Xia, J. Chen, G. Liu, M.S. Javed, X. Wang, C. Hu, Aligning graphene sheets in PDMS for improving output performance of triboelectric nanogenerator, Carbon N Y 111 (2017) 569–576.

[348] R. Sun, L. Gao, M. Shou, B. Li, X. Chen, F. Wang, X. Mu, L. Xie, C. Liao, Tribo-material based on a magnetic polymeric composite for enhancing the performance of triboelectric nanogenerator, Nano Energy 78 (2020) 105402.

[349] X. Pu, J.W. Zha, C.L. Zhao, S.B. Gong, J.F. Gao, R.K.Y. Li, Flexible PVDF/nylon-11 electrospun fibrous membranes with aligned zno nanowires as potential triboelectric nanogenerators, Chem. Eng. J. 398 (2020) 125526.

[350] H.H. Singh, N. Khare, Improved performance of ferroelectric nanocomposite flexible film based triboelectric nanogenerator by controlling surface morphology, polarizability, and hydrophobicity, Energy 178 (2019) 765–771.

[351] J.H. Choi, Y. Ra, S. Cho, M. La, S.J. Park, D. Choi, Electrical charge storage effect in carbon based polymer composite for long-term performance enhancement of the triboelectric nanogenerator, Compos. Sci. Technol. 207 (2021) 108680.

[352] N. Amorntep, A. Namvong, W. Wongsinlatam, T. Remsungnen, A. Siritaratiwat, C. Srichan, S. Sriphan, P. Pakawanit, A. Ariyarit, W. Supasai, N. Jutong, S. Narkglom, C. Surawanitkun, Electrical performance enhancement of a triboelectric nanogenerator based on epoxy resin/$BaTiO_3$ by Al nanopowder addition for low power electronic devices, Nanotechnology 34 (2023) 425401.

[353] X. García-Casas, A. Ghaffarinehad, F.J. Aparicio, J. Castillo-Seoane, C. López-Santos, J.P. Espinós, J. Cotrino, J.R. Sánchez-Valencia, Á. Barranco, A. Borrás, Plasma engineering of microstructured piezo – triboelectric hybrid nanogenerators for wide bandwidth vibration energy harvesting, Nano Energy 91 (2022) 106673.

[354] I. Firdous, M. Fahim, L. Wang, W.J. Li, Y. Zi, W.A. Daoud, Boosting current output of triboelectric nanogenerator by two orders of magnitude via hindering interfacial charge recombination, Nano Energy 89 (2021) 106315.

[355] B. Xi, L. Wang, B. Yang, Y. Xia, D. Chen, X. Wang, Boosting output performance of triboelectric nanogenerator based on $BaTiO_3$: la embedded nanofiber membrane for energy harvesting and wireless power transmission, Nano Energy 110 (2023) 108385.

[356] P.C. Lee, Y.C. Ou, R.C. Wang, C.P. Liu, Enhanced output performance of zno thin film triboelectric nanogenerators by leveraging surface limited ga doping and insulting bulk, Nano Energy 89 (2021) 106394.

[357] S.N. Chen, M.Z. Huang, Z.H. Lin, C.P. Liu, Enhancing charge transfer for ZnO nanorods based triboelectric nanogenerators through Ga doping, Nano Energy 65 (2019) 104069.

[358] S.N. Chen, C.H. Chen, Z.H. Lin, Y.H. Tsao, C.P. Liu, On enhancing capability of tribocharge transfer of ZnO nanorod arrays by Sb doping for anomalous output performance improvement of triboelectric nanogenerators, Nano Energy 45 (2018) 311–318.

[359] K. Ghosh, C. Iffelsberger, M. Konečný, J. Vyskočil, J. Michalička, M. Pumera, Nanoarchitectonics of triboelectric nanogenerator for conversion of abundant mechanical energy to green hydrogen, Adv. Energy Mater. 13 (2023) 2203476.

[360] W. Li, W. Zhang, Y. Xu, G. Wang, T. Xu, S. Nie, C. Si, Lignin-derived materials for triboelectric nanogenerators with emphasis on lignin multifunctionality, Nano Energy 128 (2024) 109912.

[361] Y. Yu, X. Wang, Chemical modification of polymer surfaces for advanced triboelectric nanogenerator development, Extreme Mech. Lett. 9 (2016) 514–530.

[362] S. Li, J. Nie, Y. Shi, X. Tao, F. Wang, J. Tian, S. Lin, X. Chen, Z.L. Wang, Contributions of different functional groups to contact electrification of polymers, Adv. Mater. 32 (2020) 2001307.

[363] F.R. Fan, J. Luo, W. Tang, C. Li, C. Zhang, Z. Tian, Z.L. Wang, Highly transparent and flexible triboelectric nanogenerators: performance improvements and fundamental mechanisms, J Mater Chem A Mater 2 (2014) 13219–13225.

[364] S.H. Shin, D. Park, J.Y. Jung, P. Park, J. Nah, An ultraviolet and electric field activated photopolymer–ferroelectric nanoparticle composite for the performance enhancement of triboelectric nanogenerators, Nanoscale 10 (2018) 20995–21000.

[365] B.K. Yun, J.W. Kim, H.S. Kim, K.W. Jung, Y. Yi, M.S. Jeong, J.H. Ko, J.H. Jung, Base-treated polydimethylsiloxane surfaces as enhanced triboelectric nanogenerators, Nano Energy 15 (2015) 523–529.

[366] S. Li, Y. Fan, H. Chen, J. Nie, Y. Liang, X. Tao, J. Zhang, X. Chen, E. Fu, Z.L. Wang, Manipulating the triboelectric surface charge density of polymers by low-energy helium ion irradiation/implantation, Energy Environ. Sci. 13 (2020) 896–907.

[367] S. Wang, Y. Xie, S. Niu, L. Lin, C. Liu, Y.S. Zhou, Z.L. Wang, Maximum surface charge density for triboelectric nanogenerators achieved by ionized-air injection: methodology and theoretical understanding, Adv. Mater. 26 (2014) 6720–6728.

[368] S. Wang, Y. Zi, Y.S. Zhou, S. Li, F. Fan, L. Lin, Z.L. Wang, Molecular surface functionalization to enhance the power output of triboelectric nanogenerators, J Mater Chem A Mater 4 (2016) 3728–3734.

[369] G. Song, Y. Kim, S. Yu, M.O. Kim, S.H. Park, S.M. Cho, D.B. Velusamy, S.H. Cho, K.L. Kim, J. Kim, E. Kim, C. Park, Molecularly engineered surface triboelectric nanogenerator by self-assembled monolayers (mets), Chem. Mater. 27 (2015) 4749–4755.

[370] Y.H. Kwon, S.H. Shin, J.Y. Jung, J. Nah, Scalable and enhanced triboelectric output power generation by surface functionalized nanoimprint patterns, Nanotechnology 27 (2016) 205401.

[371] Y. Feng, Y. Zheng, S. Ma, D. Wang, F. Zhou, W. Liu, High output polypropylene nanowire array triboelectric nanogenerator through surface structural control and chemical modification, Nano Energy 19 (2016) 48–57.

[372] S. Potu, M. Navaneeth, A. Bhadoriya, A. Bora, Y. Sivalingam, A. Babu, M. Velpula, B. Gollapelli, R.K. Rajaboina, U.K. Khanapuram, H. Divi, P. Kodali, L. Bochu, Enhancing triboelectric nanogenerator performance with metal–organic-framework-modified zno nanosheets for self-powered electronic devices and energy harvesting, ACS Appl. Nano Mater. 6 (2023) 22701–22710.

[373] Y.P. Jeon, J.H. Park, T.W. Kim, Highly-enhanced triboelectric nanogenerators based on zinc-oxide nanoripples acting as a triboelectric layer, Appl. Surf. Sci. 445 (2018) 50–55.

[374] J. Zhou, J. Zhang, Y. Deng, H. Zhao, P. Zhang, S. Fu, X. Xu, H. Li, Defect-mediated work function regulation in graphene film for high-performing triboelectric nanogenerators, Nano Energy 99 (2022) 107411.

[375] B.B. Yu, X. Hu, H. Wang, Q. Liang, L. Wang, Y. Wu, Q. Qin, L.B. Huang, Improved perovskite triboelectric nanogenerators by effective defect passivation and interface modulation, Appl. Phys. Lett. 122 (2023) 133902.

[376] Y. Li, Y. Luo, S. Xiao, C. Zhang, C. Pan, F. Zeng, Z. Cui, B. Huang, J. Tang, T. Shao, X. Zhang, J. Xiong, Z.L. Wang, Visualization and standardized quantification of surface charge density for triboelectric materials, Nat. Commun. 15 (2024) 6004.

[377] R.D. Cruise, S.O. Starr, K. Hadler, J.J. Cilliers, Triboelectric charge saturation on single and multiple insulating particles in air and vacuum, Sci. Rep. 13 (2023) 15178.

[378] X. Li, Q. Yang, D. Ren, Q. Li, H. Yang, X. Zhang, Y. Xi, A review of material design for high performance triboelectric nanogenerators: performance improvement based on charge generation and charge loss, Nanoscale Adv. (2024) 4522–4544.

[379] J. Zhu, M. Zhu, Q. Shi, F. Wen, L. Liu, B. Dong, A. Haroun, Y. Yang, P. Vachon, X. Guo, T. He, C. Lee, Progress in teng technology—a journey from energy harvesting to nanoenergy and nanosystem, EcoMat 2 (2020) 12058.

[380] G. Shen, Y. Hu, J. Li, J. Wen, J. Ma, A piezo-triboelectric hybrid nanogenerator based on charge pumping strategy, Energy Convers. Manag. 292 (2023) 117368.

[381] Z. Yang, Y. Yang, F. Liu, B. Li, Y. Li, X. Liu, J. Chen, C. Wang, L. Ji, Z.L. Wang, J. Cheng, Thousandfold boosting instantaneous current of triboelectric nanogenerator based on decoupled charge pump and discharge tube, Nano Energy 98 (2022) 107264.

[382] S.H. Chung, J.H. Son, K. Cha, M. Choi, H. Jung, M.K. Kim, J. Hong, S. Lee, Boosting power output of fluttering triboelectric nanogenerator based on charge excitation through multi-utilization of wind, Nano Energy 111 (2023) 108389.

[383] Z. Yang, J. Shen, X. Qu, Z. Lai, L. Ji, J. Cheng, Charge pumping triboelectric nanogenerator with dust clearance and elastic support for wind energy harvesting, Nano Energy 131 (2024) 110263.

[384] G. Li, G. Liu, W. He, L. Long, B. Li, Z. Wang, Q. Tang, W. Liu, C. Hu, Miura folding based charge-excitation triboelectric nanogenerator for portable power supply, Nano Res. 14 (2021) 4204–4210.

[385] K. Wang, X. Wang, Y. Sun, Z. Wu, H. Zhang, K. Xiao, J. Du, J. Li, J. Luo, Macroscopic liquid superlubric triboelectric nanogenerator: an in-depth understanding of solid-liquid interfacial charge behavior, Nano Energy 129 (2024) 110038.

[386] J. Wang, H. Wu, S. Fu, G. Li, C. Shan, W. He, C. Hu, Enhancement of output charge density of TENG in high humidity by water molecules induced self-polarization effect on dielectric polymers, Nano Energy 104 (2022) 107916.

[387] M.D. Hussain, B. Dudem, D.I. Kutsarov, S.R.P. Silva, Exploring charge regeneration effect in interdigitated array electrodes-based TENGs for a more than 100-fold enhanced power density, Nano Energy 130 (2024) 110112.

[388] L. Xu, H. Wu, G. Yao, L. Chen, X. Yang, B. Chen, X. Huang, W. Zhong, X. Chen, Z. Yin, Z.L. Wang, Giant voltage enhancement via triboelectric charge supplement channel for self-powered electroadhesion, ACS Nano 12 (2018) 10262–10271.

[389] G. Vauche, C. Corbier, Enhanced performance in energy of low frequency triboelectric-nanogenerator systems, J. Microelectromech. Syst. 33 (2024) 209–216.

[390] P. Wu, P. Yang, Z. Liu, G. Huang, X. Tao, S. Qin, X. Dong, L. Zheng, H. Li, X. Chen, Z.L. Wang, Boosting the output of liquid–solid triboelectric nanogenerator by an external charge-pumping strategy, Adv. Energy Mater. 14 (2024).

[391] S. Rana, B. Singh, RGO-embedded polymer nanocomposite layer for improved performance of triboelectric nanogenerator, J. Electron. Mater. (2024).

[392] H. Ma, S. Li, Z. Zheng, X. Wei, Biodegradable and recyclable composite membrane of relaxor ferroelectrics and bacterial cellulose with excellent output performance for triboelectric nanogenerator application, J. Mater. Sci. Mater. Electron. 34 (2023) 1757.

[393] Y. Nan, X. Wang, H. Xu, Y. Wu, H. Zhou, Y. Sun, T. Yu, Y. Huang, Synergistic effects of charge transport and trapping in tribomaterials for boosted triboelectric nanogenerators, Nano Energy 110 (2023)108345.

[394] S. Zhang, Y. Chen, D. Wang, P. He, Solid–liquid contact TENG using a melting near-field direct writing PCL nano-fiber structure, Int J Smart Nano Mater 14 (2023) 90–102.

[395] H.J. Yoon, S.S. Kwak, S.M. Kim, S.W. Kim, Aim high energy conversion efficiency in triboelectric nanogenerators, Sci. Technol. Adv. Mater. 21 (2020) 683–688.

[396] D.K. Tran, S. Veeralingam, J.W. Kim, Self-repairing thermoplastic polyurethane-based triboelectric nanogenerator with molybdenum disulfide charge-trapping for advanced wearable devices, Nano Energy 127 (2024) 109714.

[397] L. Gao, X. Chen, F. Wang, D. Tong, X. He, X. Mu, Enhancing the output charge density of triboelectric nanogenerator via building charge blocking layer, in: Proceedings of the IEEE International Conference on Micro Electro Mechanical Systems (MEMS), Institute of Electrical and Electronics Engineers Inc., 2021, pp. 238–241.

[398] K.G. Motora, C.M. Wu, C.R.M. Jose, Boosting the triboelectric performances of biowaste chitosan keratin triboelectric nanogenerator using carbon composite film as charge storage and charge recombination blocking intermediate layer, Chem. Eng. J. 492 (2024) 152413.

[399] N. Cui, L. Gu, Y. Lei, J. Liu, Y. Qin, X. Ma, Y. Hao, Z.L. Wang, Dynamic behavior of the triboelectric charges and structural optimization of the friction layer for a triboelectric nanogenerator, ACS Nano 10 (2016) 6131–6138.

[400] N. Wang, Y. Liu, Y. Feng, J. Yang, Y. Wu, B. Zhang, Y. Li, B. Li, S. Wang, E. Ye, Y. W. Zhang, X.J. Loh, F. Zhou, Z. Li, D. Wang, Revamping triboelectric output by deep trap construction, Adv. Mater. 36 (2024).

[401] S. Im, E. Frey, D.J. Lacks, J. Genzer, M.D. Dickey, Enhanced triboelectric charge stability by air-stable radicals, Adv. Sci. 10 (2023) e2304459.

[402] Q. Guo, X. Yang, Y. Wang, W. Xu, J. Duan, Q. Tang, Dielectric hole collector toward boosting charge transfer of CsPbBr 3 hybrid nanogenerator by coupling triboelectric and photovoltaic effects, Adv. Funct. Mater. 31 (2021) 2101348.

[403] M. Lai, B. Du, H. Guo, Y. Xi, H. Yang, C. Hu, J. Wang, Z.L. Wang, Enhancing the output charge density of TENG via building longitudinal paths of electrostatic charges in the contacting layers, ACS Appl. Mater. Interfaces 10 (2018) 2158–2165.

[404] Y. Wang, H. Du, H. Yang, Z. Xi, C. Zhao, Z. Qian, X. Chuai, X. Peng, H. Yu, Y. Zhang, X. Li, G. Hu, H. Wang, M. Xu, A rolling-mode triboelectric nanogenerator with multi-tunnel grating electrodes and opposite-charge-enhancement for wave energy harvesting, Nat. Commun. 15 (2024) 6834.

[405] C. Wang, H. Guo, P. Wang, J. Li, Y. Sun, D. Zhang, An advanced strategy to enhance TENG output: reducing triboelectric charge decay, Adv. Mater. 35 (2023) 2209890.

[406] Z. Cao, Y. Chu, S. Wang, Z. Wu, R. Ding, X. Ye, A strategy to reduce air breakdown effect and boost output energy for contact-separation mode triboelectric nanogenerator, in: 21st International Conference on Solid-State Sensors, Actuators and Microsystems, TRANSDUCERS 2021, Institute of Electrical and Electronics Engineers Inc., 2021, pp. 451–454.

[407] J. Wang, B. Zhang, Z. Zhao, Y. Gao, D. Liu, X. Liu, P. Yang, Z. Guo, Z.L. Wang, J. Wang, Boosting the charge density of triboelectric nanogenerator by suppressing air breakdown and dielectric charge leakage, Adv. Energy Mater. 14 (2024).

[408] L. Liu, J. Li, Z. Tian, H. Wu, S. Zhou, X. Chen, Y. Zhu, X. Yang, W. Ou-Yang, Suppressing charge recombination by synergistic effect of ferromagnetic dual-tribolayer for high output triboelectric nanogenerator, Nano Today 57 (2024).

[409] J. Zheng, C. Lin, J. Zhao, K. Wang, J. Liu, N. Cui, L. Gu, The regulation and its application of the charge decay rate in triboelectric nanogenerator, Nanotechnology 35 (2024).

[410] X. Xia, Y. Zi, Heat-excitation-based triboelectric charge promotion strategy, Adv. Sci. 11 (2024).

[411] T. Hu, H. Wang, W. Harmon, D. Bamgboje, Z.L. Wang, Current progress on power management systems for triboelectric nanogenerators, IEEE Trans. Power Electron. 37 (2022) 9850–9864.

[412] S. Niu, X. Wang, F. Yi, Y.S. Zhou, Z.L. Wang, A universal self-charging system driven by random biomechanical energy for sustainable operation of mobile electronics, Nat. Commun. 6 (2015).

[413] F. Xi, Y. Pang, W. Li, T. Jiang, L. Zhang, T. Guo, G. Liu, C. Zhang, Z.L. Wang, Universal power management strategy for triboelectric nanogenerator, Nano Energy 37 (2017) 168–176.

[414] J. Zhuo, Z. Zheng, R. Ma, X. Zhang, Y. Wang, P. Yang, L. Cao, J. Chen, J. Lu, G. Chen, G. Chen, J. Fu, Z. Wu, J. Wang, X. Wang, G. Yang, F. Yi, A breathable and woven hybrid energy harvester with optimized power management for sustainably powering electronics, Nano Energy 112 (2023).

[415] X. Xia, H. Wang, P. Basset, Y. Zhu, Y. Zi, Inductor-free output multiplier for power promotion and management of triboelectric nanogenerators toward self-powered systems, ACS Appl. Mater. Interfaces 12 (2020) 5892–5900.

[416] H. Qin, G. Cheng, Y. Zi, G. Gu, B. Zhang, W. Shang, F. Yang, J. Yang, Z. Du, Z. L. Wang, High energy storage efficiency triboelectric nanogenerators with unidirectional switches and passive power management circuits, Adv. Funct. Mater. 28 (2018).

[417] A. Kawaguchi, H. Uchiyama, M. Matsunaga, Y. Ohno, Simple and highly efficient intermittent operation circuit for triboelectric nanogenerator toward wearable electronic applications, APEX 14 (2021) 057001.

[418] W. Harmon, D. Bamgboje, H. Guo, T. Hu, Z.L. Wang, Self-driven power management system for triboelectric nanogenerators, Nano Energy 71 (2020).

[419] D.W. Kim, J.H. Lee, J.K. Kim, U. Jeong, Material aspects of triboelectric energy generation and sensors, NPG Asia Mater. 12 (2020).

[420] S. Lv, X. Zhang, T. Huang, H. Yu, Q. Zhang, M. Zhu, Trap distribution and conductivity synergic optimization of high-performance triboelectric nanogenerators for self-powered devices, ACS Appl. Mater. Interfaces 13 (2021) 2566–2575.

[421] H.G. Menge, N.D. Huynh, C. Cho, D. Choi, Y.T. Park, Designable functional polymer nanocomposites via layer-by-layer assembly for highly deformable power-boosted triboelectric nanogenerators, Compos. B Eng. 230 (2022) 109513.

[422] W. Kim, J.H. Park, H.J. Hwang, Y.S. Rim, D. Choi, Interfacial molecular engineering for enhanced polarization of negative tribo-materials, Nano Energy 96 (2022) 107110.

[423] D. Choi, Y. Lee, Z.H. Lin, S. Cho, M. Kim, C.K. Ao, S. Soh, C. Sohn, C.K. Jeong, J. Lee, M. Lee, S. Lee, J. Ryu, P. Parashar, Y. Cho, J. Ahn, I.D. Kim, F. Jiang, P. S. Lee, G. Khandelwal, S.J. Kim, H.S. Kim, H.C. Song, M. Kim, J. Nah, W. Kim, H. G. Menge, Y.T. Park, W. Xu, J. Hao, H. Park, J.H. Lee, D.M. Lee, S.W. Kim, J. Y. Park, H. Zhang, Y. Zi, R. Guo, J. Cheng, Z. Yang, Y. Xie, S. Lee, J. Chung, I. K. Oh, J.S. Kim, T. Cheng, Q. Gao, G. Cheng, G. Gu, M. Shim, J. Jung, C. Yun, C. Zhang, G. Liu, Y. Chen, S. Kim, X. Chen, J. Hu, X. Pu, Z.H. Guo, X. Wang, J. Chen, X. Xiao, X. Xie, M. Jarin, H. Zhang, Y.C. Lai, T. He, H. Kim, I. Park, J. Ahn, N.D. Huynh, Y. Yang, Z.L. Wang, J.M. Baik, D. Choi, Recent advances in triboelectric nanogenerators: from technological progress to commercial applications, ACS Nano 17 (2023) 11087–11219.

[424] C. Wang, X. Li, L. Wang, G. Liu, B. Nie, Y. Qiu, B. Fan, C. Yan, X. Chen, H. Tian, C. Wang, J. Shao, Metal micropatterning by triboelectric spark discharge, Adv. Funct. Mater. 32 (2022).

[425] Y. Bai, H. Feng, Z. Li, Theory and applications of high-voltage triboelectric nanogenerators, Cell Rep. Phys. Sci. 3 (2022) 101108.

[426] L. Zheng, Y. Wu, X. Chen, A. Yu, L. Xu, Y. Liu, H. Li, Z.L. Wang, Self-Powered electrostatic actuation systems for manipulating the movement of both microfluid and solid objects by using triboelectric nanogenerator, Adv. Funct. Mater. 27 (2017).

[427] C. Li, Y. Yin, B. Wang, T. Zhou, J. Wang, J. Luo, W. Tang, R. Cao, Z. Yuan, N. Li, X. Du, C. Wang, S. Zhao, Y. Liu, Z.L. Wang, Self-powered electrospinning system driven by a triboelectric nanogenerator, ACS Nano 11 (2017) 10439–10445.

[428] J. Cheng, W. Ding, Y. Zi, Y. Lu, L. Ji, F. Liu, C. Wu, Z.L. Wang, Triboelectric microplasma powered by mechanical stimuli, Nat. Commun. 9 (2018) 3733.

[429] C.L. Li, W.Z. Song, D.J. Sun, M. Zhang, J. Zhang, Y.Q. Chen, S. Ramakrishna, Y. Z. Long, A self-priming air filtration system based on triboelectric nanogenerator for active air purification, Chem. Eng. J. 452 (2023) 139428.

[430] S. Li, J. Jiang, N. Zhai, J. Liu, K. Feng, Y. Chen, Z. Wen, X. Sun, J. Zhong, A half-wave rectifying triboelectric nanogenerator for self-powered water splitting towards hydrogen production, Nano Energy 93 (2022) 106870.

[431] G. Cheng, Z.H. Lin, L. Lin, Z. Du, Z.L. Wang, Pulsed nanogenerator with huge instantaneous output power density, ACS Nano 7 (2013) 7383–7391.

[432] G. Cheng, H. Zheng, F. Yang, L. Zhao, M. Zheng, J. Yang, H. Qin, Z. Du, Z.L. Wang, Managing and maximizing the output power of a triboelectric nanogenerator by controlled tip–electrode air-discharging and application for UV sensing, Nano Energy 44 (2018) 208–216.

[433] J. Kim, H. Cho, M. Han, Y. Jung, S.S. Kwak, H. Yoon, B. Park, H. Kim, H. Kim, J. Park, S. Kim, Ultrahigh power output from triboelectric nanogenerator based on serrated electrode via spark discharge, Adv. Energy Mater. 10 (2020).

[434] H. Wu, S. Wang, Z. Wang, Y. Zi, Achieving ultrahigh instantaneous power density of 10 mw/m^2 by leveraging the opposite-charge-enhanced transistor-like triboelectric nanogenerator (OCT-TENG), Nat. Commun. 12 (2021) 5470.

[435] Z. Lin, G. Cheng, S. Lee, K.C. Pradel, Z.L. Wang, Harvesting water drop energy by a sequential contact-electrification and electrostatic-induction process, Adv. Mater. 26 (2014) 4690–4696.

[436] Q. Zhang, Y. Li, H. Cai, M. Yao, H. Zhang, L. Guo, Z. Lv, M. Li, X. Lu, C. Ren, P. Zhang, Y. Zhang, X. Shi, G. Ding, J. Yao, Z. Yang, Z.L. Wang, A single-droplet electricity generator achieves an ultrahigh output over 100 v without pre-charging, Adv. Mater. 33 (2021).

[437] X. Li, X. Ning, L. Li, X. Wang, B. Li, J. Li, J. Yin, W. Guo, Performance and power management of droplets-based electricity generators, Nano Energy 92 (2022) 106705.

[438] Y. Zhou, Y. Zeng, J. Wang, X. Li, P. Wang, W. Ma, C. Wang, J. Li, W. Jiang, D. Zhang, Enhancement of the voltage output of droplet electricity generators using high dielectric high-entropy oxide composites, Energy Environ. Sci. 17 (2024) 3580–3593.

[439] T. Liu, W. Mo, X. Zou, B. Luo, S. Zhang, Y. Liu, C. Cai, M. Chi, J. Wang, S. Wang, D. Lu, S. Nie, Liquid–solid triboelectric probes for real-time monitoring of sucrose fluid status, Adv. Funct. Mater. 33 (2023).

[440] Z. Yuan, L. Guo, Recent advances in solid-liquid triboelectric nanogenerator technologies, affecting factors, and applications, Sci. Rep. 14 (2024) 10456.

[441] V.D. Trung, P.A. Le, J. Natsuki, W. Zhao, T.V.B. Phung, T. Natsuki, Recent developments in droplet-based devices, Mater. Today Chem. 36 (2024) 101943.

[442] S. Sriphan, U. Pharino, K. Chaithaweep, N. Vittayakorn, Equivalent circuit model and simulation for dynamic sliding droplet-based triboelectric nanogenerators, Nano Energy 130 (2024) 110100.

[443] S. Pongampai, T. Charoonsuk, N. Pinpru, R. Muanghlua, W. Vittayakorn, N. Vittayakorn, High performance flexible tribo/piezoelectric nanogenerators based on BaTiO$_3$/chitosan composites, Integrated Ferroelectrics Int. J. 223 (2021) 137–151.

[444] Y. Song, N. Wang, Y. Wang, R. Zhang, H. Olin, Y. Yang, Y. Song, N. Wang, Y. Yang, Y. Wang, R. Zhang, H. Olin, Direct current triboelectric nanogenerators, Adv. Energy Mater. 10 (2020) 2002756.

[445] C. Xu, J. Yu, Z. Huo, Y. Wang, Q. Sun, Z.L. Wang, Pursuing the tribovoltaic effect for direct-current triboelectric nanogenerators, Energy Environ. Sci. 16 (2023) 983–1006.

[446] Y. Yang, H. Zhang, Z.L. Wang, Direct-current triboelectric generator, Adv. Funct. Mater. 24 (2014) 3745–3750.

[447] D. Liu, X. Yin, H. Guo, L. Zhou, X. Li, C. Zhang, J. Wang, Z.L. Wang, A constant current triboelectric nanogenerator arising from electrostatic breakdown, Sci. Adv. 5 (2019) eaav6437–eaav6437.

[448] Z. Zhao, Y. Dai, D. Liu, L. Zhou, S. Li, Z.L. Wang, J. Wang, Rationally patterned electrode of direct-current triboelectric nanogenerators for ultrahigh effective surface charge density, Nat. Commun. 11 (2020) 6186.

[449] C. Chen, H. Guo, L. Chen, Y.C. Wang, X. Pu, W. Yu, F. Wang, Z. Du, Z.L. Wang, Direct current fabric triboelectric nanogenerator for biomotion energy harvesting, ACS Nano 14 (2020) 4585–4594.

[450] H. Ryu, J.H. Lee, U. Khan, S.S. Kwak, R. Hinchet, S.W. Kim, Sustainable direct current powering a triboelectric nanogenerator via a novel asymmetrical design, Energy Environ. Sci. 11 (2018) 2057–2063.

[451] X. Li, C. Zhang, Y. Gao, Z. Zhao, Y. Hu, O. Yang, L. Liu, L. Zhou, J. Wang, Z. L. Wang, A highly efficient constant-voltage triboelectric nanogenerator, Energy Environ. Sci. 15 (2022) 1334–1345.

[452] R.D.I.G. Dharmasena, H.M. Cronin, R.A. Dorey, S.R.P. Silva, Direct current contact-mode triboelectric nanogenerators via systematic phase shifting, Nano Energy 75 (2020) 104887.

[453] S. Sriphan, N. Vittayakorn, Tribovoltaic effect: fundamental working mechanism and emerging applications, Mater. Today Nano 22 (2023) 100318.

[454] S. Lin, Z. Lin Wang, The tribovoltaic effect, Mater. Today 62 (2023) 111–128.

[455] S. Sriphan, S. Worathat, U. Pharino, N. Chanlek, P. Pakawanit, K. Choodam, P. Kanjanaboos, T. Maluangnont, N. Vittayakorn, Highly flexible tribovoltaic nanogenerator based-on p-n junction interface: comparative study on output dependency dominated by photovoltaic effect in freestanding-mode, Adv. Funct. Mater. 33 (2023).

[456] A. Šutka, M. Zubkins, A. Linarts, L. Lapčinskis, K. Malnieks, O. Verners, A. Sarakovskis, R. Grzibovskis, J. Gabrusenoks, E. Strods, K. Smits, V. Vibornijs, L. Bikse, J. Purans, Tribovoltaic device based on the w/wo$_3$ schottky junction operating through hot carrier extraction, J. Phys. Chem. C 125 (2021) 14212–14220.

[457] X. Xu, J. Li, X. Tao, Q. Yan, H. Wu, Z. Guan, L. Liu, X. Chen, W. Ou-Yang, Study of interfacial design for direct-current tribovoltaic generators, Nano Energy 94 (2022) 106957.

[458] Z. Zhang, T. He, J. Zhao, G. Liu, Z.L. Wang, C. Zhang, Tribo-thermoelectric and tribovoltaic coupling effect at metal-semiconductor interface, Mater. Today Phys. 16 (2021) 100295.

[459] R. Xu, Q. Zhang, J.Y. Wang, D. Liu, J. Wang, Z.L. Wang, Direct current triboelectric cell by sliding an n-type semiconductor on a p-type semiconductor, Nano Energy 66 (2019) 104185.

[460] Z. Wang, Z. Zhang, Y. Chen, L. Gong, S. Dong, H. Zhou, Y. Lin, Y. Lv, G. Liu, C. Zhang, Achieving an ultrahigh direct-current voltage of 130 v by semiconductor heterojunction power generation based on the tribovoltaic effect, Energy Environ. Sci. 15 (2022) 2366–2373.

[461] S. Worathat, U. Pharino, P. Pakawanit, A. Rattanachata, R. Muanghlua, S. Hajra, H.J. Kim, S. Sriphan, N. Vittayakorn, Frictional heat-assisted performance enhancement in dynamic schottky contact of Al/Ag$_2$Se-based tribovoltaic nanogenerator, J. Materiomics 11 (2025) 100854.

[462] S. Sriphan, S. Worathat, P. Pakawanit, S. Hajra, H.J. Kim, N. Vittayakorn, Tribovoltaic performance of the schottky contact between metal and PZT ceramic, Ceram. Int. 50 (2024) 52067–52074.

[463] L. Ren, A. Yu, W. Wang, D. Guo, M. Jia, P. Guo, Y. Zhang, Z.L. Wang, J. Zhai, P-n junction based direct-current triboelectric nanogenerator by conjunction of tribovoltaic effect and photovoltaic effect, Nano Lett. 21 (2021) 10099–10106.

[464] S. Sriphan, T. Charoonsuk, T. Maluangnont, P. Pakawanit, C. Rojviriya, N. Vittayakorn, Multifunctional nanomaterials modification of cellulose paper for efficient triboelectric nanogenerators, Adv. Mater. Technol. 5 (2020).

[465] T. Charoonsuk, R. Muanghlua, S. Sriphan, S. Pongampai, N. Vittayakorn, Utilization of commodity thermoplastic polyethylene (PE) by enhanced sensing performance with liquid phase electrolyte for a flexible and transparent triboelectric tactile sensor, Sustain. Mater. Technol. 27 (2021) e00239.

[466] H. Guo, T. Li, X. Cao, J. Xiong, Y. Jie, M. Willander, X. Cao, N. Wang, Z.L. Wang, Self-sterilized flexible single-electrode triboelectric nanogenerator for energy harvesting and dynamic force sensing, ACS Nano 11 (2017) 856–864.

[467] Q. Leng, H. Guo, X. He, G. Liu, Y. Kang, C. Hu, Y. Xi, Flexible interdigital-electrodes-based triboelectric generators for harvesting sliding and rotating mechanical energy, J. Mater. Chem. A 2 (2014) 19427–19434.

[468] B. Wu, Z. Zhang, X. Xue, C. Hao, W. Zhang, R. Bi, Q. Wang, C. Xue, A stretchable triboelectric generator with coplanar integration design of energy harvesting and strain sensing, Sci. China Technol. Sci. 65 (2022) 221–230.

[469] Y. Wu, Y. Luo, J. Qu, W.A. Daoud, T. Qi, Liquid single-electrode triboelectric nanogenerator based on graphene oxide dispersion for wearable electronics, Nano Energy 64 (2019) 103948.

[470] J. Xiong, P. Cui, X. Chen, J. Wang, K. Parida, M.F. Lin, P.S. Lee, Skin-touch-actuated textile-based triboelectric nanogenerator with black phosphorus for durable biomechanical energy harvesting, Nat. Commun. 9 (2018) 4280.

[471] S.A. Han, W. Seung, J.H. Kim, S.W. Kim, Ultrathin noncontact-mode triboelectric nanogenerator triggered by giant dielectric material adaption, ACS Energy Lett. (2021) 1189–1197.

[472] S. Chung, J. Chung, M. Song, S. Kim, D. Shin, Z. Lin, B. Koo, D. Kim, J. Hong, S. Lee, Triboelectric nanogenerators: nonpolar liquid lubricant submerged triboelectric nanogenerator for current amplification via direct electron flow, Adv. Energy Mater. 11 (2021).

[473] W. Li, L. Lu, C. Zhang, K. Loos, Y. Pei, Durable and high-performance triboelectric nanogenerator based on an inorganic triboelectric pair of diamond-like-carbon and glass, Adv. Sci. 11 (2024) e2309170–e2309170.

[474] P. Chen, J. An, S. Shu, R. Cheng, J. Nie, T. Jiang, Z.L. Wang, Super-durable, low-wear, and high-performance fur-brush triboelectric nanogenerator for wind and water energy harvesting for smart agriculture, Adv. Energy Mater. 11 (2021).

[475] M.M. Rastegardoost, O.A. Tafreshi, Z. Saadatnia, S. Ghaffari-Mosanenzadeh, P. Serles, T. Filleter, C.B. Park, H.E. Naguib, Highly durable triboelectric nanogenerators based on fibrous fluoropolymer composite mats with enhanced mechanical and dielectric properties, Mater. Today Energy 38 (2023) 101431.

[476] W.J. Bartz, Tribology, lubricants and lubrication engineering — a review, Wear 49 (1978) 1–18.

[477] J. Chung, D. Heo, G. Shin, D. Choi, K. Choi, D. Kim, S. Lee, Triboelectric nanogenerators: ion-enhanced field emission triboelectric nanogenerato, Adv. Energy Mater. 9 (2019).

[478] S. Sriphan, T. Charoonsuk, T. Maluangnont, N. Vittayakorn, Piezoelectric energy harvesting for low-power smart electronics, in: Encyclopedia of Materials: Electronics, Elsevier, Amsterdam, 2023, pp. 369–404.

[479] M. Rakshita, N. Madathil, A.A. Sharma, P.P. Pradhan, D.P. Kasireddi, A. K, U. K. Khanapuram, R.K. Rajaboina, H. Divi, Phosphor-based triboelectric nanogenerators for mechanical energy harvesting and self-powered systems, ACS Appl. Electron. Mater. 6 (2024) 1821–1828.

[480] A. Kulandaivel, S. Potu, R.K. Rajaboina, U.K. Khanapuram, Exploring wettability: a key to optimizing liquid–solid triboelectric nanogenerators, ACS Appl. Mater. Interfaces 16 (2024) 58029–58059.

[481] V.L. Sunitha, P. Supraja, K.A.K.D. Prasad, M. Navaneeth, A. Babu, V. Mahesh, K. U. Kumar, D. Haranath, R.R. Kumar, Wood plastic composites (WPC) waste based triboelectric nanogenerator for mechanical energy harvesting and self-powered applications, Mater. Lett. 351 (2023) 134995.

[482] A. Alagumalai, W. Shou, O. Mahian, M. Aghbashlo, M. Tabatabaei, S. Wongwises, Y. Liu, J. Zhan, A. Torralba, J. Chen, Z. Wang, W. Matusik, Self-powered sensing systems with learning capability, Joule 6 (2022) 1475–1500.

[483] G.M. Rani, S.M. Ghoreishian, R. Umapathi, V. Vivekananthan, Y.S. Huh, A biocompatible triboelectric nanogenerator-based edible electronic skin for morse code transmitters and smart healthcare applications, Nano Energy 128 (2024) 109899.

[484] G.M. Rani, C.M. Wu, K.G. Motora, R. Umapathi, C.R.M. Jose, Acoustic-electric conversion and triboelectric properties of nature-driven CF-CNT based triboelectric nanogenerator for mechanical and sound energy harvesting, Nano Energy 108 (2023) 108211.

[485] G.M. Rani, C.M. Wu, K.G. Motora, R. Umapathi, Waste-to-energy: utilization of recycled waste materials to fabricate triboelectric nanogenerator for mechanical energy harvesting, J. Clean. Prod. 363 (2022) 132532.

[486] B. Zhang, Z. Wu, Z. Lin, H. Guo, F. Chun, W. Yang, Z.L. Wang, All-in-one 3d acceleration sensor based on coded liquid–metal triboelectric nanogenerator for vehicle restraint system, Mater. Today 43 (2021) 37–44.

[487] Y. Sun, Y. Yu, Q. Gao, X. Zhang, J. Zhang, Y. Wang, S. He, H. Li, Z.L. Wang, T. Cheng, Enhancing performance of triboelectric nanogenerator by accelerating the charge transfer strategy, Nano Energy 121 (2024) 109194.

[488] Z. Guan, L. Liu, X. Xu, A. Liu, H. Wu, J. Li, W. Ou-Yang, A self-powered acoustic sensor excited by ultrasonic wave for detecting and locating underwater ultrasonic sources, Nano Energy 104 (2022) 107879.

[489] W. Zhang, X. Chen, J. Zhao, X. Wang, X. Li, T. Liu, B. Luo, Y. Qin, S. Zhang, M. Chi, S. Wang, S. Nie, Cellulose template-based triboelectric nanogenerators for self-powered sensing at high humidity, Nano Energy 108 (2023) 108196.

[490] S. Panda, H. Jeong, S. Hajra, P.M. Rajaitha, S. Hong, H.J. Kim, Biocompatible polydopamine based triboelectric nanogenerator for humidity sensing, Sensor. Actuator. B Chem. 394 (2023) 134384.

[491] Y. Jiang, Y. Zhang, C. Ning, Q. Ji, X. Peng, K. Dong, Z.L. Wang, Ultrathin eardrum-inspired self-powered acoustic sensor for vocal synchronization recognition with the assistance of machine learning, Small 18 (2022).

[492] J. Qin, X. Yang, C. Shen, Y. Chang, Y. Deng, Z. Zhang, H. Liu, C. Lv, Y. Li, C. Zhang, L. Dong, C. Shan, Carbon nanodot-based humidity sensor for self-powered respiratory monitoring, Nano Energy 101 (2022) 107549.

[493] S.A. Khan, M.M. Rehman, S. Ameen, M. Saqib, M. Khan, W.Y. Kim, High performance triboelectric nanogenerator based on purified chitin nanopaper for the applications of self-powered humidity sensing, gait monitoring, and hyperhidrosis sensor, Sustain. Mater. Technol. 40 (2024) e00867.

[494] K. Dai, Z.Y. Huo, X. Miao, P. Xiong, H. Zhang, X. Wang, Z. You, S.W. Kim, Self-powered triboelectric functional devices and microsystems in health-care applications: an energy perspective, EnergyChem 5 (2023) 100109.

[495] Y. Gai, Y. Jiang, Z. Li, Advances in health rehabilitation devices based on triboelectric nanogenerators, Nano Energy 116 (2023) 108787.

[496] X. Qin, H. Shi, Z. Wen, B. Chu, H. Li, H. Wang, Y. He, X. Sun, Triboelectric-responsive drug delivery hydrogel for accelerating infected wound healing, Adv. Healthcare Mater. 13 (2024).

[497] W. Wang, C. Fu, Y. Du, H. Zheng, Y. Zhang, Y. Song, W. Sun, X. Wang, Q. Ma, Aqueous-aqueous triboelectric nanogenerators empowered multifunctional wound healing system with intensified current output for accelerating infected wound repair, Adv. Healthcare Mater. 13 (2024).

[498] X. Liu, Y. Wang, G. Wang, Y. Ma, Z. Zheng, K. Fan, J. Liu, B. Zhou, G. Wang, Z. You, Y. Fang, X. Wang, S. Niu, An ultrasound-driven implantable wireless energy harvesting system using a triboelectric transducer, Matter 5 (2022) 4315–4331.

[499] O. Yue, X. Wang, M. Hou, M. Zheng, D. Hao, Z. Bai, X. Zou, B. Cui, C. Liu, X. Liu, Smart nanoengineered electronic-scaffolds based on triboelectric nanogenerators as tissue batteries for integrated cartilage therapy, Nano Energy 107 (2023) 108158.

[500] H. Zhong, K. Zhang, M. Zhou, C. Xing, Y. An, Q. Zhang, J. Guo, S. Liu, Z. Qu, S. Feng, G. Ning, An implantable self-driven diaphragm pacing system based on a microvibration triboelectric nanogenerator for phrenic nerve stimulation, ACS Appl. Mater. Interfaces 16 (2024) 43199–43211.

[501] S. Yao, X. Zhao, X. Wang, T. Huang, Y. Ding, J. Zhang, Z. Zhang, Z.L. Wang, L. Li, Bioinspired electron polarization of nanozymes with a human self-generated electric field for cancer catalytic therapy, Adv. Mater. 34 (2022).

[502] S. Yao, M. Zheng, Z. Wang, Y. Zhao, S. Wang, Z. Liu, Z. Li, Y. Guan, Z.L. Wang, L. Li, Self-powered, implantable, and wirelessly controlled no generation system for intracranial neuroglioma therapy, Adv. Mater. 34 (2022).

[503] X. Huo, S. Luo, Z. Cao, Y. Zhou, Y. Hu, Z. Lin Wang, Z. Wu, An implantable sensor based on shape memory polymers and triboelectric nanogenerators: monitoring ureteral peristalsis to assess bladder volume, Chem. Eng. J. 497 (2024) 154971.

[504] T. Zhang, C. Yao, X. Xu, Z. Liu, Z. Liu, T. Sun, S. Huang, X. Huang, S. Farah, P. Shi, H. Chen, X. Xie, Nanopores-templated CNT/PDMS microcolumn substrate for the fabrication of wearable triboelectric nanogenerator sensors to monitor human pulse and blood pressure, Adv. Mater. Technol. 10 (2025) 2400749.

[505] Y. Wu, Y. Li, Y. Zou, W. Rao, Y. Gai, J. Xue, L. Wu, X. Qu, Y. Liu, G. Xu, L. Xu, Z. Liu, Z. Li, A multi-mode triboelectric nanogenerator for energy harvesting and biomedical monitoring, Nano Energy 92 (2022) 106715.

[506] B. Chu, X. Qin, Q. Zhu, H. Wang, Z. Wen, X. Sun, Y. He, S.T. Lee, Triboelectric current stimulation alleviates in vitro cell migration and in vivo tumor metastasis, Nano Energy 100 (2022) 107471.

[507] B. Yu, L. Zhou, X. Zhang, G. Hu, H. Min, Y. Qiu, T. Huang, Y. Wang, M. Zhu, H. Yu, Respiration-mediated self-switched triboelectric nanogenerator for wearable point-of-care prevention and alarm of asthma, Nano Energy 106 (2023) 108058.

[508] C. Xiong, Z. Liu, Q. Li, Y. Shang, Z. Jiang, C. Tang, S. Zhong, Z. Wang, Q. Hu, Q. Cai, Q. Sun, L. Wan, L. Li, An intelligent triboelectric sensing system for monitoring and early warning of dry eye syndrome, Nano Energy 122 (2024) 109326.

[509] Y. Wang, X. Zhang, G. Chen, M. Lu, Y. Zhao, Multifunctional structural color triboelectric microneedle patches for psoriasis treatment, Matter 6 (2023) 1555–1568.

[510] R. Riaz, B. Dudem, M.A. Costa Angeli, A. Douaki, M. Ahmad, A. Mejia-Aguilar, R. Monsorno, P. Lugli, S.R.P. Silva, L. Petti, Surface textured double layer triboelectric nanogenerator for autonomous and ultra-sensitive biomedical sensing, Adv. Mater. Technol. 8 (2023).

[511] L. Dong, M. Wang, J. Wu, C. Zhu, J. Shi, H. Morikawa, Stretchable, adhesive, self-healable, and conductive hydrogel-based deformable triboelectric nanogenerator for energy harvesting and human motion sensing, ACS Appl. Mater. Interfaces 14 (2022) 9126–9137.

[512] J. Oh, M. Kang, J. Park, T.Y. Kim, K. Park, J. Seo, Autonomously self-healing, adhesive, and stretchable triboelectric nanogenerator using multifunctional hydrogel-elastomer double layer with a power management circuit, Adv. Electron. Mater. 10 (2024).

[513] L. Zhao, Q. Ling, X. Fan, H. Gu, Self-healable, adhesive, anti-drying, freezing-tolerant, and transparent conductive organohydrogel as flexible strain sensor, triboelectric nanogenerator, and skin barrier, ACS Appl. Mater. Interfaces 15 (2023) 40975–40990.

[514] Y. Li, Z. Tian, X. Gao, H. Zhao, X. Li, Z.L. Wang, Z. Yu, D. Yang, All-weather self-powered intelligent traffic monitoring system based on a conjunction of self-healable piezoresistive sensors and triboelectric nanogenerators, Adv. Funct. Mater. 33 (2023).

[515] Y. Xia, Y. Zhu, X. Zhi, W. Guo, B. Yang, S. Zhang, M. Li, X. Wang, C. Pan, Transparent self-healing anti-freezing ionogel for monolayered triboelectric nanogenerator and electromagnetic energy-based touch panel, Adv. Mater. 36 (2024).

[516] Y. Feng, J. Yu, D. Sun, C. Dang, W. Ren, C. Shao, R. Sun, Extreme environment-adaptable and fast self-healable eutectogel triboelectric nanogenerator for energy harvesting and self-powered sensing, Nano Energy 98 (2022) 107284.

[517] Y.X. Wang, P.K. Tsao, M. Rinawati, K.J. Chen, K.Y. Chen, C. Chang, M.H. Yeh, Designing zif-67 derived NiCo layered double hydroxides with 3d hierarchical structure for enzyme-free electrochemical lactate monitoring in human sweat, Chem. Eng. J. 427 (2022) 131687.

[518] R. Umapathi, G.M. Rani, E. Kim, S. Park, Y. Cho, Y.S. Huh, Sowing kernels for food safety: importance of rapid on-site detection of pesticide residues in agricultural foods, Food Front 3 (2022) 666–676.

[519] R. Umapathi, S.M. Ghoreishian, G.M. Rani, Y. Cho, Y.S. Huh, Review—Emerging trends in the development of electrochemical devices for the on-site detection of food contaminants, ECS Sensors Plus 1 (2022) 044601.

[520] Z. Tian, Z. Zhu, S. Yue, Y. Liu, Y. Li, Z.Z. Yu, D. Yang, Self-powered, self-healing, and anti-freezing triboelectric sensors for violation detection in sport events, Nano Energy 122 (2024) 109276.

[521] B. Bagchi, P. Datta, C.S. Fernandez, L. Xu, P. Gupta, W. Huang, A.L. David, D. Siassakos, S. Homer-Vanniasinkam, M.K. Tiwari, A stretchable, self-healing and semi-transparent nanogenerator for energy harvesting and sensing, Nano Energy 107 (2023) 108127.

[522] W. He, S. Li, P. Bai, D. Zhang, L. Feng, L. Wang, X. Fu, H. Cui, X. Ji, R. Ma, Multifunctional triboelectric nanogenerator based on flexible and self-healing sandwich structural film, Nano Energy 96 (2022) 107109.

[523] T. Zhao, J. Wang, Y. Liu, X. Li, Y. Bai, B. Luo, M. Chi, S. Zhang, T. Liu, Y. Shao, G. Du, P. Zhang, Z. Liu, S. Wang, S. Nie, Self-healing and toughness triboelectric materials enabled by dynamic nanoconfinement quenching, Adv. Funct. Mater. 34 (2024).

[524] H. Zhang, D. Zhang, Z. Wang, G. Xi, R. Mao, Y. Ma, D. Wang, M. Tang, Z. Xu, H. Luan, Ultrastretchable, self-healing conductive hydrogel-based triboelectric nanogenerators for human–computer interaction, ACS Appl. Mater. Interfaces 15 (2023) 5128–5138.

[525] Y. Qin, J. Mo, Y. Liu, S. Zhang, J. Wang, Q. Fu, S. Wang, S. Nie, Stretchable triboelectric self-powered sweat sensor fabricated from self-healing nanocellulose hydrogels, Adv. Funct. Mater. 32 (2022).

[526] S. Chou, H. Lu, T. Liu, Y. Chen, Y. Fu, Y. Shieh, Y. Lai, S. Chen, An environmental-inert and highly self-healable elastomer obtained via double-terminal aromatic disulfide design and zwitterionic crosslinked network for use as a triboelectric nanogenerator, Adv. Sci. 10 (2023).

[527] A. Shen, H. Xuan, Y. Jia, S. Gu, R.E. Neisiany, W. Shu, W. Sun, Z. You, Dynamic healing-assembly for biocompatible, biodegradable, stretchable and self-healing triboelectric nanogenerators, Chem. Eng. J. 491 (2024) 151896.

[528] L. Xu, Y. Yang, Y. Mao, Z. Li, Self-powerbility in electrical stimulation drug delivery system, Adv. Mater. Technol. 7 (2022).

[529] K. Wang, Q. Ding, M. Qi, W. Zhang, Y. Hou, R. Cao, C. Li, L. Xu, L. Wang, J.S. Kim, Integrated bilayer microneedle dressing and triboelectric nanogenerator for intelligent management of infected wounds, Adv. Funct. Mater. 34 (2024).

[530] C. Wang, G. He, H. Zhao, Y. Lu, P. Jiang, W. Li, Enhancing deep-seated melanoma therapy through wearable self-powered microneedle patch, Adv. Mater. 36 (2024).

[531] Q. Ouyang, X. Feng, S. Kuang, N. Panwar, P. Song, C. Yang, G. Yang, X. Hemu, G. Zhang, H.S. Yoon, J.P. Tam, B. Liedberg, G. Zhu, K.T. Yong, Z.L. Wang, Self-powered, on-demand transdermal drug delivery system driven by triboelectric nanogenerator, Nano Energy 62 (2019) 610–619.

[532] C. Zhao, Q. Shi, H. Li, X. Cui, Y. Xi, Y. Cao, Z. Xiang, F. Li, J. Sun, J. Liu, T. Li, W. Wei, B. Xiong, Z. Li, Shape designed implanted drug delivery system for in situ hepatocellular carcinoma therapy, ACS Nano 16 (2022) 8493–8503.

[533] C. Wu, P. Jiang, W. Li, H. Guo, J. Wang, J. Chen, M.R. Prausnitz, Z.L. Wang, Self-powered iontophoretic transdermal drug delivery system driven and regulated by biomechanical motions, Adv. Funct. Mater. 30 (2020).

[534] Z. Liu, J. Nie, B. Miao, J. Li, Y. Cui, S. Wang, X. Zhang, G. Zhao, Y. Deng, Y. Wu, Z. Li, L. Li, Z.L. Wang, Self-powered intracellular drug delivery by a biomechanical energy-driven triboelectric nanogenerator, Adv. Mater. 31 (2019).

[535] Q. Chen, W. Deng, J. He, L. Cheng, P.G. Ren, Y. Xu, Enhancing drug utilization efficiency via dish-structured triboelectric nanogenerator, Front. Bioeng. Biotechnol. 10 (2022).

[536] L. Jiang, L. Zhang, C. Dai, B. Zhao, Y. Yang, Z. Wu, C. Qu, L. Zou, Z.H. Lin, Y. B. Miao, Y. Shi, A self-generated electricity-driven drug delivery system for precision management of myopia, Nano Energy 119 (2024) 109040.

[537] Z. Chen, Y. Lai, S. Xu, M. Zhu, Y. Sun, Y. Cheng, G. Zhao, A self-powered controllable microneedle drug delivery system for rapid blood pressure reduction, Nano Energy 123 (2024) 109344.

[538] Z. Lin, G. Cheng, Y. Yang, Y.S. Zhou, S. Lee, Z.L. Wang, Triboelectric nanogenerator as an active uv photodetector, Adv. Funct. Mater. 24 (2014) 2810–2816.

[539] S. Singh, R.K. Tripathi, M.K. Gupta, G.I. Dzhardimalieva, I.E. Uflyand, B. Yadav, 2-D self-healable polyaniline-polypyrrole nanoflakes based triboelectric nanogenerator for self-powered solar light photo detector with DFT study, J. Colloid Interface Sci. 600 (2021) 572–585.

[540] Y. Zhang, M. Peng, Y. Liu, T. Zhang, Q. Zhu, H. Lei, S. Liu, Y. Tao, L. Li, Z. Wen, X. Sun, Flexible self-powered real-time ultraviolet photodetector by coupling triboelectric and photoelectric effects, ACS Appl. Mater. Interfaces 12 (2020) 19384–19392.

[541] L. Han, M. Peng, Z. Wen, Y. Liu, Y. Zhang, Q. Zhu, H. Lei, S. Liu, L. Zheng, X. Sun, H. Li, Self-driven photodetection based on impedance matching effect between a triboelectric nanogenerator and a MoS_2 nanosheets photodetector, Nano Energy 59 (2019) 492–499.

[542] B. Baro, T. Mayu, A. Ghorai, S. Bayan, Tribo-piezoelectric hybrid nanogenerators based on ZnO nanorods and $CsPbBr_3$ nanoparticle/PVDF-HFP films for self-powered photodetectors, ACS Appl. Nano Mater. 7 (2024) 14504–14515.

[543] M. Peng, H. Ji, S. Liu, P. Lv, Y. Kuang, Y. Liu, Y. Liu, X. Sun, Z. Wen, A self-powered triboelectric UV photodetector based on coupling impedance matching and photoresistive effect by sensing-electrode model, Nano Energy 109 (2023) 108294.

[544] A. Mirsepah, L. Shooshtari, R. Mohammadpour, A. Esfandiar, A. Irajizad, Wearable broadband MoS_2 photodetector for dual heart rate and UV detection powered by PDMS-MXene TENG, Chem. Eng. J. 499 (2024) 155953.

[545] T. Wang, G. Gu, W. Shang, J. Gan, W. Zhang, H. Luo, B. Zhang, P. Cui, J. Guo, F. Yang, G. Cheng, Z. Du, A self-powered photodetector using a pulsed triboelectric nanogenerator for actual working environments with random mechanical stimuli, Nano Energy 90 (2021) 106518.

[546] Y. Kumaresan, G. Min, A.S. Dahiya, A. Ejaz, D. Shakthivel, R. Dahiya, Kirigami and mogul-patterned ultra-stretchable high-performance ZnO nanowires-based photodetector, Adv. Mater. Technol. 7 (2022).

[547] J. Wang, K. Xia, J. liu, T. Li, X. Zhao, B. Shu, H. Li, J. Guo, M. Yu, W. Tang, Z. Zhu, Self-powered silicon pin photoelectric detection system based on triboelectric nanogenerator, Nano Energy 69 (2020) 104461.

[548] X. Guo, T. He, Z. Zhang, A. Luo, F. Wang, E.J. Ng, Y. Zhu, H. Liu, C. Lee, Artificial intelligence-enabled caregiving walking stick powered by ultra-low-frequency human motion, ACS Nano 15 (2021) 19054–19069.

[549] Q. Zhang, T. Jin, J. Cai, L. Xu, T. He, T. Wang, Y. Tian, L. Li, Y. Peng, C. Lee, Wearable triboelectric sensors enabled gait analysis and waist motion capture for IoT-based smart healthcare applications, Adv. Sci. 9 (2022).

[550] Y. Liu, F. Zhuo, J. Zhou, L. Kuang, K. Tan, H. Lu, J. Cai, Y. Guo, R. Cao, Y. Fu, H. Duan, Machine-learning assisted handwriting recognition using graphene oxide-based hydrogel, ACS Appl. Mater. Interfaces 14 (2022) 54276–54286.

[551] R. Mao, D. Zhang, Z. Wang, H. Zhang, D. Wang, M. Tang, L. Zhou, H. Cai, H. Xia, Deep-learning-assisted low-cost flexible cotton yarn-based triboelectric nanogenerator for ultra-sensitive human-computer merging interfaces, Nano Energy 111 (2023) 108418.

[552] J. Zhu, Z. Sun, J. Xu, R.D. Walczak, J.A. Dziuban, C. Lee, Volatile organic compounds sensing based on bennet doubler-inspired triboelectric nanogenerator and machine learning-assisted ion mobility analysis, Sci Bull (Beijing) 66 (2021) 1176–1185.

[553] P. Maharjan, K. Shrestha, T. Bhatta, H. Cho, C. Park, M. Salauddin, M.T. Rahman, S.S. Rana, S. Lee, J.Y. Park, Keystroke dynamics based hybrid nanogenerators for biometric authentication and identification using artificial intelligence, Adv. Sci. 8 (2021).

[554] H. Luo, J. Du, P. Yang, Y. Shi, Z. Liu, D. Yang, L. Zheng, X. Chen, Z.L. Wang, Human–machine interaction via dual modes of voice and gesture enabled by triboelectric nanogenerator and machine learning, ACS Appl. Mater. Interfaces 15 (2023) 17009–17018.

[555] K. Shrestha, P. Maharjan, T. Bhatta, S. Sharma, M.T. Rahman, S. Lee, M. Salauddin, S.S. Rana, J.Y. Park, A high-performance rotational energy harvester integrated with artificial intelligence-powered triboelectric sensors for wireless environmental monitoring system, Adv. Eng. Mater. 24 (2022).

[556] H. Zhao, M. Xu, M. Shu, J. An, W. Ding, X. Liu, S. Wang, C. Zhao, H. Yu, H. Wang, C. Wang, X. Fu, X. Pan, G. Xie, Z.L. Wang, Underwater wireless communication via TENG-generated Maxwell's displacement current, Nat. Commun. 13 (2022).

[557] Z. Guan, L. Liu, X. Xu, A. Liu, H. Wu, J. Li, W. Ou-Yang, A self-powered acoustic sensor excited by ultrasonic wave for detecting and locating underwater ultrasonic sources, Nano Energy 104 (2022).

[558] Z. Tian, L. Su, H. Wang, H. Wang, Y. Zi, Underwater self-powered all-optical wireless ultrasonic sensing, positioning and communication with ultrafast response time and ultrahigh sensitivity, Adv. Opt. Mater. 10 (2022).

[559] Y. Xi, J. Wang, Y. Zi, X. Li, C. Han, X. Cao, C. Hu, Z. Wang, High efficient harvesting of underwater ultrasonic wave energy by triboelectric nanogenerator, Nano Energy 38 (2017) 101–108.

[560] S. Hajra, S. Panda, S. Song, H. Song, B.K. Panigrahi, S.M. Jeong, Y.K. Mishra, H. J. Kim, Simultaneous triboelectric and mechanoluminescence sensing toward self-powered applications, Adv. Sustain. Syst. 8 (2024) 2400609.

[561] S. Hajra, S. Panda, S. Song, B.K. Panigrahi, P. Pakawanit, S.M. Jeong, H.J. Kim, Flexible composite material for self-powered applications via triboelectricity and mechanoluminescence: PDMS/ZnS:Cu composites, Nano Energy 114 (2023) 108668.

[562] X. Zhang, Z. Li, W. Du, Y. Zhao, W. Wang, L. Pang, L. Chen, A. Yu, J. Zhai, Self-powered triboelectric-mechanoluminescent electronic skin for detecting and differentiating multiple mechanical stimuli, Nano Energy 96 (2022) 107115.

[563] Y.M. Wei, R. Han, C. Wang, B. Yu, Q.M. Liang, X.C. Yuan, J. Chang, Q. Zhao, H. Liao, B. Tang, J. Yan, L. Cheng, Z. Yang, Self-preservation strategy for approaching global warming targets in the post-paris agreement era, Nat. Commun. 11 (2020) 1624.

[564] H. Rastegar, G. Eweje, A. Sajjad, The impact of environmental policy on renewable energy innovation: a systematic literature review and research directions, Sustain. Dev. 32 (2024) 3859–3876.

[565] G. Min, Y. Xu, P. Cochran, N. Gadegaard, D.M. Mulvihill, R. Dahiya, Origin of the contact force-dependent response of triboelectric nanogenerators, Nano Energy 83 (2021) 105829.

[566] Y. Xu, G. Min, N. Gadegaard, R. Dahiya, D.M. Mulvihill, A unified contact force-dependent model for triboelectric nanogenerators accounting for surface roughness, Nano Energy 76 (2020) 105067.

[567] J. Cheng, X. Zhang, T. Jia, Q. Wu, Y. Dong, D. Wang, Triboelectric nanogenerator with a seesaw structure for harvesting ocean energy, Nano Energy 102 (2022) 107622.

[568] Q. Zhang, M. He, X. Pan, D. Huang, H. Long, M. Jia, Z. Zhao, C. Zhang, M. Xu, S. Li, High performance liquid-solid tubular triboelectric nanogenerator for scavenging water wave energy, Nano Energy 103 (2022) 107810.

[569] Q. Gao, Y. Xu, X. Yu, Z. Jing, T. Cheng, Z.L. Wang, Gyroscope-structured triboelectric nanogenerator for harvesting multidirectional ocean wave energy, ACS Nano 16 (2022) 6781–6788.

[570] W. Liu, L. Xu, G. Liu, H. Yang, T. Bu, X. Fu, S. Xu, C. Fang, C. Zhang, Network topology optimization of triboelectric nanogenerators for effectively harvesting ocean wave energy, iScience 23 (2020).

[571] H. Jing, C. Han, Z. An, Z. Cao, Z. Li, Z. Wu, Noninertial driven multifaceted fluff and halbach array hybrid nanogenerator: achieving shore-based water wave energy harvesting, ACS Appl. Electron. Mater. 6 (2024) 6671–6680.

[572] X. Liang, T. Jiang, G. Liu, Y. Feng, C. Zhang, Z.L. Wang, Spherical triboelectric nanogenerator integrated with power management module for harvesting multidirectional water wave energy, Energy Environ. Sci. 13 (2020) 277–285.

[573] X. Li, Y. Cao, X. Yu, Y. Xu, Y. Yang, S. Liu, T. Cheng, Z.L. Wang, Breeze-driven triboelectric nanogenerator for wind energy harvesting and application in smart agriculture, Appl. Energy 306 (2022) 117977.

[574] X. Fan, J. Chen, J. Yang, P. Bai, Z. Li, Z.L. Wang, Ultrathin, rollable, paper-based triboelectric nanogenerator for acoustic energy harvesting and self-powered sound recording, ACS Nano 9 (2015) 4236–4243.

[575] C. Xu, X. Fu, C. Li, G. Liu, Y. Gao, Y. Qi, T. Bu, Y. Chen, Z.L. Wang, C. Zhang, Raindrop energy-powered autonomous wireless hyetometer based on liquid–solid contact electrification, Microsyst Nanoeng 8 (2022) 30.

[576] M. Xu, T. Zhao, C. Wang, S.L. Zhang, Z. Li, X. Pan, Z.L. Wang, High power density tower-like triboelectric nanogenerator for harvesting arbitrary directional water wave energy, ACS Nano 13 (2019) 1932–1939.

[577] P. Munirathinam, A. Anna Mathew, V. Shanmugasundaram, V. Vivekananthan, Y. Purusothaman, S.J. Kim, A. Chandrasekhar, A comprehensive review on

triboelectric nanogenerators based on real-time applications in energy harvesting and self-powered sensing, Mater. Sci. Eng., B 297 (2023) 116762.
[578] R. Walden, C. Kumar, D.M. Mulvihill, S.C. Pillai, Opportunities and challenges in triboelectric nanogenerator (TENG) based sustainable energy generation technologies: a mini-review, Chem. Eng. J. Adv. 9 (2022) 100237.
[579] Y. Zhang, Q. Zeng, Y. Wu, J. Wu, S. Yuan, D. Tan, C. Hu, X. Wang, An ultra-durable windmill-like hybrid nanogenerator for steady and efficient harvesting of low-speed wind energy, Nano-Micro Lett. 12 (2020) 175.
[580] C. Chen, Z. Wen, J. Shi, X. Jian, P. Li, J.T.W. Yeow, X. Sun, Micro triboelectric ultrasonic device for acoustic energy transfer and signal communication, Nat. Commun. 11 (2020) 4143.
[581] H. Yong, J. Chung, D. Choi, D. Jung, M. Cho, S. Lee, Highly reliable wind-rolling triboelectric nanogenerator operating in a wide wind speed range, Sci. Rep. 6 (2016) 33977.
[582] L. Long, W. Liu, Z. Wang, W. He, G. Li, Q. Tang, H. Guo, X. Pu, Y. Liu, C. Hu, High performance floating self-excited sliding triboelectric nanogenerator for micro mechanical energy harvesting, Nat. Commun. 12 (2021) 4689.
[583] S. Fu, W. He, H. Wu, C. Shan, Y. Du, G. Li, P. Wang, H. Guo, J. Chen, C. Hu, High output performance and ultra-durable DC output for triboelectric nanogenerator inspired by primary cell, Nano-Micro Lett. 14 (2022) 155.
[584] Q. Mu, W. He, C. Shan, S. Fu, S. Du, J. Wang, Z. Wang, K. Li, C. Hu, Achieving high-efficiency wind energy harvesting triboelectric nanogenerator by coupling soft contact, charge space accumulation, and charge dissipation design, Adv. Funct. Mater. 34 (2024) 2309421.
[585] L. He, C. Zhang, B. Zhang, O. Yang, W. Yuan, L. Zhou, Z. Zhao, Z. Wu, J. Wang, Z. L. Wang, A dual-mode triboelectric nanogenerator for wind energy harvesting and self-powered wind speed monitoring, ACS Nano 16 (2022) 6244–6254.
[586] X. Gao, F. Xing, F. Guo, Y. Yang, Y. Hao, J. Chen, B. Chen, Z.L. Wang, A turbine disk-type triboelectric nanogenerator for wind energy harvesting and self-powered wildfire pre-warning, Mater. Today Energy 22 (2021) 100867.
[587] M.A.M. Hasan, W. Zhu, C.R. Bowen, Z.L. Wang, Y. Yang, Triboelectric nanogenerators for wind energy harvesting, Nat. Rev. Electr. Eng. 1 (2024) 453–465.
[588] A. Ahmed, I. Hassan, M. Hedaya, T. Abo El-Yazid, J. Zu, Z.L. Wang, Farms of triboelectric nanogenerators for harvesting wind energy: a potential approach towards green energy, Nano Energy 36 (2017) 21–29.
[589] Y. Feng, L. Zhang, Y. Zheng, D. Wang, F. Zhou, W. Liu, Leaves based triboelectric nanogenerator (TENG) and TENG tree for wind energy harvesting, Nano Energy 55 (2019) 260–268.
[590] W. Sun, Z. Ding, Z. Qin, F. Chu, Q. Han, Wind energy harvesting based on fluttering double-flag type triboelectric nanogenerators, Nano Energy 70 (2020) 104526.
[591] S. Cui, Y. Zheng, J. Liang, D. Wang, Triboelectrification based on double-layered polyaniline nanofibers for self-powered cathodic protection driven by wind, Nano Res. 11 (2018) 1873–1882.
[592] J.A. Choi, J. Jeong, M. Kang, S. Pyo, Vertical blinds-inspired triboelectric nanogenerator for wind energy harvesting and self-powered wind speed monitoring, ACS Appl. Electron. Mater. 6 (2024) 2534–2543.
[593] Y. Shin, S. Cho, S. Han, G.Y. Jung, Omni-directional wind-driven triboelectric nanogenerator with cross-shaped dielectric film, Nano Converg 8 (2021) 25.
[594] Y. Wang, E. Yang, T. Chen, J. Wang, Z. Hu, J. Mi, X. Pan, M. Xu, A novel humidity resisting and wind direction adapting flag-type triboelectric nanogenerator for wind energy harvesting and speed sensing, Nano Energy 78 (2020) 105279.
[595] Z. Ren, L. Wu, Y. Pang, W. Zhang, R. Yang, Strategies for effectively harvesting wind energy based on triboelectric nanogenerators, Nano Energy 100 (2022) 107522.
[596] X. Dong, Z. Liu, P. Yang, X. Chen, Harvesting wind energy based on triboelectric nanogenerators, Nanoenergy Advances 2 (2022) 245–268.
[597] S. Liu, X. Guo, J. Wang, Y. Yu, L. Meng, T. Cheng, Directional adaptive triboelectric nanogenerator with wind-wave synergy, ACS Appl. Mater. Interfaces 16 (2024) 46237–46246.
[598] S. Liu, X. Li, Y. Wang, Y. Yang, L. Meng, T. Cheng, Z.L. Wang, Magnetic switch structured triboelectric nanogenerator for continuous and regular harvesting of wind energy, Nano Energy 83 (2021) 105851.
[599] N. Yang, Y. Li, Z. Xu, Y. Zhu, Q. He, Z. Wang, X. Zhang, J. Liu, C. Liu, Y. Wang, M. Zhou, T. Cheng, Z.L. Wang, A blade-type triboelectric-electromagnetic hybrid generator with double frequency up-conversion mechanism for harvesting breeze wind energy, ACS Appl. Mater. Interfaces 16 (2024) 33404–33415.
[600] Y. Zeng, Y. Luo, Y. Lu, X. Cao, Self-powered rain droplet sensor based on a liquid-solid triboelectric nanogenerator, Nano Energy 98 (2022) 107316.
[601] D.L. Vu, C.D. Le, C.P. Vo, K.K. Ahn, Surface polarity tuning through epitaxial growth on polyvinylidene fluoride membranes for enhanced performance of liquid-solid triboelectric nanogenerator, Compos. B Eng. 223 (2021) 109135.
[602] P. He, J. Ding, L. Lei, W.Q. Tao, A four-electrode droplet triboelectric nanogenerator providing multimodal output, Cell Rep. Phys. Sci. 5 (2024).
[603] Y. Yang, B. Cao, C. Yang, Z. Wang, H. Zhang, L. Fang, W. He, P. Wang, A droplet-based multi-position and multi-layered triboelectric nanogenerator for large-scale raindrop energy harvesting, AIP Adv. 13 (2023) 055123.
[604] Y. Zheng, J. Li, T. Xu, H. Cui, X. Li, Triboelectric nanogenerator for droplet energy harvesting based on hydrophobic composites, Materials 16 (2023).
[605] G. Lee, H. Kang, J. Yun, D. Chae, M. Jeong, M. Jeong, D. Lee, M. Kim, H. Lee, J. Rho, Integrated triboelectric nanogenerator and radiative cooler for all-weather transparent glass surfaces, Nat. Commun. 15 (2024) 6537.
[606] Y. Hu, R. Sun, S. Li, C. Liu, J. Zhao, J. Mo, D. Luo, Y. Pan, Optimizing raindrop energy harvesting: exploring water droplet spreading effects on ide-based TENG for sustainable power generation, Nano Energy 123 (2024) 109358.
[607] S. Jang, M. La, S. Cho, Y. Yun, J.H. Choi, Y. Ra, S.J. Park, D. Choi, Monocharged electret based liquid-solid interacting triboelectric nanogenerator for its boosted electrical output performance, Nano Energy 70 (2020) 104541.
[608] Z. Li, B. Cao, Z. Zhang, L. Wang, Z.L. Wang, Rational TENG arrays as a panel for harvesting large-scale raindrop energy, IEnergy 2 (2023) 93–99.
[609] J.H. Lee, S. Kim, T.Y. Kim, U. Khan, S.W. Kim, Water droplet-driven triboelectric nanogenerator with superhydrophobic surfaces, Nano Energy 58 (2019) 579–584.
[610] T. Dang, J. Zhao, J. Zeng, T. Bu, J. Li, Y. Dai, Z. Dong, Y. Feng, Y. Chen, C. Zhang, Self-powered VO_2 phase transition based on triboelectric nanogenerator, J Mater Chem A Mater 12 (2024) 19052–19059.
[611] Q. Zhang, C. Jiang, X. Li, S. Dai, Y. Ying, J. Ping, Highly efficient raindrop energy-based triboelectric nanogenerator for self-powered intelligent greenhouse, ACS Nano 15 (2021) 12314–12323.
[612] W. Wang, W. Tang, P. Wang, Z. Liu, Z. Wang, S. Qiao, Triboelectric Nanogenerator Based on a Water Droplet Spring with a Concave Spherical Surface for Harvesting Wave Energy and Detecting Pressure, 2023, p. 12.
[613] Y. Liu, N. Sun, J. Liu, Z. Wen, X. Sun, S.T. Lee, B. Sun, Integrating a silicon solar cell with a triboelectric nanogenerator via a mutual electrode for harvesting energy from sunlight and raindrops, ACS Nano 12 (2018) 2893–2899.
[614] D. Yoo, S.C. Park, S. Lee, J.Y. Sim, I. Song, D. Choi, H. Lim, D.S. Kim, Biomimetic anti-reflective triboelectric nanogenerator for concurrent harvesting of solar and raindrop energies, Nano Energy 57 (2019) 424–431.
[615] C. Ye, D. Liu, P. Chen, L.N.Y. Cao, X. Li, T. Jiang, Z.L. Wang, An integrated solar panel with a triboelectric nanogenerator array for synergistic harvesting of raindrop and solar energy, Adv. Mater. 35 (2023) 2209713.
[616] X. Liu, A. Yu, A. Qin, J. Zhai, Highly integrated triboelectric nanogenerator for efficiently harvesting raindrop energy, Adv. Mater. Technol. 4 (2019) 1900608.
[617] W. Wang, Y. Zhang, G. Wu, Z. Zhao, Y. Wu, H. Zheng, Triboelectric–electromagnetic hybrid nanogenerator for harvesting blue energy and creating an ocean wave warning system, Nanoscale Adv. 6 (2024) 3566–3572.
[618] M. Salman, V. Sorokin, K. Aw, Systematic literature review of wave energy harvesting using triboelectric nanogenerator, Renew. Sustain. Energy Rev. 201 (2024) 114626.
[619] Y. Jiang, X. Liang, T. Jiang, Z.L. Wang, Advances in triboelectric nanogenerators for blue energy harvesting and marine environmental monitoring, Engineering 33 (2024) 204–224.
[620] C. Zhang, Y. Hao, X. Lu, W. Su, H. Zhang, Z.L. Wang, X. Li, Advances in TENGs for marine energy harvesting and in situ electrochemistry, Nano-Micro Lett. 17 (2025) 124.
[621] W. Zhang, W. He, S. Dai, F. Ma, P. Lin, J. Sun, L. Dong, C. Hu, Wave energy harvesting based on multilayer beads integrated spherical TENG with switch triggered instant discharging for self-powered hydrogen generation, Nano Energy 111 (2023) 108432.
[622] Z. Wen, H. Guo, Y. Zi, M.H. Yeh, X. Wang, J. Deng, J. Wang, S. Li, C. Hu, L. Zhu, Z. L. Wang, Harvesting broad frequency band blue energy by a triboelectric–electromagnetic hybrid nanogenerator, ACS Nano 10 (2016) 6526–6534.
[623] O. Ellabban, H. Abu-Rub, F. Blaabjerg, Renewable energy resources: current status, future prospects and their enabling technology, Renew. Sustain. Energy Rev. 39 (2014) 748–764.
[624] Z. Yuan, C. Wang, J. Xi, X. Han, J. Li, S.T. Han, W. Gao, C. Pan, Spherical triboelectric nanogenerator with dense point contacts for harvesting multidirectional water wave and vibration energy, ACS Energy Lett. 6 (2021) 2809–2816.
[625] J. Feng, H. Zhou, Z. Cao, E. Zhang, S. Xu, W. Li, H. Yao, L. Wan, G. Liu, 0.5 m triboelectric nanogenerator for efficient blue energy harvesting of all-sea areas, Adv. Sci. 9 (2022) 2204407.
[626] Y. Bai, L. Xu, C. He, L. Zhu, X. Yang, T. Jiang, J. Nie, W. Zhong, Z.L. Wang, High-performance triboelectric nanogenerators for self-powered, in-situ and real-time water quality mapping, Nano Energy 66 (2019) 104117.
[627] Y. Hu, H. Qiu, Q. Sun, Z.L. Wang, L. Xu, Wheel-structured triboelectric nanogenerators with hyperelastic networking for high-performance wave energy harvesting, Small Methods 7 (2023) 2300582.
[628] D. Jiang, F. Guo, M. Xu, J. Cai, S. Cong, M. Jia, G. Chen, Y. Song, Conformal fluorine coated carbon paper for an energy harvesting water wheel, Nano Energy 58 (2019) 842–851.
[629] X. Liang, Z. Liu, Y. Feng, J. Han, L. Li, J. An, P. Chen, T. Jiang, Z.L. Wang, Spherical triboelectric nanogenerator based on spring-assisted swing structure for effective water wave energy harvesting, Nano Energy 83 (2021) 105836.
[630] Z.L. Wang, T. Jiang, T. Ma, R. Yang, Nanogenerators for blue energy, MRS Bull. 50 (2025) 450–458.
[631] J. Ye, C. He, X. Gong, H. Zhang, X. Li, Blue energy harvesting based on triboelectric nanogenerators (TENG): structural design, performance optimization, and application prospects, J. Alloys Compd. 1014 (2025) 178710.
[632] Y. Hao, C. Wu, K. Zang, L. Zhang, J. Zhou, D. Zhao, Research advances of triboelectric nanogenerators for blue energy: research status, challenges and future outlook, Nano Energy 142 (2025) 111223.
[633] I.W. Ock, J. Yin, S. Wang, X. Zhao, J.M. Baik, J. Chen, Advances in blue energy fuels: harvesting energy from ocean for self-powered electrolysis, Adv. Energy Mater. 15 (2025) 2400563.
[634] L. Pan, J. Wang, P. Wang, R. Gao, Y.C. Wang, X. Zhang, J.J. Zou, Z.L. Wang, Liquid-FEP-based U-tube triboelectric nanogenerator for harvesting water-wave energy, Nano Res. 11 (2018) 4062–4073.
[635] S.L. Zhang, M. Xu, C. Zhang, Y.C. Wang, H. Zou, X. He, Z. Wang, Z.L. Wang, Rationally designed sea snake structure based triboelectric nanogenerators for

effectively and efficiently harvesting ocean wave energy with minimized water screening effect, Nano Energy 48 (2018) 421–429.

[636] Z. Zhao, Z. Zhang, L. Xu, F. Gao, B. Zhao, Z. Kang, Q. Liao, Y. Zhang, Tumbler-shaped hybrid triboelectric nanogenerators for amphibious self-powered environmental monitoring, Nano Energy 76 (2020) 104960.

[637] X. Wu, X. Li, J. Ping, Y. Ying, Recent advances in water-driven triboelectric nanogenerators based on hydrophobic interfaces, Nano Energy 90 (2021) 106592.

[638] C. Fang, T. Tong, T. Bu, Y. Cao, S. Xu, Y. Qi, C. Zhang, Overview of power management for triboelectric nanogenerators, Adv. Intell. Syst. 2 (2020) 1900129.

[639] S.F. Leung, H.C. Fu, M. Zhang, A.H. Hassan, T. Jiang, K.N. Salama, Z.L. Wang, J. H. He, Blue energy fuels: converting ocean wave energy to carbon-based liquid fuels via CO_2 reduction, Energy Environ. Sci. 13 (2020) 1300–1308.

[640] Y. Wang, A. Matin Nazar, J. Wang, K. Xia, D. Wang, X. Ji, P. Jiao, Rolling spherical triboelectric nanogenerators (RS-TENG) under low-frequency ocean wave action, J. Mar. Sci. Eng. 10 (2022).

[641] X. Yang, L. Xu, P. Lin, W. Zhong, Y. Bai, J. Luo, J. Chen, Z.L. Wang, Macroscopic self-assembly network of encapsulated high-performance triboelectric nanogenerators for water wave energy harvesting, Nano Energy 60 (2019) 404–412.

[642] Y. Duan, H. Xu, S. Liu, P. Chen, X. Wang, L. Xu, T. Jiang, Z.L. Wang, Scalable rolling-structured triboelectric nanogenerator with high power density for water wave energy harvesting toward marine environmental monitoring, Nano Res. 16 (2023) 11646–11652.

[643] H. Chen, J. Wang, A. Ning, Optimization of a rolling triboelectric nanogenerator based on the nano–micro structure for ocean environmental monitoring, ACS Omega 6 (2021) 21059–21065.

[644] Z. Xu, L. Chen, Z. Zhang, J. Han, P. Chen, Z. Hong, T. Jiang, Z.L. Wang, Durable roller-based swing-structured triboelectric nanogenerator for water wave energy harvesting, Small 20 (2024) 2307288.

[645] I. Kim, D. Kim, 3D printed double roller-based triboelectric nanogenerator for blue energy harvesting, Micromachines 12 (2021).

[646] Z. Lin, B. Zhang, H. Guo, Z. Wu, H. Zou, J. Yang, Z.L. Wang, Super-robust and frequency-multiplied triboelectric nanogenerator for efficient harvesting water and wind energy, Nano Energy 64 (2019) 103908.

[647] X. Miao, H. Yang, Z. Li, M. Cheng, Y. Zhao, L. Wan, A. Yu, J. Zhai, A columnar multi-layer sliding triboelectric nanogenerator for water wave energy harvesting independent of wave height and direction, Nano Res. 17 (2024) 3029–3034.

[648] C. Zhang, L. He, L. Zhou, O. Yang, W. Yuan, X. Wei, Y. Liu, L. Lu, J. Wang, Z. L. Wang, Active resonance triboelectric nanogenerator for harvesting omnidirectional water-wave energy, Joule 5 (2021) 1613–1623.

[649] H. Wen, P. Yang, G. Liu, S. Xu, H. Yao, W. Li, H. Qu, J. Ding, J. Li, L. Wan, Flower-like triboelectric nanogenerator for blue energy harvesting with six degrees of freedom, Nano Energy 93 (2022) 106796.

[650] T. Jiang, Y. Yao, L. Xu, L. Zhang, T. Xiao, Z.L. Wang, Spring-assisted triboelectric nanogenerator for efficiently harvesting water wave energy, Nano Energy 31 (2017) 560–567.

[651] K. Munirathinam, D.S. Kim, A. Shanmugasundaram, J. Park, Y.J. Jeong, D.W. Lee, Flowing water-based tubular triboelectric nanogenerators for sustainable green energy harvesting, Nano Energy 102 (2022) 107675.

[652] Y. Huang, T. Du, C. Xiang, Y. Zhang, J. Si, H. Yu, H. Yuan, P. Sun, M. Xu, Research progress of acoustic energy harvesters based on nanogenerators, Int. J. Energy Res. 2023 (2023) 5568046.

[653] A. Albareda, R. Pérez, Non-linear behaviour of piezoelectric ceramics, in: L. Pardo, J. Ricote (Eds.), Multifunctional Polycrystalline Ferroelectric Materials: Processing and Properties, Springer Netherlands, Dordrecht, 2011, pp. 681–726.

[654] G. Zhu, Y. Zhou, Z. Si, Y. Cheng, F. Wu, H. Wang, Y. Pan, J. Xie, C. Li, A. Chen, R. Wang, J. Sun, A multi-hole resonator enhanced acoustic energy harvester for ultra-high electrical output and machine-learning-assisted intelligent voice sensing, Nano Energy 108 (2023) 108237.

[655] H. Yuan, H. Yu, X. Liu, H. Zhao, Y. Zhang, Z. Xi, Q. Zhang, L. Liu, Y. Lin, X. Pan, M. Xu, A high-performance coniform helmholtz resonator-based triboelectric nanogenerator for acoustic energy harvesting, Nanomaterials 11 (2021).

[656] X. Xiao, L. Liu, Z. Xi, H. Yu, W. Li, Q. Wang, C. Zhao, Y. Huang, M. Xu, Research on an optimized quarter-wavelength resonator-based triboelectric nanogenerator for efficient low-frequency acoustic energy harvesting, Nanomaterials 13 (2023).

[657] H. Zhao, X. Xiao, P. Xu, T. Zhao, L. Song, X. Pan, J. Mi, M. Xu, Z.L. Wang, Dual-tube helmholtz resonator-based triboelectric nanogenerator for highly efficient harvesting of acoustic energy, Adv. Energy Mater. 9 (2019) 1902824.

[658] J. Yang, J. Chen, Y. Liu, W. Yang, Y. Su, Z.L. Wang, Triboelectrification-based organic film nanogenerator for acoustic energy harvesting and self-powered active acoustic sensing, ACS Nano 8 (2014) 2649–2657.

[659] Y.H. Ko, S.H. Lee, J.W. Leem, J.S. Yu, High transparency and triboelectric charge generation properties of nano-patterned PDMS, RSC Adv. 4 (2014) 10216–10220.

[660] M. Yuan, C. Li, H. Liu, Q. Xu, Y. Xie, A 3D-printed acoustic triboelectric nanogenerator for quarter-wavelength acoustic energy harvesting and self-powered edge sensing, Nano Energy 85 (2021) 105962.

[661] W. Sun, G. Ji, J. Chen, D. Sui, J. Zhou, J. Huber, Enhancing the acoustic-to-electrical conversion efficiency of nanofibrous membrane-based triboelectric nanogenerators by nanocomposite composition, Nano Energy 108 (2023) 108248.

[662] J. Yang, J. Chen, Y. Su, Q. Jing, Z. Li, F. Yi, X. Wen, Z. Wang, Z.L. Wang, Eardrum-inspired active sensors for self-powered cardiovascular system characterization and throat-attached anti-interference voice recognition, Adv. Mater. 27 (2015) 1316–1326.

[663] F. Chen, Y. Wu, Z. Ding, X. Xia, S. Li, H. Zheng, C. Diao, G. Yue, Y. Zi, A novel triboelectric nanogenerator based on electrospun polyvinylidene fluoride nanofibers for effective acoustic energy harvesting and self-powered multifunctional sensing, Nano Energy 56 (2019) 241–251.

[664] M. Javadi, A. Heidari, S. Darbari, Realization of enhanced sound-driven CNT-based triboelectric nanogenerator, utilizing sonic array configuration, Curr. Appl. Phys. 18 (2018) 361–368.

[665] B. Kim, H.J. Yoon, Y.J. Kim, B.J. Park, J.H. Jung, S.W. Kim, Ultrasound-driven triboelectric nanogenerator with biocompatible 2-hydroxyethyl methacrylate, ACS Energy Lett. 8 (2023) 3412–3419.

[666] H. Zhao, M. Xu, M. Shu, J. An, W. Ding, X. Liu, S. Wang, C. Zhao, H. Yu, H. Wang, C. Wang, X. Fu, X. Pan, G. Xie, Z.L. Wang, Underwater wireless communication via teng-generated Maxwell's displacement current, Nat. Commun. 13 (2022) 3325.

[667] D.M. Lee, N. Rubab, I. Hyun, W. Kang, Y.J. Kim, M. Kang, B.O. Choi, S.W. Kim, Ultrasound-mediated triboelectric nanogenerator for powering on-demand transient electronics, Sci. Adv. 8 (2024) eabl8423.

Dr K. Uday Kumar received his M. Sc (Electronics and Instrumentation) degree from the University College of Science, Osmania University, India. He obtained his Ph.D. degree in Physics from the Indian Institute of Technology Madras (IIT Madras), Chennai in 2016. He is currently an Assistant Professor at the Department of Physics, National Institute of Technology Warangal, India. His research focuses on Metal-Organic-Frameworks, Metal oxides, and 2D materials for different energy harvesting applications.

Dr Gokana Mohana Rani received her Master's Degree in Organic Chemistry from the Sri Padmavathi Mahila Visvavidyalayam, Tirupati Andhra Pradesh, India in 2015. She worked as a researcher at the Department of Chemistry, University of Delhi, Delhi, India. In August 2022 she obtained her PhD in Materials Science and Engineering from the National Taiwan University of Science and Technology, Taipei, China. Her research interests focus on energy harvesting and storage materials.

Dr Swati Panda is currently a postdoctoral student at Daegu Gyeongbuk Institute of Science and Technology (DGIST), South Korea. She recieved her PhD from DGIST, South Korea in Robotics and Mechatronics Engineering. She received her Bachelor's degree from Utkal University, Odisha, India in 2018. She pursued her Master's degree from Siksha O Anusandhan University, India with a specialization in Biotechnology in 2020. Her research interests focus on developing self-powered biosensors and biodegradable/biocompatible materials-based piezoelectric/triboelectric energy harvesters.

Dr Sugato Hajra is currently a postdoctoral researcher at Daegu Gyeongbuk Institute of Science and Technology (DGIST) South Korea. He received a Bachelor in Technology degree from Siksha O Anusandhan University, India, in 2017. He pursued his M. Tech. degree with a specialization in VLSI and Embedded Systems at Siksha O Anusandhan University, and also served as a joint researcher at the Advanced Multifunctional and Materials Laboratory in the Institute of Technical Education and Research, Bhubaneswar, India in 2019. He received the Ph.D. degree in the Department of Robotics and Mecharonics Engineering in 2024 from DGIST, South Korea. His research interests mainly include lead-free piezoelectric/multiferroics materials, metal–organic frameworks, solid-state electronic devices, and hybrid energy harvesters.

Dr Reddicherla Umapathi received his Master's Degree in Industrial Chemistry in March 2012 from Sri Venkateswara University, Tirupati, Andhra Pradesh, India. He obtained his Ph.D. in Chemistry in October 2017 from University of Delhi, Delhi, India. He worked as postdoctoral research fellow at the Chungnam National University, Daejeon, Republic of Korea (12/2017–02/2019) and National Taiwan University, Taipei, Taiwan (03/2019 -10/2019). Since November 2019, he is working as a Principal Researcher at the Department of Biological Sciences and Bioengineering, Inha University, Incheon. He is an Associate Fellow of Andhra Pradesh Akademi of Sciences, Andhra Pradesh, India. His research areas focus on triboelectric and piezoelectric nanogenerators, and advanced composite materials for electrochemical sensing applications.

Mr Kushal Ruthvik Kaja is currently a doctoral student at the Daegu Gyeongbuk Institute of Science and Technology. He received a Bachelor's degree from Andhra Loyola College, India, in 2021. He received his Master's in Physics from VIT-AP University, India, in 2023. His research interests focus on solid–solid, solid–liquid and waste-based triboelectric energy harvesters.

Mr Mohamed A. Belal is a PhD candidate in the Robotics and Mechatronics Engineering Department, Daegu Gyeongbuk Institute of Science and Technology (DGIST), South Korea. He worked as a lab engineer and research assistant at the Egypt-Japan University of Science and Technology (Egypt, 2021–2024). He received a master's degree in organic chemistry from the Chemistry Department at Alexandria University (Egypt, 2019) and a BSc in Chemistry/Physics from the Faculty of Science at Damanhur University (Egypt, 2007–2011). His research interest focuses on gas sensors, supercapacitors, and inkjet printing technologies.

Dr Yogendra Kumar Mishra is a Professor and the leader of the Smart Materials group at Mads Clausen Institute, NanoSYD, University of Southern Denmark (SDU). Before joining SDU, he led a group at the Functional Nanomaterials Chair, Kiel University, Germany, following anAlexander von Humboldt fellowship. He earned his habilitation (2015) in Materials Science from Kiel University and a PhD in Physics (2008) from Jawaharlal Nehru University (JNU) in New Delhi, India. He developed a new flame-based process for tetrapod nanostructuring and their 3D networks as cellular solids, which found many applications, including their use as sacrificial templates for structuring new materials. The Smart Materials group's main focus is to develop a new class of advanced materials for future green and sustainable technologies.

Dr Hoe Joon Kim is currently an Associate Professor in Robotics and Mechatronics Engineering with the Daegu Gyeongbuk Institute of Science and Technology (DGIST), Daegu, South Korea, and also holds a courtesy appointment in the Information and Communication Engineering Department at DGIST. He received the B.S. degree from Johns Hopkins University, Baltimore, MD, USA, in 2009, and the M.S. and Ph.D. degrees from the University of Illinois at Urbana–Champaign, Urbana, IL, USA, in 2011 and 2015, respectively, all in mechanical engineering. His research interests focus on piezoelectric MEMS resonators for RF wireless communication, nanogenerators, chemical/physical sensing, environmental monitoring, and emerging nanomaterials.

Dr Krystian Mistewicz received his MSc in physics with honors from the Mathematics and Physics Faculty at Silesian University of Technology (Gliwice, Poland) in 2010, and a Ph. D. in physics with distinction from the University of Silesia (Katowice, Poland) in 2015. He is currently an assistant professor at the Institute of Physics at Silesian University of Technology. He was a visiting research scholar at the University of Wisconsin–Madison (USA). His research interests are focused on nanotechnology, sonochemistry, ferroelectric nanomaterials for gas sensors, photovoltaic devices, and piezoelectric energy generators.

Dr Naratip Vittayakorn is a Professor of Materials Science and the Director of Advanced Materials Research (AMR) at King Mongkut's Institute of Technology Ladkrabang (KMITL) in Thailand. He earned his doctoral degree from Chiang Mai University, Thailand, and furthered his expertise as a visiting scientist at Iowa State University. With his impressive academic career, he has authored over 300 scholarly publications and holds 5 patents. His contributions to the fields of electroceramics, piezoelectricity, triboelectric nanogenerators, and the advancement of energy harvesting technology are noteworthy

Dr Yun Suk Huh is a university professor in the Department of Biological Engineering and the director of the NanoBio High-Tech Materials Research Center at INHA University, Korea. He received his Ph.D. in the Department of Chemical and Biomolecular Engineering from KAIST, Daejeon, Republic of Korea, in 2007. Before joining INHA University in 2013, he worked at KBSI in Daejeon for three years and served as a postdoctoral researcher at KAIST and Cornell University in the USA from 2007 to 2010. His research interests include the development of energy storage and conversion technologies, microfluidics, bio-hybrid nanomaterials for drug delivery and bioimaging, triboelectric nanogenerator devices, and the removal of radionuclides from the environment.

Dr Jiaqian Qin is Researcher at Metallurgy and Materials Science Research Institute, Chulalongkorn University (CU), Thailand. He received his PhD in physics from Sichuan University in 2010. Before joining CU in 2012, he has worked as JSPS Postdoctoral Researcher at Ehime University, Japan, for two years. His lab mainly works on rechargeable batteries. For details, please see the lab website: http://jiaqianqin.com.

Dr R. Rakesh Kumar received his Ph.D. from the Department of Instrumentation and Applied Physics, Indian Institute of Science Bangalore, India. He worked as visiting faculty at the Department of Physics, IISER-Bhopal in 2015. He is currently an Assistant Professor at the National Institute of Technology (NIT) Warangal, in the Dept. Of. Physics from 2018 onwards. His research interests are piezo and triboelectric nanogenerators, 2D materials, waste-to-energy, and self-powered sensors.